IECO

Volume 8 No 4 Year 2025

■ Volume 8

■ No 4

■ Year 2025

University of Sistan and Baluchestan

Iranian Association of Electrical and Electronics Engineers

International Journal Of

Industrial Electronics Control and Optimization

In This Issue:

Research Articles:

IECO

International Journal of Industrial Electronics Control and Optimization

About Journal

The University of Sistan and Baluchestan entered into strategic partnership with Iranian Association of Electrical and Electronic Engineers (IAEEE) to publish the **International Journal of Industrial Electronics Control and Optimization (IECO)**. The IECO is a refereed international journal which presents to the international scientific community important results of work in these fields, whether in the form of modeling simulation, analysis, fundamental research, development, application, design or real-time implementation. The scope of IECO is broad, encompassing all aspects of Industrial Electronics, Control and Optimization.

Note: International Journal of Industrial Electronics, Control and Optimization (IECO) has qualified to **ACADEMIC RESEARCH JOURNAL (ELMI-PAJOHESHI)** status certified by the ministry of Science, Research and Technology of Iran (No. 231566/3/18 dated 1396/10/09), and is published by the University of Sistan and Baluchestan through a formal partnership (No. 952/2/1500 dated 1395/11/04) with Iranian Association of Electrical and electronic Engineers (IAEEE) in order to develop scientific and research cooperation.

Aims and Scope

International Journal of Industrial Electronics, Control and Optimization (IECO) is a Peer reviewed journal of advanced and state-of-the-art in the science and engineering of Industrial Electronics, Control and Optimization. Its Scope encompasses the applications of Industrial Electronics, power systems, control, optimization and computational intelligence for the enhancement of industrial and manufacturing system and processes. The scope of the journal include the following:

I. Industrial Electronics

- Low and high-power converters
- Renewable energy
- Drive control techniques
- Techniques for advanced power semiconductor devices
- Power quality and utility applications
- Communications
- Flexible AC Transmission Systems (FACTS)
- Control in power electronics
- Electromagnetic and thermal performance of electronic power converters
- Motion control, robotics, sensors and actuators
- Fault detection and diagnosis
- Power systems
- Factory automation, communication, and computer networks

II. Control

- Adaptive control
- Control of process systems
- Control theory
- Data processing
- Design of control systems
- Hybrid systems
- Identification and observation
- Intelligent systems
- Model-predictive control
- Optimal control
- Robust control
- Fractional order systems

III. Optimization

- Ant Colony
- Chaos Theory
- Evolutionary Computing
- Fuzzy Computing
- Hybrid Methods
- Immunological Computing
- Neuro Computing
- Particle Swarm
- Probabilistic Computing
- Rough Sets
- Wavelet

International Journal Of
Industrial Electronics Control and Optimization
Print ISSN: 3517-2645
Online ISSN: 3568-2645
Homepage: https://ieco.usb.ac.ir/

A Multiport High Step-Up DC-DC Converter with a Bidirectional Port for Battery and Photovoltaic Panels Integration in Solar Power Plants

Hamed Abdi | Naghi Rostami | Ebrahim Babaei | Bulent Bilgehan

Faculty of Electrical and Computer Engineering, University of Tabriz, Tabriz, Iran.[1,2,3]
Engineering Faculty, Near East University, 99138 Nicosia, North Cyprus, Mersin 10, Turkey.[3,4]
Corresponding author's email: e-babaei@tabrizu.ac.ir

Article Info

Article type:
Research Article

Article history:
Received: 02-March-2025
Received in revised form: 27-April-2025
Accepted: 14-May-2025
Published online: 22-Dec-2025

Keywords:
Battery storage system,
Multi-port DC-DC converter,
Non-isolated power converter,
Solar power plant.

ABSTRACT

In solar power plants with energy storage systems (ESSs), a multi-port DC-DC converter equipped with a bidirectional port is more favorable than multiple single-input converters due to its simpler control, lower cost, and higher power density. This paper proposes a novel multiport DC-DC converter equipped with a bidirectional port for solar power plants. The proposed converter integrates a multi-input cascaded structure with a switched capacitor cell, a three-winding coupled inductor, and a bidirectional port connected to the ESS. Key advantages of the proposed converter include low normalized pick inverted voltage (NPIV) on semiconductor elements, continuous input current with low ripple, high voltage gain, common ground, and high efficiency. Furthermore, the converter can operate under different operating states, enabling flexible energy management strategies within the grid. The various operating states of the proposed converter are analyzed in steady state, and the validation of the mentioned advantages is supported by presenting comparative results with other DC-DC converters. Finally, the results obtained from the analysis of the proposed converter are validated through simulations performed utilizing a co-simulation link between MATLAB and PSCAD/EMTDC software.

I. Introduction

In recent years, due to the energy crisis and global warming caused by the excessive use of fossil fuels, the utilization of renewable energy sources (RES) has significantly increased as an alternative [1]. Among these sources, photovoltaic (PV) energy has gained popularity due to the easy accessibility of sunlight. The primary challenges of PV energy lie in its strong dependence on environmental conditions and the mismatch between its output voltage (20-40 V) and the voltage levels of the DC bus (400 V) and auxiliary equipment (12-60 V) [2]. Therefore, to manage power in the grid, an ESS is employed alongside the solar power plant as the energy buffer. Additionally, DC-DC converters are utilized as interface devices to accommodate and boost the voltage of solar panels, enabling their connection to the ESS and DC bus [3].

In traditional systems, each PV string and ESS are connected to the DC bus using separate unidirectional and bidirectional converters, respectively [4]. While these systems offer high reliability, and energy management between sources and loads becomes complex due to multiple power exchange paths. Additionally, the multiple energy conversion stages result in significant losses. So, as shown in Fig.1, employing a multi-port DC-DC converter with a

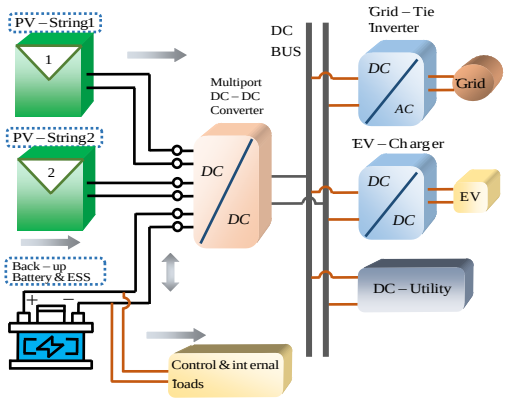

Fig. 1. Structure of DC microgrid in the presence of PV panels and ESS.

centralized controller is a more efficient solution [5], [6].

Multi-port DC-DC converters are categorized into isolated and non-isolated types [7]. Isolated multi-port converters are not commonly utilized in RES unless galvanic isolation between the input and output and high safety is required, owing to the high cost and complexity of transformer design [8]. In contrast, non-isolated multi-port DC-DC converters are widely utilized due to their design simplicity and high voltage gain. Incorporating coupled inductors and voltage-boosting cells allows non-isolated converters to achieve high voltage gains, making them suitable for DC microgrids [9]. Voltage-boosting cells encompass various types such as switched capacitors, switched inductors, resonant capacitors, and inductor-capacitor voltage multipliers [10]. Also, in the design of non-isolated converters for PV systems, key features including input current continuity, common ground between input and output, low voltage stress on semiconductors, and high efficiency should be considered [11].

In recent years, numerous research articles on high-step-up DC-DC converters have been published in various journals. In [12] and [13], two non-isolated high step-up DC-DC converters are proposed for application in solar energy systems. These converters combine basic topologies with coupled inductors and voltage multiplier cells to enhance the voltage gain. However, despite these enhancements, the converters still suffer from low voltage gain and high power losses when operating at high-duty cycles to supply the high-voltage DC bus. In [14], a high step-up DC-DC converter with a continuous input current is proposed. Although this converter provides a high voltage gain, the absence of a defined path for the leakage current of the secondary winding of the coupled inductor leads to a high voltage spike across the output diode, thereby reducing the converter's efficiency and reliability. In [15], an interleaved DC-DC converter with high voltage gain is proposed. Owing to the integration of the interleaved structure with a coupled inductor, the converter achieves a high voltage gain while maintaining low voltage stress on the semiconductor devices. However, the absence of a common ground introduces challenges related to leakage capacitance and electromagnetic interference (EMI).

Various isolated and non-isolated multi-port DC-DC converters have been introduced in the literature in recent years. In [16], a non-isolated multi-port DC-DC converter with the ability to implement independent MPPT on its input panels is presented. However, due to the absence of a bidirectional port in this configuration, integrating an ESS with the panels is impossible, which leads to an increase in the system's size, cost, and control complexity. In [17], an isolated multi-port structure is presented. This configuration provides galvanic isolation between the input and output ports, ensuring high safety. However, due to the use of two isolation transformers and a large number of capacitors, it comes with design complexities, increased size, and higher costs. The converter presented in [18] addresses the issues mentioned in the previous sources by introducing a new path for bidirectional power flow between the battery and other ports. This converter enables the implementation of various scenarios and allows for applying different energy management algorithms (EMA) to the sources and loads. However, the extensive use of inductors and the high voltage stress on semiconductor devices have led to an increase in circuit size and volume, a reduction in converter reliability, and limitations on employing low-voltage, low-resistance switches, which in turn result in higher power losses. In [19], an isolated multi-port DC-DC converter is proposed for solar energy systems. Similar to the converter presented in [18], it offers the capability to implement various energy management scenarios. However, its practical implementation is challenged by complex commutation and the use of a three-winding isolation transformer, which complicates the design and assembly process. In [20] and [21], two non-isolated multi-port converters are proposed for applications in RES and DC motor drives, respectively. These topologies employ a combination of conventional structures with switched inductor cells to enhance voltage gain. However, the large number of elements involved makes their industrial implementation challenging.

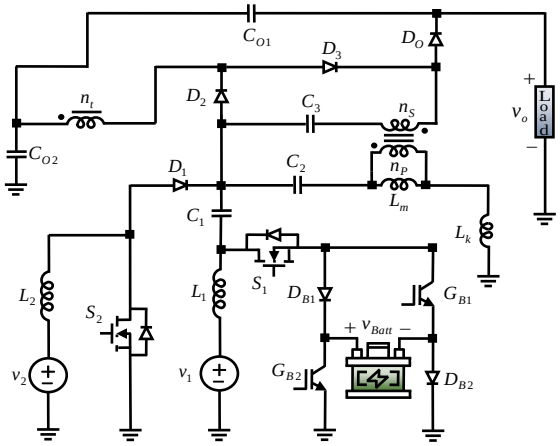

Fig. 2. Proposed structure.

Considering the challenges identified in the reviewed literature and the specific requirements for converters used in photovoltaic power plants, this paper proposes a non-isolated multi-port DC-DC converter equipped with a bidirectional port for PV applications. As depicted in Fig. 2, the proposed converter combines a cascaded multi-input topology with a switched capacitor cell, a three-winding coupled inductor, a battery, and a bidirectional port. The key features of the proposed converter include:

i. The ability to integrate two PV strings with a storage battery and auxiliary loads of the solar plant, which reduces volume, cost, losses, and control complexity.
ii. Common ground between the output and panel ports, which reduces the leakage capacitance.

iii. High voltage gain and continuous input current with a very low ripple in panel ports.
iv. Low voltage stress across semiconductor elements.
v. The ability to operate in different operating states, facilitating the implementation of various energy management strategies within the grid.

The remainder of the paper is organized as follows. Section II presents the elements of the proposed converter and explains its different operating states. In Section III, the steady-state analysis of the converter is carried out, along with design considerations for its elements. Section IV provides the results of the loss analysis. In Section V, the feasibility of implementing various EMAs using the converter is evaluated through a comprehensive control strategy. Sections VI, VII, and VIII, respectively, discuss the comparison study, simulation results, and conclusions.

II. Proposed Structure and Operation Principles

As depicted in Fig. 2, the proposed converter comprises two MOSFETs (S_1 and S_2), two IGBTs (G_{B1} and G_{B2}), six diodes ($D_1 - D_3$, D_O, D_{B1}, and D_{B2}), five capacitors (C_1 - C_3, C_{O1} and C_{O2}), two inductors (L_1 and L_1), and a coupled inductor with turn ratios of n_1 (n_S/n_P) and n_2 (n_t/n_P). The proposed converter operates in three different operating states, with the switching waveforms of the switches as well as the current and voltage waveforms of the diodes and switches illustrated in Figs. 3 and 4. Also, the equivalent circuits corresponding to the sub-modes of the proposed converter are presented in Fig. 5. The switching waveforms are illustrated under steady-state conditions, considering component parasitics. In the equations, L_m and L_k represent magnetizing and leakage inductances, respectively, with the coupling coefficient defined as $k = L_m / (L_m + L_k)$. Also, the

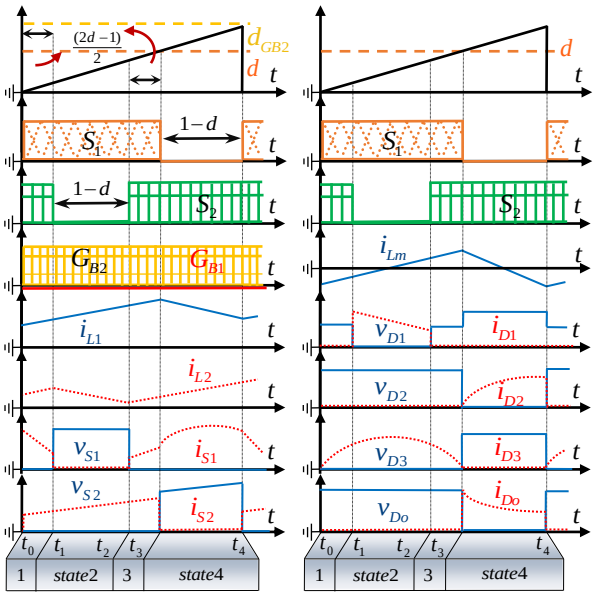

(a) (b)

Fig. 3. Switching waveforms of the proposed converter in state 1.

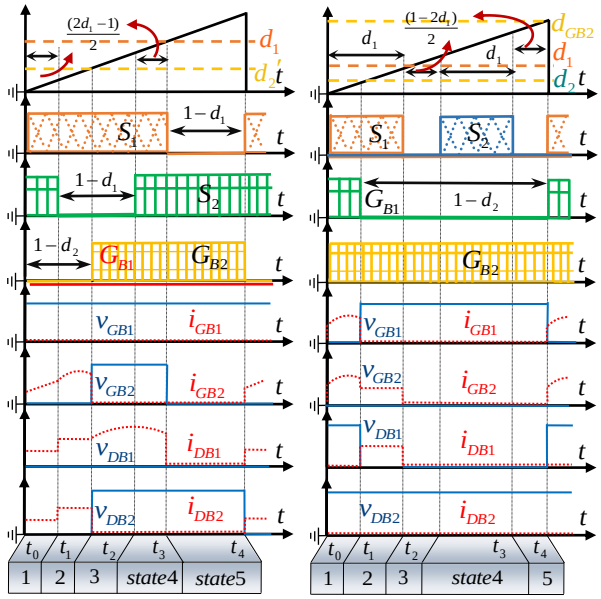

(a) (b)

Fig. 4. Switching waveforms of the proposed converter in different states. (a) state 1 and (b) state 2.

switching pattern of the proposed converter is also presented in Table I. This table provides information regarding the on/off states of switches and diodes, the charging and discharging behavior of passive components, and the battery's operational status in different operating modes.

A. First Operating State [DISO State]

Sub-modes 1 and 3 ([$t_0 \sim t_1$] and [$t_2 \sim t_3$], [Fig.5(a)]): In mode 1, as depicted in Fig. 3, switch S_1 is turned on upon receiving a pulse and remains ON during mode 3 as well. Similarly, switch S_2 is turned on at the beginning of mode 3 and remains ON in mode 1, leading to the reverse biasing of diodes D_1, D_2, and D_O and the forward biasing of diode D_3 in both sub-modes. Also, during these sub-modes, inductors L_1 and L_2 are charged by their respective input sources, while C_{O1} and C_{O2} supply the output load. Simultaneously, C_2 charges both the magnetizing inductor L_m and capacitor C_1.

Sub-mode 2 ([$t_1 \sim t_2$], [Fig.5(b)]): In mode 2, as depicted in Fig. 3, switch S_1 is still ON while switch S_2 is turned off at the beginning of the interval, leading to the reverse biasing of diodes D_2 and D_O and the forward biasing of diodes D_1 and D_3. Also, during this sub-mode, L_1 is charged by input source V_{in1}, while L_2 charges capacitor C_1; and capacitors C_{O1} and C_{O2} supply the output load. Simultaneously, capacitor C_2 charges both the magnetizing inductor L_m and capacitor C_1.

Sub-mode 4 ([$t_3 \sim t_4$], [Fig.5(c)]): As depicted in Fig. 3, in mode 4, switch S_1 is turned off at the beginning of the interval while switch S_2 is turned on upon receiving a pulse, leading to the reverse biasing of diodes D_1 and D_3 and the forward biasing of diodes D_2 and D_O. During this sub-mode, inductor L_2 is charged by input source V_{in2}, while inductor L_2 and capacitor C_1 charge capacitor C_2 and supply the load.

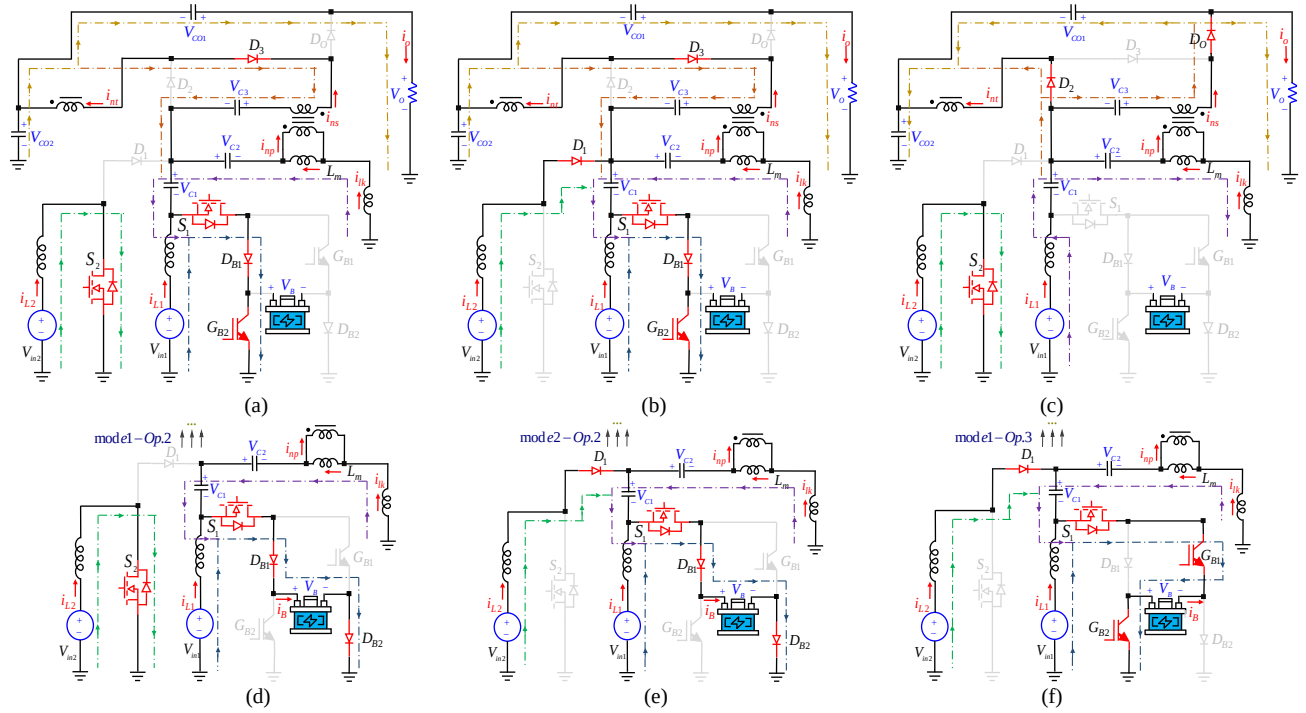

Fig. 5. Equivalent circuits related to different modes of the proposed converter in operating states 1,2, and 3. (a) State 1-mode 1 and 3, (b) State 1-mode 2, (c) State 1-mode 4, (d) State 2-mode 1, (e) State 2-mode 2, (f) State 3- mode 1.

Simultaneously, capacitor C_3 and the magnetizing inductor L_m charge capacitors C_{O1} and C_{O2} and supply the load.

B. Second Operating State [DIDO State]

This state corresponds to scenarios where the power generated by the panels exceeds the bus's demand or when the battery's state of charge (SOC) is low. As depicted in Fig. 4(a), it consists of five sub-modes. As evident from Fig. 4(a), with full turning off of switch G_{B1} and a delayed commutation of switch G_{B2}, the input sources charge the battery during sub-modes 1 and 2 (Figs. 5(d) and (e)), and the output load is supplied by the input panels simultaneously. Also, detailed patterns of switch and diode states are provided in Table I.

C. Third Operating State [TISO State]

This state pertains to scenarios where the power demanded by the DC bus exceeds the power generated by the panels and the SOC of the battery is high, prompting the battery to enter the discharge mode. As shown in Fig. 4(b), it consists of five sub-modes. As evident from Fig. 4(b), with full commutation of switch G_{B2} and commutation of switch G_{B2} in sub-mode 1, the battery is discharged to the load during sub-mode 1 (Fig. 5(f)). Also, detailed patterns of switch and diode turn-on and turn-off sequences are provided in Table I.

III. Steady-State Analysis of the Converter

A. Voltage Analysis

By applying Kirchhoff's Voltage Law (KVL) to the sub-modes corresponding to the first operating state of the proposed converter, the voltage across the magnetic elements during the ON-state of switch S_1 can be derived as follows:

$$V_{L1}{}^{ON} = V_{in1} \quad (1)$$

$$V_{L2}{}^{ON} = V_{in2} \quad (2)$$

$$V_{Lm}{}^{ON} = kV_{in1} \quad (3)$$

Similarly, by performing the same analysis during the OFF-state of switch S_1, the voltages across the magnetic elements can be calculated as follows:

$$V_{L1}{}^{OFF} = -\frac{dV_{in1}}{(1-d)} \quad (4)$$

$$V_{L2}{}^{OFF} = -\frac{dV_{in2}}{(1-d)} \quad (5)$$

$$V_{Lm}{}^{OFF} = -\frac{dkV_{in1}}{(1-d)} \quad (6)$$

Also, utilizing the volt-second balance principle for the inductors in the first operating state, the capacitor voltage relations can be expressed as follows:

$$V_{C1} = \frac{V_{in2}}{1-d} \quad (7)$$

$$V_{C2} = \frac{(1-d)V_{in1}+V_{in2}}{1-d} \quad (8)$$

$$V_{C3} = \frac{n_1k(1-d)+n_2k+1}{1-d}V_{in1} \quad (9)$$

$$V_{CO1} = \frac{k(n_1+n_2-n_2d)+1}{1-d}V_{in1} \quad (10)$$

$$V_{CO2} = \frac{(n_2kd+1)V_{in1}+V_{in2}}{1-d} \quad (11)$$

Considering (7) - (11), and utilizing KVL, the output voltage can be written as:

$$V_{O,OP1} = \frac{(k(n_1+n_2)+2)V_{in1}+V_{in2}}{(1-d)} \quad (12)$$

By applying an approach similar to that used for the first state, the capacitors and output voltage relationships for the second operating state can be derived as follows:

$$V_{C1} = \frac{2V_{in2}-(3-2d_2-2d_1)V_B}{2(1-d_1)} \quad (13)$$

TABLE I Switching Pattern of the Proposed Converter in Different States

Modes	Sub-modes	Duration	Input Port 1 (charge=Ch)	Input Port 2 (charge=Ch)	Batt. Port	Gate Signals				Diodes State (ON=1 / OFF=0)						Active Ports
						S_1	S_2	GB_1	GB_2	D_1	D_2	D_3	D_O	DB_1	DB_2	
1: No Battery Contrib-ution	1-1	$(2d-1)/2$	Ch-L_1	Ch-L_2	OFF	1	1	0	1	0	0	1	0	1	0	3
	1-2	$(1-d)$	Ch-L_1	Ch-C_1	OFF	1	0	0	1	1	0	1	0	1	0	3
	1-3	$(2d-1)/2$	Ch-L_1	Ch-L_2	OFF	1	1	0	1	0	0	1	0	1	0	3
	1-4	$(1-d)$	Supply-R_O	Ch-L_2	OFF	0	1	0	1	0	1	0	1	0	0	3
2: Battery Char-ging	2-1	$(2d_1-1)/2$	Ch-L_1/Batt	Ch-L_2	ON	1	1	0	0	0	0	0	0	1	1	4
	2-2	$\frac{3-2(d_1+d_2)}{2}$	Ch-L_1/Batt	Ch-C_1/Batt	ON	1	0	0	0	1	0	0	0	1	1	4
	2-3	$(2d_2-1)/2$	Ch-L_1	Ch-C_1	OFF	1	0	0	1	1	0	1	0	1	0	3
	2-4	$(2d_1-1)/2$	Ch-L_1	Ch-L_2	OFF	1	1	0	1	0	0	1	0	1	0	3
	2-5	$(1-d_1)$	Supply-R_O	Ch-L_2	OFF	0	1	0	1	0	1	0	1	0	0	3
3: Battery Dischar-ging	3-1	d_2	Ch-L_1	Ch-C_1	ON	1	0	1	1	1	0	1	0	0	0	4
	3-2	d_1-d_2	Ch-L_1	Ch-C_1	OFF	1	0	0	1	1	0	0	0	1	0	3
	3-3	$(1-2d_1)/2$	Supply-R_O	Supply-R_O	OFF	0	0	0	1	1	0	0	1	0	0	3
	3-4	$d_1\ d_1$	Supply-R_O	Ch-L_2	OFF	0	1	0	1	0	1	0	1	0	0	3
	3-5	$(1-2d_1)/2$	Supply-R_O	Supply-R_O	OFF	0	0	0	1	1	1	0	1	0	0	3

TABLE II Defining α and ξ coefficients

$\alpha_1 = kn_1(1-d_1) + kn_2 + 1$	$\alpha_2 = kn_2(1-d_1) + kn_1 + 1$	$\alpha_3 = 2(1 + kn_2d_1)$
$\alpha_4 = 4 + 2kn_2 + 2kn_1$	$\alpha_5 = {d_1}^2(1+kn_1) - d_1(kn_2 + 2n_1k - 1) + k(n_1+n_1)$	$\alpha_6 = {d_1}^2(1+kn_2) - d_1(kn_1 + 2n_2k - 1) + k(n_1+n_1)$
$\alpha_7 = d_1(1 + kn_2 - d_1kn_2)$	$\alpha_8 = {d_1}^2 + d_1(2 - kn_2 - n_1k) + k(n_1+n_1)$	
$\zeta_1 = {d_1}^2 + d_1(2 - kn_2 - n_1k) + k(n_1+n_1)$	$\zeta_2 = kn_1(d_1-1) - 1 + d_2 + (k - 1 - kd_1 + d_1)$	$\zeta_3 = -(5 - 4d_2 - 2d_1 + 2n_2k(1-d_2))$
$\xi_5 = {d_1}^2(kn_1 + kn_2 + 1) - d_1(2kn_1 + 2kn_2 + d_2kn_2 + d_2 + 2) + (kn_1 + kn_2 + 1 + d_2(1+n_2k))$	$\xi_6 = {d_1}^2(kn_1 + kn_2 + 1) - d_1(2kn_1 + 2kn_2 + d_2kn_1 + d_2 + 2) + (kn_1 + kn_2 + 1 + d_2(1+n_1k))$	$\xi_8 = {d_1}^2(kn_1 + kn_2 + 1) - d_1(2kn_1 + 2kn_2 + d_2kn_1 + d_2kn_2 + d_2 + 2) + (kn_1 + kn_2 + 1 + d_2(2 + n_1k + n_2k))$
$\zeta_4 = 8d_2 - 9 - 2kn_1(1-d_1) + 2k + 2d_1 - 2k(n_2 + d_2 - d_2n_2)$	$\zeta_7 = d_2(1 + n_2k - d_1n_2k)$	

$$V_{C2} = \frac{2(1-d_1)V_{in1} + 2V_{in2} - (3-2d_2-2d_1)V_B}{2(1-d_1)} \quad (14)$$

$$V_{C3} = \frac{\alpha_1 V_{in1} + \xi_1 V_B}{(1-d_1)} \quad (15)$$

$$V_{CO1} = \frac{\alpha_2 V_{in1} + \xi_2 V_B}{(1-d_1)} \quad (16)$$

$$V_{CO2} = \frac{\alpha_3 V_{in1} + 2V_{in2} + \xi_3 V_B}{2(1-d_1)} \quad (17)$$

$$V_{O,OP2} = \frac{\alpha_4 V_{in1} + 2V_{in2} + \xi_4 V_B}{2(1-d_1)} \quad (18)$$

Furthermore, it can be written for the third state as follows:

$$V_{C1} = \frac{(2d_1-1)V_{in1} + (1-d_1)V_{in2} + d_1d_2V_B}{(1-d_1)^2} \quad (19)$$

$$V_{C2} = \frac{\alpha_1 V_{in1} + \xi_1 V_B}{(1-d_1)} \quad (20)$$

$$V_{C3} = \frac{\alpha_5 V_{in1} + \xi_5 V_B}{(1-d_1)^2} \quad (21)$$

$$V_{CO1} = \frac{\alpha_6 V_{in1} + \xi_6 V_B}{(1-d_1)^2} \quad (22)$$

$$V_{CO2} = \frac{\alpha_7 V_{in1} + (1-d_1)V_{in2} + \xi_7 V_B}{(1-d_1)^2} \quad (23)$$

$$V_{O,OP3} = \frac{\alpha_8 V_{in1} + (1-d_1)V_{in2} + \xi_8 V_B}{(1-d_1)^2} \quad (24)$$

Also, α_1-α_8 and ξ_1-ξ_8 coefficients are defined in Table II.

B. Current Analysis

By neglecting the power losses of the converter and using Kirchhoff's Current Law (KCL) along with the average model, the average current of the magnetizing elements in the converter during the first operating state is calculated as follows:

$$I_{L1} = \frac{n_1+n_2+2}{(1-d)} I_O \quad (25)$$

$$I_{L2} = \frac{1}{(1-d)} I_O \quad (26)$$

$$I_{Lm} = 0 \quad (27)$$

Also, the coupled inductor winding currents are calculated as presented in Table III. Furthermore, the battery's instantaneous currents in sub-modes corresponding to states 2 and 3 are also listed in Table III. For calculating the average battery current, only the instantaneous currents in sub-modes 1 and 2 of the second state and sub-mode 1 of the third state are used. Moreover, the instantaneous currents of the capacitors in the first state and their corresponding RMS values are calculated and presented in Table IV.

C. Voltage and Current Stress of Semiconductors

Among the critical factors in selecting switches and diodes for converters are their voltage and current stresses. The NPIV of a switch represents the voltage across it during its off-state. Similarly, the current stress refers to the instantaneous current flowing through the switch during its operation. Based on these considerations, NPIV, current stresses, and rms current of switches and diodes of the converter are calculated and presented in Table V.

D. Boundary Conduction Mode

For the proposed converter to operate in continuous conduction mode (CCM), the minimum current of the input inductors must remain greater than zero. Considering this condition, along with (26) and by applying KVL in the

TABLE III Battery and coupled-inductor current relations

States	i_B in different sub-modes (Instantaneous current)
State. 2	$i_B{}^1 = \frac{n_1+n_2+2}{(1-d_1)} I_O \quad i_B{}^2 = \frac{n_1+n_2+3}{(1-d_1)} I_O \quad i_B{}^5 = 0$
	$i_B{}^3 = \frac{(1-d_1)(n_1+n_2)+(d_1+d_2-1)(n_1+n_2+3)}{(1-d_1)(d_1+d_2-1)} I_O$
	$i_B{}^4 = \frac{(1-d_1)(n_1+n_2)+(d_1+d_2-1)(n_1+n_2+2)}{(1-d_1)(d_1+d_2-1)} I_O$
State. 3	$i_B{}^1 = i_B{}^2 = \frac{n_1+n_2+2d_1+1}{d_1(1-d_1)} I_O$
States	I_B in different modes (Average current)
State. 2	$I_B = \frac{2(n_1+n_2)+7-2d_1-2d_2(n_1+n_2+3)}{2(1-d_1)} I_O$
State. 3	$I_B = \frac{d_2(n_1+n_2+2d_1+1)}{d_1(1-d_1)} I_O$

Coupled-Inductor	Coupled-inductor instantaneous current in state 1		
Sub-modes	i_{np}	i_{ns}	i_{nt}
1,2,3	$-\frac{I_O}{d}(n_1+n_2)$	$-\frac{I_O}{d}$	$-\frac{I_O}{d}$
4	$\frac{I_O}{(1-d)}(n_1+n_2)$	$\frac{I_O}{(1-d)}$	$\frac{I_O}{(1-d)}$

TABLE IV Capacitors' currents in state 1

Element	Mode 1	Mode 2	
C_1	$\frac{n_1+n_2+1}{4d} I_O$	$\frac{n_1(1-d)+n_2(1-d)+1}{d(1-d)} I_O$	
Element	Mode 3	Mode 4	RMS
C_1	$\frac{3(n_1+n_2+1)}{4d} I_O$	$-\frac{n_1+n_2+2}{(1-d)} I_O$	$\frac{n_1+n_2+2}{\sqrt{d(1-d)}} I_O$
Element	Modes 1, 2, 3	Mode 4	RMS
C_2	$-\frac{(n_1+n_2)}{d} I_O$	$\frac{(n_1+n_2)}{(1-d)} I_O$	$\frac{n_1+n_2}{\sqrt{d(1-d)}} I_O$
C_3	$\frac{1}{d} I_O$	$-\frac{1}{(1-d)} I_O$	$\frac{1}{\sqrt{d(1-d)}} I_O$
C_{O1}	$-I_O$	$\frac{d}{(1-d)} I_O$	$\frac{\sqrt{d}}{\sqrt{(1-d)}} I_O$
C_{O2}	$-\frac{1+d}{d} I_O$	$\frac{1+d}{(1-d)} I_O$	$\frac{1+d}{\sqrt{d(1-d)}} I_O$
L_k	$\frac{(n_1+n_2)}{d} I_O$	$-\frac{(n_1+n_2)}{(1-d)} I_O$	$\frac{n_1+n_2}{\sqrt{d(1-d)}} I_O$

corresponding sub-modes, the following condition for CCM operation with inductor L_2 can be derived.

$$L_2 > \frac{d(1-d)^2 R_O}{2(n_1+n_2+3) f_S} \quad (28)$$

Additionally, the graph related to this condition is plotted in Fig. 6, illustrating the values of inductor L_2 for continuous, discontinuous, and boundary conduction modes.

IV. Efficiency Analysis Results

In this section of the paper, the losses of the proposed converter are calculated following the procedure outlined in [22]. To avoid unnecessary length, only the final results are presented. In these calculations, the losses considered include conduction and switching losses of the switches and diodes, conduction losses of the capacitors, as well as both core and conduction losses of the inductors and the coupled inductor. So, based on the calculated losses, the overall efficiency of the converter is obtained using the following:

TABLE V Voltage and current stress of semiconductors

S,D		Instantaneous	RMS	NPIV
S_1	Mode 1	$\frac{(1+3d)(n_1+n_2+1)+4}{4d(1-d)}$	$\frac{(n_1+n_2+2)I_O}{(1-d)\sqrt{d}}$	$\frac{V_O}{2n+3}$
	Mode 2	$\frac{n_1+n_2+1+2d}{d(1-d)} I_O$		
	Mode 3	$\frac{(7-3d)(n_1+n_2+1)+4}{4d(1-d)}$		
S_2		$\frac{I_O}{(1-d)}$	$\frac{\sqrt{d} I_O}{(1-d)}$	$\frac{V_O}{2n+3}$
D_1		$\frac{I_O}{(1-d)}$	$\frac{I_O}{\sqrt{(1-d)}}$	$\frac{2V_O}{2n+3}$
D_2		$\frac{I_O}{(1-d)}$	$\frac{I_O}{\sqrt{(1-d)}}$	$\frac{(1+n)V_O}{2n+3}$
D_3		$\frac{I_O}{d}$	$\frac{I_O}{\sqrt{d}}$	$\frac{(1+2n)V}{2n+3}$
D_O		$\frac{I_O}{(1-d)}$	$\frac{I_O}{\sqrt{(1-d)}}$	$\frac{(1+n)V_O}{2n+3}$

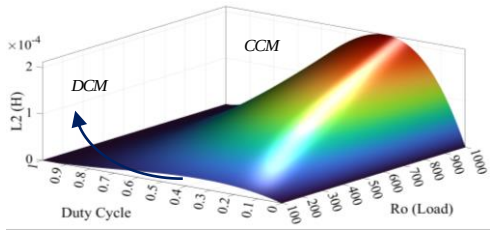

Fig. 6. Boundary condition for inductor L_2.

$$\eta(\%) = \frac{(P_{out})\times 100}{(P_{out}+(P_{cond,L}+P_{core,L}+P_{cond,S,D}+P_{sw,S,D}+P_{cond,C}))} \quad (29)$$

The calculated results for the efficiency and power losses of the proposed converter in the first operating state are illustrated in Figs. 7 and 8. Fig. 7(a) presents the efficiency of the proposed converter at various power levels and input voltages. As shown in this figure, the maximum efficiency of the converter is achieved at an output power of 100 W for all considered input voltages. Figs. 7(b) and (c) illustrate the percentage of power losses associated with different elements of the converter under various input voltages.

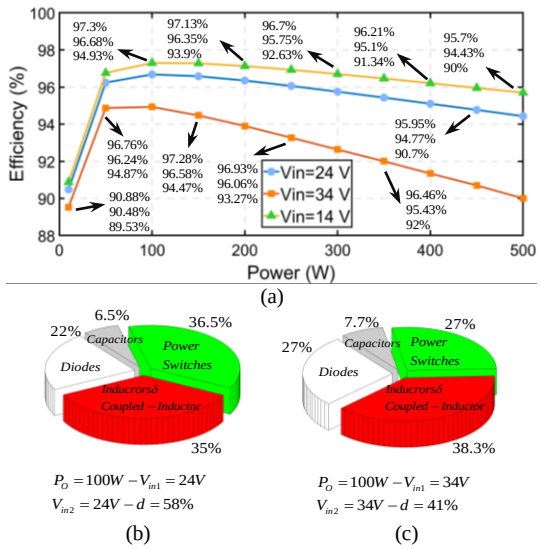

Fig. 7. (a) Efficiency curves of the proposed converter in different powers, (b) and (c) Loss percentage of the converter in different input voltages.

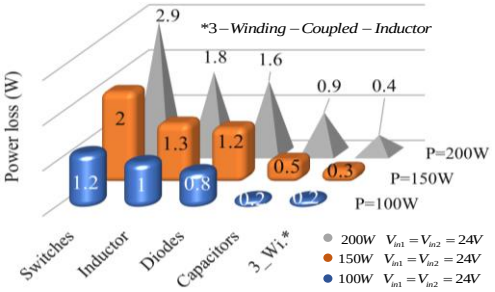

Fig. 8. Loss distribution of the converter in different powers.

V. Energy Management Algorithm for the Proposed Converter

To assess the converter's performance under various energy management conditions, it is tested using an algorithm similar to [5], shown in Fig. 9. The algorithm considers the internal loads, battery, PV panels, and DC/AC buses as system inputs/outputs, assuming normal grid and load operation. In the evening, the battery's charge rate is increased to support night-time loads. Energy management mainly depends on grid demand, PV generation, and battery SOC. If PV power is insufficient, the battery supplies the load (Scenario 3); otherwise, excess energy charges the battery or feeds auxiliary loads.

VI. Comparison Study

This section compares the proposed converter with other recent dual- and multi-port high-step-up DC-DC converters. Key specs from [6], [18], [23]–[27] are listed in Table VI, and cost estimates appear in Table VII, based on components selected for the simulation power level. Comparative analysis includes voltage gain (Figs. 10(a) and b), voltage stress (Fig. 10(c)), cost (Figs. 11(a)), and efficiency (Fig. 11(b)), using standard components detailed in Table VIII. The evaluation covers voltage gain, stress, ripple, EMI, element count, efficiency, cost, number of ports, and supported operating scenarios.

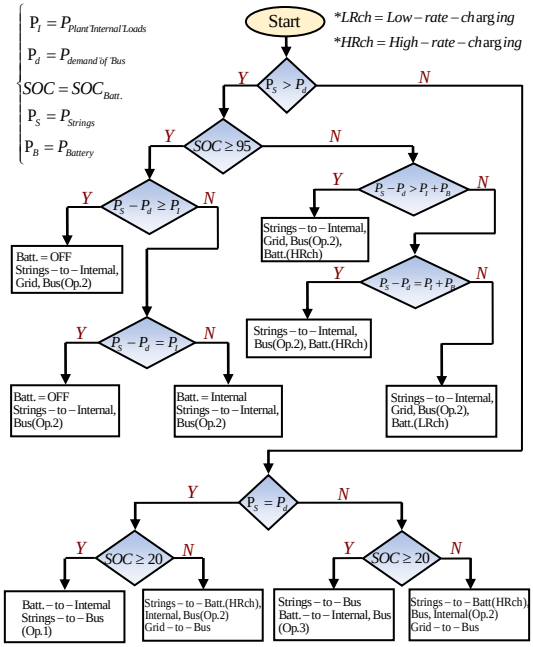

Fig. 9. Energy management algorithm for the proposed converter

As shown in Table VI and Fig. 10(a), the proposed converter achieves the highest voltage gain—27 at a 0.5 duty cycle—about 15 units more than converters [18], [25], and [26]. This is due to its use of a three-winding coupled inductor and a switched-capacitor cell, unlike [25] with only two windings and [18], [26] which lack coupled inductors.

As shown in Table IV, aside from converter [24], the proposed converter and converter [17] have the highest number of elements. This is due to their multiple ports and support for various operating scenarios, which require additional auxiliary components. Both topologies allow independent battery switching within multi-input structures, enabling flexible energy management through simpler control and relatively fewer total components. According to Fig. 10(b), the proposed converter achieves a voltage gain-to-

TABLE VI Detailed specifications of the proposed converter and the converters proposed in [6], [18], [23], [24], [25], [26], and [27]

Parameters		Multi-port Converters					Dual-Port Converters		Proposed Converter
		[6]	[18]	[23]	[24]	[25]	[26]	[27]	
Elements*	S	4	4	6	4	2	1	1	4
	D	4	5	1	6	4	6	5	6
	C	4	4	4	8	5	5	7	5
	L	4	4	4	0	2	2	4	2
	T/CI	0	0	0	2	1	0	0	1
	Total	16	17	15	20	14	14	16	18
Voltage gain		$\frac{3-2d}{(1-d)^2}$	$\frac{3}{(1-d)^2}$	$\frac{3-d}{(1-d)^2}$	$\frac{n(1+d)}{(1-d)}$	$\frac{4+2nd}{(1-d)}$	$\frac{2(2-d)}{(1-d)^2}$	$\frac{1+2d-2d^2}{(1-d)^2}$	$\frac{4n+2+d+d^2-4dn}{(1-d)^2}$
Inputs/outputs		3/1	2/1 – 3/1 – 2/2	2/1	1/2	2/1	1/1	1/1	2/1 – 3/1 – 2/2
Non-isolated		Yes	Yes	Yes	No	Yes	Yes	Yes	Yes
EMI		Low	Low	Low	Low	High	High	Low	Low
ANPIV		$\frac{9-7d}{8(3-2d)}$	$\frac{18-9d}{27}$	$\frac{13-7d}{8(3-d)}$	$\frac{4+6n}{10n(1+d)}$	$\frac{4+n}{6(2+nd)}$	$\frac{11-6d}{14(2-d)}$	$\frac{5+2d^2-d}{6(1+2d-2d^2)}$	$\frac{11+4n-4d}{20n+30}V_o$
I.C.R.*		Low	Low	Low	High	Low	Low	Low	Low
η (%)		Not given	94.2% (100 W)	94% (100 W)	95.5% (250 W)	93.34% (100 W))	94.6% (100 W)	85.4% (100 W)	96.68% (100 W)

*S**: Switch, *D**: Diode, *C**: Capacitor, *I**: Inductor, *T**: Transformer, *CI**: Coupled inductor, *I.C.R.**: Input current ripple.

TABLE VII Cost calculations of the proposed converter and the converters in [6], [18], and [24]-[26].

Ref.	Switches Cost	Diodes Cost	Capacitors Cost	Cores Cost	Total Cost
[6]	4*0.42 $	4*1.06 $	1*0.1 $, 1*0.1 $ 1*0.1 $, 1*1.5 $	4*2.5 $	17.72 $
[18]	1*12.44 $, 3*1.9 $	2*0.8 $, 1*0.7 $, 2*0.31	3*0.5 $, 1*1.5 $	4*0.4 $	25.66 $
[24]	4*0.74 $	6*0.8 $	4*0.5 $, 2*6 $	3*2.5 $	26.76 $
[25]	2*0.89 $	4*0.31 $	1*0.2 $, 1*0.2 $, 1*0.53 $ 1*1 $, 1*6 $	3*2.5 $	18.45 $
[26]	1*2.15 $	5*0.57 $	1*0.2 $, 1*0.1 $, 1*0.4 $ 1*0.4 $, 1*1 $	2*2.5 $	12.1 $
Proposed	4*0.42 $	6*1.06 $	1*0.1 $, 1*0.1 $, 1*0.4 $ 1*0.4 $, 1*0.4 $	3*2.5 $	16.94 $

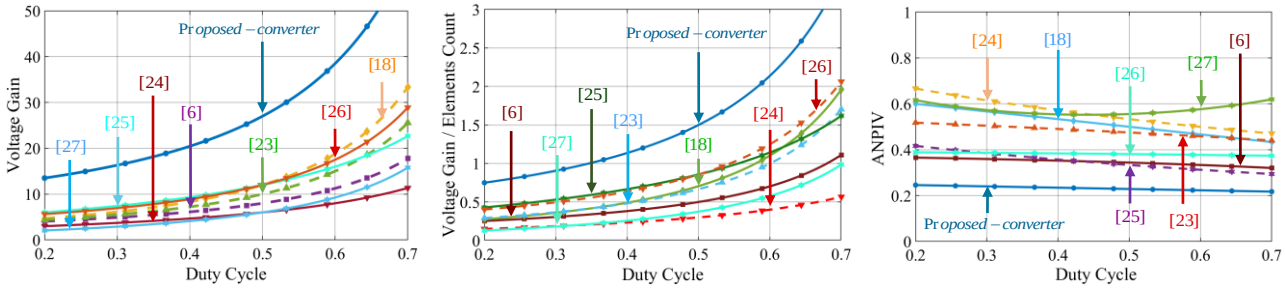

(a) (b) (c)

Fig. 10. Comparison graphs in n=2. (a) Voltage gain, (b) voltage gain/element count, and (c) ANPIV index.

element-count ratio of 3 at a 0.5 duty cycle—0.65 higher than [25] and [26], and significantly better than [24], which has a ratio of 0.3 due to its complexity and low gain. Despite the element count, the proposed converter also reaches the highest efficiency at 100 W output power, where most compared designs peak. As shown in Fig. 11(b), it maintains high efficiency across a wide power range, thanks to selective element activation and low voltage stress on semiconductors. As shown in Table IV and Fig. 10(c), the proposed converter has the lowest ANPIV index, with switch NPIV values also below average. This is due to placing voltage-boosting cells at the final stage. In contrast, converters [18], [24], and [27] show the highest ANPIV values, as their front-end switched inductor-capacitor cells increase conduction losses and reduce reliability.

As shown in Table VI, converters [25] and [26] suffer from high EMI due to the absence of a common ground between input sources and the output. In [25], this stems from the dual-input design, and in [26], from the voltage-doubler cell. In contrast, the proposed converter features a common ground between main inputs and output, reducing high-frequency circulating currents. While the battery connection via an auxiliary diode introduces slight EMI, this is mitigated by using a low-voltage battery or EMI filters in practical setups. Although converter [24] benefits from input-output isolation and low EMI, its high input current ripple makes it less ideal for PV systems.

As indicated in Table VII, converters [6], [26], and the proposed design offer the lowest overall cost, making them suitable for large-scale deployment. In contrast, Fig. 11(a) shows that converters [18] and [24] are the most expensive due to their use of high-voltage switches and multiple magnetic elements. Overall, the proposed converter stands out as a strong candidate for solar-powered DC microgrids, thanks to its high voltage gain, low ANPIV, high efficiency, low EMI, minimal input current ripple, cost-effectiveness, and broad energy management capability.

VII. Simulation Results

This section presents the simulation results of the proposed converter in all three operating states. The

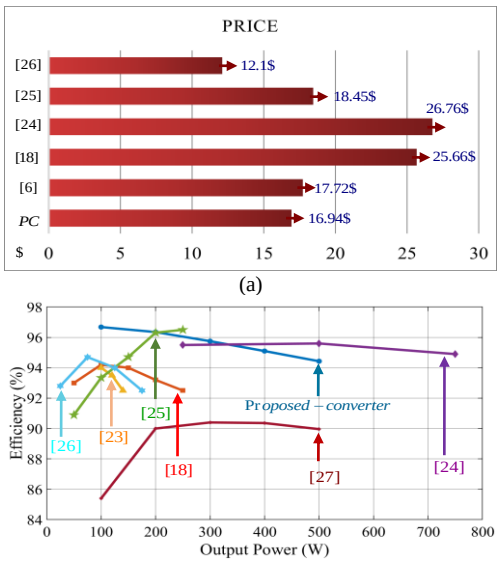

(a)

(b)

Fig. 11. (a) Cost comparison of the compared converters and (b) Efficiency comparison of the compared converters.

simulations are carried out using PSCAD software, and the data obtained are subsequently plotted using MATLAB. Also, the simulations are conducted based on the parameters listed in Table VIII, and the corresponding results are presented in Figs. 12 - 15.

Fig.12 illustrates the input and output voltages as well as the load current of the proposed converter in all three operating states. In each state, when input ports 1 and 2 are supplied with 24 V and the battery port is provided with 12 V, the converter delivers an output voltage of 400 V and an output current of 0.25 A. Figs. 13(a) – (e) depict the simulation results of the capacitor voltages in the proposed converter in the first operating state. As observed, the voltages across capacitors $C_1 - C_3$, C_{O1}, and C_{O2} are 57 , 81 , 224 , 220 , and 180 V, respectively, which confirm the values obtained from (7) - (11). Figs. 13(f) – (h) also illustrate the simulation results of the magnetic element currents in the proposed converter in the first operating state. The obtained current values for inductors L_1, L_2, and L_m are 3.7 , 0.62 , and 0 A, respectively, which validate the theoretical results derived from (25) - (27). In addition, Figs. 13(i) - (l) show the waveforms of the transformer winding currents and the leakage current. The obtained values are in good agreement with the theoretical results presented in Table III. Fig. 14 illustrates the simulated voltage and current waveforms of the semiconductors in the proposed converter during state 1. According to this figure, the voltage stresses of switches and diodes S_1, S_2, D_1, D_2, D_3, and D_O are obtained as 57, 57, 114, 170, 285, and 170 V, respectively. These results are consistent with the theoretical values calculated from the relations presented in Table V. Also, the values 6.1, 0.61, 0.6, 0.6, 0.42, and 0.62 A are obtained for I_{S1}, I_{S2}, I_{D1}, I_{D2}, I_{D3}, and I_{DO}, respectively. The obtained values follow the theoretical results presented in Table V.

Moreover, to manage the length of the paper, the complete set of simulated waveforms for operating states 2 and 3 has not been included. Instead, only the battery

TABLE VIII Simulation parameters of the proposed converter

Symbols	Values and types
Output Power	100 W
Input Voltages (V_1 and V_2)	24 V
Output voltage (V_O)	400 V
Battery voltage (V_B)	12 V
Capacitors (C_1, C_2, C_3)	47 uF/100 V, 47 uF/100 V, 47 uF/400 V
Output capacitors (C_{O1}, C_{O2})	47 uF/400 V
Input inductors (L_1, L_2)	500 uH
Magnetizing inductance (L_m)	500 uH
Leakage inductance (L_k)	1 uH
Turn ratios (n_1 and n_2)	2
Switching frequency (f_S)	50 KHz
d (State 1)	59.5%
d_1 (State 2)	66%
d_2 (State 2)	63%
d_1 (State 3)	45%
d_2 (State 3)	35%

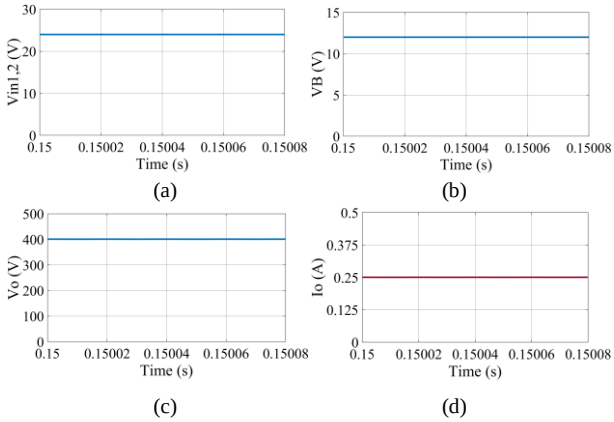

Fig. 12. Simulation results of the converter in all states

charging and discharging current waveforms for these states are presented in Fig 15. As shown in this figure, the obtained values of the battery currents are in good agreement with the calculated values presented in Table III.

Due to the dependence of the output voltage of photovoltaic (PV) panels on environmental conditions, a controller is required to stabilize the output voltage of the converter at a constant level. In the proposed converter, two control loops are needed. The first control loop is associated with the auxiliary switches, which regulate the charging and discharging power of the battery based on the algorithm presented in Fig. 9. Also, an external voltage control loop is used to regulate the output voltage of the converter. Fig. 16 illustrates a simple PI controller schematic that is applied to all operating states of the proposed converter and controls main switches S_1 and S_2. This controller receives the error between the reference and actual output voltage and generates the required pulse width to drive the switches, aiming to eliminate the voltage error.

By designing the closed-loop control system as shown in Fig. 16 and simulating it for second and third states of the proposed converter, the output voltage results under input voltage and load disturbances are obtained. These results are illustrated in Fig. 17. Fig. 17(a) illustrates the output voltage and power of the proposed converter in the second operating state. As shown, both the battery voltage and the main input source voltages remain constant, while the output load is first decreased from 1600 Ω to 533 Ω and then increased to 800 Ω. Throughout these variations, the controller demonstrates a fast dynamic response, effectively tracking the reference voltage and maintaining the output voltage at a constant 400 V. Fig. 17(b) presents the output voltage and output power of the proposed converter in the third operating state. As shown, both the output load and the battery voltage are kept constant during this state. When the main input source voltage changes from 24 V to 20 V and then returns to 28 V, the controller effectively regulates the output voltage, maintaining it at 400 V with a very short settling time.

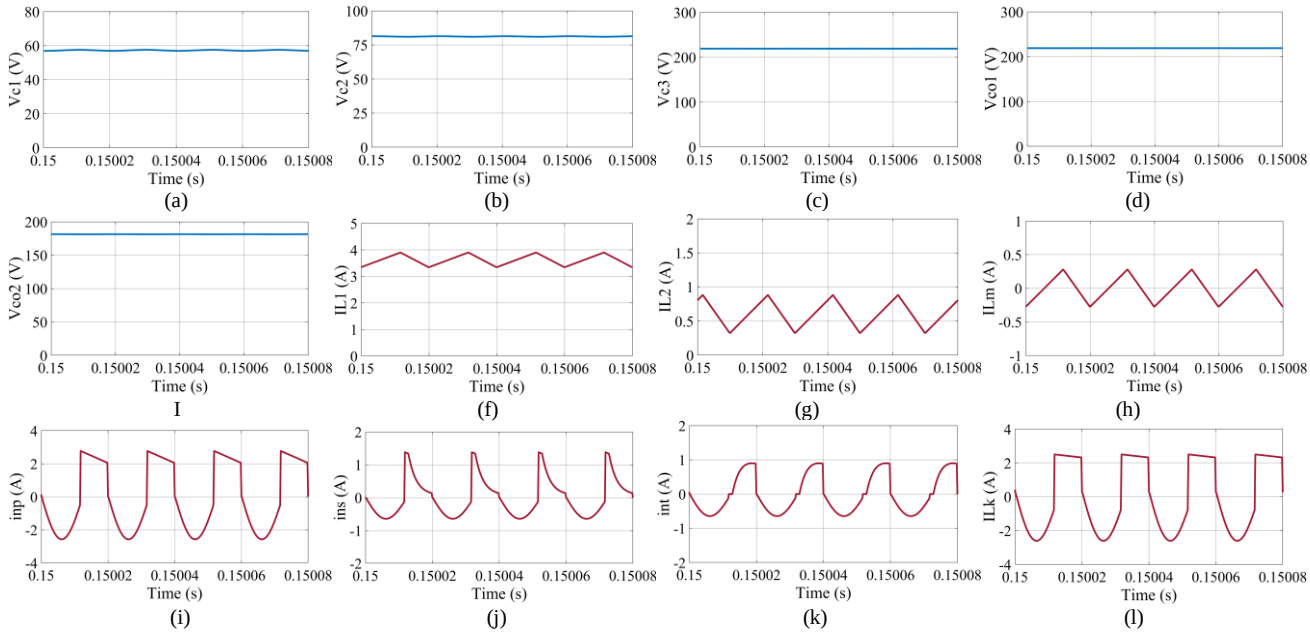

Fig. 13. Simulation results of the proposed converter in operating state 1.

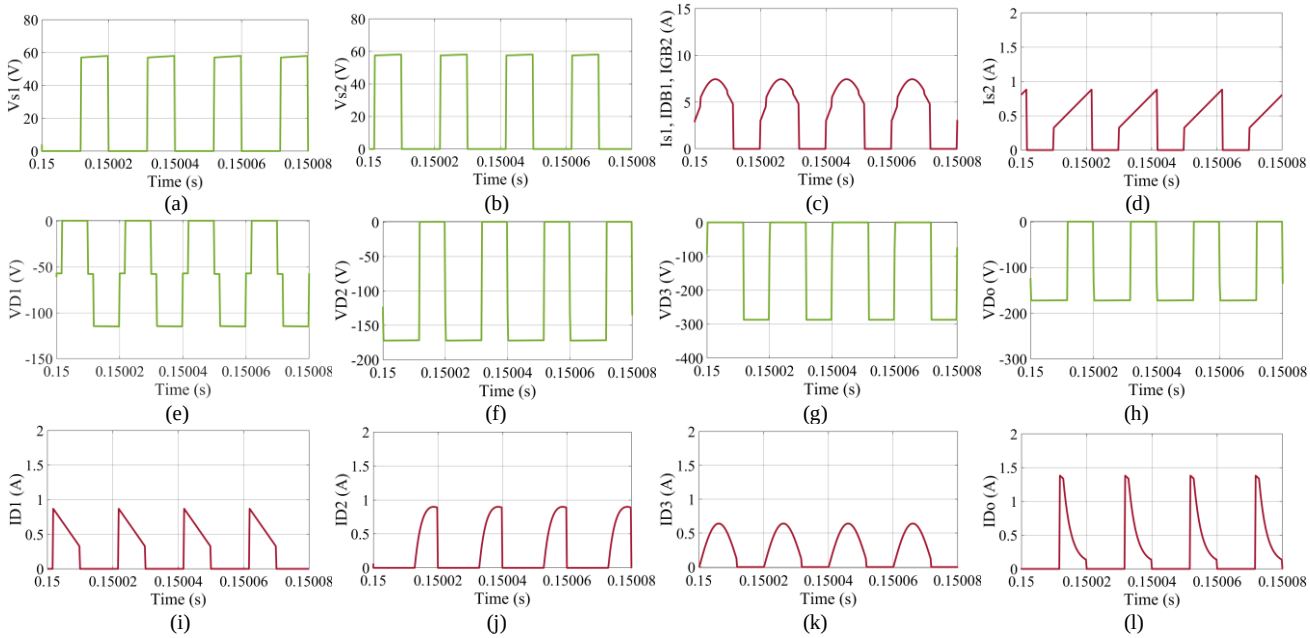

Fig. 14. Simulation results of the proposed converter in operating state 1.

VIII. Conclusion

This paper presents a non-isolated multi-port DC-DC converter equipped with a bidirectional port for integrating solar panels with storage systems in hybrid solar power plants. Based on the analysis of the proposed converter, features such as high voltage gain, low voltage stress on diodes and switches, continuous input current, high efficiency, and common ground are identified. The use of one bidirectional port and two unidirectional ports in the designed structure enables the integration of energy generation and

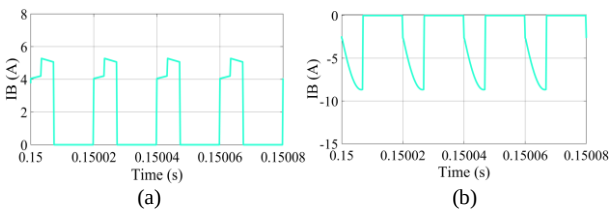

Fig. 15. Simulation results of the proposed converter for battery current. a) state 2, b) state 3.

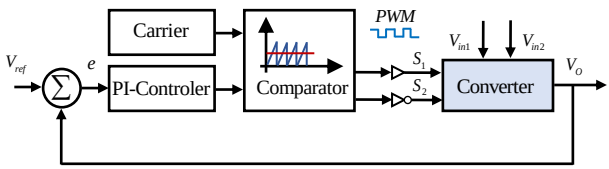

Fig. 16. Block diagram of PI controller for the proposed converter.

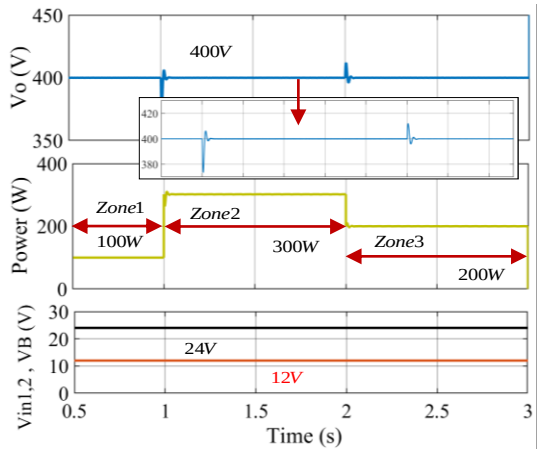

(a)

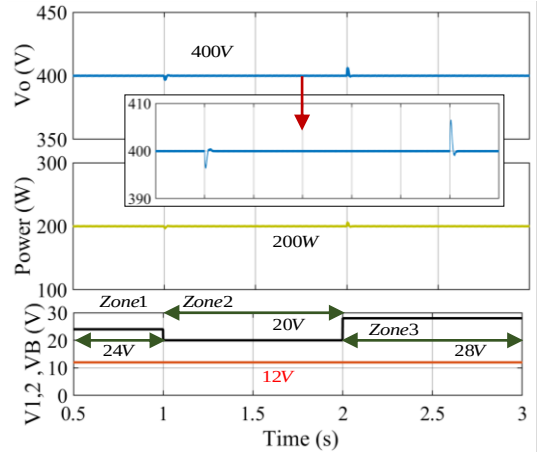

(b)

Fig. 17. Simulation results of the output voltage waveforms of the proposed converter under input voltage and load disturbance, (a) state 2, (b) state 3.

storage sources and reduces system complexity, volume, and losses. Additionally, its ability to operate in various operating states allows the implementation of different energy management strategies in the grid. In this regard, the feasibility of the proposed converter's operation under various energy management scenarios was examined through the development of an EMA. Furthermore, the proposed converter was analyzed in all operating states, and a comparison was conducted between it and similar structures presented in the references to validate the stated features. Finally, simulation results were utilized to validate the analysis results of the converter.

REFERENCES

[1] F. Karimian, A. Nahavandi, and P. Pakbaz, "A Novel Structure of High Voltage Gain DC-DC Converters for Photovoltaic (PV) Applications," *Engineering Reports*, vol. 7, no. 1, p. e13105, 2025.

[2] L. Li, X. Hou, and Y. Liao, "A Decentralized Optimal Economic Dispatch Control of Cascaded-Type DC Microgrids With Capacity and Load Voltage Constraints," *International Journal of Circuit Theory and Applications*, 2025.

[3] T. Falope, L. Lao, D. Hanak, and D. Huo, "Hybrid energy system integration and management for solar energy: A review," *Energy Conversion and Management: X*, p. 100527, 2024.

[4] P. Abolhassani, M. Maalandish, A. Nadermohammadi, M. B. B. Sharifian, M. R. Feyzi, and S. H. Hosseini, "A high step-up high step-down coupled inductor based bidirectional DC-DC converter with low voltage stress on switches," *IET Power Electronics*, vol. 17, no. 7, pp. 802-823, 2024.

[5] M. Dezhbord, P. Mohseni, S. H. Hosseini, D. Mirabbasi, and M. R. Islam, "A high step-up three-port DC-DC converter with reduced voltage stress for hybrid energy systems," *IEEE Journal of Emerging and Selected Topics in Industrial Electronics*, vol. 3, no. 4, pp. 998-1009, 2022.

[6] K. Varesi, A. A. Ghandomi, S. Hosseini, M. Sabahi, and E. Babaei, "An improved structure for multi-input high step-up DC-DC converters," in *2017 8th Power Electronics, Drive Systems & Technologies Conference (PEDSTC)*, 2017: IEEE, pp. 241-246.

[7] A. Nadermohammadi, M. Maalandish, A. Seifi, P. Abolhassani, S. H. Hosseini, and M. Farsadi, "A non-isolated single-switch ultra-high step-up DC-DC converter with coupled inductor and low-voltage stress on switch," *IET Power Electronics*, vol. 17, no. 2, pp. 251-265, 2024.

[8] E. E. Henao-Bravo, C. A. Ramos-Paja, A. J. Saavedra-Montes, D. González -Montoya, and J. Sierra -Pérez, "Design method of dual active bridge converters for photovoltaic systems with high voltage gain," Energies, vol. 13, no. 7, p. 1711, 2020.

[9] A. Imanlou, E. Babaei, and S. H. Hosseini, "A New High Voltage Gain Common-Ground Step-Up DC-DC Converter Integrating Coupled-Inductors and Switched-Capacitors," *International Journal of Circuit Theory and Applications*, 2024.

[10] P. Aghakhanlou *et al.*, "New Structure of Step-Up DC-DC Converter Based on Three Winding Coupled Inductor with High Gain Capability Featuring Integrated Renewable Energy Applications," 2024.

[11] A. Nadermohammadi *et al.*, "Cost-effective soft-switching ultra-high step-up DC-DC converter with high power density for DC microgrid application," *Scientific Reports*, vol. 14, no. 1, p. 20407, 2024.

[12] M. Elmi, M. R. Banaei, and H. Afsharirad, "Study on a Non-Isolated High Step-Up SEPIC-Based DC-DC Converter with Continuous Input Current for Photovoltaic Applications," *International Journal of Industrial Electronics Control and Optimization*, vol. 8, no. 1, pp. 95-104, 2025.

[13] S. Toofan, B. Fathipour, and E. Babaei, "A Single Switch Transformer-Less DC-DC Converter with Continuous Input Current for Photovoltaic Applications," *International Journal of Industrial Electronics Control and Optimization*, vol. 7, no. 4, pp. 281-290, 2024.

[14] K. Yari and S. Hasanpour, "A Minimum Phase DC-DC Converter with High Voltage Gain and Continuous Input Current," *International Journal of Industrial Electronics Control & Optimization*, vol. 7, no. 4, 2024.

[15] B. Akhlaghi, N. Molavi, M. Fekri, and H. Farzanehfard, "High step-up interleaved ZVT converter with low voltage stress and automatic current sharing," *IEEE Transactions on Industrial Electronics*, vol. 65, no. 1, pp. 291-299, 2017.

[16] E. Amiri, R. R. Khorasani, E. Adib, and A. Khoshkbar-Sadigh, "Multi-input high step-up DC-DC converter with independent control of voltage and power for hybrid renewable energy systems," *IEEE Transactions on Industrial Electronics*, vol. 68, no. 12, pp. 12079-12087, 2020.

[17] C.-L. Shen and L.-Z. Chen, "Dual-input isolated converter with dual-charge-pump cell for high step-up voltage ratio achievement," *IEEE Transactions on Industrial Electronics*, vol. 67, no. 11, pp. 9383-9392, 2019.

[18] S. Rostami, V. Abbasi, and N. Talebi, "Ultrahigh step-up

multiport DC-DC converter with common grounded input ports and continuous input current," *IEEE Transactions on Industrial Electronics*, vol. 69, no. 12, pp. 12859-12873, 2021.
[19] N. Bagheri, H. Alipour, L. Mohammadian, J. Beiza, and M. Ebadpour, "A Multiport isolated resonant LLC converter for grid-tied renewable energy powered bidirectional EV charger," *International Journal of Industrial Electronics Control and Optimization*, vol. 6, no. 1, pp. 37-48, 2023.
[20] G. Mohebalizadeh, H. Alipour, L. Mohammadian, and M. Sabahi, "A New Multi-Input DC/DC Converter with Coupled and Switched Inductor Applicable for Renewable Energy Sources," *International Journal of Industrial Electronics Control and Optimization*, vol. 5, no. 4, pp. 349-363, 2022.
[21] A. A. Asl, R. A. Asl, N. V. Kurdkandi, and S. H. Hosseini, "Modelling and controlling a new PV/FC/battery DC–DC converter suitable for DC motor," *The Journal of Engineering*, vol. 2022, no. 6, pp. 567-582, 2022.
[22] E. Babaei, Z. Saadatizadeh, and C. Cecati, "High step-up high step-down bidirectional DC/DC converter," *IET Power Electronics*, vol. 10, no. 12, pp. 1556-1571, 2017.
[23] K. Varesi, S. H. Hosseini, M. Sabahi, and E. Babaei, "Modular non-isolated multi-input high step-up dc-dc converter with reduced normalized voltage stress and component count," *IET Power electronics*, vol. 11, no. 6, pp. 1092-1100, 2018.
[24] S. Sathyan, H. M. Suryawanshi, A. B. Shitole, M. S. Ballal, and V. B. Borghate, "Soft-switched interleaved DC/DC converter as front-end of multi-inverter structure for microgrid applications," *IEEE Transactions on Power Electronics*, vol. 33, no. 9, pp. 7645-7655, 2017.
[25] A. Samadian, S. M. Hashemzadeh, M. G. Marangalu, M. Maalandish, and S. H. Hosseini, "A new dual-input high step-up DC-DC converter with reduced switches stress and low input current ripple," *IET Power Electronics*, vol. 14, no. 9, pp. 1669-1683, 2021.
[26] A. Mahmood et al., "A non-inverting high gain DC-DC converter with continuous input current," IEEE Access, vol. 9, pp. 54710-54721, 2021.
[27] R. Rajesh, N. Prabaharan, and T. Santhosh, "Design and analysis of a non-isolated DC-DC converter with a high-voltage conversion ratio," IEEE Transactions on Circuits and Systems II: Express Briefs, vol. 70, no. 6, pp. 2036-2041, 2022.

Hamed Abdi was born in Tabriz, Iran, completed his B.Sc. in Power Electrical Engineering at the University of Tabriz in 2019, and later pursued his M.Sc. in Power Electronics and Electrical Machines at the same institution, graduating in 2024. His academic journey has been marked by a commitment to excellence, as evidenced by his ranking as the top student in the Electrical Engineering department and his membership in the University's Talented Students Group.

Eng. Abdi has actively contributed to the field of electrical engineering through publications in reputable journals and conferences. His work includes power electronic converters, energy management systems for HEVs, and PV systems design. His dedication to advancing these areas has been recognized with accolades such as the Best Paper Award at the 16th Power Electronics & Drives: Systems and Technologies Conference (PEDESTC) in 2025.

Naghi Rostami was born in Ahar, Iran, in 1984. He received the B.Sc.degree from the Khajeh Nasir Toosi University of Technology, Tehran, Iran, in 2006, and the M.Sc. degree from the University of Tehran, Tehran, Iran, in 2008, and the ph.D. degree from the University of Tabriz, Tabriz, Iran, in 2013, all in electrical engineering.

He is currently an Assistant Professor at the Department of Electrical Engineering, University of Tabriz. He is involved with the electric machines branch with proficiency in finite-element software. His current research interests include electric machines and drives, and electric and hybrid vehicles.

Ebrahim Babaei received the Ph.D. degree in Electrical Engineering from the University of Tabriz, in 2007. He is the author and co-author of one book and more than 720 journal and conference papers. He also holds 26 patents in the area of power electronics. His current research interests include the analysis, modeling, design, and control of Power Electronics Converters and their applications, Renewable Energy Sources, and FACTS Devices.

Prof. Babaei has been the Editor-in-Chief of the Journal of Electrical Engineering of the University of Tabriz, since 2013. He was an Associate Editor of the IEEE Transactions on Industrial Electronics from 2015 to 2023. He is also currently an Associate Editor of the IEEE Transactions on Power Electronics, IEEE Open Journal of the Industrial Electronics Society, Iranian Journal of Science and Technology, Transactions of Electrical Engineering, and International Journal of Circuit Theory and Applications. He was selected by the Ministry of Science Research and Technology as the distinguished researcher of Iran in the field of engineering in 2022.

Bülent Bilgehan is the Dean of the Faculty of Engineering at Near East University. He holds a Ph.D. in Electrical and Electronics Engineering and specializes in Internet of Things (IoT), wireless communications, UAV systems, and intelligent optimization techniques. His research focuses on Industry 5.0, healthcare technologies, and disaster-resilient communication networks. Dr. Bilgehan has authored numerous publications in peer-reviewed journals and presented at international conferences. He actively leads national and international research projects and supervises graduate research in emerging technologies.

International Journal Of
Industrial Electronics Control and Optimization
Print ISSN: 3517-2645
Online ISSN: 3568-2645
Homepage: https://ieco.usb.ac.ir/

Optimal Deep Rate Control for Intra Coding in High-Efficiency Video Coding Standard

Mehdi Rezaei [1] | Arshnoos Nakhaei [2] | Yaser Rahimi[3] | Pouria Jafari[4]

Faculty of Engineering, University of Sistan and Baluchestan, Zahedan, Iran.[1,2,3,4]
Corresponding author's email: mehdi.rezaei@ece.usb.ac.ir

Article Info

Article type:
Research Article

Article history:
Received: 09-December-2024
Received in revised form: 28-January-2025
Accepted: 19-February-2025
Published online: 22-Dec-2024

Keywords:
Coding Tree Unit (CTU),
Convolutional Neural Network (CNN),
High-Efficiency Video Coding (HEVC),
Rate Control, R-Q Model.

ABSTRACT

This paper proposes a novel Optimal Deep Rate Controller (ODRC) designed for intra-coding configuration of the High-Efficiency Video Coding standard. The ODRC incorporates a Convolutional Neural Network-based Rate-Quantization Model (CRQM) to effectively predict bits consumption across the entire Quantization Parameter (QP) range at the Coding Tree Unit (CTU) level. The proposed rate controller employs an optimization algorithm to minimize the buffering delay required for video communications. By establishing a specific search space through the CRQM, a greedy search algorithm is utilized to determine the optimal frame-level QP, thereby minimizing discrepancies between buffer occupancy and target occupancy. Unlike CTU-level rate controllers, which can introduce quality variations due to QP fluctuations among CTUs, the frame-level ODRC maintains consistent objective quality across CTUs within a frame. The ODRC is integrated within the standard reference software HM-16.20. Comparative evaluations with the default rate controller, RC-HM, in the same software, demonstrate the superior performance of ODRC in terms of both delay and bit error ratio. Experimental results indicate that ODRC achieves a notably lower average buffering delay of 0.02s and a lower bit error ratio of 11.25%, in contrast to RC-HM's 0.3s and 44.72%, respectively, emphasizing its effectiveness for HEVC low-delay applications.

I. Introduction

High-Efficiency Video Coding (HEVC) [1] has significantly advanced video compression. It offers a 50% bitrate reduction compared to H.264/AVC [2] while maintaining visual quality, especially for high-resolution content. Despite these advancements, transferring high-quality video over networks faces several challenges due to bandwidth, delay, and buffer capacity limitations. To address these challenges, an effective Rate Controller (RC) is crucial for optimizing bit allocation across various coding units, such as Group of Pictures (GOPs), frames, and Coding Tree Units (CTUs). This optimization ensures a high-quality video experience under different network conditions [3-11].

Rate control strategies in HEVC for intra-frames and inter-frames differ significantly due to their inherent coding characteristics. In inter-frame coding, RC can use a Rate-Distortion (R-D) model updated according to previous encoding results. Conversely, in intra-frame coding, RC relies only on information within the same frame. Consequently, intra-frames require more sophisticated RC approaches to achieve the desired bitrate. Utilizing content-based R-D or Rate-Quantization (R-Q) models can improve the performance of these RC approaches.

II. Related works

So far, various rate control algorithms have been proposed for intra-frame coding within the HEVC standard. The large group of rate control algorithms, commonly called conventional RCs, typically operate in three steps: bit allocation, bitrate control, and parameter updating. During the initial step, a bit budget is allocated to a coding level based on factors such as target bitrate, buffer occupancy, and frame complexity. In the subsequent step, the allocated bitrate and coding complexity are incorporated as inputs for a content-based R-D or R-Q model to determine an appropriate Quantization Parameter (QP) for each coding

level. Finally, the model parameters are updated based on previous encoding results to improve the model accuracy. However, the model can be very inaccurate for the first intra-frame and the intra-frames inserted in scene cuts. Representative examples of conventional frame-level and CTU-level RCs for HEVC can be found in [12-15] and [16-19], respectively.

Conventional rate control algorithms typically employ closed-form analytical models to estimate QPs based on rate, distortion, and hand-engineered content complexity metrics such as mean absolute difference and the sum of absolute Hadamard transformed differences [12-19]. However, these models often struggle to accurately represent the complex relationships between rate, distortion, and video content characteristics, which can result in suboptimal rate-distortion performance. To tackle this issue, some researchers have recently turned to machine learning techniques to extract more relevant features from video content, facilitating the development of more robust and accurate rate control models. Among these techniques, convolutional neural networks (CNNs) have emerged as an effective image and video analysis tool [20-25].

CNNs have emerged as a powerful tool for transforming complex images and videos to the feature space with compressed representations. Within the domain of R-D modeling, CNN-based approaches can be divided into two primary categories. The first category leverages CNNs to estimate parameters for established models such as R-D and R-Q. For instance, [20, 21] proposed a CNN to predict optimal R-λ model parameters, demonstrating the strong dependency of these parameters on both video content and QP. However, the training of these models was limited to a specific QP range. Building upon this, [22] introduced a CNN-based framework to predict parameters for the exponential R-Q model, incorporating multiple CNNs for feature extraction and weight estimation.

The second category of methods focuses on directly estimating rate control parameters, such as bit count, distortion, or QP, using CNNs [23-25]. Early CNN-based models [23-25] were limited in their applicability due to constraints on QP range and input frame size. The model presented in [23] proposes a CNN-based model to predict bit count and Structural Similarity Index Map (SSIM) under constrained conditions of QP range and fixed input frame size. Similarly, [24] employs two CNNs to estimate the rate and Mean Squared Error (MSE) for intra-frames at a limited set of QPs. To address these limitations, our previous work [25] introduced a Convolutional Rate-Quantization Model (CRQM) operating at the CTU level. This model offers significant advancements by enabling simultaneous accurate estimation of bit consumption across all QP values for each CTU and adapting to diverse frame sizes.

The reviewed studies primarily focus on two approaches to predict the rate and distortion of Intra-frames: closed-form rate-distortion models and CNN-based models. These works do not explicitly address rate control mechanisms [12-24]. Beyond these core approaches, a study in [26] investigates novel NN architectures and optimization strategies for selecting the QP to control the bitrate at the CTU level. However, this model's effectiveness is constrained by its training on a limited QP range, which may hinder its adaptability to diverse rate requirements.

This paper proposes an optimal deep rate controller (ODRC) for intra-frame coding in HEVC. The ODRC aims to achieve precise and optimal rate control. The proposed method leverages our previously developed CRQM [25] to accurately predict the bit consumption of each coding CTU across various QPs. A greedy search algorithm, informed by the CRQM's predictions, determines the optimal frame-level QP, minimizing the discrepancies between buffer occupancy and a target value. This results in efficient operation with low buffering delay, making the ODRC well-suited for low-latency applications.

The key contributions of this paper are as follows:

- This paper proposes an optimal deep rate controller for precise rate control in HEVC intra-frame configuration.
- In contrast to the rate controllers presented in [20-22] that rely on CNNs to update the parameters of conventional RD models, the proposed ODRC provides precise results even at the start of scene cuts.
- Unlike the approach in [23], which employs a CNN-based RD model constrained to fixed video frame size, ODRC is adaptable to varying frame sizes.
- Compared to the rate controller in [24], which uses a CNN-based RD model limited to a narrow QP range, the proposed ODRC can operate on the entire range of QP values.
- While the work in [25] focuses on CTU-level bitrate control using a CNN-based RD model, ODRC operates at the frame level to provide a uniform visual quality for each frame.
- By integrating our CRQM, which estimates bit consumption across the entire QP range, with a low-complexity greedy search algorithm, ODRC efficiently determines the optimal frame-level QP to minimize buffer occupancy discrepancies.

The remainder of the paper is organized as follows: Section 2 outlines the Methodology, Section 3 presents the test results, and Section 4 provides the conclusions.

III. Methodology

The increasing demand for low-delay applications, such as real-time video conferencing, and the growing prevalence of ultra-high-definition (UHD) video content present significant challenges for video transferring systems. The proposed RC in this paper can provide an accurate bitrate close to the target bitrate for the intra-frames. Therefore, it can be used for low-delay UHD applications within the

HEVC standard. The proposed RC can be used for all intra-coding configurations or intra-frames in other coding configurations.

Figure 1 illustrates the block diagram of the proposed rate control algorithm. The core components of the proposed system, including the virtual buffer and proposed RC, are discussed in detail in the sequel.

A. Overview of the CRQM model

The CRQM [25] introduces a novel intra-prediction approach utilizing both Coding Tree Unit (CTU) and reference pixel information. As illustrated in Figure 2, each 64×64 Coding Tree Block (CTB) is extended with reference pixels, creating 66×66 input blocks. Reference pixels extending to the right and bottom are rotated and concatenated to the right and bottom edges of the CTBs, respectively. Three resulting 66×66 blocks are subsequently fed into a CNN to extract features. Figure 3 illustrates the architecture of the CNN-based model. The first convolutional layer employs a kernel size of 9×9 with a stride of 8×8, while all subsequent convolutional layers utilize 2×2 kernels and strides. ReLU activation is applied across all convolutional layers. The features extracted by the final convolutional layer are combined with the CTB standard deviation (STD) and passed through two fully connected layers, each comprising 40 neurons with ReLU and tanh activation functions, respectively. The output layer, consisting of 51 neurons with a tanh function, generates the estimated bit counts for each QP.

B. Virtual Buffer

The proposed system employs a virtual buffer to simulate the decoder buffer in a constant bandwidth communication channel. The buffer occupancy, O_i, is dynamically updated after encoding each frame as:

$$O_i = O_{i-1} + B_T - B_i \tag{1}$$

where B_i denotes the number of bits consumed to encode i^{th} frame. The initial buffer occupancy, O_0, is initialized to 60% of the total buffer capacity, simulating the initial buffering delay. The core objective of the proposed control mechanism is to maintain the buffer occupancy close to this initial level, defined as the target buffer occupancy, O_T, throughout the transmission process. The target bits per

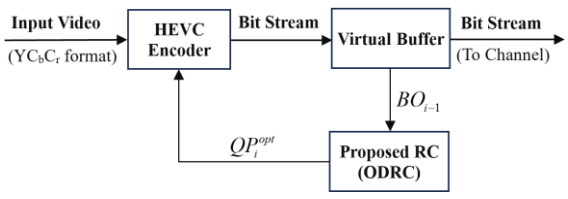

Fig. 1. Block Diagram of the Proposed Rate Control Algorithm

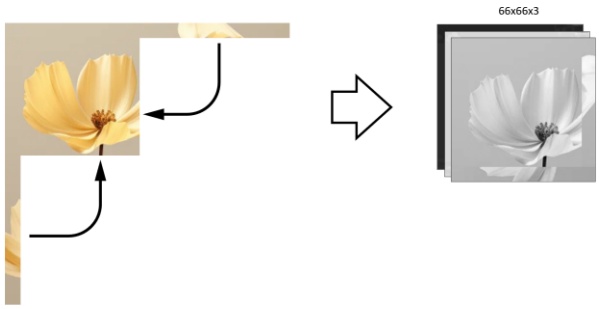

Fig. 2. Preparing Inputs of Convolutional Neural Network-based Rate-Quantization Model (CRQM)

frame, B_T, is calculated as:

$$B_T = \frac{R_T}{f} \tag{2}$$

where R_T denotes the target bitrate and f stands for the frame rate.

C. Content-based Intra Deep Controller

The proposed rate control algorithm aims to maintain the buffer occupancy close to the target level, O_T, by selecting an optimal QP for each frame. The optimal QP for i^{th} frame, QP_i^{opt}, is then determined using a greedy search optimization algorithm to minimize the absolute difference between O_i^{Est} and O_T:

$$QP_i^{opt} = \underset{\forall QP \in \{1,\ldots,51\}}{\arg\min} \left| O_i^{Est} - O_T \right|. \tag{3}$$

where O_i^{Est} denotes the estimated buffer occupancy after encoding i^{th} frame and it is calculated by:

$$O_i^{Est} = O_{i-1} + B_T - B_i^{Est}, \tag{4}$$

where B_i^{Est} shows the estimated bits for i^{th} frame that is computed as Eq. (5).

$$B_i^{Est} = \sum_{j=1}^{N_i} b_{i,j}^{Est} \tag{5}$$

N_i denotes the number of CTUs within i^{th} frame, and $b_{i,j}^{Est}$ represents the estimated bit consumption for the j^{th} CTU of the i^{th} frame, determined by the CRQM [25].

IV. Test Results

a) Implementation Details

This subsection presents a comparative performance evaluation of the proposed rate controller (ODRC), implemented in the HEVC reference software HM-16.20 [27], against the default rate controller (RC-HM) included in the same software. RC-HM employs the λ-domain R-D model and considers the standard Hypothetical Reference Decoder buffering model. Given its implementation on HM,

its performance is benchmarked against many RCAs, potentially facilitating cross-verification.

Simulations were conducted using the RAISE dataset [28] at four QP values: 22, 27, 32, and 37. The target bitrate, $R_T = B_T \times f$, derived from CQRM, was used as the anchor target bitrate for both rate control methods. During the experiments, the virtual buffer capacity was set to 60% of the target bitrate. The ODRC initialized its buffer occupancy at 60% of the virtual buffer capacity, while RC-HM used its default 90% initialization as its optimum value.

A subset of 500 frames at a resolution of 4948×3280 pixels was randomly selected from the RAISE dataset to create five 100-frame video sequences with a frame rate of 30 frames per second. Unlike the test video datasets, in which the consequent frames are very similar in each video sequence, the used dataset can simulate about 500 video sequences, which is a large number for test purposes.

b) Dataset

c) Quantitative and Qualitative Analysis

Given that the proposed rate controller is tailored for intra-frames, which are encoded independently without reference to other frames, each frame's quality does not influence subsequent frames' quality. Therefore, the performance evaluation of the proposed rate controller emphasizes its effectiveness in controlling bitrate and achieving rate control accuracy.

Table 1 summarizes the comparative results. From the controlling aspect, the proposed controller successfully prevents both buffer overflow and underflow for all encoded bitstreams, demonstrating robust bitrate control. For a quantitative comparison of rate control performance, the minimum buffering delay required on the receiver side, proportional to the minimum buffer size, is measured and reported in Table 1. The minimum buffering delay is computed as follows.

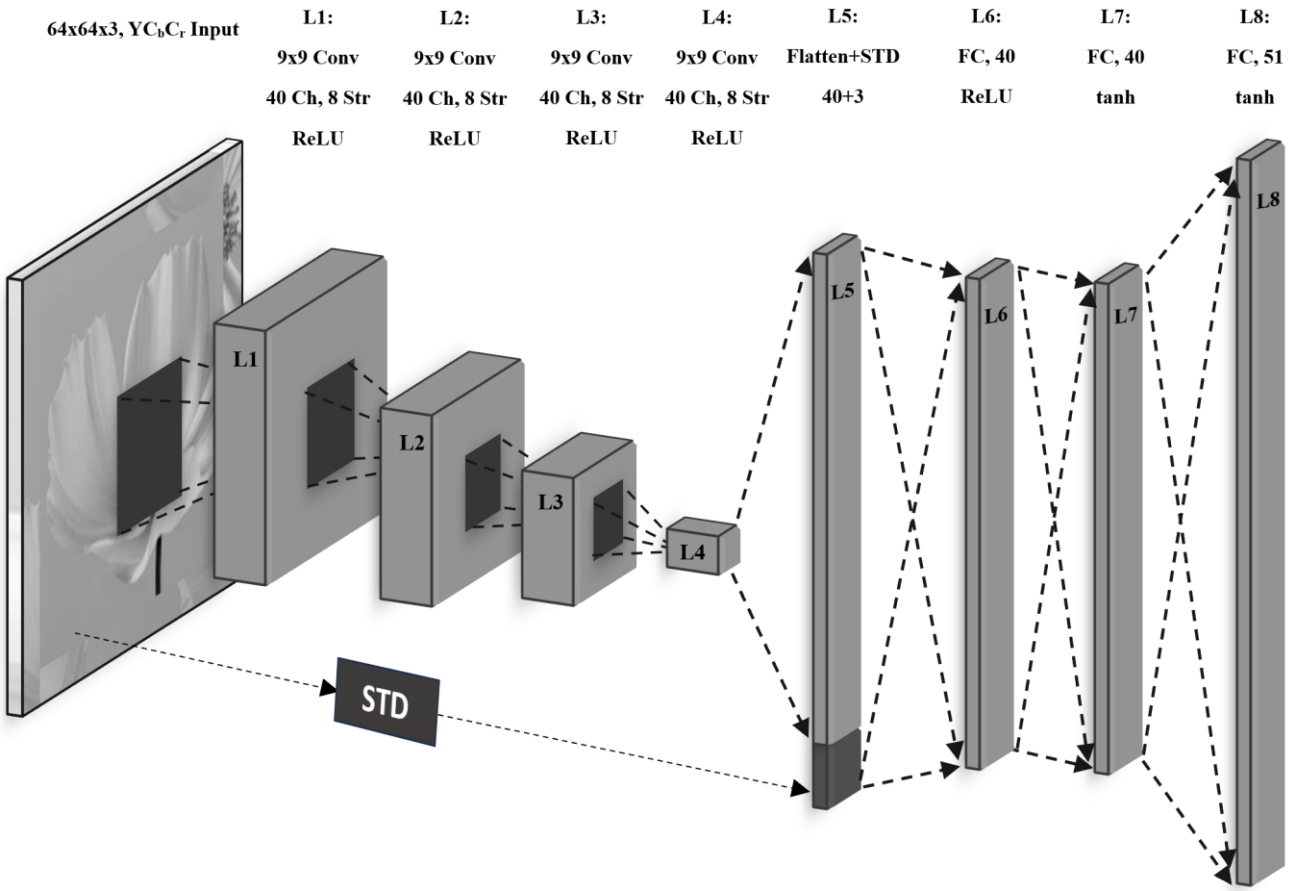

Fig. 3 Convolutional Neural Network-based Rate-Quantization Model (CRQM) architecture to estimate the CTU bit consumption [25].

$$Delay_{\min} = \alpha \frac{O_{\max} - O_{\min}}{R_T}, \quad (6)$$

where $O_{\max}$ and $O_{\min}$ are the maximum and minimum buffer occupancy throughout the encoded video sequence. α for ODRC and HM-RC is set to 0.6 and 0.9, respectively.

bitstreams, demonstrating robust bitrate control. For a quantitative comparison of rate control performance, the minimum buffering delay required on the receiver side, proportional to the minimum buffer size, is measured and reported in Table 1. The minimum buffering delay is computed as follows.

$$Delay_{\min} = \alpha \frac{O_{\max} - O_{\min}}{R_T}, \quad (6)$$

where $O_{\max}$ and $O_{\min}$ are the maximum and minimum buffer occupancy throughout the encoded video sequence. α for ODRC and HM-RC is set to 0.6 and 0.9, respectively.

TABLE 1. EXPERIMENT RESULTS OF THE PROPOSED RATE CONTROLLER (ODRC) AND DEFAULT RATE CONTROLLER (HM-RC) ON TEST SEQUENCES IN TERMS OF AVERAGE QP, BITRATE (KBIT/S), DELAY (S), AND BIT ERROR RATIO (%)

Video Seq.	method	Avg. QP	Bitrate (Kbit/s)	Delay (s)	BER%
Video1	ODRC	21.58	274735.7	0.01	9.90
		26.05	131805.1	0.01	6.00
		30.97	61852.2	0.01	8.69
		35.66	30693.0	0.01	7.86
	HM-RC	21.75	276519.8	0.25	38.26
		26.29	127072.7	0.27	38.6
		31.17	62239.1	0.28	45.74
		35.99	31010.7	0.33	48.40
Video2	ODRC	21.69	266452.2	0.02	15.28
		26.61	121270.0	0.02	12.76
		31.38	58626.2	0.02	13.56
		36.00	28756.7	0.02	11.06
	HM-RC	21.88	266584.5	0.29	45.74
		26.67	121456.7	0.31	45.68
		31.46	58670.5	0.34	46.70
		36.28	28835.2	0.33	48.05
Video3	ODRC	21.60	257655.8	0.03	13.89
		26.39	119579.0	0.02	14.24
		30.91	59154.4	0.02	12.06
		35.51	29669.1	0.02	9.73
	HM-RC	21.57	257437.0	0.25	42.14
		26.48	119544.4	0.28	48.10
		31.58	59144.6	0.33	55.82
		36.58	29664.5	0.41	58.75
Video4	ODRC	21.75	287710.8	0.02	12.39
		26.65	133234.5	0.02	13.25
		31.20	65525.3	0.03	10.90
		35.88	32543.9	0.03	11.54
	HM-RC	22.37	287966.1	0.29	46.80
		27.03	133720.5	0.24	45.10
		31.9	66475.7	0.44	53.23
		36.96	32524.0	0.48	57.32
Video5	ODRC	21.89	295528.8	0.01	11.05
		26.76	139093.1	0.02	11.57
		31.29	140149.0	0.01	9.35
		35.92	34219.5	0.01	9.85
	HM-RC	21.75	296576.2	0.15	36.76
		26.40	140149.4	0.19	39.44
		31.34	69255.1	0.26	43.92
		36.42	34291.9	0.27	9.85
Average	ODRC	21.702	276416.7	**0.02**	**12.50**
		26.49	128996.3	**0.02**	**11.56**
		31.15	77061.4	**0.02**	**10.91**
		35.79	31176.4	**0.02**	**10.01**
	HM-RC	21.86	277016.7	**0.25**	**41.94**
		26.57	128388.7	**0.26**	**43.38**
		31.49	63157.0	**0.33**	**49.08**
		36.45	31265.3	**0.36**	**44.47**

Likewise, to compare the algorithms in terms of rate control accuracy, the bit error ratio is examined as an indicator of deviation between the target and actual bitrates. The bit error ratio is computed as follows:

$$BER\% = 100\left(\frac{1}{N_F}\sum_{i=1}^{N_F}\frac{|B_T - B_i|}{B_T}\right), \quad (7)$$

where N_F shows the number of frames in each sequence.

Table 1 demonstrates the significant performance advantage of ODRC over RC-HM in terms of both buffering delay and bit error ratio. ODRC achieves an average buffering delay of 0.02s and a bit error ratio of 11.25%, while RC-HM exhibits substantially higher values of 0.30s and 44.72%, respectively. This disparity in performance is directly attributable to the accuracy of the CRQM model employed by the proposed rate control algorithm. The high accuracy of this model enables precise rate control, minimizing deviations from the target buffer occupancy and, consequently, reducing buffering delays.

To further evaluate the proposed RC performance, Figure 4 presents sample results of virtual buffer fullness for the test sequences encoded by ODRC and HM-RC algorithms at the QP of 32. These graphs are plotted according to the frame encoding order. The solid horizontal line represents the buffer size, while the dashed lines indicate the target buffer occupancy for each algorithm. As observed, the buffer occupancy of the HM-RC-encoded bitstream exhibits a more significant deviation from the target than the ODRC-encoded bitstream, which remains closer to its target. Consequently, transmitting the HM-RC-encoded bitstream necessitates a larger buffer size to prevent overflow or underflow, resulting in increased delay compared to ODRC.

Regarding the previous studies reviewed in this paper, the presented works in [12-24] studies focus on rate-distortion modeling without directly addressing a rate control mechanism. Therefore, the proposed RC in this paper cannot be compared with these works. Only the study presented in [26] explores an RC that operates at the CTU level.

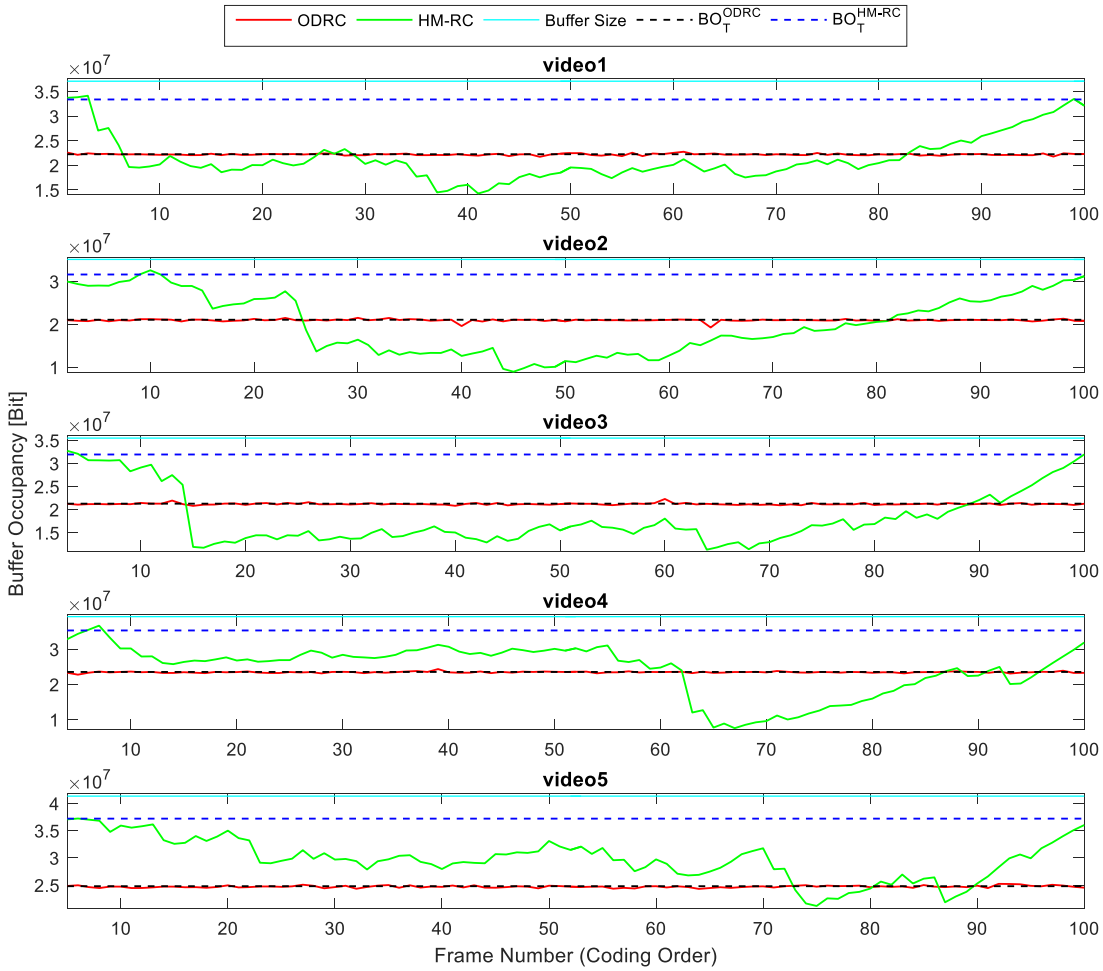

Fig. 4. The buffer occupancy graphs for test sequences encoded by the proposed rate controller (ODRC) and default rate controller (HM-RC) at QP of 32

Consequently, comparing the accuracy of this algorithm with our RC, which operates at the frame level, would be unfair. Furthermore, the work in [26] does not provide frame-level performance metrics such as BER and delay, which are key performance indicators in our study. Notably, the BER metric in [26] is evaluated at the sequence level and, therefore, unreliable for comparison, as it depends on the length of the video sequence and frame size.

V. Conclusions

This paper introduces a novel optimal intra-frame rate control algorithm designed to enhance the performance of low-latency applications in the HEVC standard. The proposed controller utilizes the CRQM to achieve precise bit consumption prediction at the CTU level, enabling frame-level QP determination by a greedy search optimization algorithm. These determinations are based on the deviation between the target and estimated buffer occupancy, ensuring stable and accurate rate control. Integrated into the HEVC reference software HM-16.20, the proposed ODRC algorithm was evaluated against the default rate controller (RC-HM). Experimental results demonstrate that ODRC significantly outperforms RC-HM, achieving notable reductions in both bit error ratio and buffering delay. These results underscore the enhanced performance of ODRC on the aspects of controlling bitrate and rate control accuracy, making it well-suited for real-time video applications requiring high efficiency and accuracy.

REFERENCES

[1] G. J. Sullivan, J.-R. Ohm, W.-J. Han, and T. Wiegand, "Overview of the high efficiency video coding (HEVC) standard," IEEE Transactions on circuits and systems for video technology, vol. 22, no. 12, pp. 1649-1668, 2012, doi: 10.1109/TCSVT.2012.2221191.

[2] T. Wiegand, G. J. Sullivan, G. Bjontegaard, and A. Luthra, "Overview of the H. 264/AVC video coding standard," IEEE Transactions on circuits and systems for video technology, vol. 13, no. 7, pp. 560-576, 2003, doi: 10.1109/TCSVT.2003.815165.

[3] I. Ahmad, V. Swaminathan, A. Aved, and S. Khalid, "An overview of rate control techniques in HEVC and SHVC video encoding," Multimedia Tools and Applications, vol. 81, no. 24, pp. 34919-34950, 2022, doi: 10.1007/s11042-021-11249-5.

[4] A. A. Ramanand, I. Ahmad, and V. Swaminathan, "A survey of rate control in HEVC and SHVC video encoding," in 2017 IEEE International Conference on Multimedia & Expo Workshops (ICMEW), pp. 145-150, 2017, doi: 10.1109/ICMEW.2017.8026268.

[5] J. Zou and B. Li, "Rate Control in HEVC: A Survey," in Signal and Information Processing, Networking and Computers: Proceedings of the 5th International Conference on Signal and Information Processing, Networking and Computers (ICSINC), pp. 578-583, 2019, doi: 10.1007/978-981-13-7123-3_67.

[6] H. Esmaeeli and M. Rezaei, "Methods and Criteria for Evaluating Controllability of Video Bit Rate in HEVC-SCC," International Journal of Industrial Electronics Control and Optimization, vol. 4, no. 3, pp. 313-320, 2021, doi: 10.22111/ieco.2021.37880.1344.

[7] X. Wei, M. Zhou, H. Wang, H. Yang, L. Chen, and S. Kwong, "Recent advances in rate control: From optimization to implementation and beyond," IEEE Transactions on Circuits and Systems for Video Technology, vol. 34, no. 1, pp. 17-33, 2023, doi: 10.1109/TCSVT.2023.3287561.

[8] C. Yang, Y. Liu, Q. Liu, C. Zhang, and W. Wang, "Joint frame-level and CTU-level rate control based on constant perceptual quality," Multimedia Systems, vol. 30, no. 3, p. 133, 2024, doi: 10.1007/s00530-024-01329-5.

[9] Y. Yan, G. Xiang, H. Jia, J. Chen, X. Huang, and X. Xie, "Two-stage perceptual quality oriented rate control algorithm for HEVC," ACM Transactions on Multimedia Computing, Communications and Applications, vol. 20, no. 5, pp. 1-20, 2024, doi: 10.1145/3636510.

[10] C. Zhang and W. Gao, "Learned rate control for frame-level adaptive neural video compression via dynamic neural network," in European conference on computer vision, Springer, pp. 239-255, 2025, doi: 10.1007/978-3-031-73013-9_14.

[11] L. Jia, H. Ren, Z. Zhang, L. Song, and K. Jia, "Visual information fidelity based frame level rate control for H. 265/HEVC," Signal Processing: Image Communication, vol. 131, p. 117245, 2025, doi: 10.1016/j.image.2024.117245.

[12] Y. Zhou, L. Tian, and X. Ning, "Intra frame constant rate control scheme for high efficiency video coding," in 2013 International Conference on Computing, Networking and Communications (ICNC), pp. 648-652, 2013, doi: 10.1109/ICCNC.2013.6504163.

[13] C. Sheng, F. Chen, Z. Peng, and W. Chen, "An adaptive bit mismatch rectification algorithm for intra frame rate control in HEVC," in 2015 8th International Congress on Image and Signal Processing (CISP), pp. 80-84, 2015, doi: 10.1109/CISP.2015.7407854.

[14] B. Hosking, D. Agrafiotis, D. Bull, and N. Eastern, "An adaptive resolution rate control method for intra coding in HEVC," in 2016 IEEE International Conference on Acoustics, Speech and Signal Processing (ICASSP), pp. 1486-1490, 2016, doi: 10.1109/ICASSP.2016.7471924.

[15] Z. Ma, J. Xiao, T. Tian, and S. Sun, "Research and optimization for adaptive intra frame complexity rate control based on HEVC," in 2017 17th International Symposium on Communications and Information Technologies (ISCIT), pp. 1-5, 2017, doi: 10.1109/ISCIT.2017.8261179.

[16] F. Cen, Q. Lu, and W. Xu, "Efficient rate control for intra-frame coding in high efficiency video coding," in 2014 International Conference on Signal Processing and Multimedia Applications (SIGMAP), pp. 54-59, 2014, doi: 10.5220/000506710054005.

[17] M. Wang, K. N. Ngan, and H. Li, "An efficient frame-content based intra frame rate control for high efficiency video coding," IEEE Signal Processing Letters, vol. 22, no. 7, pp. 896-900, 2014, doi: 10.1109/LSP.2014.2377032.

[18] P. Wang, C. Ni, G. Zhang, and K. Li, "R-Lambda model based CTU-level rate control for intra frames in HEVC," Multimedia Tools and Applications, vol. 78, no. 1, pp. 125-139, 2019, doi: 10.1007/s11042-017-5507-y.

[19] V. Sanchez, "Rate control for HEVC intra-coding based on piecewise linear approximations," in 2018 IEEE International Conference on Acoustics, Speech and Signal Processing (ICASSP), pp. 1782-1786, 2018, doi: 10.1109/ICASSP.2018.8461970.

[20] Y. Li, B. Li, D. Liu, and Z. Chen, "A convolutional neural network-based approach to rate control in HEVC intra coding," in 2017 IEEE Visual Communications and Image

Processing (VCIP), pp. 1-4, 2017, doi: 10.1109/VCIP.2017.8305050.
[21] X. Lu, B. Zhou, X. Jin, and G. Martin, "A rate control scheme for HEVC intra coding using convolution neural network (CNN)," in 2020 Data Compression Conference (DCC), pp. 382-382, 2020, doi: 10.1109/DCC47342.2020.00055.
[22] L. Wei, Z. Yang, Z. Wang, and G. Wang, "A CNN-based optimal CTU λ decision for HEVC intra rate control," IEICE TRANSACTIONS on Information and Systems, vol. 104, no. 10, pp. 1766-1769, 2021, doi: 10.1587/transinf.2021EDL8047.
[23] B. Xu, X. Pan, Y. Zhou, Y. Li, D. Yang, and Z. Chen, "CNN-based rate-distortion modeling for H. 265/HEVC," in 2017 IEEE Visual Communications and Image Processing (VCIP), pp. 1-4, 2017, doi: 10.1109/VCIP.2017.8305151.
[24] M. Santamaria, E. Izquierdo, S. Blasi, and M. Mrak, "Estimation of rate control parameters for video coding using CNN," in 2018 IEEE Visual Communications and Image Processing (VCIP), pp. 1-4, 2018, doi: 10.1109/VCIP.2018.8698721.
[25] Y. Rahimi, M. Rezaei, and P. Jafari, "Content-based coding tree unit level rate-quantization model for intra-coding in high efficiency video coding standard using convolutional neural network," Journal of Electronic Imaging, vol. 31, no. 3, pp. 033026-033026, 2022, doi: 10.1117/1.JEI.31.3.033026.
[26] J.-H. Hu, W.-H. Peng, and C.-H. Chung, "Reinforcement learning for HEVC/H. 265 intra-frame rate control," in 2018 IEEE International Symposium on Circuits and Systems (ISCAS), pp. 1-5, 2018, doi: 10.1109/ISCAS.2018.8351575.
[27] https://vcgit.hhi.fraunhofer.de/jvet/HM/-/tree/HM-16.20, ed.
[28] D.-T. Dang-Nguyen, C. Pasquini, V. Conotter, and G. Boato, "Raise: A raw images dataset for digital image forensics," in Proceedings of the 6th ACM multimedia systems conference, pp. 219-224, 2015, doi: 10.1145/2713168.2713194.

Mehdi Rezaei (M'04) received the B.Sc. and M.Sc. degrees in electronics engineering from the Amir Kabir University of Technology (Polytechnic of Tehran) and Tarbiat Modares University, Tehran, Iran in 1992 and 1996, respectively, and also Ph.D. degree in Signal Processing from the Tampere University of Technology (TUT), Finland in 2008. His research interests include multimedia signal processing and communications. He has published several papers in these fields. During his Ph.D. program, he collaborated closely with the Nokia Research Center and filed several patents. He also received the Nokia Foundation Award in 2005 and 2006. Now, he is an Associate Professor in the Communications Engineering Department, University of Sistan and Baluchestan, Iran.

Arshnoos Nakhaei received the B.S. degree in communications engineering from Sistan and Baluchestan University, Zahedan, Iran, in 2015, and also the M.Sc. degree in communications systems engineering at Sistan and Baluchestan University, Iran, in 2018. He is currently pursuing a Ph.D. degree in communications systems engineering. His research interests include multimedia signal processing and communications.

Yaser Rahimi received the B.Sc. degree in Communication Engineering from Isfahan University of Technology (IUT), Iran, in 2005 and the M.Sc. degree in Electronic Engineering from Mazandaran University, Iran, in 2007, and He PhD from university of Sistan and Baluchestan, Iran, in 2023. His current research interests include Deep Learning, Video Compression, signal and image processing

Pouria Jafari received B.Sc. degree in electronics engineering from Sistan and Baluchestan University, Zahedan, Iran in 2004, the M.Sc. degree in control engineering from Tabriz University, Tabriz, Iran, in 2006, and the Ph.D. degree in control engineering from Khajeh Zasir Toosi University of Technology, Tehran, Iran, in 2017. He is currently an Assistant Professor of Electrical Engineering Department, University of Sistan and Baluchestan, Iran. His research interests include deep learning, neural networks, fuzzy logic control and fractional order systems.

International Journal Of
Industrial Electronics Control and Optimization
Print ISSN: 3517-2645
Online ISSN: 3568-2645
Homepage: https://ieco.usb.ac.ir/

Hybrid AI for Enhanced Voltage Control in Three-Phase Boost Rectifiers

Alireza Khoshsaadat [1] | Arash Khoshooei[2] | Mohammad Abedini* [3] | Mohammadreza Mirzaei[4]

[1]Department of Electrical Engineering, Shahid Beheshti University, Tehran, Iran
[2]Assistant Professor, Jundi-Shapur University of Technology, Dezful, Iran,
[3] Department of Electrical Engineering, Faculty of Engineering, Ayatollah Boroujerdi University, Boroujerd, Iran
[4] Master of Electrical Engineering, Planning and Management of Electrical Energy Systems, Ayatollah Boroujerdi University, Iran
* Corresponding Author: m.abedini@abru.ac.ir

Article Info

Article type:
Research Article

Article history:
Received: 14-August-2024
Received in revised form: 08-November-2024
Accepted: 30-November-2024
Published online: 22-Dec-2025

Keywords:
ANFIS Controller,
Voltage-Oriented Control,
Direct Power Control,
Rectifier.

ABSTRACT

Three-phase boost rectifier is a Voltage-Source Converter that converts three-phase AC input voltage to a higher DC voltage. In this paper, an artificial intelligent-based system, with learning and adapting capability, is proposed for utilizing in the two voltage-based control methods of rectifiers, with the names of Voltage Oriented Control (VOC) and Direct Power Control (DPC). For implementation of this intelligent controller, a hybrid structure of the Fuzzy Logic (FL) and Neural Networks (NNs) that named as Adaptive Network-based Fuzzy Inference System (ANFIS) is applied. Among the common network training algorithms, the error back propagation algorithm is known as the most common solution by providing an efficient computational method. Thus this method is used to design the training process of the controller. According to the results, this neuro-fuzzy-based control model is applicable in both VOC and DPC methods and increases the quality of the output current and DC voltage with low ripple, short settling time and also dynamic operation. Implementation of the proposed controller is simple and requires only 49 fuzzy rules. Compared to other similar controllers with NN and FL, it has fewer layers and its accuracy is suitable. To evaluate of the designed controller performance, it is simulated and applied in both VOC and DPC systems and the results are compared with PID Controller counterpart.

I. Introduction

Three-phase Pulse Width Modulation (PWM) rectifiers are workhorses in power electronics, converting AC input into DC output using either voltage-based or virtual flux-based control methods. These control methods categorized in two main categories: voltage-based and virtual flux-based. Voltage-based control, like Voltage-Oriented Control (VOC) and Direct Power Control (DPC), directly utilizes the line voltage vector for regulation and control. In contrast, virtual flux-based control, by introducing Virtual Flux Direct Power Control (VF-DPC), calculates a virtual voltage reference, eliminating the need for physical voltage sensors. VF-DPC achieves this target by replacing the line voltage vector with a virtual flux estimation and leading to reduced harmonic distortion and a more sinusoidal line current in many cases. Virtual Flux-Oriented Control (VFOC) is another approach that leverages virtual flux for DC voltage control [1, 2].

While all control methods for three-phase PWM rectifiers aim for near-unity power factor and sinusoidal input current, they achieve this approaches with distinct merits and limitations.

VOC and VFOC prioritize static and dynamic performance. They achieve this by using an internal current control loop as a crucial element in their operation.

DPC and VF-DPC take a different approach. They focus on instantaneous control of direct and reactive power, eliminating the need for an internal current control loop and a dedicated PWM block. Instead, they rely on a switching table based on the difference between reference and estimated power values to select the appropriate switching strategy [3, 4, 5].

Sliding Mode Direct Power Control (SMC-DPC) is a robust control technique for Doubly Fed Induction Generators (DFIGs) [6, 7, 8]. It boosts fast power convergence and resilience against parameter variations, but

can introduce some of power chattering [9].

Double synchronous reference frame controllers, explored in [10, 11]. It offers improved performance through the addition of a decoupling network to manage unwanted current oscillations. Literature also discuss variations of switching tables for active front-ends to enhance performance (e.g., [12, 13]), but the methodology for their formation is often lacking detailed explanation.

According to the literature review and combination of artificial intelligent systems, this paper proposes a novel control method for voltage-based methods (VOC and DPC) in three-phase PWM rectifiers. The core of this method is an Adaptive Network-based Fuzzy Inference System (ANFIS) controller that combines the strengths of Neural Network (NN) and Fuzzy Logic (FL). This hybrid approach offers increased flexibility and adaptability to change system conditions.

The ANFIS controller utilizes a single NN architecture with 5 layers to implement the entire fuzzy system. A learning algorithm based on Forward Signal and Backward Error Back-Propagation (FSBEBP) is used to adjust the parameters within the Sugeno-based fuzzy controller and optimize system performance.

The ANFIS controller uses a 5-layer NN architecture to implement the key functionalities of a FL system. The hidden layers within this network act as both membership function mappers and a fuzzy inference engine. The underlying fuzzy rules, based on engineering knowledge of the controlled rectifier, are translated into this NN structure.

The proposed controller utilizes a specific architecture with 2, 14, 49, 49, and 1 nodes in each of the 5 layers. This architecture allows the ANFIS controller to effectively implement the fuzzy control strategy. The proposed ANFIS controller is evaluated for both VOC and DPC strategies in rectifier control. The results demonstrate its superiority over traditional PID controllers. Unlike PID controllers, which require manual adjustments for varying system conditions, the ANFIS controller can inherently adapt, offering significant advantages.

II. Neural Networks, Fuzzy Logic, and Hybrid Neuro-Fuzzy Systems

Both FL and NNs are powerful tools for building intelligent systems, but they have distinct characteristics that should be considered.

A. Neural Network

Artificial NNs are a well-known machine learning technique for processing data through analytical layers. Similar to neurons in the human brain, NNs are composed of interconnected neurons, which are called nodes. These nodes are connected to each other through axons called weights that their values are in range of 0-1. In a NN system, nodes are placed together and form layers.

Using of NNs has their advantages and disadvantages. Advantages of NNs are as below [14, 15]:

. Has redundant nature and thus, when a part of the NN fails, it can continue processing based on their parallel nature;

. Can perform non-linear process that a linear system cannot;

· Has high robustness against disturbances due of learning ability;

And disadvantages of NNs are as below:

. Cumbersome mass of calculation;

· Difficulty in determining the optimum architecture, such as number of neurons and layers.

B. Fuzzy Logic

Unlike deterministic sets, a fuzzy set allows an element to belong relatively to a set. This relative membership is defined by the degree of membership and is indicated by the degree of membership can take a value between 0 (for an element that does not belong to the set at all) and 1 (for an element that completely belongs to the set). The set membership function is the relationship between the elements of the set and their degree of belonging. General advantages of the FL systems are:

. Human-like reasoning: FL can handle uncertainties and express knowledge using linguistic variables, making it easier to understand and integrate expert knowledge into the system.

. Adaptability: FL systems can be easily extended by adding new rules, allowing for knowledge-based growth without significant structural changes.

. Reduced overshoot and oscillation: FL systems can often achieve smooth control outputs with low overshoot and oscillation.

And disadvantages of FL systems are:

. Limited generalization: FL systems struggle with situations outside their defined rule base, lacking the ability to generalize effectively to unseen scenarios.

. Expert Dependence: Designing effective fuzzy systems requires expert knowledge to define the appropriate rules, potentially limiting their accessibility.

For understanding FL, Fig. 1 illustrates a typical fuzzy system with four key components:

1) Fuzzification Unit: this unit transforms crisp (exact) inputs into fuzzy values, indicating the degree of their membership in various fuzzy sets.

2) Knowledge Base: this core element stores the fuzzy rules that govern system behavior. It's essentially a collection of expert knowledge expressed in linguistic terms.

3) Inference Engine: this unit applies the fuzzy rules from the knowledge base to the fuzzified inputs, determining the appropriate control action. It mimics human decision-making to some extent.

4) Defuzzification Unit: this unit converts the inferred fuzzy control values back into crisp outputs that can be applied to the system.

By combining these components, FL systems can provide robust control strategies even with imprecise or incomplete information.

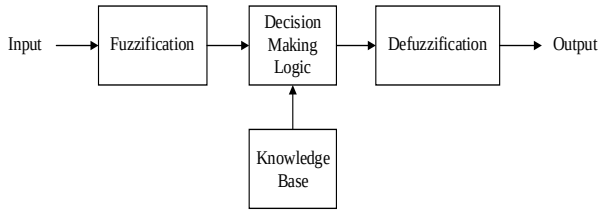

Fig. 1. Basic model of a FL system.

C. Hybridization of FL and NN

In this study, in order to design a suitable controller for the switching process in the rectifier, an adaptive neural fuzzy inference system is used. This system is a modeling framework that is presented as a combination of FL and artificial NN. This hybrid model is presented in order to overcome the weaknesses in both FL and artificial NN methods. In fact, inspired by fuzzy systems, the initial knowledge is shown in a set of constraints in order to reduce the optimization search space. While the structured network using backpropagation is inspired by the artificial NN. In this model, artificial NN is used to adjust the membership functions.

Also, the presence of non-linear membership functions in the neuro-fuzzy method leads to a significant reduction in the cost of implementing a simple plan based on the rules and memory used; therefore, it is clear that the combination of NN and fuzzy systems reduces the limitations of each of these two methods and leads to the proposal of a data mining method to solve complex engineering problems. Adaptive neural fuzzy inference system (ANFIS) is one of the well-known methods in the simultaneous combination of NN and fuzzy systems [24]. This method is used to identify the behavior of non-linear systems using the set of input and output data defined for the model. Adaptive neural fuzzy inference system is a structured model of fuzzy inference system. The used ANFIS is based on Sugeno fuzzy method to make fuzzy rules using input and output data defined. In the part IV, more detailed of this design will represented.

III. Model of Three-phase Rectifier, VOC and DPC Control Strategies

A. Model of a 6-switches Three-phase Rectifier

Fig. 2 depicts a typical 6-switches three-phase PWM rectifier circuit with a specific switch configuration. A universal bridge topology for arrangement of the switch is applied in Fig. 2. By this architecture, unity power factor and bidirectional energy flow can be achieved.

The figure presents the following elements and subsystems:

1) Input phase voltages: U_a, U_b, U_c.

2) Filter components: L (inductance) and R (resistance) of the filter.

3) Input and switching elements: A, B, and C (input phases) and S_a, S_b, S_c (switching legs for the three-phase rectifier).

4) Output and load: Udc (DC output voltage), C (filter capacitor), and R_L (equivalent load resistance).

Equation (1) will present the mathematical model of this three-phase PWM rectifier in the synchronous rotating frame.

$$\begin{aligned} L\frac{di_d}{dt} &= u_d - Ri_d - \omega L i_q - S_d U_{dc} \\ L\frac{di_q}{dt} &= u_q - Ri_q + \omega L i_d - S_q U_{dc} \end{aligned} \tag{1}$$

And using the KCL law in the output node:

$$C\frac{dU_{dc}}{dt} = i_d S_d + i_q S_q - \frac{U_{dc}}{R_L} \tag{2}$$

where the d and q indices are the transformed variable from abc phases to the d-q frame. This model can be easily implemented using SIMULINK [2].

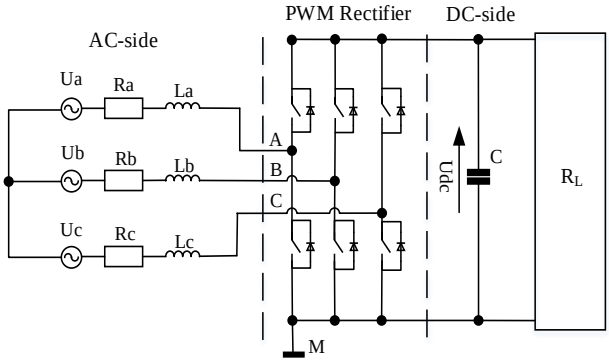

Fig. 2. Three-phase PWM rectifier circuit model.

B. Model of VOC strategy

The VOC method is based on the some transformation from three-phase a, b, c reference system to a synchronous rotating reference frame d-q, through a two phase stationary reference system α-β. With these transformations, the control voltages remain constant and become DC values and the control process is simplified.

As mentioned previously, closed-loop current control is used in this method [2]. The VOC has some advantages as:

. Fixed frequency method can be applied for switching process.

. Advanced PWM pattern can be used.

. Cheaper A/D converter is used.

Meanwhile, VOC has some disadvantages such as:
. Relative complex algorithm.
. Lower power factor in comparison with other methods.
. Decoupling structure for controlling of the active and reactive power is required [3].

Implementation of the VOC model for rectifier control has four main stages as below:
1) PWM unit: that controls the pulse width of the switches of the rectifier. This work performs with comparing of the triangular carrier with the modulator sinusoidal wave that comes from decoupled controller unit with the $V_{dc}/2$ amplitude.
2) Decoupled controller unit: in this unit, the voltage controller produces the reference i_d for the decoupled current controller at first (references i_q is zero because rectifier has no reactive power exchanging with the grid); then using references of the i_d and i_q, proper control signal will produce with the two decoupled controllers. This unit is demonstrated in the Fig. 3. Also, an ANFIS controller applied for this part of the system is applied that will be represented in the next section.
3) Phase Locked Loop (PLL) unit: This unit gives the voltage angle of the three phase system, and this angle was used for all abc to d-q transformation blocks in the model.
4) Rectifier unit: model of this unit represented in Fig. 2.
Putting together of the aforementioned building blocks of the VOC, the block-diagram of the controlled rectifier is represented in Fig. 4.

Fig. 4 has 4 major parts, as mentioned previously, and also two three-phase to d-q frame transformer blocks.

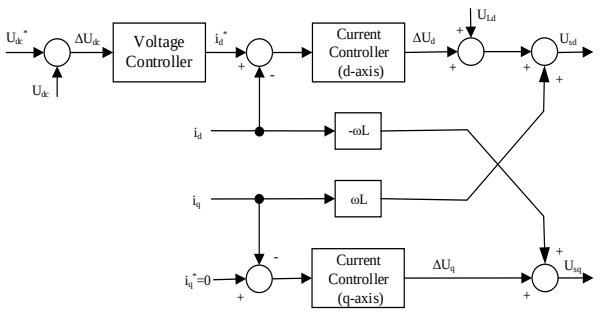

Fig. 3. SIMULINK diagram of the decoupled controller unit.

C. Model of DPC strategy

Direct Power Control (DPC) is a control method for three-phase PWM rectifiers that prioritizes simplicity and efficiency. Unlike other methods, DPC bypasses the need for an internal current control loop and complex coordinate transformations. Instead, it relies on readily available information like network voltage position and power errors to directly select the appropriate voltage vector from a predefined switching table [6, 7]. This approach streamlines the control process and enables independent control of active and reactive power (decoupled control) [8, 9]. Generally,

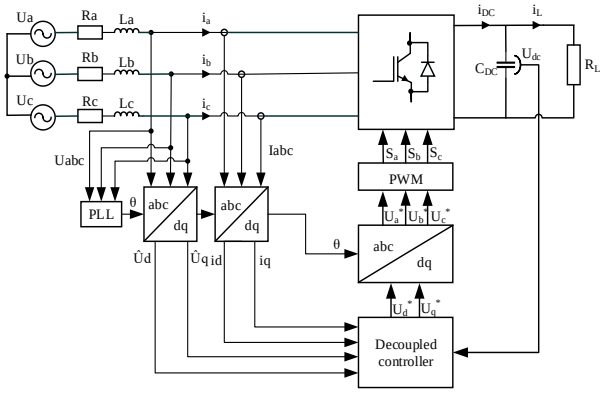

Fig. 4. The VOC method for PWM rectifier.

DPC has advantages as:
. PWM block system, current controllers, and coordinate transformation are not needed.
. Has decoupled active and reactive power control and good dynamic response and a simple algorithm.
. Can estimate instantaneous variables appropriately.
Also, DPC has some disadvantages such as:
. Variable switching frequency.
. Fast and complicated processor and also A/D converter are required.

For implementing of the DPC method we have 4 major parts as below:
1) Instantaneous power estimator unit: this unit estimate the active and reactive power of the line based on the voltage of line by the product of the three-phase voltages and currents. This work need to the high value of the line inductance and sampling frequency, and also depends on the switching states. The below equations represented the instantaneous active and reactive powers:

$$p = L\left(\frac{di_a}{dt}i_a + \frac{di_b}{dt}i_b + \frac{di_c}{dt}i_c\right) + U_{dc}\left(S_a i_a + S_b i_b + S_c i_c\right)$$
$$q = \frac{1}{\sqrt{3}}\left\{3L\left(\frac{di_a}{dt}i_c - \frac{di_c}{dt}i_a\right) - U_{dc}\left(S_a(i_b - i_c) + S_b(i_c - i_a) + S_c(i_a - i_b)\right)\right\} \quad (3)$$

These estimated powers are compared with their reference values and the produced errors are fed to fixed band hysteresis comparators to generate two digital signals *dp* and *dq*. For the unity power factor operation, the reference value of the reactive power q_{ref} is set to zero.
2) Switching table unit: The switching pattern for the rectifier switches is stored in a lookup table (LUT) within this unit. This table influences factors such as instantaneous power and current ripple, switching frequency, and overall dynamic performance. The LUT values are based on:
. Digitized signals dp and dq representing the instantaneous errors of active and reactive power, respectively (provided by hysteresis comparators).
. Power source voltage vector position.

Typically, the voltage vectors is divided into 12 sectors. Table I illustrates the lookup table layout with predefined switching functions (S_a, S_b, S_c) assigned to each sector.

TABLE I SWITCHING LOOK-UP TABLE.

dp	dq	γ_1	γ_2	γ_3	γ_4	γ_5	γ_6	γ_7	γ_8	γ_9	γ_{10}	γ_{11}	γ_{12}
1	0	101	111	100	000	110	111	010	000	011	111	001	000
	1	111	111	000	000	111	111	000	000	111	111	000	000
0	0	101	100	100	110	110	010	010	011	011	001	001	101
	1	100	110	110	010	010	011	011	001	001	101	101	100

3) Controller unit: this unit uses the error between DC output voltage and output DC reference voltage, as input. The reference of the active power for hysteresis active power controller is obtained from this unit. Our ANFIS controller is applied instead of this controller unit.

4) Rectifier unit: as explained for the VOC method, model of this unit is represented in the previous sections is used for DPC method either. In Fig. 5, the block-diagram of the DPC method is represented.

IV. Design of ANFIS

The set of rules considered for a fuzzy inference system of the Takagi-Sugno-Kang type is expressed as if-then rules as follows [18,19]:

IF X_i is A_i and Y_i is B_i, THEN $f_k=p_kX_i+q_kY_i+r_k$

The rule-base as a look-up-table is provided to define the expert's knowledge for applying of the FL controller arrangement. If "Z" is the form of the linear syntax of the "X" and "Y", this type of fuzzy rules named as "sugeno" that given in Fig. 4 with seven sets Negative Big (NEB), Negative Medium (NEM), Negative Small (NES), Zero (ZE), Positive Small (POS), Positive Medium (POM), and Positive Big (POB) as the fuzzy values [17]. The number of first layer nodes is determined using the number of inputs and the number of membership functions for each input. But the number of nodes in other layers depends on the number of rules in the fuzzy rule set. Table II shows the provided rules as inference engine. Although the number of rules can be increased, minimum rules have been used to reduce calculations in controller design. For implementing of the controlling system, the error between output DC voltage and reference DC voltage and derivative of that (shown with *"e"* or "X_1", and *"de"* or "X_2" respectively) are considered as the two input of the FL controller. Every of two fuzzified input is divided to the 7 fuzzy confine. Finally noting to the two inputs and scaling of them, we have output table with 49 arrays for inference system. This process are implemented using 5 layer NN, in ANFIS architecture, for partaking from parallel processing and learning ability of the NN, neighbor to the inference capability of the FL. Fig. 7 demonstrations the organization of the offered ANFIS, which has been used as controller. As shown in Fig. 5, architecture of the NN has five layers as following:

1) First layer: The first layer: each node in this layer determines a degree of membership for the inputs. In fact, this layer will convert any input value into a specific fuzzy range. The fuzzy function in this layer can be expressed as follows:

$$O_{ij}^1 = \mu_{ij}(x_i) \qquad i=1,2, \qquad j=1,2,...,14; \tag{4}$$

where, μ_{ij} is equal to j[th] the membership function for the input x_i and O_{ij}^1 is the output of the node ij.

Due to the good performance and satisfactory performance of the triangular membership function in various engineering applications, the membership function used in this study is a triangular type. The mathematical relationship of this membership function is as follows:

$$\mu(x) = \max[\min(\frac{x-a}{b-a}, \frac{c-x}{c-b}), 0]; \tag{5}$$

where a, b and c are the set of parameters.

2) Second layer: Each node in this layer (k), which is presented as circular nodes (Π), (See Fig. 7), produces the output using the received inputs.

$$O_k^2 = \mu_{e1}(X_1^2)\mu_{e2}(X_2^2)\ ;\ k=1,...,49; e_1, e_2 = 1,...,7; \tag{6}$$

3) Third layer: In layer of node k[th], the ratio of the fire power of the law k[th] to the fire power of the whole law has been determined as follows [22]:

$$O_i^3 = \overline{W_k} = \frac{W_k}{(\sum_{k=1}^{k=49} W_k)}; i, k = 1, 2, ..., 49; \tag{7}$$

4) Fourth layer: Each node in this layer acts as a weighted output of the fuzzy inference system as follows:

$$O_i^4 = \overline{W_k} f_k = \overline{W_k}(p_k X_1 + q_k X_2 + r_k), k = 1, ..., 49; \quad (8)$$

Where W_K is the output of the non-fuzzy layer and f_K is the output of the rule M[th] of the Takagi-Sugno-Kang fuzzy inference system. Also, p_k ,q_k and r_k are the set of parameters. 5) Fifth layer: In this layer, the single circular node, Σ, calculates all outputs as the sum of all inputs as follows:

$$O_1^5 = \sum_{k=1}^{k=49} \overline{W_k} f_k \quad (9)$$

This node is only used because we have only one output. Noting that the square nodes which are adaptive nodes have control parameters while the circle nodes which are fixed node has none.

The proposed ANFIS controller utilizes a learning algorithm called Forward Signal and Backward Error Back-Propagation (FSBEBP) to adjust its internal parameters. This algorithm works in two stages:

1) Forward Pass: In this stage, the input vector is fed through the ANFIS network layer by layer. Each layer performs its designated calculations, ultimately producing an output value.

2) Backward Pass: Here, the error between the actual output and the desired output is calculated. This error is then propagated backward through the network layer by layer. Similar to traditional Backpropagation, the FSBEBP algorithm uses the gradient descent technique to modify the network's internal parameters (premise parameters) based on the calculated errors. This process aims to minimize the overall error and improve the controller's performance [20-22].

So it can be written as:

$$\frac{\partial E_k}{\partial g_i} = \eta \frac{\partial E_k}{\partial O_k} \frac{\partial O_k}{\partial g_i} = \eta (O_k - y_k) \frac{\partial O_k}{\partial g_i} \quad (10)$$

where, η is the learning rate of the NN-based network, g_i is the consequence parameter and O_i is the output of i-th layer. Also, E_k is the cost function of the error and can be calculated as follows:

$$E_k = \frac{1}{2}(d_k - O_k)^2 \quad (11)$$

where, d_k is the desired response of the k-th layer and O_k is the output of the k-th layer. The error rate for consequence parameters can be expressed as follows:

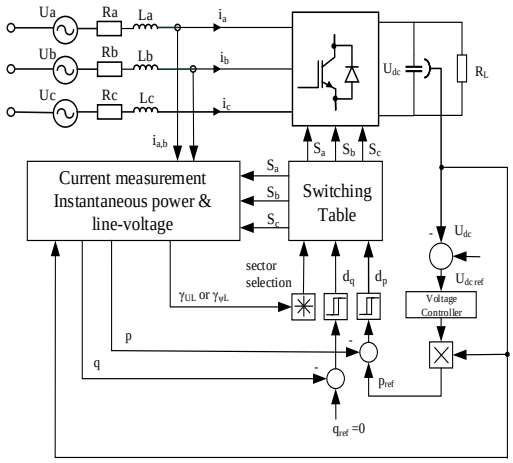

Fig. 5. Block diagram of the DPC of PWM rectifier.

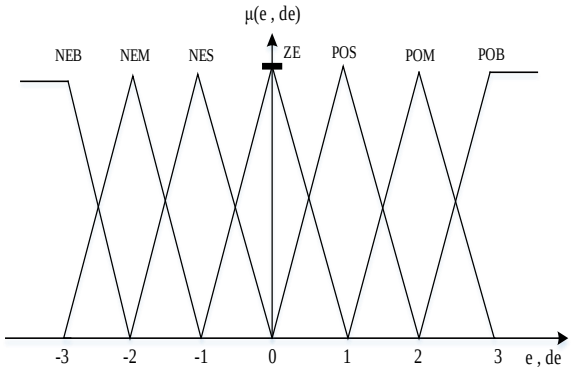

Fig. 6. Membership functions for the error between the output DC voltage and reference DC voltage and derivative of the error, as two inputs of the fuzzy system.

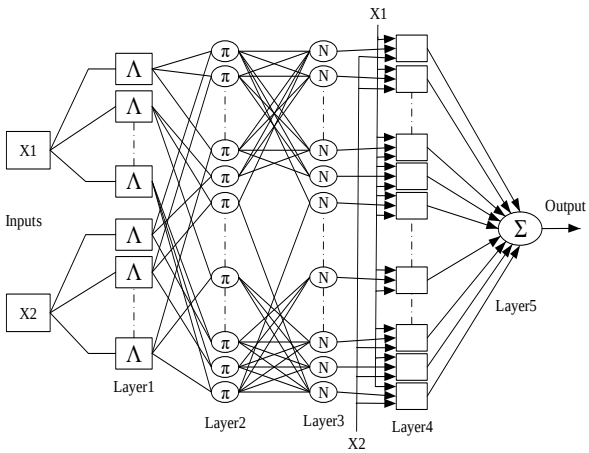

Fig. 7. Architecture of the proposed ANFIS controller (X1 and X2 are *e* and *de*).

TABLE II FUZZY INFERENCE ENGINE TABLE.

e / de	NEB	NEM	NES	ZE	POS	POM	POB
NEB	POB	POB	POM	POS	POS	POS	**ZE**
NEM	POB	POM	POS	POS	POS	ZE	**NES**
NES	POM	POS	ZE	ZE	ZE	NES	**NEM**
ZE	POM	POS	ZE	ZE	ZE	NES	**NEM**
POS	POM	POS	ZE	ZE	ZE	NES	**NEM**
POM	POS	ZE	POS	NES	NES	NEM	**NEB**
POB	**ZE**	**NES**	**NES**	**NES**	**NEM**	**NEB**	**NEB**

$$\frac{\partial E_k}{\partial g_c} = \frac{\partial E_k}{\partial O_5}\frac{\partial O_5}{\partial O_4}\frac{\partial O_4}{\partial g_c} \tag{12}$$

THEN-part of the Sugeno rules can be calculated as:

$$\frac{\partial O_4}{\partial p_k} = \overline{W_k}X \;,\; \frac{\partial O_4}{\partial q_k} = \overline{W_k}Y \;,\; \frac{\partial O_4}{\partial r_k} = \overline{W_k}; \tag{13}$$

where, *k* is the suggested rule.

For updating of the premise parameters we will have:

$$\frac{\partial E_k}{\partial g_p} = \eta \frac{\partial E_k}{\partial O_5}\frac{\partial O_5}{\partial O_4}\frac{\partial O_4}{\partial O_3}\frac{\partial O_3}{\partial O_2}\frac{\partial O_2}{\partial O_1}\frac{\partial O_1}{\partial g_p} \tag{14}$$

where, g_p is the premise parameter. With computation of the each section of the equation we have:

$$\frac{\partial E_k}{\partial g_c} = \eta(O_5 - d_5) f_k \frac{\sum_{j=1}^{j=49} w_j - w_i}{(\sum_{j=1}^{j=49} w_j)^2} \frac{\partial(\prod_{k=1,k\neq m}^{49} T_k)}{\partial T_m}\frac{\partial O_1}{\partial g_p} \tag{15}$$

where $\frac{\partial O_1}{\partial g_p}$ is the derivative of the output of the first layer.

This layer maps its output to the three parameters (a, b, and c) of a triangular membership function. However, there is a constraint: for a specific parameter (a, b, or c), a specific equation must be satisfied.

V. Simulation Results and Analysis

After introducing of VOC and DPC methods for applying on the three-phase rectifier, and design of the ANFIS controller, we use this controller in both methods, as voltage controller block, and presented the output of the simulations. Finally results are compared to the situation that PID controller is applied as voltage controller in VOC and DPC methods.

Whole of the design process is performed in the MATLAB/SIMULINK environment. As mentioned previously, the universal 6-switch bridge model of the switching rectifier is applied for both VOC and DPC methods. Also, control block of the VOC and DPC controllers are presented in Fig. 8.

A. ANFIS controller in VOC method

For this part of simulation, the VOC method is simulated. Fig. 9 presents this strategy in the SIMULINK. The proposed ANFIS controller applied as voltage controller block, and current controller blocks for d and q axis (same as Fig. 3), use PID controllers which are designed according to the procedure described in [3]. The learning rate of the coefficient of the ANFIS is set to η=0.0003. In this system, output DC voltage is set to 400V. A resistive load of 250Ω is connected to the DC link. In order to examine the load regulation capability of the rectifier, a 750Ω resistive load is paralleled to primary 250Ω load using one breaker during simulation. To evaluate the PID controller performance, a controller that its parameters are designed according to [3], is used as voltage controller. Two decoupled current controllers' parameters are similar in both PID and ANFIS-based controllers.

In Fig. 10 (a,b), output DC voltage of the rectifier, and also input voltage and current of the rectifier is shown, and the ANFIS controller is applied for controlling of the system. In Fig. 11 (a,b), this simulations is repeated when PID controller is used as the controller of the system. It should be mentioned that the input current of the rectifier is multiplied by 10.

From simulation results it is obvious that the VOC-based controlling system of the Three-phase rectifier, when using the ANFIS controller, has lower ripple and shorter settling time in both output voltage and current in comparison with PID controller. Also, the sudden variation in the output load has little effect on the operation of the system when using the ANFIS controller and this controller can adapted rapidly with the new condition. Furthermore, when ANFIS is used, input voltage and current of the rectifier are absolutely in phase and it has no reactive power exchanging with grid. Numerical comparison is presented in the table III, between ANFIS and PID controllers for VOC application.

B. ANFIS controller in DPC method

In this section, DPC is simulated based on the previous description of this method. Fig. 12 presents this strategy in

SIMULINK. ANFIS controller applied as a voltage controller block of the Fig. 5. The learning rate of the coefficient of the ANFIS is set to η=0.0007. Rectifier features and also scenario of examining the load regulation capability are same a previous simulation.

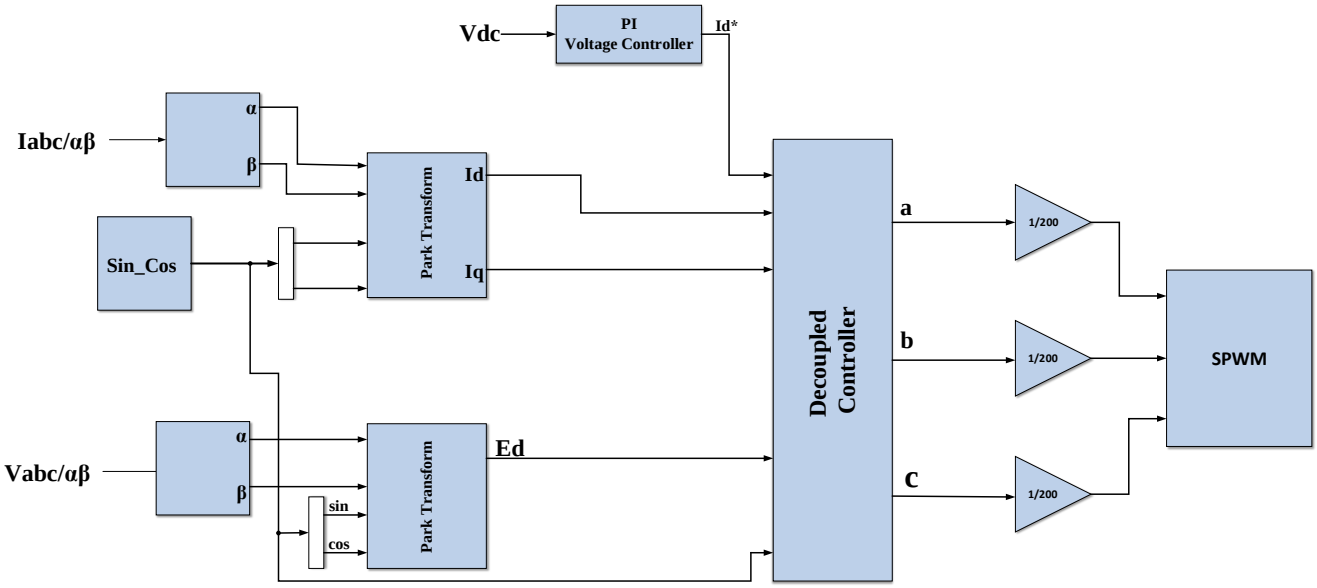

(a) VOC controller

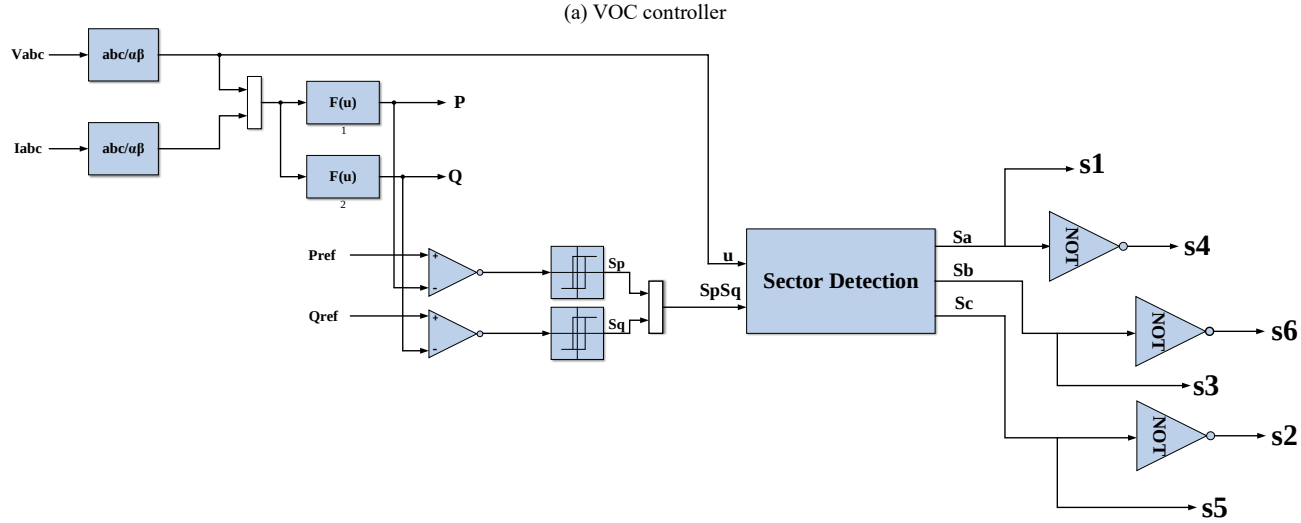

(b) DPC controller

Fig. 8. Block diagram of the VOC and DPC controller in SIMULINK.

To evaluate the PID controller performance, a controller that its parameters are designed according to [3], is used as a voltage controller instead of the voltage controller unit in the DPC system.

In Fig. 13 (a,b), output DC voltage of the rectifier, input voltage and current of the rectifier, are demonstrated. The proposed ANFIS system is applied for controlling of the system. In Fig. 14 (a,b) this work is repeated when PID controller is used as controller. It should be considered that the input current of the rectifier is multiplied by 10.

From simulation results it is clear that the DPC-based controlling system of the three-phase rectifier, when using the ANFIS controller, has lower ripple and shorter settling time in output voltage in comparison with PID controller. Also it can be found that the sudden changes in the output load has the few effect on the operation of the system when using the proposed ANFIS and this controller can adapted with the new condition. Also when ANFIS is used, input voltage and current of the rectifier are absolutely in phase and it has no reactive power exchanging with grid. Numerical comparison is shown in the table IV, between ANFIS and PID controllers for DPC application

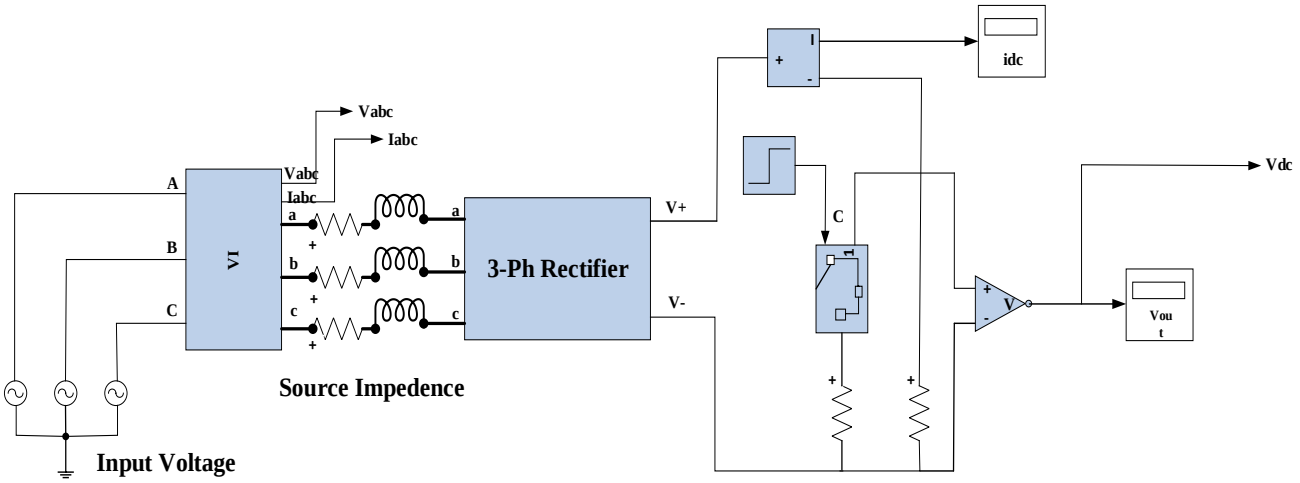

Fig. 9. Block diagram of the VOC method in SIMULINK.

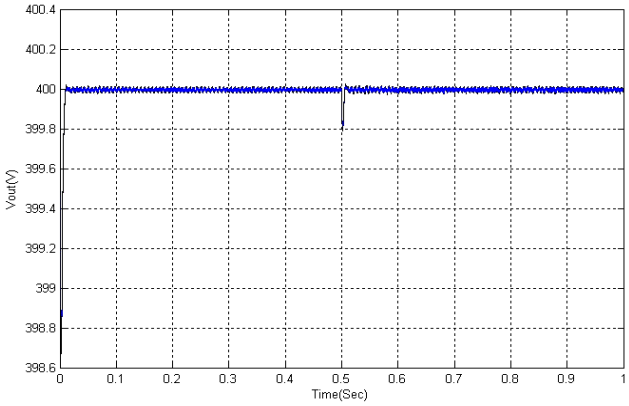

(a) Output DC voltage

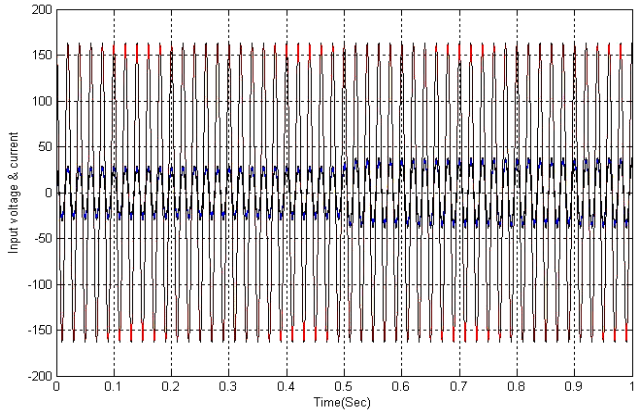

(b) Input voltage and current (blue is current, red is voltage)

Fig.10. Output DC voltage of the rectifier, and also input voltage and current of the rectifier, when the ANFIS controller is applied for controlling of the VOC-based system

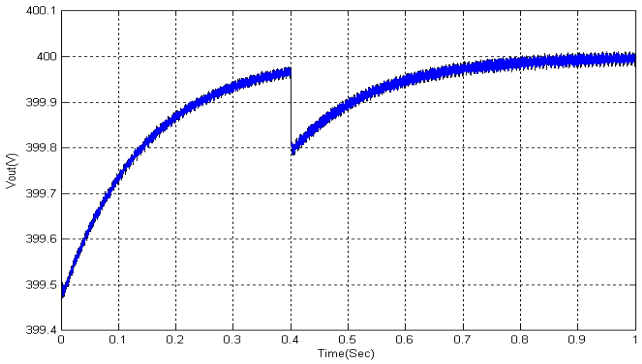

(a) Output DC voltage

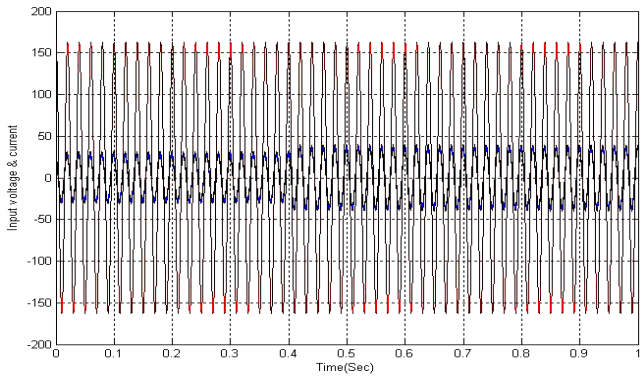

(b) Input voltage and current (blue is current, red is voltage)

Fig. 11. Output DC voltage of the rectifier, and also input voltage and current of the rectifier, when the PID controller is applied for controlling of the VOC-based system.

TABLE III COMPARISON OF UNDERSHOOT AND SETTLING TIME BETWEEN ANFIS AND PID CONTROLLERS FOR VOC METHOD.

Works (Parameters)	Undershoot	Settling time
PID (DC output voltage)	0.15%	0.5s
ANFIS (DC output voltage)	0.25%	0.02s
PID (DC output current)	0.002%	0.05s
ANFIS (DC output current)	0.001%	0.01s
PID (output voltage ripple)	0.03V	
ANFIS (output voltage ripple)	0.02V	

TABLE IV COMPARISON OF OVERSHOOT AND SETTLING TIME BETWEEN ANFIS AND PID CONTROLLERS FOR DPC METHOD.

Works (Parameters)	Undershoot	Settling time
PID (DC output voltage)	0.125%	0.12s
ANFIS (DC output voltage)	0.03759%	0.3s
PID (output voltage ripple)	0.01V	
ANFIS (output voltage ripple)	0.005V	

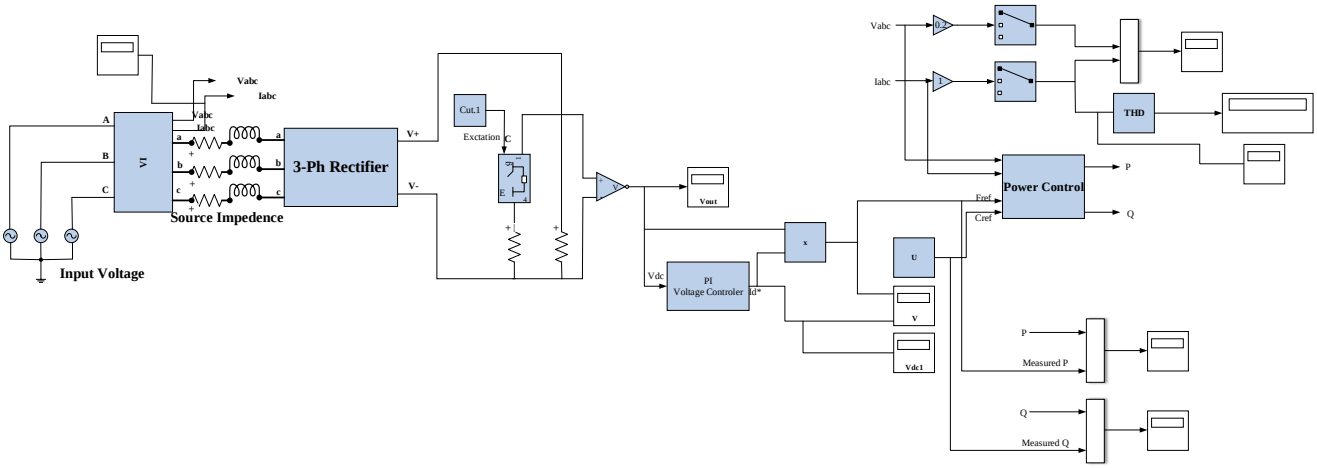

Fig. 12. Block diagram of the DPC method in SIMULINK.

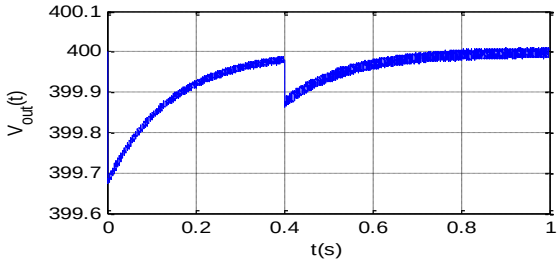

(a) Output DC voltage

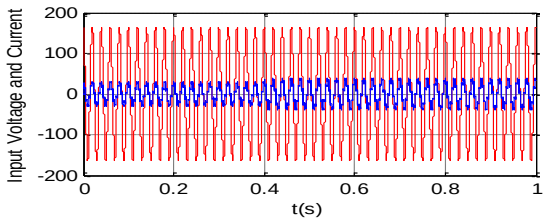

(b) Input voltage and current (blue is current, red is voltage)

Fig. 13. Output DC voltage of the rectifier, input voltage and current of the rectifier, when the ANFIS controller is applied for controlling of the DPC-based system.

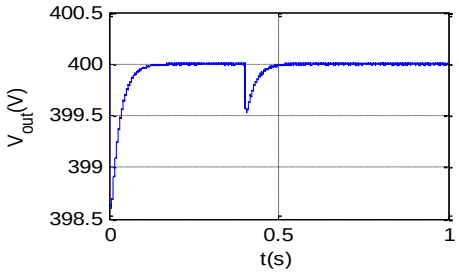

(a) Output DC voltage

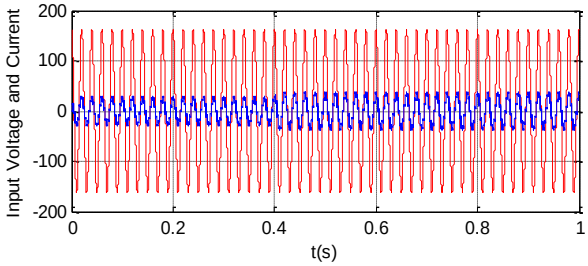

(b) Input voltage and current (blue is current, red is voltage)

Fig. 14. Output DC voltage of the rectifier, input voltage and current of the rectifier of rectifier, when the PID controller is applied for controlling of the DPC-based system.

VI. Conclusion

This paper proposed a novel hybrid intelligent controller for 6-switch three-phase PWM rectifiers. This Adaptive Neuro-Fuzzy Inference System (ANFIS) controller utilizes the strengths of both FL and NNs to enhance the static and dynamic performance of Voltage Oriented Control (VOC) and Direct Power Control (DPC) methods. The fuzzy control process is implemented through a specifically designed 5-layer NN architecture. This architecture facilitates the implementation of the fuzzy control strategy. The network has 2 nodes in the first layer, 14 nodes in the second, 49 nodes in both the third and fourth layers, and finally 1 node in the output layer. The learning process utilizes the Forward Signal and Backward Error Back-Propagation (FSBEBP) algorithm. FSBEBP relies on a single error signal to propagate adjustments throughout the network, for effectively updating the parameters within the ANFIS structure.

REFERENCES

[1] N. Nandola, B. Wang, X. Wu, R. Burgos, "Control of DC Microgrid Based flexible Cold-Rolling Steel Mill Plant – an Application of Grid Supporting Rectifier," IEEE 24th Workshop on Control and Modeling for Power Electronics (COMPEL), pp.1-7, 2023.

[2] A. Zhetessov, G. Venkataramanan, "Systematic Adaptive Robust State Feedback Control for Active Front-End Rectifiers," 2022 24th European Conference on Power Electronics and Applications (EPE'22 ECCE Europe), pp.1-11, 2022.

[3] A. Khan, M. Hosseinzadehtaher, M. B. Shadmand, S. Bayhan, H. Abu-Rub, "On the Stability of the Power Electronics-Dominated Grid: A New Energy Paradigm," IEEE Industrial Electronics Magazine, vol.14, no.4, pp. 65-78, 2020.

[4] C. M. Emeghara, S. M. Mahajan, A. Arzani, "Direct Power Control of a Surface-Mounted Permanent Magnet Synchronous Generator Wind Turbine for Offshore Applications," IEEE Access, vol.11, pp. 62409-62423, 2023.

[5] W. Ende and H. Shenghua, "Robust Control of the Three-Phase Voltage-Source PWM Rectifier Using EKF Load Current Observer," Journal of Electrical Review, R. 89, pp. 189-193, NR 3a/2015.

[6] J. Hu, L. Shang, Y. He, and Z. Q. Zhu, "Direct Active and Reactive Power Regulation of Grid-Connected DC/AC Converters Using Sliding Mode Control Approach," IEEE Trans. Power Electron., vol. 26, no. 2017.

[7] S. Maganti, N. P. Padhy, "Analysis and Design of PLL Less Current Control for Weak Grid-Tied LCL-Type Voltage Source Converter," IEEE Journal of Emerging and Selected Topics in Power Electronics, vol.10, no.4, pp. 4026-4040, 2022

[8] S. Samanta, S. Barman, J. P. Mishra, P. Roy, B. K. Roy, "Design of an Interconnection and Damping Assignment-Passivity Based Control Technique for Energy Management and Damping Improvement of a DC Microgrid," IET Generation, Transmission & Distribution, vol.14, no.11, pp. 2082-2091, 2020.

[9] Y. Gui, C. Kim, C. C. Chung, J. M. Guerrero, Y. Guan, and J. C. Vasquez, "Improved Direct Power Control for Grid-Connected Voltage Source Converters," IEEE Trans. Ind. Electron., vol. 65, no. 10, pp. 8041–8051, 2018.

[10] L. Tai, M. Lin, H. Li, Y. Li, "A Novel Three-Vector-Based Model Predictive Direct Power Control for Three-Phase PWM Rectifier," Electronics, 10 (21), Article number: 2579, 2021.

[11] J. Jang, "Self-Learning Fuzzy Controller Based on Temporal Back-Propagation," IEEE Transaction on Neural Network, Vol. 3, pp.714-723, September 1992.

[12] A. Kumar and G. Srungavarapu "A Novel Voltage Sensorless DPC Approach of AFE Rectifier Based on Virtual Flux and Dynamic DC Link Reference Design," 2016 IEEE Annual India Conf. (INDICON), Bangalore, 2016, pp. 1–6

[13] A. Baktash, A. Vahedi, and M. A. S. Masoum "New Switching Table for Improved Direct Power Control of Three-Phase PWM Rectifier," Aust. J. Electr. Electron. Eng., 2015, 5, (2), pp. 161–167.

[14] C. Lin and Y. Lu, "A Neural Fuzzy System with Fuzzy Supervised Learning," IEEE, Transaction on Systems, Man and Cybernetics, Vol. 26, No. 5, October 1996.

[15] M. R. Mosavi, A. Rahmati and A. Khoshsaadat, "Design of Efficient Adaptive Neuro-Fuzzy Controller Based on Supervisory Learning Capable for Speed and Torque Control of BLDC Botor," PRZEGLĄD ELEKTROTECHNICZNY (Electrical Review), Vol. 88, pp. 238-246, 2012.

[16] S. Tano, T. Oyama and T. Arnould, "Deep Combination of Fuzzy Inference and Neural Network in Fuzzy Inference, Journal on Fuzzy Sets and Systems, Vol. 82, No. 2, pp.151-160, 1996.

[17] T. Takagi and M. Sugeno, "Fuzzy Identification of Systems and its Applications to Modeling and Control," IEEE Transaction. On Systems, Man and Cybernetics, Vol. 15, pp. 116-132, 1985.

[18] A. Khoshsaadat, M. R. Mosavi, J. S. Moghani, A. Khoshooei, "Design of a Controller with ANFIS Architecture Attendant Learning Ability for SSSC-Based Damping Controller Applied in Single Machine Infinite Bus System," Iranian Journal of Electrical and Electronic Engineering (IJEEE), Vol. 10, No. 3, pp. 212-222, 2014.

[19] Y. Q. Zhang, and A Kandel, "Compensatory Neuro-Fuzzy Systems With Fast Learning Algorithms," IEEE Transaction on Neural Networks, Vol. 9, No. 1, January 1998.

[20] R. Zaheri, A. Khoshsaadat, J. S. Moghani. M. Abedi, "Fast Transient Hybrid Neuro-Fuzzy Controller for STATCOM During Unbalanced Voltage Sags," AUT Journal of Electrical Engineering, Vol. 50, No. 1, pp. 67-74, 2018.

[21] R. Sivakumar, C. Sahana, P. A. Savitha, "Design of ANFIS-Based Estimation and Control for MIMO Systems," International Journal of Engineering Research

and Applications, Vol. 2, Issue 3, pp. 2803-2809, May-Jun 2012.

[22] T. C. Lin and C. S. Lee, "Neural Network Based Fuzzy Logic Control and Decision System," IEEE Transactions on Computers, Vol.40, No.12, pp.1320-1336, December 2009.

Alireza Khoshsaadat was born in Boroujerd, Iran, in 1986. He received his B.Sc. degree in Electrical Engineering (EE) from Shahid Beheshti University (SBU), Tehran, Iran, in 2009, his M.Sc. degree in EE from Iran University of Science and Technology (IUST), Tehran, Iran, in 2011, and his Ph.D. degree in EE from Amirkabir University of Technology (AUT), Tehran, Iran, in 2018. He is currently a faculty member at department of electrical engineering in Shahid Beheshti University (SBU), Tehran, Iran, as an assistant professor. His research interests include analysis, design and development of power electronics converters especially with the approach of application in Electric Vehicle (EV) subsystems and chargers.

Arash Khoshooei received the B.Sc. degree in Electrical Engineering (EE) from Shahid Chamran University, Ahvaz, Iran, in 2002, and the M.Sc. degree in EE from Amirkabir University of Technology (AUT), Tehran, Iran, in 2004. He joined as a lecturer to Jundi-Shapur University of Technology (JSU), Dezful, Iran in 2005. He received the PhD degree in Power Electronics from AUT in 2018. During 2015 to 2016, he was a visiting student at the Technical University of Catalonia (UPC), Barcelona, Spain. In 2018 he backed to JSU as an assistant professor. His research interests include modeling and control of power electronics converters and integration of distributed generation systems.

Mohammad Abedini was born in Boroujerd, Iran, in 1986. He received his B.Sc. degree in electrical engineering from the Islamic Azad University of Ayatollah Boroujerdi , Iran, in 2006, and his M.Sc. and Ph.D. degrees in electrical engineering from Bu-Ali Sina University in 2008 and 2010,respectively. He is currently an associate professor at Ayatollah Borujerdi University. His current research interests include microgrids and distribution systems.

Mohammadreza Mirzaei was born in Boroujerd, Iran, in 1999. He holds a bachelor's degree in Power Engineering from Ayatollah Boroujerdi University and is currently pursuing a master's degree at the same university, specializing in Planning and Management of Electrical Energy Systems. His research interests include planning and optimization of electrical energy systems.

International Journal Of
Industrial Electronics Control and Optimization
Print ISSN: 3517-2645
Online ISSN: 3568-2645
Homepage: https://ieco.usb.ac.ir/

Observer-Based Distributed Consensus Control for Nonlinear Lipschitz and One-Side Lipschitz Fractional-Order Multi-Agent Systems

Farshid AazamManesh [1] | Elham Amini Boroujeni [2] | Fateme Bazarkhak [2] | Mahdi Pourgholi [3]

Technical and Vocational School, Technical and Vocational University, Ilam, Iran. 1
Department of Electrical and Computer Engineering, Faculty of Engineering, Kharazmi University, Tehran, Iran. 2
Faculty of Electrical Engineering, Shahid Beheshti University, Tehran, Iran.3
Corresponding author's email: m_pourgholi@sbu.ac.ir

Article Info

Article type:
Research Article

Article history:
Received: 21-December-2024
Received in revised form: 01-March-2025
Accepted: 12-April-2025
Published online: 22-Dec-2025

Keywords:
Consensus,
Distributed Control,
Fractional-Order Systems,
Nonlinear Systems,
Observer Design.

ABSTRACT

In this paper, an observer-based controller design for fractional-order multi-agent systems is discussed. By introducing a novel algorithm and leveraging appropriate lemmas and theoretical frameworks, we propose a stable observer and a distributed consensus protocol tailored for multi-agent systems within the Lipschitz and one-sided Lipschitz classes of nonlinear systems. Lipschitz systems have a bounded rate of change, ensuring proportional output to input differences, while one-sided Lipschitz systems relax this constraint, allowing differential growth in one direction for efficiency. The stability of the observer and the controller in achieving the consensus problem is demonstrated using the Lyapunov's second method. The proposed approach is rigorously developed, ensuring that the designed observer and controller meet the necessary stability criteria. Extensive simulation results validate the theoretical findings, showcasing the method's effectiveness and robustness in practical scenarios. Specifically, the simulations demonstrate that the proposed method achieves global Mittag-Leffler stability, with the estimated states converging to the actual states with minimal deviation. The method's advantages include its ability to handle a broader class of nonlinear systems, including those with large Lipschitz constants, and its robustness to uncertainties and nonlinearities. These simulations confirm the theoretical predictions and illustrate the practical applicability of our approach in real-world multi-agent systems, such as swarm robotics, power grids, and sensor networks.

I. Introduction

Fractional-order calculus has emerged as a powerful mathematical tool for modeling and control in various engineering domains, including control systems [1-3], nuclear reactor analysis [4], and biological systems such as tumor growth models, reaction-diffusion processes, and bacterial chemotaxis in diffusion gradient chambers [5, 6]. Unlike traditional integer-order models, fractional-order systems leverage fractional derivative and integral operators, enabling more accurate descriptions of complex dynamic behaviors [7]. For instance, fractional-order models have proven superior in characterizing friction phenomena in real-world engineering applications compared to their integer-order counterparts [8]. Consequently, significant research efforts have been directed toward developing fractional-order controllers to enhance the performance of closed-loop systems [9, 10].

A critical challenge in control engineering is that not all system states are directly measurable. This limitation has spurred considerable interest in observer-based controller design and stability analysis. Recent advancements include the development of observer-based controllers for linear systems with unknown inputs using linear matrix inequality (LMI) techniques [11], as well as for nonlinear fractional-order systems by reformulating Lyapunov stability conditions into LMIs [12]. Reduced-order observers have also been proposed for nonlinear fractional-order systems satisfying Lipschitz conditions, with stability guarantees derived using Lyapunov methods [13]. Notably, the one-sided Lipschitz condition, a generalization of the traditional Lipschitz class, offers greater flexibility by allowing

negative Lipschitz constants, thereby expanding the scope of applicable matrix inequalities [14, 15]. Building on these foundations, researchers have designed full-order and reduced-order observers for one-sided Lipschitz nonlinear fractional-order systems using LMI-based approaches [16]. Additionally, adaptive observer designs have been developed for systems satisfying one-sided Lipschitz and quadratic inner-boundedness conditions [17, 18].

Parallel to these developments, multi-agent systems (MAS) have garnered significant attention due to their broad applicability in areas such as unmanned aerial vehicle coordination [19], spacecraft interaction control [20], mobile robot rendezvous [21], underwater vehicle operations [22], traffic management [23], and data density control [24]. MAS consist of interconnected agents that collaboratively perform complex tasks through local interactions, offering a cost-effective and scalable alternative to centralized systems. A fundamental objective in MAS is achieving consensus, wherein the states or outputs of all agents converge to a common value [25]. While consensus in integer-order MAS has been extensively studied [26, 27], the extension to fractional-order systems remains an active area of research. For example, consensus in second-order MAS with nonlinear dynamics has been investigated under both fixed and switching topologies [28], and distributed control strategies have been proposed for one-sided Lipschitz nonlinear MAS [29]. Fractional-order proportional-integral (FOPI) controllers have also been employed to regulate DC microgrids using consensus-based approaches [30], and consensus in fractional-order MAS has been analyzed using LMI techniques and Razumikhin theory [31]. However, these studies often assume full state measurability, limiting their practical applicability.

Motivated by these advancements and challenges, this paper proposes a novel observer-based consensus control algorithm for one-sided Lipschitz nonlinear fractional-order multi-agent systems. Leveraging Lyapunov's second method, the proposed approach formulates sufficient stability conditions in the form of LMIs, which are solved using the YALMIP toolbox. The contributions of this work are threefold: (1) a systematic observer design for state estimation in fractional-order MAS, (2) a consensus control framework for one-sided Lipschitz nonlinear systems, and (3) numerical validation of the proposed method's efficacy.

The remainder of the paper is organized as follows: Section II presents the mathematical preliminaries and problem formulation. Section III details the observer design for state estimation and consensus control. Section IV provides numerical simulations to demonstrate the proposed method's effectiveness. In section V limitations of the proposed method and suggests directions for future research are provided. Finally, Section VI concludes the paper with key insights and future research directions.

II. Preliminaries

The relationship between agents in a multi-agent factorial system is determined by a weighted graph. A graph $G(v, \mathcal{E})$ is a pair that consists of a set of vertices $v(G) = \{v_1, v_2, \dots v_N\}$ and edges $\mathcal{E}(G) \subseteq \{(v_i, v_j): v_i, v_j \in v(G)\}$ (i.e., the graph is in general directed and has no self-loops). The graph is said to be undirected if $(v_i, v_j) \in \mathcal{E}(G) \Leftrightarrow (v_j, v_i) \in \mathcal{E}(G)$. The weighting matrix $W = [w_{ij}] \in R^{N\times N}$ for a graph is a matrix with $w_{ij} \geq 0$ elements ($w_{ij} > 0$, if with $w_{ij} \in \mathcal{E}(G)$, and $w_{ij} = 0$ otherwise). The in-degree matrix D is defined as $D = diag(d_1, d_2, d_3, \dots, d_N)$ with $d_i = \sum_{j=1}^{N} w_{ij}$. The Laplacian matrix L of directional graph G is defined as $L = D - W$ [32].

A directed tree where all the vertices of the graph are connected by its constituent edges is called a spanning tree of a directed graph [33].

A. Problem Formulation

Definition 1 [34]: The uniform formula of a fractional integral with $\alpha \in (0, 1)$ is defined by

$$ {}_{t0}D_t^{-\alpha} f(t) = \frac{1}{\Gamma(\alpha)} \int_{t0}^{t} \frac{f(\tau)}{(t-\tau)^{1-\alpha}} d\tau , \quad (1) $$

where ${}_{t0}D_t^{-\alpha} f(t)$ is the fractional integral of order α of a function $f(t)$, $\Gamma(.)$ is the Gamma function. For an arbitrary real number p. The Caputo derivative operator of fractional order is defined by

$$ {}_{t0}^{C}D_t^{p} f(t) = {}_{t0}D_t^{-q} \left[\frac{d^{[p]+1}}{dt^{[p]+1}} f(t)\right]. \quad (2) $$

where $q = [p] - p + 1$ and $[p]$ stands for the integer part of p.

Definition 2. [35]: Mittag-Leffler function as a complex-valued function of a complex argument z can be presented as:

$$ E_{\alpha,\beta}(z) = \sum_{k=0}^{\infty} \frac{z^k}{\Gamma(k\alpha + \beta)}, \quad (3) $$

where $\alpha, \beta \in C$, $Re\{\alpha\} > 0$, and C is the set of complex numbers, when $\beta = 1$, $E_\alpha(z) = E_{\alpha,1}(z)$.

Lemma 1. [36]: If $x \in R^n$ be a differentiable vector:

$$ \frac{1}{2} {}_{t_0}^{C}D_t^{\alpha}\{x^T(t)x(t)\} \leq x^T(t) {}_{t_0}^{C}D_t^{\alpha} x(t), \quad \forall t \geq t_0, \alpha \in (0,1). \quad (4) $$

Now, suppose the dynamics of each agent can be described as [37]:

$$ {}_{t_0}^{C}D_t^{\alpha} x_i = Ax_i + Bu_i + F_i(x_i, u_i) , \quad i\epsilon\{1,2, \dots N\}. \quad (5) $$

$$ y_i = Cx_i $$

where $A\epsilon R^{n\times n}$, $B\epsilon R^{n\times m}$, $C\epsilon R^{m\times n}$, $F_i(x_i,u_i)\epsilon R^{n\times 1}$ is the nonlinear term, and ${}_{t_0}^{C}D_t^{\alpha}$ represents the Caputo fractional derivative.

Definition 3. [38]: The vector value function $F_i(x_i,u_i)$: $R^n \times R^m \rightarrow R^n$ is a nonlinear Lipschitz continuous function with a Lipschitz constant r such that:

$$\left\|F_i(x_{i_1},u_i)\right\| - \left\|F_i(x_{i_2},u_i)\right\| \le r\left\|x_{i_1}-x_{i_2}\right\|, \quad (6)$$
$$x_{i_1}, x_{i_2} \in R^n, u_i \in R^m .$$

Definition 4. [38]: The vector value function $F_i(x_i,u_i)$: $R^n \times R^m \rightarrow R^n$ is one-sided Lipschitz, where γ_s is a one-sided Lipschitz constant such that:

$$< sF_i(x_{i_1},u_i) - sF_i(x_{i_2},u_i),\ (x_{i_1}-x_{i_2}) > \le \quad (7)$$
$$\gamma_s\left\|x_{i_1}-x_{i_2}\right\|^2, \quad x_{i_1},x_{i_2}\in R^n, u_i \in R^m.$$

where s is a symmetric positive definite matrix, $\langle\cdot,\cdot\rangle$ denotes the inner product and $\|\cdot\|$ is the Euclidean norm.

Definition 5. [39]: Suppose $x_{eq}=0$ is the equilibrium point of the system (5) with $0<\alpha<1$ and t_0=0. Now, suppose $V(t,x(t))$: $[0,\infty)\times R^n \mapsto R$ is a continuously differentiable function and local Lipschitz with respect to x such that:

$$\alpha_1\|x\|^a \le V\big(t,x(t)\big) \le \alpha_2\|x\|^{ab} \quad (8)$$

Likewise,

$$ {}_{t_0}^{C}\mathcal{D}_t^{\beta}\, V\big(t,x(t)\big) \le -\alpha_3\|x\|^{ab}, \quad t\ge t_0, \quad (9)$$
$$x\in\mathbb{D}, \quad \beta\in(0,1).$$

where α_1, α_2, α_3 and a, b are positive fixed numbers. In this case, the equilibrium point $x_{eq}=0$ is Mittag–Leffler stable. If the assumptions hold globally on R^n then $x_{eq}=0$ is globally Mittag–Leffler stable.

Considering the quasi-state vector of the batch system as $x=[x_1^T,\dots x_N^T]^T$, the nonlinear term is $\mathbf{F}(\boldsymbol{x},\boldsymbol{u})=[F_1(x_1,u_1),\dots,F_N(x_N,u_N)]^T$ and u_i is input vector for each i^{th} agent.

Assumption1. [13] The pair (A,C) is observable, $s_i=s_i^T$ is a positive definite matrix, and we can get a positive scalar θ such that:

$$-\theta s_i - A^T s_i - s_i A + C^T C = 0 \quad (10)$$

Assumption 2. For a linear system, if the pair (A,B) is stabilizable, then there exists a matrix k that can be obtained such that $\lambda(A+Bk)<\frac{\alpha\pi}{2}$, and $x_i^T s_i x_i$ can be chosen as a Lyapunov function such that:

$$s_i(A+Bk)+(A+Bk)^T s_i = -Q_i, \quad Q_i>0. \quad (11)$$

Now, by considering the control law for distributed systems:

$$u_i = -ck\sum_{j\in N_i} w_{ij}\big(\hat{x}_j-\hat{x}_i\big). \quad (12)$$

where $\hat{x}_i$and $\hat{x}_j$ are state estimates in (16). In addition, $c>0\in R$, N_i is the agent i^{th} neighbors, $k\in R^{m\times n}$ is feedback matrix and w_{ij} is considered equal to 1 for any $j\in N_i$ in this model. The general system dynamics (5) can be rewritten as follows:

$$ {}_{t_0}^{C}D_t^{\alpha}x = (I_N\otimes A)x - (cL\otimes Bk)\hat{x} + \mathbf{F}(\boldsymbol{x},\boldsymbol{u}) \quad (13)$$
$$y=(I_N\otimes C)x .$$

where $\otimes$ represents the Kronecker product, $L=L(G)$ is the Laplacian matrix graph G. In addition, if $I_N\otimes A=\bar{A}$, $-(cL\otimes Bk)=\bar{\mathrm{B}}$, and $(I_N\otimes C)=\bar{C}$, then (13) can be rewritten as follows:

$$ {}_{t_0}^{C}D_t^{\alpha}x = \bar{A}\boldsymbol{x} + \bar{\mathrm{B}}\hat{x} + \mathbf{F}(\boldsymbol{x},\boldsymbol{u}) \quad (14)$$
$$y=\bar{C}x$$

Lemma 2. [17] Considering the nonlinear Lipschitz continuous function in (6) and Assumption 2 are met, then r has the following upper bound:

$$r<\frac{\lambda_{min}(Q)}{2\lambda_{max}(s)}. \quad (15)$$

where $Q=diag([Q_1,Q_2,\dots,Q_N])$ and $s=diag([s_1,s_2,\dots,s_N])$. Then, the feedback law $u_i=-ck\sum_{j\in N_i}w_{ij}(\hat{x}_j-\hat{x}_i)$ globally Mittag Leffler stabilizes the system (14).

III. Main Results

A. Design observer

A.1. Observer for Lipschitz class of nonlinear system

In this section, a fractional-order state observer for system (5) is introduced as follows:

$$ {}_{t_0}^{C}D_t^{\alpha}\hat{x}_i = A\hat{x}_i + Bu_i + \mathbf{F}(\hat{\boldsymbol{x}},\boldsymbol{u}) + \boldsymbol{\mathcal{L}_i}\,(C\hat{x}_i - y_i); t\ge t_0. \quad (16)$$

where $\hat{x}_i\epsilon R^{N.d}$ are state estimates, $\boldsymbol{\mathcal{L}_i}$ is the observer of the gain. According to (12), (16) can be rewritten as:

$$ {}_{t_0}^{C}D_t^{\alpha}\hat{x} = (I_N\otimes A)\hat{x} - (cL\otimes Bk)\hat{x} + \boldsymbol{F}(\hat{\boldsymbol{x}},\boldsymbol{u}) + (I_N\otimes\boldsymbol{\mathcal{L}_i})(\bar{C}\hat{x}-y), \quad t\ge t_0. \quad (17)$$

Considering the definitions given for the parameters of (14), then (17) yields that:

$$ {}_{t_0}^{C}D_t^{\alpha}\hat{x} = \bar{A}\hat{x} + \bar{B}\hat{x} + \mathbf{F}(\hat{\boldsymbol{x}}, \boldsymbol{u}) + \boldsymbol{\mathcal{L}}(\bar{C}\hat{x} - y), \quad t \geq t_0. \tag{18} $$

where $(I_N \otimes \boldsymbol{\mathcal{L}_i}) = \boldsymbol{\mathcal{L}}$.

Theorem1. A sufficient condition for the stability of the observer (18) is that the Lipschitz constant is smaller than:

$$ r < \frac{\lambda_{min}(\theta s)}{2\lambda_{max}(s)} \tag{19} $$

Proof:

Note that if observer (18) can provide an accurate estimate of the state vector in (14), then:

$$ \lim_{t\to\infty}(\hat{x} - x) = 0 \tag{20} $$

The difference between the system's state vector and the observer's state vector is defined as follows:

$$ e = \hat{x} - x \tag{21} $$

By considering the Lyapunov function candidate as:

$$ V(e) = e^T s e \tag{22} $$

and substituting (21) in (22), we have:

$$ V(e) = (\hat{x} - x)^T s(\hat{x} - x) \tag{23} $$

Taking Caputo derivative from (21) yields

$$ \begin{aligned} {}_{t_0}^{C}D_t^{\alpha}e &= (I_N \otimes A)\hat{x} - (cL \otimes Bk)\hat{x} + \mathbf{F}(\hat{\boldsymbol{x}}, \boldsymbol{u}) \\ &\quad + (I_N \otimes \boldsymbol{\mathcal{L}_i})(\bar{C}\hat{x} - y) \\ &\quad - (I_N \otimes A)x + (cL \otimes Bk)\hat{x} \\ &\quad - \mathbf{F}(\boldsymbol{x}, \boldsymbol{u}) \\ &= \big((I_N \otimes A) + \boldsymbol{\mathcal{L}}\bar{C}\big)e + \Delta\mathbf{F} \\ &= (\bar{A} + \boldsymbol{\mathcal{L}}\bar{C})e + \Delta\mathbf{F} \end{aligned} \tag{24} $$

where $(I_N \otimes A) = \bar{A}$ and $\Delta\mathbf{F} = \mathbf{F}(\hat{\mathbf{x}}, \mathbf{u}) - \mathbf{F}(\mathbf{x}, \mathbf{u})$. Assumption 1 can be defined for N −agent:

$$ \bar{A}^T s + s\bar{A} = -\theta s + \bar{C}^T\bar{C} \tag{25} $$

Using condition (6), (24), (25), and Lemma1, we have:

If $\boldsymbol{\mathcal{L}} = -\frac{1}{2}s^{-1}\,\bar{C}^T$ is considered, then the sufficient condition for ${}_{t_0}^{C}D_t^{\alpha}V(e) < 0$ is $r < \frac{\lambda_{min}(\theta s)}{2\lambda_{max}(s)}$ and the proof is completed.

A.2. Observer for One-Sided Lipschitz

Theorem2. When Lemma 2 is met, the sufficient condition for stability of observer (18) is that the Lipschitz constant is smaller than:

$$ \begin{aligned} {}_{t_0}^{C}D_t^{\alpha}V(e) &\leq 2e^T(t)\, s\, {}_{t_0}^{C}D_t^{\alpha}e(t) \\ &\leq e^T[-\theta s + \bar{C}^T\bar{C} + \bar{C}^T\boldsymbol{\mathcal{L}}^T s \\ &\quad + s\boldsymbol{\mathcal{L}}\bar{C}]e + 2e^T s\Delta F \\ &\leq -(\theta s - \bar{C}^T\bar{C} - \bar{C}^T\boldsymbol{\mathcal{L}}^T s \\ &\quad - s\boldsymbol{\mathcal{L}}\bar{C})\|e\|^2 + 2\|s\|\|e\|\|\Delta F\| \\ &\leq -\lambda_{min}(\theta s - \bar{C}^T\bar{C} \\ &\quad - 2s\boldsymbol{\mathcal{L}}\bar{C})\|e\|^2 + 2r\lambda_{max}(s)\|e\|^2. \end{aligned} \tag{26} $$

$$ \lambda_{min}(\theta s) - 2\gamma_s > 0 \tag{27} $$

Proof:

From (4), (22), and (24) it can be concluded that:

$$ \begin{aligned} {}_{t_0}^{C}D_t^{\alpha}V(e) &\leq e^T[-\theta s + \bar{C}^T\bar{C} + \bar{C}^T\boldsymbol{\mathcal{L}}^T s + s\boldsymbol{\mathcal{L}}\bar{C}]e \\ &\quad + 2e^T s\Delta F \\ &\leq -e^T\theta s e + e^T\bar{C}^T\bar{C}e \\ &\quad + e^T\bar{C}^T\boldsymbol{\mathcal{L}}^T s e + e^T s\boldsymbol{\mathcal{L}}\bar{C}e \\ &\quad + 2e^T s\Delta F \end{aligned} \tag{28} $$

Also, using (7), (28) yields:

$$ \begin{aligned} {}_{t_0}^{C}D_t^{\alpha}V(e) &\leq -\lambda_{min}(\theta s - \bar{C}^T\bar{C} - 2s\boldsymbol{\mathcal{L}}\bar{C})|e|^2 \\ &\quad + 2\gamma_s|e|^2 \end{aligned} \tag{29} $$

If $\boldsymbol{\mathcal{L}} = -\frac{1}{2}s^{-1}\,\bar{C}^T$ then $\lambda_{min}(\theta s) - 2\gamma_s > 0$ and the proof is completed.

The propose observer-based distributed Control for a multi-agent system is illustrated in Figure 1

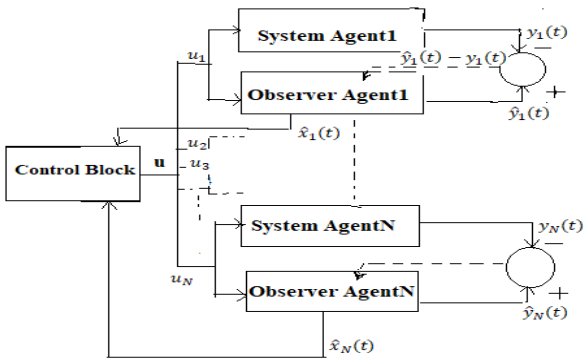

Figure 1. Block diagram portraying the system agents along with the observer and the feedback control unit

B. Achieving consensus

Theorem 3. If Assumptions 1 and 2, and Lipschitz condition (6) are such that:

$$r < \frac{1}{2} inf\left(\frac{1}{\lambda_{max}(s)}, \frac{\lambda_{min}(\theta s)}{\lambda_{max}(s)}\right) \quad (30)$$

Then, observer (18) and feedback controller $u_i = -ck\sum_{j\in N_i} w_{ij}(\hat{x}_j - \hat{x}_i)$ will be globally Mittag-Leffler stable for the dynamical system (14).

Proof:

By utilizing (18), (21), and (24), we have:

$$ {}_{t_0}^{C}D_t^{\alpha} e(t) = \left(\bar{A} - \frac{1}{2} s^{-1}\ \bar{C}^T\bar{C}\right) e + \mathbf{F}(\hat{\mathbf{x}}, \mathbf{u}) - \mathbf{F}(\hat{\mathbf{x}} - \mathbf{e}, \mathbf{u}). \quad (31)$$

By introducing the following Lyapunov function:

$$V(\hat{x}, e) = \delta V_1(\hat{x}) + V_2(e) \quad , \quad \delta > 0 \quad (32)$$

where $V_1(\hat{x})$ and $V_2(e)$ are:

$$V_1(\hat{x}) = \hat{x}^T s \hat{x} \quad (33)$$
$$V_2(e) = e^T s e$$

Taking derivative from both sides, we have

$$ {}_{t_0}^{C}D_t^{\alpha} V(\hat{x}, e) = \delta\, {}_{t_0}^{C}D_t^{\alpha} V_1(\hat{x}) + {}_{t_0}^{C}D_t^{\alpha} V_2(e) \quad (34)$$

Using (18), (33), (34) and Theorem 1, it can be concluded that:

$$ {}_{t_0}^{C}D_t^{\alpha} V_1(\hat{x}) \le \hat{x}^T[s(\bar{A} + \bar{B}) + (\bar{A} + \bar{B})^T s]\hat{x} + 2\hat{x}^T s\mathbf{F}(\hat{\boldsymbol{x}}, \boldsymbol{u}) - \hat{x}\bar{C}^T\bar{C}e. \quad (35)$$

Inspired by Assumption 2 for N-agent and the Cauchy-Schwarz inequality:

$$ {}_{t_0}^{C}D_t^{\alpha} V_1(\hat{x}) \le -\|\hat{x}\|^2 + 2\hat{x}^T s\mathbf{F}(\hat{x}, \mathbf{u}) + \|\hat{x}\|\|\bar{C}^T\bar{C}\|\|e\| \quad (36)$$

Using condition Lipschitz and knowing that $\mathbf{F}(\mathbf{0}, \mathbf{u}) = 0$, then

$$ {}_{t_0}^{C}D_t^{\alpha} V(\hat{x}, e) \le \delta[-1 + 2r\lambda_{max}(s)]\|\hat{x}\|^2 + \delta\|\bar{C}^T\bar{C}\|\|e\|\|\hat{x}\| + D_{t_0,t}^{\alpha} V_2(e). \quad (37)$$

If (30) holds, according to theorem 1, when $= \lambda_{min}(\theta s) - 2r\lambda_{max}(s) > 0$, then:

$$ {}_{t_0}^{C}D_t^{\alpha} V_2(e) \le -l\|e\|^2 \quad (38)$$

Now considering $1 - 2r\lambda_{max}(s) > 0$, and $\|\bar{C}^T\bar{C}\| > 0$. Thus, by selecting δ as (39) the Mittag- Leffler stability ensures the stability of the observer:

$$\delta < \frac{\left(1 - 2r\lambda_{max}(s)\right)l}{\|\bar{C}^T\bar{C}\|^2} \quad (39)$$

Algorithm 1 is proposed for distributed observer-based control for consensus in fractional-order systems *(DOC-FO)* for *N-agent* where θ has a real value.

Algorithm1: DOC − FO Algorithm for N − Agent

$Input: A, B, C, \theta$
1. $if\ \ \theta > 0$
2. Give $(10) \leftarrow \theta$
3. $Compute\ s \leftarrow \ (10)$
4. $if\ \ s > 0 \ \ and\ s^T = s$
5. $else$
6. $back\ to\ step\ 1$
7. $Compute\ k \leftarrow \ (11)$
8. $if\ \ Re(\bar{A} + \bar{B}) < 0$
9. $u_i = ck\sum_{j\in N_i} w_{ij}(\hat{x}_j - \hat{x}_i)$
10. $else$
11. $back\ to\ step\ 2$
12. end
13. end

IV. Nmerical Example

The simulation is based on five agents with the observer and control unit as shown in Figure 2 and the relations (14) and (18) for each agent**.**

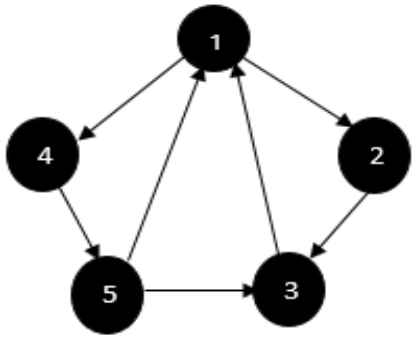

Figure 2. Topology of graph

The matrices of the system (5) considering $x_i \in R^2$ are shown in (40). The order of the fractional derivative is considered as: $\alpha = 0.9$.

$$A_i = \begin{bmatrix} 0 & 2 \\ -1 & -2 \end{bmatrix}, \quad B = [0\ \ 1]^T \ , \ C = [\,1\ \ 0], \quad F_i(x_i, u_i) = \frac{1}{6}\begin{bmatrix} \sqrt{{x_{i_1}}^2 + {x_{i_2}}^2} \\ sin(x_{i_1})\, cos\,(u_i) \end{bmatrix} \quad (40)$$

where $= I$, $s_i = \begin{bmatrix} 0.25 & 0 \\ 0 & 0.5 \end{bmatrix}$ and $r \simeq 0.16 < \frac{\lambda_{min}(Q)}{\lambda_{max}(\theta s)} = 1$, with $\theta = 4$, the pair (A, C) is observable and by solving (10), we have:

$$r < \frac{1}{2}\left(\frac{\lambda_{min}(\theta s)}{\lambda_{max}(s)}\right) = 1 \; and \; \gamma_s < \frac{1}{2}(\lambda_{min}(\theta s)) = 0.5 \quad (41)$$

The system (40) is global Mittag-Leffler stable and estimated states have converged towards the true values. Feedback matrix$k = [0 \;\; 0.4804]$, and $c = 2$ for the following initial conditions:

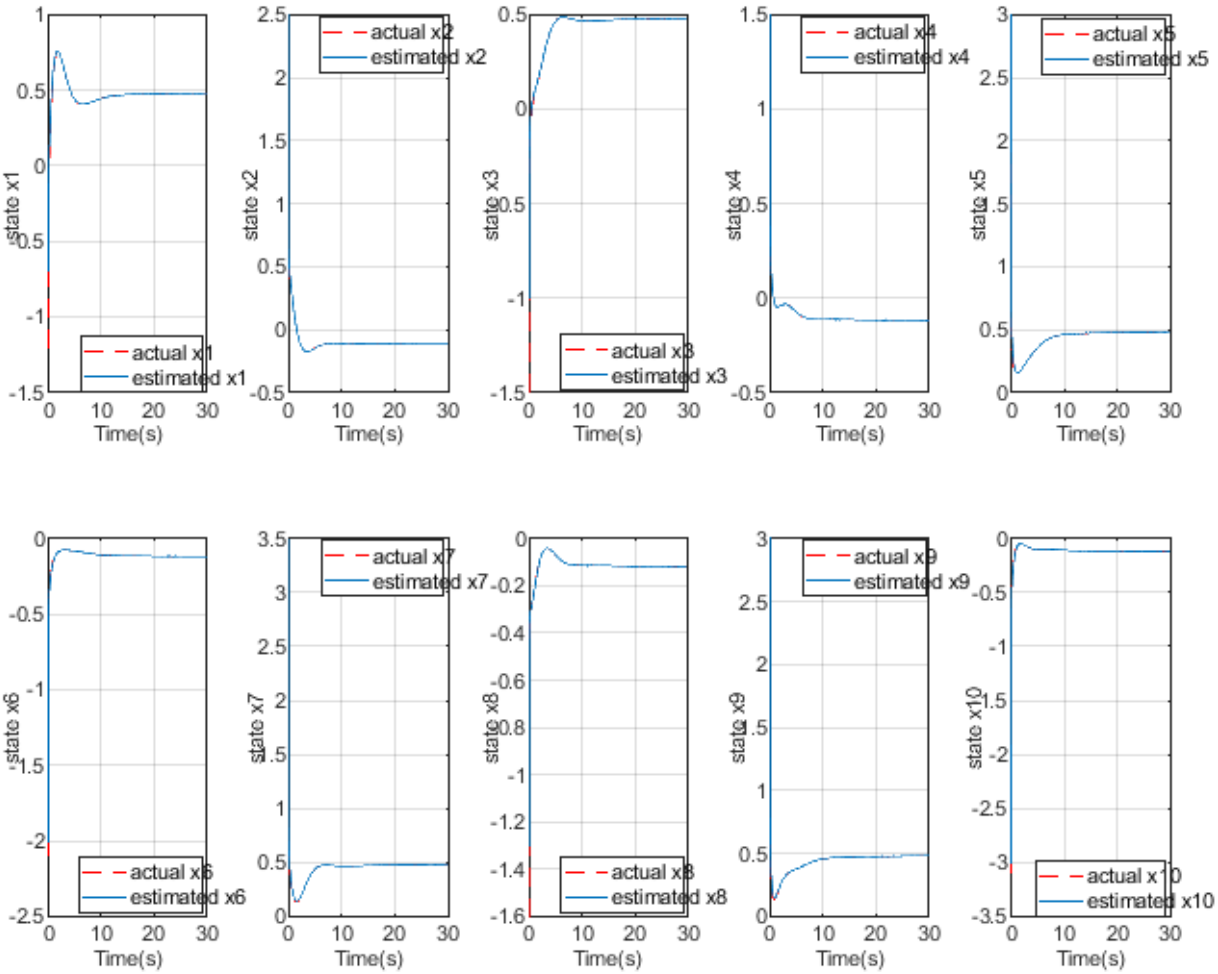

Figure 3 presents the simulation results

$x_1(0) = [-1.5; 2]$, $\hat{x}_1(0) = [-0.8; 2.5]$,

$x_2(0) = [-1.5; 1.2]$, $\hat{x}_2(0) = [-1.1; 1.5]$,

$x_3(0) = [2.5; -2.1]$, $\hat{x}_3(0) = [2.9; -2]$,

$x_4(0) = [3; -1.6]$, $\hat{x}_4(0) = [3.4; -1.3]$,

$x_5(0) = [2.4; -3.1]$, $\hat{x}_5(0) = [2.8; -3]$,

Figure 3 presents the simulation results comparing the actual system states with the estimated states obtained from the proposed observer. The results demonstrate that the estimated states closely track the actual states, with minimal deviation observed over the simulation period. This alignment indicates the effectiveness of the estimation algorithm in accurately reconstructing the system states. Furthermore, the convergence of the estimated states to the actual states reliability of the proposed methodology under the given operating conditions. These findings underscore the potential of the approach for practical applications in state estimation and control systems.

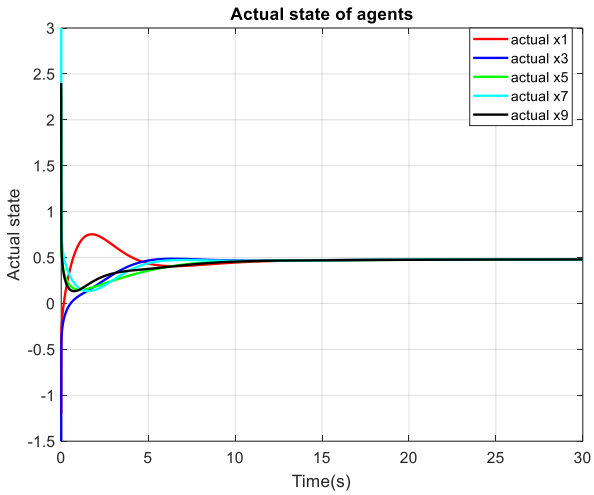

Figure 4. Consensus for the first actual state

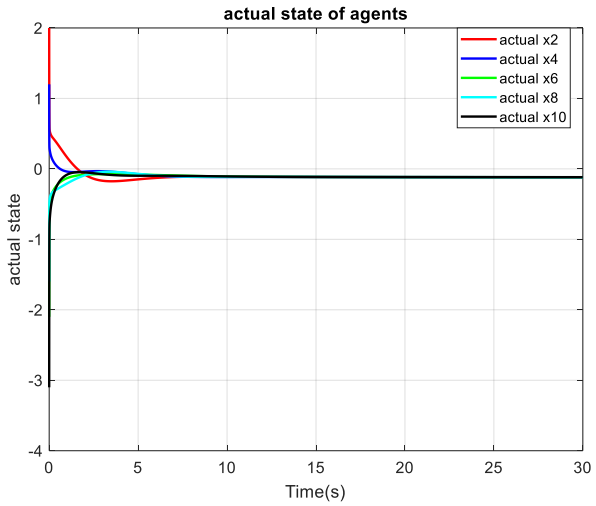

Figure 5. Consensus for the second actual state

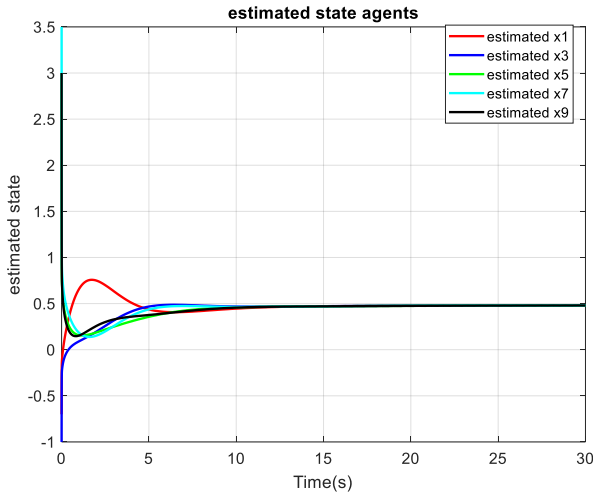

Figure 6. Consensus for the first estimated state

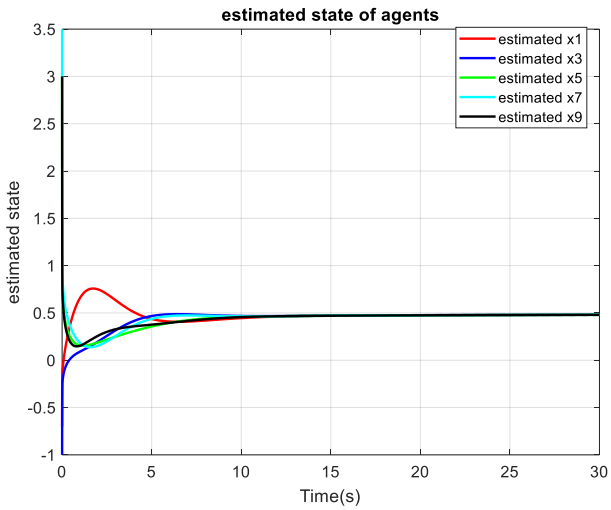

Figure 7. Consensus for the second estimated state

As illustrated in Figure 4 through Figure 7, the simulation results clearly demonstrate that the states of all agents exhibit a consistent trend of convergence over time, ultimately aligning with the average of the initial conditions of the states. This behavior is indicative of the system's inherent consensus dynamics, which drive the agents toward a unified state. The convergence rate, as observed in the figures, is influenced by the network topology and the interaction weights among agents, as described by the proposed control protocol. The results validate the theoretical analysis presented earlier, confirming that the designed control strategy effectively achieves consensus in a distributed multi-agent system.

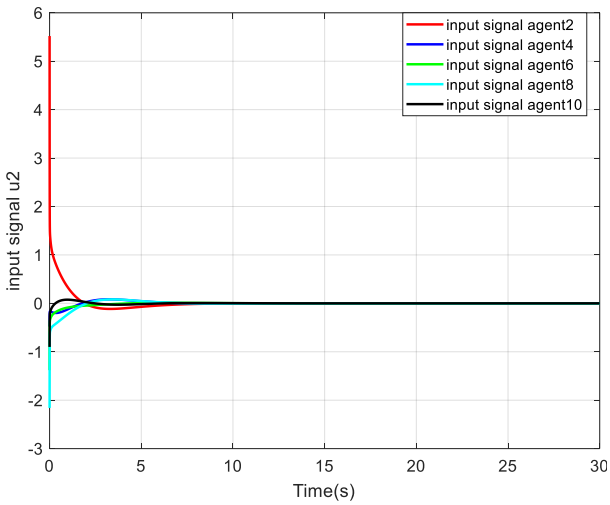

Figure 8. Input signal u2

Figure 8 shows the second input signal for five agents. As it is clear from the relationships, the first input signal is always zero because the value of zero in the first row of matrix B is zero. The control effort in the proposed method is optimized through the use of a state feedback law and a distributed consensus protocol. The control input u_i is designed as:

$$u_i = -ck \sum_{j \in N_i} w_{ij} (\hat{x}_j - \hat{x}_i).$$

where c is a positive scalar, k is the feedback matrix, and w_{ij} represents the interaction weights between agents. This design ensures that the control effort is distributed efficiently among agents, minimizing unnecessary energy consumption.

Traditional methods often rely on centralized control or simpler feedback mechanisms, which may require higher control effort, especially in systems with large Lipschitz constants or complex nonlinearities. The proposed method, by leveraging fractional-order dynamics and one-sided Lipschitz conditions, reduces the control effort while maintaining stability and performance. The proposed method achieves global Mittag-Leffler stability, which ensures that the system states converge to consensus asymptotically. The synchronization time is influenced by the network topology and the interaction weights among agents. The use of fractional-order dynamics allows for faster convergence in systems with memory and hereditary effects, which are common in real-world applications. The

norm of the error signals $\| e \|$, where $e = \hat{x} - x$, is minimized through the design of a stable observer and a distributed consensus protocol. The error dynamics are analyzed using Lyapunov's second method, ensuring that the error converges to zero over time. The proposed method guarantees that the norm of the error signals remains bounded and converges to zero, even in the presence of nonlinearities and uncertainties.

V. Limitations of the Study

While this study presents a robust observer-based controller design for fractional-order multi-agent systems within the Lipschitz and one-sided Lipschitz frameworks, several limitations should be acknowledged. First, the proposed approach assumes ideal communication conditions among agents, neglecting potential communication delays that are prevalent in real-world multi-agent systems. The presence of delays can significantly impact the stability and performance of the consensus protocol, and future work should address this limitation by incorporating delay compensation mechanisms. Additionally, the study focuses on fixed network topologies, which may not fully capture the dynamic nature of real-world systems where network topologies can change over time due to agent mobility or link failures. Extending the proposed framework to handle stochastic switching topologies would enhance its applicability to more complex and realistic scenarios. Furthermore, the analysis is confined to Mittag-Leffler stability, and the concept of fixed-time stability, which guarantees convergence within a predefined time regardless of initial conditions, is not explored. Investigating fixed-time stability could provide stronger guarantees for time-critical applications. Lastly, while the one-sided Lipschitz condition broadens the applicability of the proposed method to a wider class of nonlinear systems, the design and implementation complexity may increase for systems with highly nonlinear dynamics or exogenous disturbances. Future research should explore these aspects to further improve the robustness and practicality of the proposed approach.

VI. Conclusion

Many existing research methods are limited to stabilizing dynamical systems with small Lipschitz constants and often fail to provide effective solutions when the Lipschitz constant becomes large. To address this limitation, this paper leverages the concept of one-sided Lipschitz continuity, which was initially introduced in mathematical literature and is capable of encompassing a broader family of nonlinear systems. By utilizing this framework, we propose an observer-based distributed consensus control design tailored for nonlinear fractional-order multi-agent systems within both Lipschitz and one-sided Lipschitz classes. The proposed controller, designed using a state feedback law, ensures global Mittag-Leffler stability of the system, thereby offering a robust solution for a wider range of nonlinear dynamics. This advancement not only overcomes the constraints of traditional methods but also provides a foundation for further exploration in more complex scenarios, such as systems with communication delays, stochastic switching topologies, or exogenous disturbances. Future research could extend this work to incorporate fixed-time stability guarantees or address time-varying network conditions, further enhancing the applicability and robustness of the proposed approach in real-world multi-agent systems.

REFERENCES

[1] Javan, Ali Akbar Kekha, and Assef Zare. "Images encryption based on robust multi-mode finite time synchronization of fractional-order hyper-chaotic Rikitake systems." Multimedia Tools and Applications vol.83, no.1, pp. 1103-1123, 2024.

[2] M. Nazifi, M. Pourgholi, "Adaptive Fractional-Order Consensus Control of Cyber-Physical Power Systems in The Presence of Unbounded Perturbations." International Journal of Industrial Electronics Control and Optimization (2024).

[3] F. Aazam Manesh, M. Pourgholi, and E. Amini Boroujeni, "Fractional-Order Multi-agent Formation Using Distributed NMPC Design with Obstacles and Collision Avoidance and Connectivity Maintenance," *Journal of Control, Automation and Electrical Systems,* pp. 1-11, 2022.

[4] M. Sallah and C. Margeanu, "Effect of fractional parameter on neutron transport in finite disturbed reactors with quadratic scattering," 2016.

[5] A. El-Sayed, S. Rida, and A. Arafa, "On the solutions of time-fractional bacterial chemotaxis in a diffusion gradient chamber," *International Journal of Nonlinear Science,* vol. 7, no. 4, pp. 485-492, 2009.

[6] E. Balci, S. Kartal, and I. Ozturk, "Comparison of dynamical behavior between fractional order delayed and discrete conformable fractional order tumor-immune system," *Mathematical Modelling of Natural Phenomena,* vol. 16, p. 3, 2021.

[7] A. Kilbas, H. M. Srivastava, and J. J. Trujillo, *Theory and applications of fractional differential equations*. elsevier, 2006.

[8] M. Shahvali, M.-B. Naghibi-Sistani, and J. Askari, "Adaptive fault compensation control for nonlinear uncertain fractional-order systems: static and dynamic event generator approaches," *Journal of the Franklin Institute,* vol. 358, no. 12, pp. 6074-6100, 2021.

[9] Varga, Bence, J.K. Tar, and R. Horváth, "Fractional order inspired iterative adaptive control," *Robotica*, vol.42, no. 2, pp. 482-509, 2024.

[10] Chendrayan, J. Hoon Jeong, and Y. H. Joo, "Stochastic exponential stabilization and optimal control results for a class of fractional order equations," *Chaos, Solitons & Fractals*, vol. 185, no. 1, pp.15087, 2024.

[11] H. Kheloufi, A. Zemouche, F.Bedouhene, and M. Boutayeb, "On LMI conditions to design observer-based controllers for linear systems with parameter uncertainties," *Automatica,* vol. 49, no. 12, pp. 3700-3704, 2013.

[12] A. Boroujeni and H. R. Momeni, "Observer based control of a class of nonlinear fractional order systems using LMI," *International Journal of Science and Engineering Investigations,* vol. 1, no. 1, pp. 48-52, 2012.

[13] M. Pourgholi and E. A. Boroujeni, "An iterative LMI-based reduced-order observer design for fractional-order chaos synchronization," *Circuits, Systems, and Signal Processing,* vol. 35, no. 6, pp. 1855-1870, 2016.

[14] S. Ahmad and M. Rehan, "On observer-based control of one-sided Lipschitz systems," *Journal of the Franklin Institute,* vol. 353, no. 4, pp. 903-916, 2016.

[15] H. Chu, X. Liu, W. Zhang, and Y. Cai, "Observer-based consensus tracking of multi-agent systems with one-sided Lipschitz nonlinearity," *Journal of the Franklin Institute,* vol. 353, no. 7, pp. 1594-1614, 2016.

[16] T. Kaczorek, "Reduced-order perfect nonlinear observers of fractional descriptor discrete-time nonlinear systems," *International Journal of Applied Mathematics and Computer Science,* vol. 27, no. 2, 2017.

[17] A. Jmal, O. Naifar, A. Ben Makhlouf, N. Derbel, and M. A. Hammami, "On observer design for nonlinear Caputo fractional-order systems," *Asian journal of control,* vol. 20, no. 4, pp. 1533-1540, 2018.

[18] M. Karkhaneh and M. Pourgholi, "Adaptive observer design for one-Sided Lipschitz class of nonlinear systems," *The Modares Journal of Electrical Engineering,* vol. 11, no. 4, pp. 45-51, 2012.

[19] Y. Bai, A. Marino, and J. Wang, "Observer-based distributed fault detection and isolation for second-order multi-agent systems using relative information," *Journal of the Franklin Institute,* vol. 358, no. 7, pp. 3779-3802, 2021.

[20] X. Xue, X. Yue, and J. Yuan, "Connectivity Preservation and Collision Avoidance Control for Spacecraft Formation Flying with Bounded Actuation," in *Advances in Guidance, Navigation and Control*: Springer, 2022, pp. 3685-3697.

[21] C. Thompson and P. Reverdy, "Multi-Agent Recurrent Rendezvous Using Drive-Based Motivation," *arXiv preprint arXiv:2109.13408,* 2021.

[22] Y. Xu, T. Li, and S. Tong, "Event-triggered adaptive fuzzy bipartite consensus control of multiple autonomous underwater vehicles," *IET Control Theory & Applications,* vol. 14, no. 20, pp. 3632-3642, 2020.

[23] M. Rodriguez, "Intelligent Intersection Management through Gradient-Based Multi-Agent Coordination of Traffic Lights and Vehicles," University of Maryland, College Park, 2021.

[24] H. Bai and J. T. Wen, "Cooperative load transport: A formation-control perspective," *IEEE Transactions on Robotics,* vol. 26, no. 4, pp. 742-750, 2010.

[25] W. Ren and R. W. Beard, *Distributed consensus in multi-vehicle cooperative control* (no. 2). Springer, 2008.

[26] Z. Li, Z. Duan, and G. Chen, "Dynamic consensus of linear multi-agent systems," *IET Control Theory & Applications,* vol. 5, no. 1, pp. 19-28, 2011.

[27] H. Zhao, S. Xu, and D. Yuan, "An LMI approach to consensus in second-order multi-agent systems," *International Journal of Control, Automation and Systems,* vol. 9, no. 6, pp. 1111-1115, 2011.

[28] W. Yu, G. Chen, M. Cao, and J. Kurths, "Second-order consensus for multiagent systems with directed topologies and nonlinear dynamics," *IEEE Transactions on Systems, Man, and Cybernetics, Part B (Cybernetics),* vol. 40, no. 3, pp. 881-891, 2009.

[29] M. Rehan, A. Jameel, and C. K. Ahn, "Distributed consensus control of one-sided Lipschitz nonlinear multiagent systems," *IEEE Transactions on Systems, Man, and Cybernetics: Systems,* vol. 48, no. 8, pp. 1297-1308, 2017.

[30] M. Doostinia, M. T. Beheshti, S. A. Alavi, and J. M. Guerrero, "Distributed control strategy for DC microgrids based on average consensus and fractional-order local controllers," *IET Smart Grid,* 2021.

[31] L. Chen, X. Li, Y. Chen, R. Wu, A. M. Lopes, and S. Ge, "Leader-follower non-fragile consensus of delayed fractional-order nonlinear multi-agent systems," *Applied Mathematics and Computation,* vol. 414, p. 126688, 2022.

[32] R. Olfati-Saber, "Flocking for multi-agent dynamic systems: Algorithms and theory," *IEEE Transactions on automatic control,* vol. 51, no. 3, pp. 401-420, 2006.

[33] W. Ren and R. W. Beard, "Consensus seeking in multiagent systems under dynamically changing interaction topologies," *IEEE Transactions on automatic control,* vol. 50, no. 5, pp. 655-661, 2005.

[34] I. Podlubny, "Fractional differential equations: an introduction to fractional derivatives, fractional differential equations, to methods of their solution and some of their applications", Elsevier, vol 198, 1998.

[35] B. Duan and Z. Zhang, "A Rational Approximation Scheme for Computing Mittag-Leffler Function with Discrete Elliptic Operator as Input," *Journal of Scientific Computing,* vol. 87, no. 3, pp. 1-20, 2021.

[36] M. A. Duarte-Mermoud, N. Aguila-Camacho, J. A. Gallegos, and R. Castro-Linares, "Using general quadratic Lyapunov functions to prove Lyapunov uniform stability for fractional order systems," *Communications in Nonlinear Science and Numerical Simulation,* vol. 22, no. 1-3, pp. 650-659, 2015.

[37] M. N. Soorki and M. S. Tavazoei, "Adaptive robust control of fractional-order swarm systems in the presence of model uncertainties and external disturbances," *IET control theory & applications,* vol. 12, no. 7, pp. 961-969, 2018.

[38] Y. Li, Y. Chen, and I. Podlubny, "Mittag–Leffler stability of fractional order nonlinear dynamic systems," *Automatica,* vol. 45, no. 8, pp. 1965-1969, 2009.

Farshid Aazam Manesh received his Master's degree in Electrical Control Engineering from Shahid Beheshti University, Iran in 2021. He is currently involved as a lecturer at Ilam Technical and Vocational University. His research interests include Multi-agent systems, Model predictive control, Adaptive control, Quadrotor dynamics, Robotics, Fault diagnosis and tolerance, Fractional calculus, Nonlinear Systems.

Elham Amini Boroujeni is an Assistant Professor at Kharazmi University, Tehran, Iran. She received her B.Sc. from the University of Tehran in 2006 and her M.Sc. and Ph.D. in Control Engineering from Tarbiat Modares University in 2009 and 2014, respectively. Her research focuses on nonlinear control, robust control, fractional-order systems, and multi-agent systems control.

Fateme Bazarkhak received her bachelor's degree from Qom University of Technology and her master's degree from Kharazmi University in 2021. Her interests include fractional-order systems, multi-agent systems, nonlinear systems, and fault diagnosis.

Mahdi Pourgholi is an Associate Professor at Shahid Beheshti University (SBU), Tehran, Iran. He received his PhD in Control Engineering from Tarbiat Modares University in 2010. His research interests include nonlinear control, fuzzy systems, and cooperative control of multi-agent systems.

International Journal Of
Industrial Electronics Control and Optimization
Print ISSN: 3517-2645
Online ISSN: 3568-2645
Homepage: https://ieco.usb.ac.ir/

Adaptive Backstepping Control of two-group SEIAR Epidemic Model in the Presence of Input Saturation and External Disturbances

Fariba Nobakht[1] | Hussein Eliasi[2]

Faculty of Electrical and Computer Engineering, University of Birjand, Birjand, Iran.[1,2]
Corresponding author's email: h_eliasi@birjand.ac.ir

Article Info

Article type:
Research Article

Article history:
Received: 2024-11-03
Received in revised form: 2025-02-01
Accepted: 2025-02-19
Published online: 22-Dec-2025

Keywords:
Backstepping sliding mode control,
Input saturation,
Nonlinear adaptive control,
SEIAR mathematical model.

ABSTRACT

This paper proposes a robust adaptive control strategy based on integral backstepping for nonlinear epidemic systems under input saturation, model uncertainties, and external disturbances. The proposed method combines backstepping for systematic control design, sliding mode control for robustness, and adaptive control to handle unknown parameters dynamically. To address input saturation, a novel auxiliary design system combined with Nussbaum gain functions is introduced, mitigating saturation effects and ensuring stability. The epidemic dynamics are modeled using the SEIAR framework, which includes Susceptible, Exposed, Infected, Asymptomatic, and Recovered populations. The controller employs three control inputs—vaccination, social distancing measures, and treatment of infected individuals—to drive the populations of susceptible, exposed, and infected individuals to zero. Simulation results demonstrate that the proposed control scheme effectively eliminates infections, ensuring that the recovered population converges to the total population size. The method provides precise trajectory tracking despite input constraints and external disturbances. These findings highlight its strong potential for real-world epidemic management, particularly in resource-limited and uncertain environments.

I. Introduction

Mathematical modelling plays a vital role in enhancing our understanding of how infectious diseases spread. By breaking down the complex mechanisms of disease transmission, epidemic models offer valuable insights into the dynamics and patterns of outbreaks [1]. These models not only forecast the progression of epidemics—such as the number of infections, hospitalizations, and fatalities—but also assess the effectiveness of various control measures [2].

Traditional epidemic models (see e.g., [3], [4]) often assume that all individuals share the same susceptibility to infection and follow uniform transmission dynamics. However, factors such as age, gender, community, education level, and geographic location can significantly impact disease spread. To better capture these dynamics, populations are categorized into distinct groups, each with specific epidemic parameters. This approach, represented by multi-group epidemic models, has been extensively studied and provides a more accurate understanding of disease spread within and between groups (see e.g., [5], [6], [7]) . These models offer valuable insights for designing more effective strategies to control and prevent infectious diseases.

Various strategies have been implemented to control epidemics, including social distancing, lockdowns, hygiene practices, face masks, laboratory testing, contact tracing, and monitoring infected or exposed individuals. To optimize these measures, researchers have developed different controllers for infectious disease models. Optimal control theory has been used to evaluate interventions aimed at reducing disease transmission, considering both ongoing and final costs over finite or infinite time horizons (see e.g., [5], [8], [9], [10], and [11]).

Optimal control strategies typically assume full knowledge of all dynamic terms and parameters. However, pandemic model parameters—such as disease spread, mortality, and contact rates—are inherently uncertain and influenced by social and disease-related factors [12]. These

unknown variables must be accounted for when designing outbreak control measures. To tackle this, robust and adaptive control techniques are used to maintain stable performance despite uncertainties within the model [13, 14, 15].

Sliding mode control (SMC) is a robust technique for managing nonlinear systems, offering resilience against parameter variations and disturbances [14]. However, the conventional SMC approach, which uses the sign function for switching, can cause chattering—an undesirable phenomenon that can destabilize the system. To mitigate this, several techniques have been developed, including boundary layer methods, hysteresis-based approaches, alternative switching functions like saturation, and higher-order sliding mode control [16].

Backstepping is a structured method for designing tracking and regulation strategies, particularly for "strict-feedback" systems. It employs a recursive process where state variables are treated as virtual controls. However, this approach lacks robustness against parametric variations. By integrating sliding mode control, backstepping effectively addresses parameter uncertainties and enhances system stability [17, 18, 19]. This combined method divides the nonlinear system into subsystems, applying sliding mode control to each while using the Lyapunov function to ensure the convergence of position-tracking errors under any initial condition.

The integrator backstepping technique offers significant advantages by transforming nonlinear systems into a strict-feedback form [19, 16]. When paired with sliding mode control, it minimizes chattering in the control input and improves robustness against modeling uncertainties and external disturbances. Furthermore, incorporating an integrator within the control structure enhances precision in achieving steady-state control, making this approach highly effective for a wide range of applications.

Input saturation is a prevalent challenge in real-world control systems, where control inputs are constrained by physical or practical limitations. In the context of epidemic disease management, input saturation occurs when health systems are overwhelmed and unable to respond effectively or promptly to outbreaks. This can result from various factors, including sudden surges in cases, lack of preparedness, limited availability of resources, and social or behavioral resistance to interventions. For example, inadequate infrastructure, insufficient training, and poor coordination among healthcare providers can lead to critical shortages of medical supplies, personnel, and facilities. Additionally, public reluctance to adopt measures such as vaccination or social distancing can further undermine the effectiveness of control strategies. These limitations introduce significant nonlinearities into epidemiological models, making it difficult to accurately predict the spread and impact of diseases. Addressing actuator saturation is therefore essential for developing reliable models that can inform effective decision-making.

To tackle input constraints, anti-windup compensator (AWC) techniques are employed to maintain system stability and performance under saturation conditions. By incorporating anti-windup mechanisms, controllers can adapt to input limitations, ensuring accurate regulation of system behavior and reliable predictions despite actuator constraints. Anti-windup controller techniques are broadly categorized into two approaches: one-step and two-step design procedures. One-step approaches develop feedback controllers that inherently account for input saturation, while two-step procedures involve designing an optimal controller without considering saturation initially and later augmenting it with anti-windup compensation [20, 21]. These methods enhance the robustness of control systems, enabling effective management of epidemics even under resource limitations

Various strategies have been proposed to design anti-windup controllers for addressing input saturation challenges. These include adaptive backstepping control algorithms [22], sliding mode tracking control methods [23], and terminal sliding mode controllers for systems with unknown uncertainties and input saturation constraints [24]. Additionally, integral backstepping sliding mode control approaches have been developed for systems like unmanned autonomous helicopters [16]. These methods aim to ensure that systems with saturating actuators closely replicate the performance of their unsaturated counterparts, enhancing reliability and stability.

This article introduces a novel nonlinear anti-windup control method that combines backstepping with adaptive sliding mode control (ABSMC) to stabilize a nonlinear multi-input, multi-output (MIMO) system under input saturation, modelling uncertainties, and external disturbances. The anti-windup compensator is designed using a one-step strategy to address challenges arising from input limitations in real-world scenarios. To manage input saturation and prevent actuator failures, an auxiliary system is incorporated.

Input saturation, being a non-smooth function, poses a challenge for backstepping, which requires differentiable functions. To address this, a continuous approximation is used to estimate the saturation, ensuring a controlled approximation error and enabling the system to be expanded for controller development. However, managing the derivative of the estimated function introduces additional complexity, which is resolved using a Nussbaum function. The Nussbaum function serves as a powerful mathematical tool, effectively addressing the nonlinearities introduced by input saturation. It ensures the stability and positivity of system states while also enhancing the robustness of the controller. By working in conjunction with the auxiliary design system, the Nussbaum function contributes to a

resilient and adaptive control scheme capable of maintaining stability and performance even under challenging conditions. The controller is applied to a bi-model epidemic, which includes five groups of individuals and three control methods: vaccination, antiviral treatment, and social distancing. The controller seeks to reduce the number of susceptible, infected, and exposed individuals to zero, even under input saturation, which also minimizes the number of asymptomatic individuals. Meanwhile, the recovered population stabilizes at its peak level, aligning with the overall population trend. Compared to existing research on the control of epidemiological systems, this work makes several significant contributions:

a. A robust adaptive backstepping sliding mode controller has been developed to manage MIMO epidemic systems affected by input saturation, time-varying external disturbances, and uncertainties.

b. Multigroup epidemic models provide more detailed and accurate information about disease spread compared to models that treat the population as a whole. This richer information can guide better decisions regarding the control and prevention of infectious diseases.

c. The controller accounts for uncertainties in the nonlinear dynamics of the epidemic model, allowing it to adapt to variations and unexpected changes in the disease transmission process. This enhances control performance and resilience in real-world scenarios.

d. The proposed control approach introduces a novel auxiliary design system and Nussbaum gain functions to address actuator saturation. These techniques ensure effective management of input saturation, enabling the controller to achieve the desired objectives despite input constraints.

e. The model incorporates a time-varying total population ($\dot{N}(t) \neq 0$) and includes critical factors such as birth and natural death rates, as well as the loss of immunity in recovered individuals over time. These factors significantly influence disease dynamics and the effectiveness of control measures.

The remainder of this paper is organized into five sections. Section II introduces and provides a detailed explanation of the dynamic two-group SEIAR model, including a proof of the results related to its positivity property. This property is crucial to the system, as it ensures that negative populations do not occur at any time. Section III focuses on the design of the adaptive backstepping sliding mode control for the MIMO nonlinear system. In Section IV, we present numerical simulation results that demonstrate the applicability of the proposed anti-windup control approach to the nonlinear model. Finally, Section V concludes the paper.

II. Nonlinear Two-group SEIAR Model

Multi-group epidemic models are mathematical frameworks that divide a population into multiple groups based on specific characteristics, such as age, gender, education level, occupation, and risk factors, among others. Each group is assumed to have its own set of parameters related to disease transmission, susceptibility, and recovery. The proposed SEIAR epidemic model builds upon the traditional SEIR model, as outlined in [25], by introducing two modes of transmission. This extension aims to account for the differing transmission and recovery rates exhibited by older individuals or those with underlying health conditions compared to other groups. Additionally, these individuals often have more complex medical needs and may require more intensive care. The model introduces separate compartments for exposed, infected, and asymptomatic individuals to capture these differences and provide a more detailed representation of disease dynamics. The nonlinear system that describes the dynamics of bi-modal epidemics is represented by:

$$\begin{aligned}
\dot{S}(t) &= \nu N - \frac{\beta_1 S I_1}{N} - \frac{\beta_2 S I_2}{N} - \mu^S S + \omega R(t) \\
\dot{\mathrm{E}}_1(\mathrm{t}) &= \frac{\beta_1 S I_1}{N} - (\kappa_1 + \mu_1^E) E_1 \\
\dot{E}_2(t) &= \frac{\beta_2 S I_2}{N} - (\kappa_2 + \mu_2^E) E_2 \\
\dot{I}_1(t) &= p_1 \kappa_1 E_1 - (\gamma_1 + \mu_1^I) I_1 \\
\dot{I}_2(t) &= p_2 \kappa_2 E_2 - (\gamma_2 + \mu_2^I) I_2 \\
\dot{A}_1(t) &= (1 - p_1) \kappa_1 E_1 - (\eta_1 + \mu_1^A) A_1 \\
\dot{A}_2(t) &= (1 - p_2) \kappa_2 E_2 - (\eta_2 + \mu_2^A) A_2 \\
\dot{R}(t) &= \gamma_1 (1 - \rho_1) I_1 + \gamma_2 (1 - \rho_2) I_2 \\
&\quad + \eta_1 A_1 + \eta_2 A_2 - (\mu^R + w) R
\end{aligned} \tag{1}$$

Therefore, this system includes eight positive state variables that represent the different compartments in the epidemiological model. The state variables and parameters are listed in Table 1.

TABLE I INTERPRETATION OF SYSTEM STATES

Variable	Description
S	Susceptible individuals
E_1	People with chronic illness who were exposed
E_2	People without chronic illness who were exposed
I_1	People with chronic illness who are infected
I_2	People without chronic illness who are infected
A_1	People with chronic illness who are asymptomatic
A_2	People without chronic illness who are asymptomatic
R	Recovered individuals

In this model, (S) denotes the number of individuals who are susceptible (i.e., those who are not yet infected), (E) represents the number of people exposed to infection (infected but not yet able to transmit the virus), and (I) includes infected individuals who are capable of transmitting the disease to susceptible individuals. (A) denotes the

number of asymptomatic carriers, while compartment (R) includes those who have recovered and possess immunity to the disease. Finally, (N) represents the total population size, expressed as: (i.e., $N(t) = S(t) + E_1(t) + E_2(t) + I_1(t) + I_2(t) + A_1(t) + A_2(t) + R(t)$).

The model equations describe how susceptible individuals (S) come into contact with infected individuals (I_i) at a rate of β_i, leading to their transition to the exposed group (E_i). Exposed individuals become infected at a rate of κ_i and are divided into two groups: those who develop symptoms and those who remain asymptomatic. A portion of the individuals who have been exposed enters the infected group, while the remainder transitions to the asymptomatic group, as described in [4] .Asymptomatic individuals (A_i) move from their group to the recovered category (R) at a rate of η_i. Infected individuals (I_i) also leave their group at a rate of γ_i, with a proportion of $(1-\rho_i)$ recovering and the remaining proportion (ρ_i) succumbing to the infection. The model takes into account the decreasing immunity of recovered individuals, using parameter ω to determine the average duration of immunity. After this period, individuals who have recovered transition back to the susceptible group. The symbols ν, and μ represents the birth rate and mortality rate from natural causes, respectively.

All the model parameters $(\beta_i, \kappa_i, p_i, \gamma_i, \eta_i, \omega_i, \nu)$, and μ assumed to be positive to accurately reflect real-world conditions. A conceptual flow diagram that visualizes the relationships among the dynamics of the model is shown in Fig. 1.

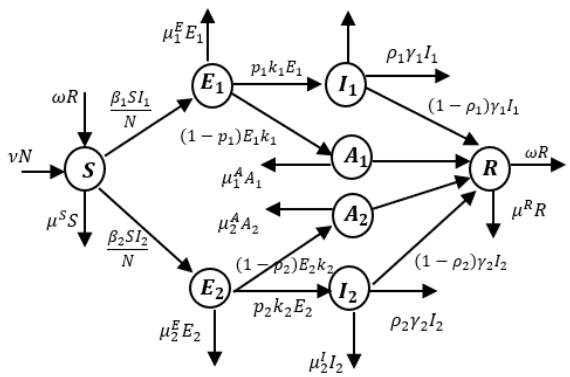

Fig. 1. Conceptual flow diagram of the two-group SEIAR model with death/birth rate.

The total population dynamics at time t can be calculated by summing all the equations in (1), leading to:

$$\dot{N}(t) = \nu N - \mu^S S - \mu_1^E E_1 - \mu_2^E E_2 - (\mu_1^I + \gamma_1\rho_1) I_1 - (\mu_2^I + \gamma_2\rho_2) I_2 - \mu^R R \quad (2)$$

We develop the epidemic model by incorporating parallel interventions, including vaccination, antiviral treatment, and social distancing strategies, as represented by the following system of differential equations:

$$\begin{aligned}
\dot{S}(t) &= -\frac{\beta_1 I_1 S}{N}(1 - sat(u_2)) \\
&\quad -\frac{\beta_2 I_2 S}{N}(1 - sat(u_3)) - \mu^S S + \nu N \\
&\quad +\omega R(t) - N sat(u_1) + d_S(t) \\
\dot{E}_1(t) &= \frac{\beta_1 S I_1}{N}\big(1 - \mathrm{sat}(u_2)\big) - (\kappa_1 + \mu_1^E) E_1 \\
&\quad +d_{E_1}(t) \\
\dot{E}_2(t) &= \frac{\beta_2 S I_2}{N}(1 - sat(u_3)) - (\kappa_2 + \mu_2^E) E_2 \\
&\quad +d_{E_2}(t) \\
\dot{I}_1(t) &= p_1\kappa_1 E_1 - (\gamma_1 + \mu_1^I) I_1 - \mathrm{sat}(u_4) I_1 \\
&\quad +d_{I_1}(t) \\
\dot{I}_2(t) &= p_2\kappa_2 E_2 - (\gamma_2 + \mu_2^I) I_2 - \mathrm{sat}(u_5) I_2 \\
&\quad +d_{I_2}(t) \\
\dot{A}_1(t) &= (1-p_1)\kappa_1 E_1 - (\eta_1 + \mu_1^A) A_1 \\
&\quad +d_{A_1}(t) \\
\dot{A}_2(t) &= (1-p_2)\kappa_2 E_2 - (\eta_2 + \mu_2^A) A_2 \\
&\quad +d_{A_2}(t) \\
\dot{R}(t) &= \gamma_1(1-\rho_1) I_1 + \gamma_2(1-\rho_2) I_2 \\
&\quad +\eta_1 A_1 + \eta_2 A_2 - (\mu^R + w) R \\
&\quad +sat(u_4) I_1 + sat(u_5) I_2 + N sat(u_1) \\
&\quad +d_R(t)
\end{aligned} \quad (3)$$

The equations include five control inputs, $(u_1(t), u_2(t), u_3(t), u_4(t))$, and $u_5(t)$ which are crucial for achieving the desired outcome. The control function $0 \le u_1(t) \le 1$ quantifies the rate at which the total population is vaccinated. Similarly, the control factors $0 \le u_2(t) \le 1$, and $0 \le u_3(t) \le 1$ effectively reduces the contact rate through social distancing measures. The control functions $0 \le u_4(t) \le 1$ and $0 \le u_5(t) \le 1$ measure the rate at which infectious individuals, both with and without comorbidities, receive treatment during each period, thereby aiding in recovery. The saturation function of the control inputs $(i.e., sat(u))$ is defined as follows:

$$sat\big(u(t)\big) = \begin{cases} sign\big(u(t)\big)u_M, & |u(t)| \ge u_M \\ u(t), & |u(t)| < u_M \end{cases} \quad (4)$$

where u_M represents the saturation limit of the input. The vector of perturbations caused by uncertainties and time-varying external disturbances, denoted as $d_i(t), i \in \{S, E_1, E_2, I_1, I_2, A_1, A_2, R\}$, plays a crucial role in enhancing the robustness and accuracy of the model. By considering various sources of uncertainties and disturbances, such as migration and travel patterns, changes in public health policies, and economic factors, the model can better capture the complexities and dynamics of the real world. This approach leads to more reliable predictions and improved decision-making capabilities. We assume that the upper bound of $d(t)$ is unknown. Our proposed control strategy aims to track desired descending reference signals for the state variables S, E_1, E_2, I_1, and I_2. Consequently, the controller seeks to reduce the number of susceptible, exposed, and infected individuals to zero $(i.e., S \rightarrow$

$0, E_1 \to 0, E_2 \to 0, I_1 \to 0$ and $I_2 \to 0$) by monitoring specific situations and employing control inputs. In these scenarios, it is demonstrated that the other state variables are constrained and approach zero $(i.e., A_1, A_2 \to 0)$. As a result, the population removed by immunity asymptotically tracks the total population. $(i.e., R \to N)$.

A. Positivity and Boundedness of the Solution

For an epidemic model to be effective for its intended applications, it must yield positive and bounded solutions. Consequently, the solutions of system (1) must be constrained to remain positive and bounded in accordance with the given initial conditions:

$\big(S(0), E_1(0), E_2(0), I_1(0), I_2(0), A_1(0), A_2(0), R(0)\big) \in R_8^+$

Proposition 1. In the positive orthant of R_8^+, the system (1) must exhibit positivity and invariance.

Proof. When the value of (S) reaches zero at a time (t), all other state variables are also effectively reset to zero at that time. At time (t), this condition is expressed as:

$$\dot{S}(t)\big|_{S(t)=0} = \nu N + \omega R \geq 0$$

Due to the positivity of the model parameters, as well as the number of recovered individuals and the total population, (S) will only increase and will not decrease. Similarly, the remaining state variables also exhibit this behavior.

$$\dot{E}_1(t)\big|_{E_1(t)=0} = \frac{\beta_1 S I_1}{N} \geq 0$$
$$\dot{E}_2(t)\big|_{E_2(t)=0} = \frac{\beta_2 S I_2}{N} \geq 0$$
$$\dot{I}_1(t)\big|_{I_1(t)=0} = p_1 \kappa_1 E_1 \geq 0$$
$$\dot{I}_2(t)\big|_{I_2(t)=0} = p_2 \kappa_2 E_2 \geq 0$$
$$\dot{A}_1(t)\big|_{A_1(t)=0} = (1-p_1)\kappa_1 E_1 \geq 0$$
$$\dot{A}_2(t)\big|_{A_2(t)=0} = (1-p_2)\kappa_2 E_2 \geq 0$$
$$\dot{R}(t)\big|_{R(t)=0} = \gamma_1(1-\rho_1)I_1 + \gamma_2(1-\rho_2)I_2 + \eta_1 A_1 + \eta_2 A_2 \geq 0$$

As a result, in R_8^+, all of the state variables are nonnegative and form an invariant set for model (1).

Proposition 2. In the feasible region Γ, the system (1) is bounded.

$$\Gamma = \{(S, E_1, E_2, I_1, I_2, A_1, A_2, R) \in R_8^+ : 0 \leq S(t) + E_1(t) + E_2(t) + I_1(t) + I_2(t) + A_1(t) + A_2(t) + R(t) \leq \frac{\nu N}{\mu^*}\}$$

where $\mu^* = \min\{\mu^S, \mu_1^E, \mu_2^E, \mu_1^I + \gamma_1\rho_1, \mu_2^I + \gamma_2\rho_2, \mu^R\}$

Proof. The sum of all equations in the model (1) results in the following equation for the total population.

$$\begin{aligned}\dot{N}(t) &= \nu N - \mu^S S - \mu_1^E E_1 - \mu_2^E E_2 - \mu^R R \\ &\quad -(\mu_1^I + \gamma_1\rho_1)I_1 - (\mu_2^I + \gamma_2\rho_2)I_2 \\ &\leq \nu N - \mu^*(S + E_1 + E_2 + I_1 + I_2 + R)\end{aligned} \quad (5)$$

One can obtain from equation (5) that

$$N(t) \leq N(0)e^{-\mu^* t} + \frac{\nu N}{\mu^*}(1 - e^{-\mu^* t})$$
$$N(t) \leq \frac{\nu N}{\mu^*}, \quad if\ N(0) \leq \frac{\nu N}{\mu^*}$$

It can be verified that Γ is positively invariant with respect to (1).

B. The basic Reproduction number

In epidemic theory, the basic reproduction number, commonly denoted as R_0, is one of the most critical concepts due to its ability to predict the course of an epidemic. It represents the average number of secondary infections caused by a single infected individual during their infectious period [4] .The value of R_0 is instrumental in determining the stability of operating points [5]. If $R_0 < 1$, the disease-free equilibrium is locally asymptotically stable, indicating that the epidemic will self-eradicate. If $R_0 > 1$, the disease-free equilibrium is unstable, and there will always be a non-zero number of infectious individuals within the population. System (1) always has the disease-free equilibrium. To find this equilibrium, all infected variables must be set to zero $(i.e., E_1 = E_2 = I_1 = I_2 = A_1 = A_2 = 0)$ and the remaining variables are solved accordingly. Thus, the equilibrium of the population in the absence of disease is obtained as follows:

$$Q_0 = (\tfrac{\nu N}{\mu^S}, 0, 0, 0, 0, 0, 0, 0)$$

One common approach to calculating R_0 is the next-generation matrix method [4]. This method involves constructing a matrix that represents the average number of new infections generated by an infected individual across each compartment of the epidemiological model. Let $\chi_1(t) = [E_1\ I_1\ A_1]^T$, and $\chi_2(t) = [E_2\ I_2\ A_2]^T$.

Then, the dynamics of the system can be described by the following equations:

$$\dot{\chi}_i = \mathcal{F}_i(\chi) - \mathcal{V}_i(\chi) \quad (6)$$

Here, $\mathcal{F}_i(\chi)$ represents the rate of appearance of new individuals in group (i), while $\mathcal{V}_i(\chi)$ signifies the difference between the rate at which individuals enter group (i) and the rate at which they leave it. For individuals with underlying health conditions, in the virus-free environment Q_0, The non-negative matrices $F = = \left[\frac{\partial \mathcal{F}_i}{\partial x_j}\right]$ and $V = \left[\frac{\partial \mathcal{V}_i}{\partial x_j}\right]$ are defined as follows:

$$F_1 = \begin{bmatrix} 0 & \frac{\beta_1 S}{N} & 0 \\ 0 & 0 & 0 \\ 0 & 0 & 0 \end{bmatrix}$$

$$V_1 = \begin{bmatrix} (\kappa_1 + \mu_1^E) & 0 & 0 \\ -p_1\kappa_1 & (\gamma_1 + \mu_1^I) & 0 \\ -(1-p_1)k_1 & 0 & (\eta_1 + \mu_1^A) \end{bmatrix}$$

Set $R_0^1 = \Omega(\mathcal{F}_1 {\mathcal{V}_1}^{-1})$, Where $\Omega(\mathrm{A})$ denotes the spectral radius of matrix A. Thus, the basic reproduction ratio for individuals suffering from serious disease is given by:

$$R_0^1 = \frac{\beta_1 p_1 k_1 \nu}{\mu^s(k_1 + \mu_1^E)(\gamma_1 + \mu_1^I)} \quad (7)$$

Similarly, for individuals with comorbidities, the basic reproduction number is given by

$$R_0^2 = \frac{\beta_2 p_2 k_2 \nu}{\mu^s(k_2 + \mu_2^E)(\gamma_2 + \mu_2^I)} \quad (8)$$

Hence, the basic reproduction ratio of the system (1) is given by [5].

$R_0 = max\{ R_0^1, R_0^2\}$

III. Design of Robust Controller

A. System Description and Preliminaries

Consider the following class of MIMO continuous-time nonlinear plants:

$$\dot{x}(t) = f\big(x(t)\big) + \sum_{j=1}^{m} g_j(x(t))sat(u_j(t)) + d(t),$$
$$y_i(t) = h_i\big(x(t)\big),\ i = j = 1,2,\cdots,m \quad (9)$$

where $y(t) \in \mathbb{R}^m, u(t) \in \mathbb{R}^m$, and $x(t) \in \mathbb{R}^n$ represent the output signal vector, the input signal vector, and the system's state vector, respectively. The term $f\big(x(t)\big) = \theta_f f_0\big(x(t)\big)$ denotes a smooth vector field, while $g(x(t)) = \theta_g g_0\big(x(t)\big)$ represents a smooth $m \times m$ nonlinear matrix. Here, θ_f and θ_g account for model uncertainties. $d(t)$ denotes an external disturbance with unknown bound. The control objective is to design a robust control scheme that ensures the outputs $y_i(t)$ track the desired trajectory $y_{d_i}(t)$. Tracking errors must remain within specified constraints while ensuring that all closed-loop signals are both bounded and positive.

B. Backstepping Control

Backstepping is a recursive design technique used to asymptotically stabilize controllers for systems in strict feedback form [19] .To design an appropriate backstepping controller, it is essential to derive the strict feedback form of the control system [26]. If the nonlinear system is not in strict feedback form, methods such as input-output linearization or alternative techniques can be employed to transform the system into the desired standard form. This transformation allows for the application of backstepping design techniques, facilitating the development of an effective controller for the nonlinear system. Assume that the system (9) is transformed into the following parametric strict-feedback system with zero dynamics via a diffeomorphism $[\psi^T, \eta^T]^T = \Phi(x)$ as follows [20]:

$$\dot{\eta} = q(\eta, \psi) \quad (10)$$

$$\dot{\psi}_{i,k} = \psi_{i,k+1},\ 1 \le k \le r_i - 1, 1 \le i \le m$$
$$\dot{\psi}_{i,r_i} = \theta_{b_i} b_i(\eta,\psi) + \sum_{j=1}^{m} \theta_{a_{ij}} a_{ij}(\eta,\psi) sat\big(u_j\big) + d_i(t), 1 \le j \le \mathrm{m} \quad (11)$$

Where $\eta(t) = [\eta_{r+1}(t)\ \eta_{r+2}(t)\ \cdots\ \eta_n(t)]^T$, $q(\eta,\psi)$, and $b_i(\eta,\psi) = L_f^{r_i} h_i(x)$ are known smooth vector functions. The term $a_{ij}(\eta,\psi) = L_{g_j} L_f^{r_i - 1} h_i(x)$ represents $(i,j) - th$ element of a known non-singular $m \times m$ matrix $\mathrm{A}(\eta,\psi)$, defined for all $[\psi^T, \eta^T]^T \in \mathbb{R}^n$. Here, θ_{a_i} and θ_{b_i} are vectors of unknown constant parameters. The integer r_i denotes the smallest relative degree of the $i - th$ with respect to any of the m inputs, and $r = r_1 + r_2 + \cdots + r_m$ is defined as the sum of individual relative degrees.

The relationship between the applied control $sat(u_j(t))$, and the control input $u_j(t)$ exhibits a sharp discontinuity when the absolute value of $u_j(t)$ reaches the saturation level u_{M_j}. This discontinuity presents a challenge for the direct application of the backstepping technique. To address this issue, we approximate the saturation function with a smooth function. A commonly used approximation is the hyperbolic tangent function, defined as follows [16]:

$$g(u_i) = u_{M_i} \tanh\left(\frac{u_i}{u_{M_i}}\right) = u_{M_i} \frac{e^{\frac{u_i}{u_{M_i}}} - e^{-\frac{u_i}{u_{M_i}}}}{e^{\frac{u_i}{u_{M_i}}} + e^{-\frac{u_i}{u_{M_i}}}} \quad (12)$$

Then $sat(u_j(t))$ in (11) can be expressed as follows

$$sat\left(u_j(t)\right) = g\big(u_j\big) + d\big(u_j\big) = u_{M_j} \tanh\left(\frac{u_j}{u_{M_j}}\right) + d\big(u_j\big) \quad (13)$$

where $d\big(u_j\big) = sat\big(u_j\big) - g(u_j)$ is a bounded function, and its bound can be obtained as

$$\big|d\big(u_j\big)\big| = \big|sat\big(u_j\big) - g\big(u_j\big)\big| \le u_{M_j}(1 - \tanh(1)) = 0.2785 u_{M_j} \quad (14)$$

So, the equations (10) and (11) can be written as

$$\dot{\eta} = q(\eta,\psi) \quad (15)$$

$$\dot{\psi}_{i,k} = \psi_{i,k+1},\ \ 1 \le k \le r_i - 1,\ \ 1 \le i,j \le m \quad (16)$$

$$\dot{\psi}_{i,r_i} = \theta_{b_i} b_i(\eta,\psi) + \sum_{j=1}^{m} \theta_{a_{ij}} a_{ij}(\eta,\psi) g\big(u_j\big) + \Delta d_i(t)$$

where $\Delta d_i(t) = \sum_{j=1}^{m} \theta_{a_{ij}} a_{ij}(\eta,\psi) d\big(u_j\big) + d_i(t)$

Assumption 1. The nonlinear plant (9) is feedback linearizable without saturation.

Assumption 2. The desired trajectory y_{d_i} and its $r_i -$ th derivatives are known, bounded, and piecewise continuous.

Assumption3. The zero dynamics of the system $\dot{\eta} = q(\eta,\psi)$ are input-to-state stable.

Definition 1. A function N(s) is considered a Nussbaum-type function when it possesses the properties listed [27].

$$\lim_{s\to\pm\infty}\sup\frac{1}{s}\int_0^s N(\mathcal{X})d\mathcal{X}=\infty, \tag{17}$$

$$\lim_{s\to\pm\infty}\inf\frac{1}{s}\int_0^s N(\mathcal{X})d\mathcal{X}=-\infty \tag{18}$$

According to the definition, Nussbaum functions must exhibit both infinite gains and infinite switching frequencies. Examples of such functions include $\mathcal{X}^2\cos(\mathcal{X})$, $\mathcal{X}^2\sin(\mathcal{X})$, $e^{\mathcal{X}^2}\cos\left(\frac{\pi}{2}\mathcal{X}\right)$,and $e^{\mathcal{X}^2}\sin\left(\frac{\pi}{2}\mathcal{X}\right)$. The selection of this particular Nussbaum functions is based on its advantageous properties:

1. Its infinite oscillatory nature ensures adaptive control gains capable of addressing unknown input saturation levels.
2. Its smoothness and bounded derivative allow for seamless integration into the backstepping design while preserving the validity of the Lyapunov-based stability analysis.

This paper utilizes the Nussbaum function $\mathcal{X}^2\cos(\mathcal{X})$. The following lemma presents the property of Nussbaum functions.

Lemma 1 [28, 29]**:** Smooth functions $V(.)$ and $\mathcal{X}(.)$ are defined on $[0,t_f)$ with $V(t)\geq 0,\forall t\in[0,t_f)$, and $\mathcal{N}(\mathcal{X})$ is a Nussbaum gain function. If the inequality is satisfied, $V(.)$ and $\mathcal{X}(.)$ must be limited on the interval $[0,t_f)$.

$$\begin{aligned}V\leq V(0)e^{-Ct}+\frac{M}{C}(1-e^{-Ct})\\ +\frac{e^{-Ct}}{\gamma_{\mathcal{X}}}\int_0^t(\xi\mathcal{N}(\mathcal{X})\dot{\mathcal{X}}-\dot{\mathcal{X}})e^{C\tau}\,d\tau\end{aligned} \tag{19}$$

where $C>0, M>0, \gamma_{\mathcal{X}}>0$ are constants, and ξ is a positive variable.

C. Design of adaptive backstepping sliding mode controller and stability analysis

This section combines the backstepping method with adaptive sliding mode control to design an adaptive backstepping-sliding-mode controller, ensuring robust control for uncertain systems. The backstepping technique formulates a virtual control law to achieve asymptotic convergence of the tracking error to zero. Simultaneously, adaptive sliding mode control is employed to develop a robust control law that compensates for system uncertainties and disturbances. To enhance performance, integral action is incorporated into the backstepping control, mitigating steady-state bias and reducing rise time. For the system described in equations (10) and (11), integral backstepping is implemented by introducing the integral term of the tracking error, $\int_0^t\left(\psi_i(\tau)-\psi_{d_i}(\tau)\right)d\tau$ at the initial stage of backstepping. This approach maintains the strict feedback form of the system, while the relative degree of each output vector is elevated to r_i+1, necessitating r_i+1 steps of backstepping.

To address the challenge of input saturation, the control scheme incorporates a novel auxiliary design system alongside Nussbaum gain functions. Input saturation, often caused by actuator limitations, introduces significant nonlinearities that can destabilize the system. The Nussbaum function, with its oscillatory behavior and unbounded growth properties, dynamically adjusts control gains to counteract these nonlinearities without requiring precise knowledge of the saturation limits.

Additionally, the Nussbaum function ensures the boundedness and positivity of system states, which is essential in scenarios such as epidemic models, where negative states are not physically meaningful. By leveraging its adaptive characteristics, it enables accurate trajectory tracking even in the presence of disturbances or saturation effects. The auxiliary design system complements the control strategy by creating a control law that effectively manages input saturation, while the Nussbaum gain functions enhance the overall robustness of the system, ensuring precise tracking of the desired trajectory.

$$\begin{aligned}&\dot{\psi}_{i,1}=\psi_{i,2}-\psi_{d_i}\\ &\dot{\psi}_{i,2}=\psi_{i,3}\\ &\vdots\\ &\dot{\psi}_{i,r_i+1}=\theta_{b_i}b_i(\eta,\psi)\\ &\qquad+\sum_{j=1}^{m}\theta_{a_{ij}}a_{ij}(\eta,\psi)g(u_j)+\Delta d_i(t),\end{aligned} \tag{20}$$

$$\begin{aligned}&\dot{\eta}=q(\eta,\psi)\\ &y_i=\psi_{i,2},\qquad i=j=1,2,\cdots,m\\ &\dot{u}_j=-k_ju_j+w_j\end{aligned} \tag{21}$$

where k_j are positive constants and w_j are auxiliary signals to be designed in the backstepping approach. Consequently, the design of the control law transitions to the design of w_j. It is clear that all functions in equations (20) and (21) are continuous, allowing for the successful application of the backstepping technique. The design involves a procedure of r_i+2 steps for each subsystem, wherein each subsystem has a relative degree of order r_i. At each step, an error variable z_i is defined, and a stabilizing function α_i constructed to stabilize the $i-th$ output with respect to a Lyapunov function V_i. The state feedback control is provided in the final stage. The structure of the closed-loop system is illustrated in Fig. 2.

Remark 1: The augmented systems (20), and (21) differ from those examined using the conventional backstepping method. This distinction arises because $\dot{\psi}_{r_i+1}$ is directly related to the nonlinear function $g(u_j)$ rather than just u_j.

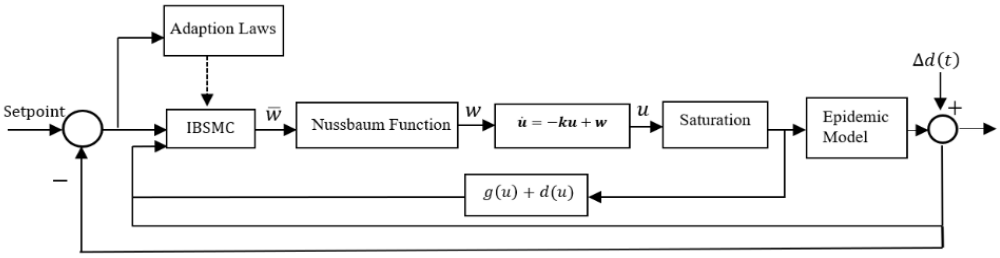

Fig. 2. Schematic diagram of adaptive backstepping sliding mode control strategy

As a result, the term $(\frac{\partial g}{\partial u_j})\dot{u}_j$ is introduced instead of $\dot{u}_j$, marking a departure from previous backstepping strategies. To address this issue, a Nussbaum function is employed.

Remark 2: System (20) contains the function $g(u_j)$, which acts as a control input for systems studied with backstepping techniques. Designing the control signal u_j without using a direct method is challenging in our current scenario. To address this issue, we intentionally include (21) to generate a reliable control signal u_j by establishing an auxiliary control signal w_i during the last step $r_i + 2$ of the backstepping procedure.

In the standard backstepping method for tracking problems, a coordinate transformation is applied to the $i-th$ output as follows:

$$z_{i,1} = \psi_{i,1} = \int_0^t (\psi_{i,2} - \psi_{d_i}) d\tau \tag{22}$$

$$z_{i,k} = \psi_{i,k} - \psi_{d_i}^{(k-2)} - \alpha_{i,k-1}, k = 2, \cdots, r_i + 1 \tag{23}$$

$$z_{i,r_i+2} = g(u_i) - \alpha_{i,r_i+1}\,, \tag{24}$$

where z_k and α_{k-1} represent the tracking error and the virtual control input that needs to be determined at the $k-th$ step, the introduction of variable z_{i,r_i+2} results from including the new state variable u_i. The design procedure for adaptive backstepping sliding mode control of a MIMO system, adhering to assumptions 1-3, comprises $r_i + 2$ steps for $i-th$ output, as follows:

Step k $(k = 1,2, \cdots, r_i)$: We define the virtual control law α_k for $i-th$ output as follows:

$$\alpha_{i,1}(z_{i,1}) = -c_{i,1} z_{i,1} \tag{25}$$

$$\alpha_{i,k} = -c_{i,k} z_{i,k} - z_{i,k-1} + \sum_{j=1}^{k-1} \left(\frac{\partial \alpha_{i,k-1}}{\partial \psi_{i,j}} \psi_{i,j+1} + \frac{\partial \alpha_{i,k-1}}{\partial \psi_{d_i}^{(j-1)}} \psi_{d_i}^{(j)}\right) \tag{26}$$

where $c_{i,k}$ are positive design parameters. The Lyapunov function is proposed as follows:

$$V_{i,k} = \sum_{j=1}^{k} \frac{1}{2} z_{i,j}^2 \tag{27}$$

Then, the derivative of $V_{i,k}$, along with equations (22) and (23), is given by:

$$\dot{V}_{i,k}(z_{i,1}, z_{i,2}, \cdots, z_{i,k}) = -\sum_{j=1}^{k} c_{i,j} z_{i,j}^2 + z_{i,k} z_{i,k+1} \tag{28}$$

Step k $= r_i + 1$: The time derivative of the tracking error $z_{i,k}$ from equations (20) and (23) is derived as follows:

$$\begin{aligned} \dot{z}_{i,k} &= \dot{\psi}_{i,k} - \psi_{d_i}^{(k-1)} - \dot{\alpha}_{i,k-1} \\ &= \theta_{b_i} b_i(\eta, \psi) + \theta_{a_i} a_i(\eta, \psi)(z_{i,k+1} \\ &\quad + \alpha_{i,k}) + \Delta d_i - \psi_{d_i}^{(k-1)} - \dot{\alpha}_{i,k-1} \end{aligned} \tag{29}$$

where $g(u_i) = z_{i,k+1} + \alpha_{i,k}$ has been utilized. We design the virtual control law $\alpha_{i,k}$ as follows:

$$\begin{aligned} \alpha_{i,k} = (\hat{\theta}_{a_i} a_i(\eta, \psi))^{-1} [&-c_{i,k} z_{i,k} - z_{i,k-1} \\ &- \hat{\theta}_{b_i} b_i(\eta, \psi) + \psi_{d_i}^{(k-1)} - \Delta d_i(t) \\ &+ \dot{\alpha}_{i,k-1}] \end{aligned} \tag{30}$$

It should be noted that $\hat{\theta}_{a_i}$ and $\hat{\theta}_{b_i}$ are the estimated values of the uncertain system parameters as described in equation (20), and these estimates have bounded errors relative to their corresponding unknown true values θ_{a_i} and θ_{b_i}, respectively. To effectively estimate the uncertainties in the θ_i vectors, the proposed control approach incorporates an adaptive estimation mechanism. This mechanism employs parameter adaptation, allowing the controller to continuously update its estimates of the uncertain parameters based on observed system outputs. Incorporating a switching term into α_k with $s_i = z_{i,k}$ as the sliding surface helps maintain robust performance despite uncertainties and external disturbances. Therefore, the virtual control $\alpha_{i,k}$ is structured in this manner.

$$\begin{aligned} \alpha_{i,k} = (\hat{\theta}_{a_i} a_i(\eta, \psi))^{-1} [&-c_{i,k} z_k - z_{i,k-1} \\ &- \hat{\theta}_{b_i} b_i(\eta, \psi) + \psi_{d_i}^{(k-1)} - \hat{\gamma}_{i,k} sgn(z_{i,k}) \\ &+ \dot{\alpha}_{i,k-1}] \end{aligned} \tag{31}$$

where $\hat{\gamma}_{i,k}$ represents the robust gains of the proposed controller, which are updated using adaptation laws to ensure stability in the presence of modeling uncertainties. Through adaptive estimation, the controller is capable of learning and adapting to the uncertainties in the θ vectors in real time. This enables the controller to effectively handle modelling uncertainties and achieve robust performance despite changing or unknown system dynamics. The discontinuity of the $sign(.)$ function introduces non-differentiability issues,

complicating the subsequent design procedure. To overcome this challenge and obtain a smooth control signal, the hyperbolic tangent function can replace the discontinuous sign function in (31). Ultimately, the stabilizing function $\alpha_{i,k}$ is verified as the follows:

$$\begin{aligned}\alpha_{i,k} = (\hat{\theta}_{a_i} a_i(\eta,\psi))^{-1}[&-c_{i,k} z_{i,k} - z_{i,k-1} \\ &-\hat{\theta}_{b_i} b_i(\eta,\psi) + \psi_{d_i}^{(k-1)} \\ &-\hat{\gamma}_{i,k} tanh\left(\frac{z_{i,k}}{\varepsilon_i}\right) + \dot{\alpha}_{i,k-1}]\end{aligned} \tag{32}$$

$\varepsilon_i > 0$ is the boundary layer coefficient. By substituting $\Psi_i = -c_{i,k} z_{i,k} - z_{i,k-1} + \psi_{d_i}^{(k-1)} + \dot{\alpha}_{i,k-1}$, it can be expressed as:

$$\begin{aligned}\alpha_{i,k} = (\hat{\theta}_{a_i} a_i(\eta,\psi))^{-1}[&\Psi_i - \\ &\hat{\gamma}_{i,k} tanh\left(\tfrac{z_{i,k}}{\varepsilon_i}\right) - \hat{\theta}_{b_i} b_i(\eta,\psi)]\end{aligned} \tag{33}$$

By introducing the regressor matrices Y_i, and the parameter vectors θ_i for (33), the parameters with uncertainties in the θ_i vectors are separated from the known dynamic variables in the Y_k matrices. This relationship can be expressed as $\alpha_{i,k} = Y_i \hat{\theta}_i$, where

$$\begin{aligned}Y_i = &\\ &[a_i(\eta,\psi)^{-1}(\Psi_i - \hat{\gamma}_{i,k} tanh\left(\frac{z_{i,k}}{\varepsilon_i}\right)) \\ &, -a_i(\eta,\psi)^{-1} b_i(\eta,\psi)] \\ \theta_i = &[\frac{1}{\theta_{a_i}} \quad \frac{\theta_{b_i}}{\theta_{a_i}}]^T\end{aligned} \tag{34}$$

By substituting the nonlinear virtual control laws from (33) into the dynamics given by (20), the closed-loop system using the proposed robust adaptive controller is obtained as follows:

$$\begin{aligned}&(\theta_{a_i} a_i(\eta,\psi))^{-1}\dot{\psi}_{i,k} - \Psi_i \\ &+(\hat{\theta}_{a_i} a_i(\eta,\psi))^{-1}\hat{\gamma}_{i,k} tanh\left(\frac{z_{i,k}}{\varepsilon_i}\right) \\ &= \left[\frac{\theta_{b_i}}{\theta_{a_i}} - \frac{\hat{\theta}_{b_i}}{\hat{\theta}_{a_i}}\right]\frac{b_i(\eta,\psi)}{a_i(\eta,\psi)}\end{aligned} \tag{35}$$

Thus, after employment of the regressor matrices Y_i and the parameter vectors θ_i, the above equations can be rewritten as follows:

$$\begin{aligned}\dot{z}_{i,k} = &-c_{i,k} z_{i,k} + a_i(\eta,\psi)\theta_{a_i} Y_i \tilde{\theta}_i \\ &-\hat{\gamma}_{i,k} tanh\left(\frac{z_{i,k}}{\varepsilon_i}\right)\end{aligned} \tag{36}$$

Where $\tilde{\theta}_i = \theta_i - \hat{\theta}_i$ represents the bounded error vector of the model parameters estimation. As the state variables and the estimation errors of unknown parameters $\tilde{\theta}_i$ are bounded, there exist positive unknown constant $\mu_{i,1}$, and $\mu_{i,2}$ such that

$$\left| a_i(\eta,\psi)\theta_{a_i} Y_i \tilde{\theta}_i \right| < \mu_{i,1} \tag{37}$$

$$\left| (\frac{\partial \alpha_{i,k}}{\partial \psi_{i,k}})[b_i(\eta,\psi)(\theta_{b_i} - \hat{\theta}_{b_i}) + a_i(\eta,\psi)(\theta_{a_i} - \hat{\theta}_{a_i}) g(u_i) \right| < \mu_{i,2} \tag{38}$$

To achieve robustness against modeling uncertainties, the parameter updates laws for updating the robust gains $\hat{\gamma}_{i,k}$, and $\hat{\gamma}_{i,k+1}$ are designed as follows:

$$\frac{d\hat{\gamma}_{i,k}(t)}{dt} = \Gamma_{i.k}\left|z_{i,k}(t)\right|, \qquad \hat{\gamma}_{i,k}(0) > 0 \tag{39}$$

$$\frac{d\hat{\gamma}_{i,k+1}(t)}{dt} = \Gamma_{i,k+1}\left|z_{i,k+1}(t)\right|, \hat{\gamma}_{i,k+1}(0) > 0 \tag{40}$$

The positive constant parameters $\Gamma_{i,k}$, and $\Gamma_{i,k+1}$ determine the rate at which the tracking errors are updated. Additionally, $\hat{\gamma}_{i,k}(0)$, and $\hat{\gamma}_{i,k+1}(0)$ represent the initial positive values of the robust gains at $t = 0$. By employing adaptive estimation, the controller can adjust to the uncertainties in the θ_i vectors in real time. This capability enables the controller to effectively manage modeling uncertainties and achieve robust performance in the presence of changing or unknown system dynamics.

Now, the Lyapunov theorem is utilized to ensure the stability and robustness of the closed-loop system, as well as tracking convergence to the desired outputs. We define a new candidate Lyapunov function as follows:

$$\begin{aligned}&V_{i,k}(z_{i,1}, z_{i,2}, \cdots, z_{i,k}) \\ &= V_{i,k-1} + \frac{1}{2} z_{i,k}^2 + \frac{1}{2\Gamma_{i,k}} (\hat{\gamma}_{i,k} - \mu_{i,1})^2 \geq 0\end{aligned} \tag{41}$$

That its time-derivative, along with equations (28) and (36), is given by:

$$\begin{aligned}\dot{V}_{i,k} &= \dot{V}_{i,k-1} + z_{i,k}\dot{z}_{i,k} + \left|z_{i,k}\right|(\hat{\gamma}_{i,k} - \mu_{i,1}) \\ &= -\sum_{j=1}^{k-1} c_{i,j} z_{i,j}^2 + z_{i,k-1} z_{i,k} \\ &\quad + z_{i,k}[-c_{i,k} z_{i,k} + a_i(\eta,\psi)\theta_{a_i} Y_i \tilde{\theta}_i \\ &\quad - \hat{\gamma}_{i,k} tanh\left(\frac{z_{i,k}}{\varepsilon_i}\right)] + \left|z_{i,k}\right|(\hat{\gamma}_{i,k} - \mu_{i,1}) \\ &= -\sum_{j=1}^{k} c_{i,j} z_{i,j}^2 + z_{i,k-1} z_{i,k} \\ &\quad + z_{i,k} a_i(\eta,\psi)\theta_{a_i} Y_i \tilde{\theta}_i \\ &\quad - z_{i,k}\hat{\gamma}_{i,k} tanh\left(\tfrac{z_{i,k}}{\varepsilon_i}\right) + \left|z_{i,k}\right|\hat{\gamma}_{i,k} \\ &\quad - \left|z_{i,k}\right|\mu_{i,1}\end{aligned} \tag{42}$$

According to the equation (37), it can be expressed as:

$$\begin{aligned}\dot{V}_{i,k} &\leq -\sum_{j=1}^{k} c_{i,j} z_{i,j}^2 + z_{i,k-1} z_{i,k} + z_{i,k}\mu_{i,1} \\ &\quad - z_{i,k}\hat{\gamma}_{i,k} tanh\left(\frac{z_{i,k}}{\varepsilon_i}\right) + \left|z_{i,k}\right|\hat{\gamma}_{i,k} \\ &\quad - \left|z_{i,k}\right|\mu_{i,1} \\ &\leq -\textstyle\sum_{j=1}^{k} c_{i,j} z_{i,j}^2 + z_{i,k-1} z_{i,k} \\ &\quad - z_{i,k}\hat{\gamma}_{i,k} tanh\left(\frac{z_{i,k}}{\varepsilon_i}\right) + \left|z_{i,k}\right|\hat{\gamma}_{i,k}\end{aligned} \tag{43}$$

It is important to note that the following inequality holds true for all values of $\varepsilon > 0$ [13].

$$0 \le |z_{i,k}| - z_{i,k}\tanh\left(\frac{z_{i,k}}{\varepsilon_i}\right) \le c\varepsilon_i, \quad (44)$$

$$c = 0.2785$$

After some arrangement, the following inequality can be obtained:

$$\dot{V}_{i,k} \le -\sum_{j=1}^{k} c_{i,j} z_{i,j}^2 + z_{i,k-1}z_{i,k} + \hat{\gamma}_{i,k}\, c\varepsilon_i \quad (45)$$

Step $k+1$: From (20), (21), and (24), we obtain

$$\begin{aligned}\dot{z}_{i,k+1} = {} & \frac{\partial g}{\partial u_i}(-k_i u_i + w_i) \\ & -\frac{\partial \alpha_{i,k}}{\partial \psi_{i,k}}(\theta_{b_i} b_i(\eta,\psi) - \Upsilon_i \\ & + \theta_{a_i} a_i(\eta,\psi) g(u) + \Delta d_i(t)) \\ & -\frac{\partial \alpha_{i,k}}{\partial \hat{\gamma}_{i,k}}\Gamma_{i,k}|z_{i,k}|\end{aligned} \quad (46)$$

$$\Upsilon_i = \sum_{j=1}^{k-1}\frac{\partial \alpha_{i,k}}{\partial \psi_{i,j}}\psi_{i,j+1} + \sum_{j=1}^{k}\frac{\partial \alpha_{i,k}}{\partial y_{d_i}^{(j-1)}}\psi_d^{(j)} \quad (47)$$

Note that $\frac{\partial g}{\partial u}$ is a variable quantity, which adds complexity to the design and analysis procedures. To address this challenge, we introduce the Nussbaum function $N(\chi)$ as follows:

$$\mathcal{N}(\mathcal{X}) = \mathcal{X}^2\cos(\mathcal{X}) \quad (48)$$

A design for the backstepping control law for w_i is formulated in the following manner

$$w_i = \mathcal{N}(\mathcal{X}_i)\bar{w}_i \quad (49)$$

$$\dot{\mathcal{X}}_i = \gamma_{\mathcal{X}_i} z_{i,k+1}\bar{w}_i \quad (50)$$

$$\begin{aligned}\bar{w}_i = {} & -c_{i,k+1}z_{i,k+1} + \Upsilon_i + \frac{\partial \alpha_{i,k}}{\partial \hat{\gamma}_{i,k}}\Gamma_{i,k}|z_{i,k}| \\ & + \frac{\partial \alpha_{i,k}}{\partial \psi_{i,k}}(\hat{\theta}_{b_i} b_i(\eta,\psi) - z_{i,k} \\ & + \hat{\theta}_{a_i} a_i(\eta,\psi) g(u)) + \frac{\partial g}{\partial u_i} k_i u_i \\ & -\mathcal{L}_i\left(\frac{\partial \alpha_{i,k}}{\partial \psi_{i,k}}\right)^2 z_{i,k+1} \\ & -\hat{\gamma}_{i,k+1}\tanh\left(\frac{z_{i,k+1}}{\varepsilon_i}\right)\end{aligned} \quad (51)$$

The coefficients $c_{i,k+1}, \mathcal{L}_i$, and $\gamma_{\mathcal{X}_i}$ are positive design parameters. To analyze the designed system, we now consider an augmented positive Lyapunov function given by:

$$\begin{aligned}V_{i,k+1}(z_{i,1}, z_{i,2}, \cdots, z_{i,k+1}) = {} & V_{i,k} + \frac{1}{2}z_{i,k+1}^2 \\ & + \frac{1}{2\Gamma_{i,k+1}}(\hat{\gamma}_{i,k+1} - \mu_{i,2})^2\end{aligned} \quad (52)$$

The Lyapunov function is positive definite. The derivative of $V_{i,k+1}$ is obtained as follows:

$$\begin{aligned}\dot{V}_{i,k+1} = {} & -\sum_{j=1}^{k} c_{i,j} z_{i,j}^2 + z_{i,k}z_{i,k+1} + \hat{\gamma}_{i,k}\, c\varepsilon_i \\ & + z_{i,k+1}(\dot{z}_{i,k+1} + \bar{w}_i - \bar{w}_i) \\ & + |z_{i,k+1}|(\hat{\gamma}_{i,k+1} - \mu_{i,2})\end{aligned} \quad (53)$$

Substituting equation (51) into (53) and using the adaptation law from (40) yields:

$$\begin{aligned}\dot{V}_{i,k+1} = {} & -\sum_{j=1}^{k} c_{i,j} z_{i,j}^2 + z_{i,k}z_{i,k+1} + \hat{\gamma}_{i,k}\, c\varepsilon_i \\ & -z_{i,k+1}\bar{w}_i + |z_{i,k+1}|(\hat{\gamma}_{i,k} - \mu_{i,2}) \\ & + z_{i,k+1}\Big(\frac{\partial g}{\partial u_i}w_i - c_{i,k+1}z_{i,k+1} - z_{i,k} \\ & -\frac{\partial \alpha_{i,k}}{\partial \psi i_{,k}}\Delta d_i - \mathcal{L}_i\left(\frac{\partial \alpha_{i,k}}{\partial \psi_{i,k}}\right)^2 z_{i,k+1} \\ & -\frac{\partial \alpha_{i,k}}{\partial \psi_{i,k}} b_i(\eta,\psi)(\theta_{b_i} - \hat{\theta}_{b_i}) \\ & -\frac{\partial \alpha_{i,k}}{\partial \psi_{i,k}} a_i(\eta,\psi)(\theta_{a_i} - \hat{\theta}_{a_i}) g(u) \\ & -\hat{\gamma}_{i,k+1}\tanh\left(\frac{z_{i,k+1}}{\varepsilon_i}\right)\Big)\end{aligned} \quad (54)$$

According to equation (38), it can be expressed as follows:

$$\begin{aligned}\dot{V}_{i,k+1} \le {} & -\sum_{j=1}^{k} c_{i,j} z_{i,j}^2 + z_{i,k}z_{i,k+1} + \hat{\gamma}_{i,k}\, c\varepsilon_i \\ & -z_{i,k+1}\bar{w}_i + |z_{i,k+1}|(\hat{\gamma}_{i,k+1} - \mu_{i,2}) \\ & + z_{i,k+1}\Big(\frac{\partial g}{\partial u_i}w_i - c_{i,k+1}z_{i,k+1} - z_{i,k} - \frac{\partial \alpha_{i,k}}{\partial \psi_{i,k}}\Delta d_i \\ & -\mu_{i,2} - \mathcal{L}_i\left(\frac{\partial \alpha_{i,k}}{\partial \psi_{i,k}}\right)^2 z_{i,k+1} - \hat{\gamma}_{i,k+1}\tanh\left(\frac{z_{i,k+1}}{\varepsilon_i}\right)\Big) \\ \le {} & -\sum_{j=1}^{k+1} c_{i,j} z_{i,j}^2 + \hat{\gamma}_{i,k}\, c\varepsilon_i - z_{i,k+1}\bar{w}_i + z_{i,k+1}\frac{\partial g}{\partial u_i}w_i \\ & -z_{ik+1}\frac{\partial \alpha_{i,k}}{\partial \psi_{i,k}}\Delta d_i - \mathcal{L}_i\left(\frac{\partial \alpha_{i,k}}{\partial \psi_{i,k}}\right)^2 z_{i,k+1}^2 \\ & + |z_{i,k+1}|\hat{\gamma}_{i,k+1} - \hat{\gamma}_{i,k+1}\, z_{i,k+1}\tanh\left(\frac{z_{i,k+1}}{\varepsilon_i}\right)\end{aligned} \quad (55)$$

By substituting equations (49) and (44) and utilizing the inequality $ab \le \frac{a^2}{2} + \frac{b^2}{2}$, one can write

$$\begin{aligned}\dot{V}_{i,k+1} \le {} & -\textstyle\sum_{j=1}^{k+1} c_{i,j} z_{i,j}^2 + \hat{\gamma}_{i,k} c\varepsilon_i + \hat{\gamma}_{i,k+1} c\varepsilon_i \\ & + z_{i,k+1}\frac{\partial g}{\partial u_i}(\mathcal{N}(\mathcal{X}_i) - 1)\bar{w}_i + \frac{1}{4\mathcal{L}_i}D_i^2\end{aligned} \quad (56)$$

where D_i is a constant which denotes the bound of $\Delta d_i(t)$ and may not be available. Substituting equation (50) into equation (56) yields:

$$\begin{aligned}\dot{V}_{i,k+1} \le {} & -CV_{i,k+1} + M_i \\ & + \frac{1}{\gamma_{\mathcal{X}_i}}(\xi_i\mathcal{N}(\mathcal{X}_i) - 1)\dot{\mathcal{X}}_i\end{aligned} \quad (57)$$

where $M_i = (\hat{\gamma}_{i,k} + \hat{\gamma}_{i,k+1})c\varepsilon_i + \frac{1}{4\mathcal{L}_i}D_i^2$, $C_i = 2min\{c_{i,1}, c_{i,2}, \cdots, c_{i,k+1}\}$, and $\frac{\partial g}{\partial u_i} = \xi_i$, $\left|\frac{\partial g}{\partial u}\right| = \left|\frac{4}{(e^{\frac{u}{u_M}}+e^{-\frac{u}{u_M}})^2}\right| \leq 1$.

By directly integrating differential inequality (57), we obtain:

$$V_{i,k+1} \leq V_{i,k+1}(0)e^{-C_i t} + \frac{1}{C_i}(M_i)(1-e^{-C_i t}) \\ \frac{e^{-C_i t}}{\gamma x_i}\int_0^t (\xi_i \mathcal{N}(\mathcal{X}_i) - 1)\,\dot{\mathcal{X}}_i e^{C_i \tau} d\tau \quad (58)$$

We can conclude that the closed-loop system is stable based on Lemma 1.

Theorem 1. Consider the uncertain nonlinear system (9) satisfying Assumptions 1– 3 and Lemma 1. An adaptive backstepping sliding mode control (49) makes outputs $y_i(t)$ track the desired trajectory $y_{d_i}(t)$ while ensuring the boundedness of all the closed-loop signals.

Proof: By applying the virtual controllers (25), (26), and (33), along with the Lyapunov functions (27), (41), and (52), and implementing the parameter update laws (39) and (40), and control law (49), the stability of the closed-loop system is ensured.

IV. Results and Discussion

In this section, we apply the proposed controller scheme to an uncertain bi-model SEIAR epidemiological model with five saturated control inputs. The system dynamics incorporate input saturation, uncertainty, and external disturbances. The values of the system parameters used in the simulations are sourced from references [4, 30], and are provided in Table 2. We validate the effectiveness of the proposed system through simulation analysis in the MATLAB Simulink environment. The performance of the proposed controller is compared with two other controllers: the dynamic anti-windup compensator (AWC) and the adaptive sliding mode controller (ASMC), as detailed in [20] and [15] respectively. In [20], the AWC addresses actuator saturation by employing a two-step design. First, a nonlinear feedback controller is developed without considering input constraints, and then a dynamic compensator is added to manage saturation This compensator leverages the difference between the generated control signal and the saturated signal as a dead-zone signal to activate the anti-windup mechanism. Additionally, we assume the following saturation levels for the control inputs:

$$sat(u_i) = \begin{cases} 0.75, & u_i \geq 0.75 \\ u_i, & 0 \leq u_i \leq 0.75,\ i = 1,2,3 \\ 0, & u_i \leq 0 \end{cases} \quad (59)$$

$$sat(u_i), = \begin{cases} 0.35, & u_i \geq 0.35 \\ u_i, & 0 \leq u_i \leq 0.35, i = 4,5 \\ 0, & u_i \leq 0 \end{cases} \quad (60)$$

TABLE II INTERPRETATION OF SYSTEM PARAMETERS [4, 30]

Parameter	Description	Values ($days^{-1}$)
ν	Rate of birth	0.0086
κ_1	Rate of becoming infectious after a latent period from E_1 to I_1	0.955
κ_2	Rate of becoming infectious after a latent period from E_2 to I_2	0.526
γ_1	The cure rate for the infected with comorbidity	0.633
γ_2	The cure rate for the infected with comorbidity	0.833
η_1	The cure rate for Asymptomatic class I	0.112
η_2	The cure rate for asymptomatic class II	0.244
p_1	Percentage of experiencing symptoms for class I	0.867
p_2	Percentage of experiencing symptoms for class II	0.667
β_1	Transmission rate from S to E_1	1.667
β_2	Transmission rate from S to E_2	1.667
μ	Natural death rate	0.0039
ω	Rate of losing immunity	0.833
ρ_1	Mortality rate of individuals caused by infection for class I	0.03
ρ_2	Mortality rate of individuals caused by infection for class II	0.02

The simulations are based on a final treatment time of $t_f = 60$ days, which represents the duration required to eradicate the disease from the population, as determined by the designer. The running time of algorithm implementation is 3.0101 seconds. To control the disease epidemic, the target reduction of the susceptible and infected compartments (I_d, E_d, S_d) over time is defined as follows:

$$S_d = (S_0 - S_f)\exp(-at) + S_f \\ E_{d_i} = (E_{0i} - E_{fi})\,exp(-at) + E_{f_i}, i = 1,2 \\ I_{d_i} = (I_{0i} - I_{fi})\,exp(-at) + I_{f_i} \quad (61)$$

Here, (a) is the adjustable population reduction rate, chosen as $a = 0.2$. The desired steady-state numbers of infected, exposed, and susceptible individuals denoted as I_{fi}, E_{fi}, and S_f are assumed to be zero ($i.e., I_f = 0,\ E_f = 0,\ S_f = 0$). The initial numbers of infected, exposed, and susceptible individuals are represented as I_0, E_0, and S_0 , respectively. respectively. The initial values of the influenza variables used in these simulations, along with the parameters for the controller, are provided in Tables 3 and 4, respectively. Additionally, the model parameters are perturbed by 80% , and $\Delta d(t) = [\,0.3\sin(4t)\ \ 0.5\sin(3t)\ \ 0.8\cos(2t)\ 0.2\sin(5t)\ 0.4\cos(t)]^T$

represents unidentified time-varying external disturbances, unmodeled dynamics, and perturbations introduced into the system.

TABLE III INITIAL VALUES OF THE STATE AND THE CONTROLLER VARIABLES

Variable	Initial value
$S(0)$	400
$E_1(0)$	120
$E_2(0)$	30
$I_1(0)$	150
$I_2(0)$	100
$A_1(0)$	50
$A_2(0)$	50
$R(0)$	100
$u(0)$	[1 0 1 1 0]
$\boldsymbol{\chi(0)}$	[0.01 0.0 0.02 0.02 0.01]

TABLE IV CONTROLLER PARAMETERS

Parameter	Description	Values
k	$[k_1\ k_2\ k_3\ k_4\ k_5]$	[20 10 10 30 20]
γ_x	$[\gamma_{x_1}\ \gamma_{x_2}\ \gamma_{x_3}\gamma_{x_4}\ \gamma_{x_5}]$	[0.01 0.01 0.01 0.1 0.11]
$\mathcal{L}$	$[\mathcal{L}_1\ \mathcal{L}_2\ \mathcal{L}_3\ \mathcal{L}_4\ \mathcal{L}_5]$	[5 10 20 10 10]
ε	$[\varepsilon_1\ \varepsilon_2\ \varepsilon_3\ \varepsilon_4\ \varepsilon_5]$	[1 1 1 10 10]

The text presents a comparative analysis of three simulation scenarios to investigate the population dynamics of the two-group SEIAR mathematical model under varying conditions. These scenarios encompass:

(I) Absence of control measures: This scenario serves as a baseline to observe the model's behavior without any interventions.

(II) Application of different controllers on an unconstrained System: Here, various controllers are applied to the model without considering any constraints. This allows for an assessment of the controllers' effectiveness in an ideal setting.

(III) Examination of the input-constrained System: in this scenario, the model incorporates input constraints, reflecting real-world limitations. The performance of the proposed dynamic compensator, AWC, and adaptive SMC is evaluated under these constraints.

The comparison of these scenarios provides insights into the impact of control strategies and saturation constraints on the population dynamics of the two-group SEIAR model. It highlights the need for careful controller design and consideration of practical limitations to achieve adequate disease. Fig.3 illustrates the temporal evolution of the populations under consideration in the absence of control measures. Numerical analysis is conducted for the susceptible, exposed, and infected classes, examining scenarios where $R_0 > 1$ and $R_0 < 1$.

Using the parameters from Table 2 and $\beta = 0.1$, the calculated basic reproduction numbers are $R_0^1 = 0.2248$ and $R_0^2 = 0.2364$. These values indicate that the infection dies out and the virus-free equilibrium is stable. In contrast, when $\beta = 1.667$, equations (7) and (8) yield $\mathrm{R}_0^1 = 3.7691$ and $\mathrm{R}_0^2 = 3.9643$, both greater than 1. Consequently, the disease becomes uniformly persistent, converging to an endemic equilibrium at (691, 47.2, 84.7, 46.3, 65.5, 104, 24.5, 123). As a result, the population will consistently contain infectious and asymptomatic individuals, implying that natural disease eradication is impossible. Therefore, control measures must be implemented to eradicate the disease. It is observed that R_0^1 is lower than R_0^2, indicating that individuals with comorbidities are more vulnerable to infection.

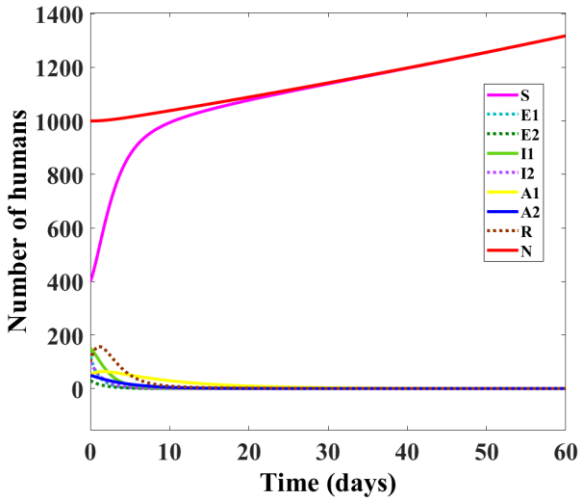

(a)

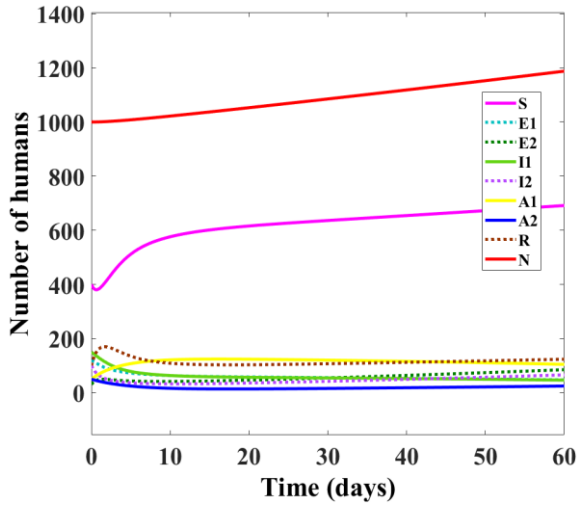

(b)

Fig.3. Open-loop response of the epidemic in the absence of control measures, when (a) $R_0 < 1$, and (b) $R_0 > 1$.

Figs. 4, 5, 6, and 7 illustrate the management of susceptible, recovered, exposed, and infected individuals in an unconstrained system under various control strategies. These figures highlight the dynamics of the epidemic compartments over time, providing a comprehensive view of how the disease evolves in response to different interventions. The implementation of these control strategies

leads to a significant and rapid decline in the basic reproduction number as the outbreak progresses. A lower R_0 signifies that each infected individual transmits the disease to fewer people, which is a critical factor in curbing an epidemic. Eventually, the model converges to a disease-free equilibrium, represented by $(0, 0, 0, 0, 0, 0, 0, N)$ as $t \to \infty$, indicating the effective eradication of the disease within the population.

As depicted in Fig. 4, the number of susceptible individuals decreases to zero, successfully achieving the intended tracking objective for this compartment. This decline suggests that the population has either recovered or acquired immunity, effectively disrupting the chain of transmission. Similarly, Fig. 5 illustrates that the number of recovered individuals steadily increases, asymptotically approaching the total population. This trend confirms a successful recovery process facilitated by the applied control mechanisms.

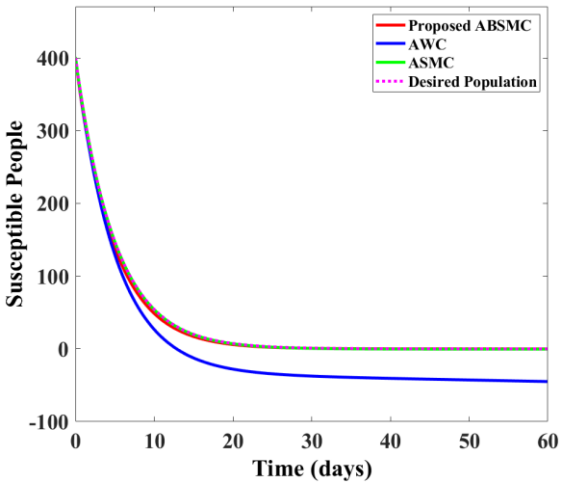

Fig.4. Changes in the number of susceptible individuals in the unconstrained system under different control strategies.

Figs. 6 and 7 present the variations in the number of exposed and infected individuals under different conditions, including scenarios with and without comorbidities. These figures emphasize how the control strategies effectively manage disease propagation in an unconstrained system. In both cases, the interventions significantly reduce the number of exposed and infected individuals over time, underscoring their efficacy in mitigating the epidemic.

This analysis highlights the importance of implementing appropriate control measures to combat infectious diseases and provides a robust framework for understanding the dynamics of disease transmission and recovery in various population groups.

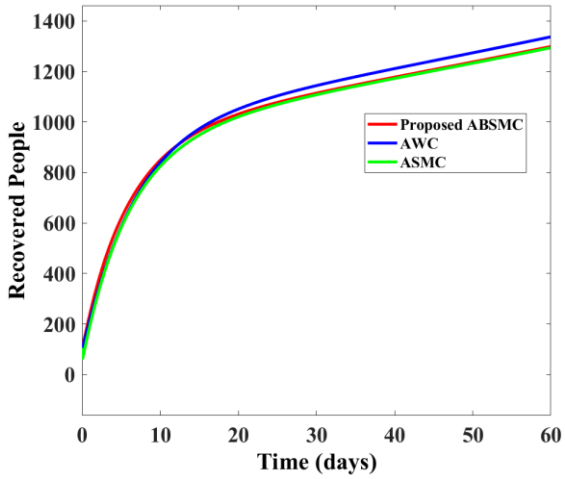

Fig.5. Changes in the number of recovered individuals in the unconstrained system under different control strategies.

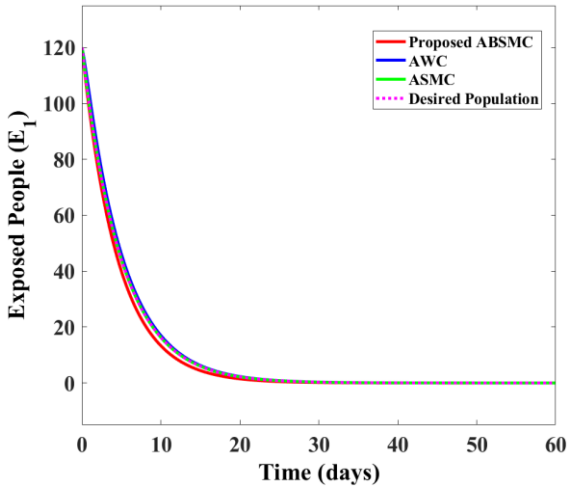

(a)

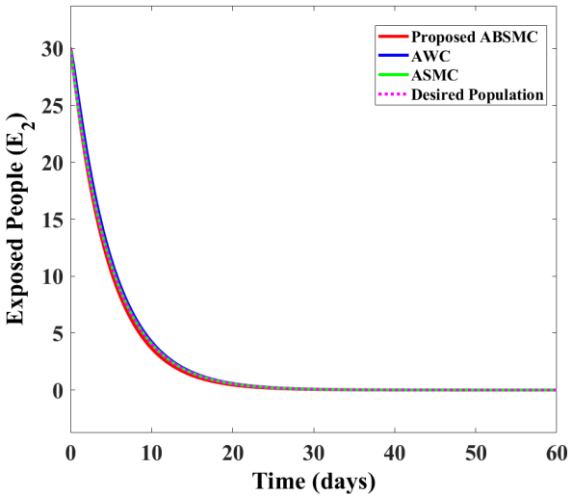

(b)

Fig.6. Changes in the number of exposed individuals in the unconstrained system under different control strategies: (a) with comorbidities and (b) without comorbidities.

However, as illustrated in Fig. 4, the anti-windup compensator (AWC) controller exhibits limitations in managing uncertainties and external disturbances, leading to the unrealistic prediction of a negative susceptible population. This drawback suggests that the AWC controller may not be fully effective in maintaining system stability under uncertain conditions. In contrast, the proposed controller demonstrates superior convergence speed, improved tracking accuracy, and greater robustness in handling the epidemic dynamics. These advantages highlight its effectiveness in optimizing disease control strategies and ensuring a more reliable response to outbreaks.

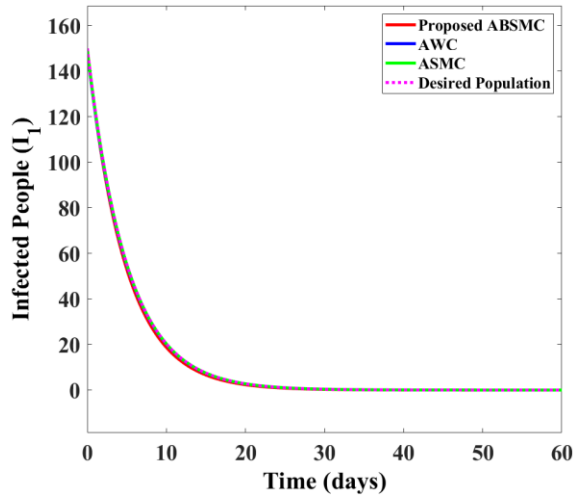

(a)

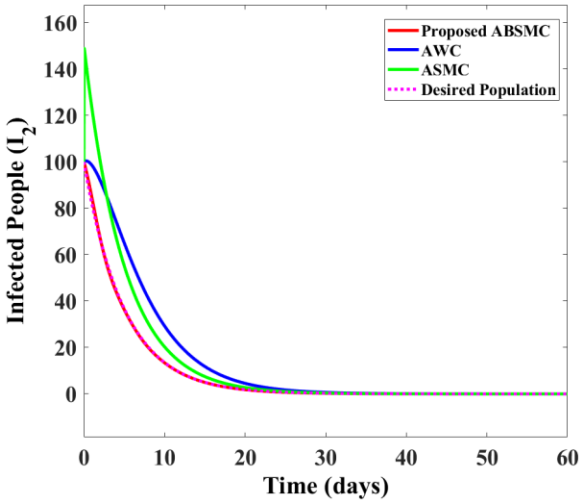

(b)

Fig.7.Changes in the number of infected individuals in the unconstrained system under different control strategies: (a) with comorbidities and (b) without comorbidities.

Now, consider a scenario where the control inputs are limited. When the actuator becomes saturated, feedback loops are disrupted, preventing the controller from effectively influencing system performance. Consequently, saturation issues can lead to significant performance degradation, resulting in oscillations, prolonged settling times, undershoots, delays, excessive overshoots, and instability. Figs. 8, 9, 10, and 11 illustrates the output of the constrained system under various control strategies after 60 days of treatment. As shown in Figs. 8 and 9, the degradation of the uncompensated system is evident in the output responses, which are characterized by undesirable oscillations and an extended settling time, ultimately compromising control performance. As a result, during the treatment period, a portion of the population remains susceptible, and recovered individuals are unable to fully converge to the total population.

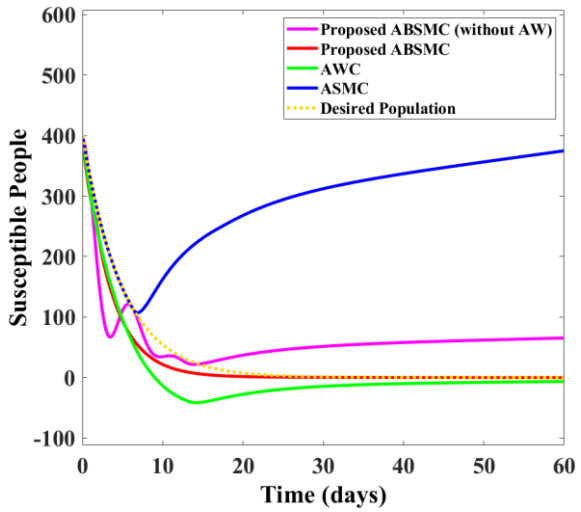

Fig.8. Change in the number of susceptible individuals in the input-constrained system under different control strategies.

After applying various control strategies to the constrained system, it is clear that overall system performance has improved. The ABSMC approach offers several advantages over other methods. It demonstrates superior tracking accuracy by minimizing tracking errors between actual system states and desired trajectories. ABSMC effectively handles input saturation, ensuring control inputs remain within feasible bounds while maintaining stability and performance. The approach provides enhanced stability by incorporating integral action to eliminate steady-state errors and improve overall stability, even in the presence of uncertainties and disturbances.

Additionally, as shown in Fig. 8, on the day 60, the difference in the number of susceptible individuals between the cases with and without the proposed ABSMC controller is approximately 66 individuals. This demonstrates that even when the vaccination input is saturated, the proposed controller effectively mitigates the negative impacts of input constraints and reduces the number of susceptible individuals.

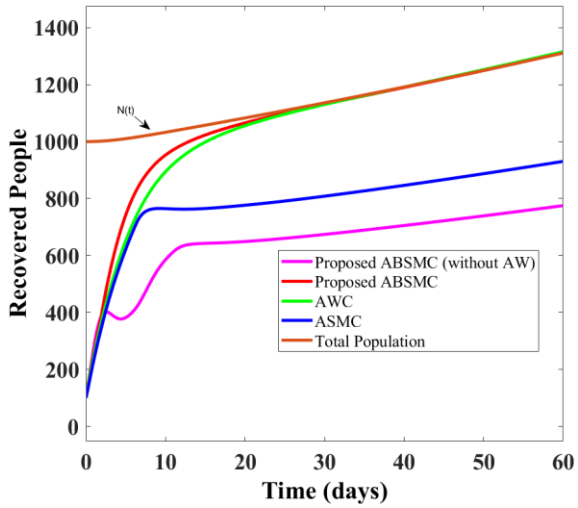

Fig.9. Change in the number of recovered individuals in the input-constrained system under different control strategies.

Furthermore, as illustrated in Fig. 9, when saturation occurs with the proposed controller, the number of recovered individuals increases over time and converges toward the final population. This behavior is due to the controller's ability to maintain stability and ensure that the system converges to the desired equilibrium point even in the presence of input saturation.

The proposed ABSMC compensator's effectiveness in handling input saturation is crucial in real-world scenarios, where resource limitations and practical constraints may restrict the implementation of control inputs. By mitigating the effects of saturation, the controller ensures that the epidemic model remains stable and converges to the desired disease-free equilibrium point, reducing the impact of the pandemic on the population.

Based on the information presented in Figs.10, and 11, the convergence rate to zero for infected and exposed individuals is faster when the proposed ABSMC compensator is employed compared to other methods. This is a crucial factor in managing pandemic diseases, as it is essential to control the timing of the disease to quickly steer the model toward a disease-free equilibrium point. The faster convergence rate achieved by the ABSMC compensator is attributed to its improved tracking accuracy, robustness to input saturation, enhanced stability, and adaptability. These advantages allow the ABSMC controller to respond effectively to changes in the epidemic dynamics and to drive the system towards the desired disease-free equilibrium point more rapidly. The implementation of the proposed compensator reduces the eradication duration of infected and exposed individuals by approximately 15 days compared to scenarios without it. By reducing the eradication duration of infected and exposed individuals, the ABSMC compensator can potentially mitigate the impact of the pandemic, reduce the burden on healthcare systems, and save lives.

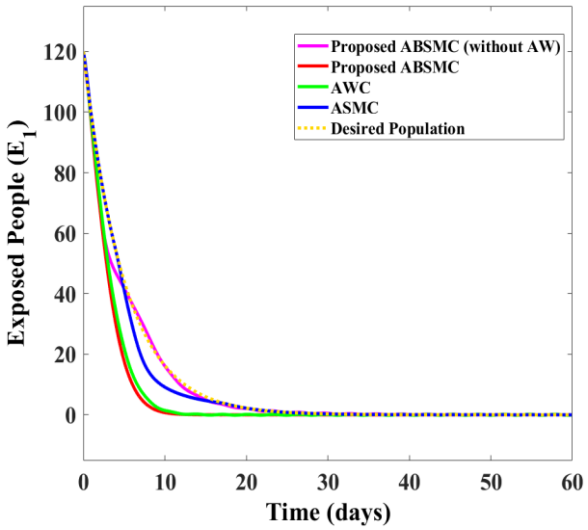

(a)

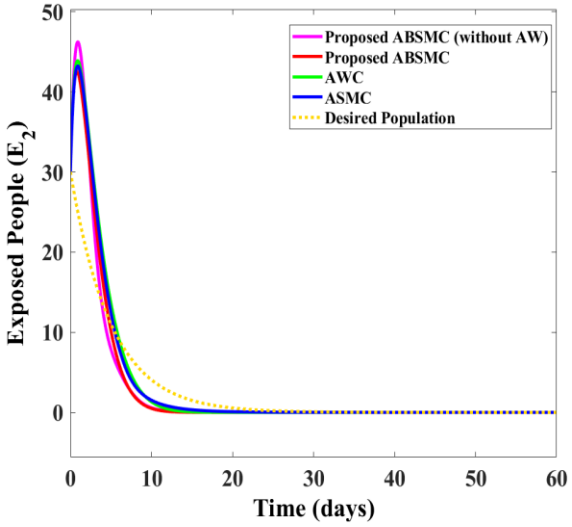

(b)

Fig.10. Change in the number of exposed individuals with and without comorbidities in the input-constrained system under different control strategies.

The implemented rates of vaccination for the susceptible compartments (u_1), social distancing for the exposed individuals (u_2, u_3), and antiviral treatment for the infected individuals (u_4, u_5) are illustrated in Figs. 12 and 13. It is important to note that the vaccination, social distancing, and antiviral treatment rates in this model must be less than $1 (0 \leq u_i(t) \leq 1, i = 1, \dots, 5)$. This constraint ensures that the control inputs remain within feasible ranges. The simulation results demonstrate that the obtained control inputs satisfy this implementation constraint. This ensures that the control strategies are practically implementable and do not violate any physical or biological constraints.

In the following, the impact of parametric uncertainty on the performance of the nonlinear robust adaptive controller is investigated. To this end, uncertainties of 20%, 40%, 60%

and 80% are applied to the initial estimation of model parameters ($\hat{\theta}$) relative to their real values (θ), as outlined in Table 2. Specifically, $\hat{\theta} = 1.2\theta, 1.4\theta, 1.6\theta$ and 1.8θ correspond to 20%, 40%, 60% and 80% uncertainty, respectively. The tracking errors for the susceptible, exposed, and infected populations—both with and without underlying diseases—under varying levels of uncertainty are depicted in Figs. 14, 15, 16, 17, and 18, respectively. As illustrated in these figures, the proposed controller effectively manages different degrees of parametric uncertainty. Even with an uncertainty level of 80%, the tracking errors remain bounded, ensuring system stability.

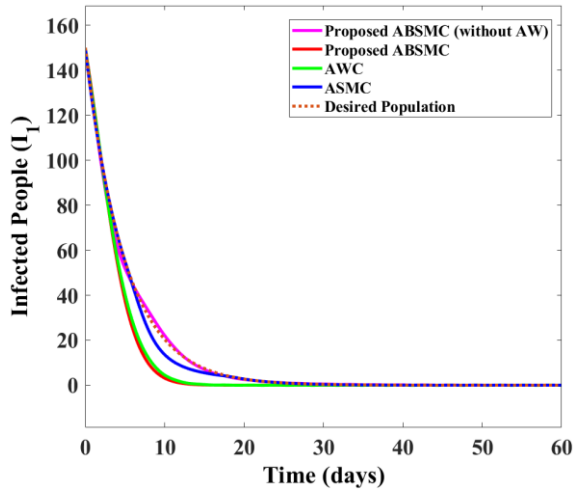

(a)

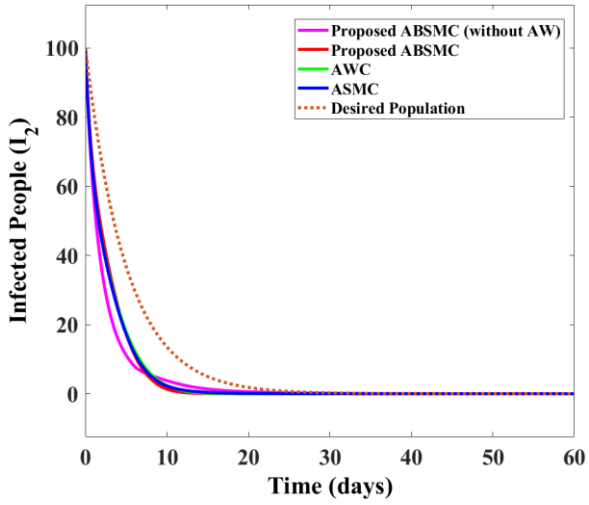

(b)

Fig.11. Change in the number of infected individuals with and without comorbidities in the input-constrained system under different control strategies

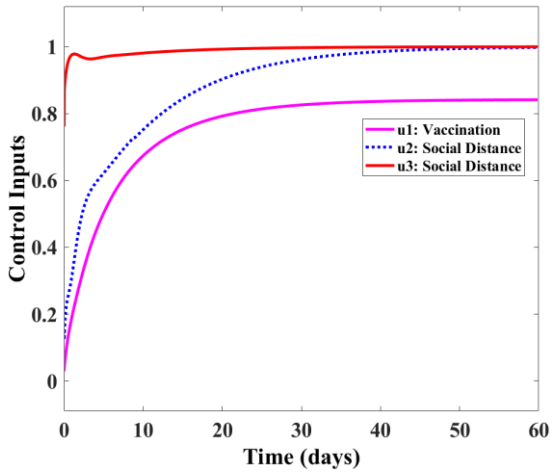

Fig. 12. The required rate of vaccination and social distancing applied to the two-group epidemic model

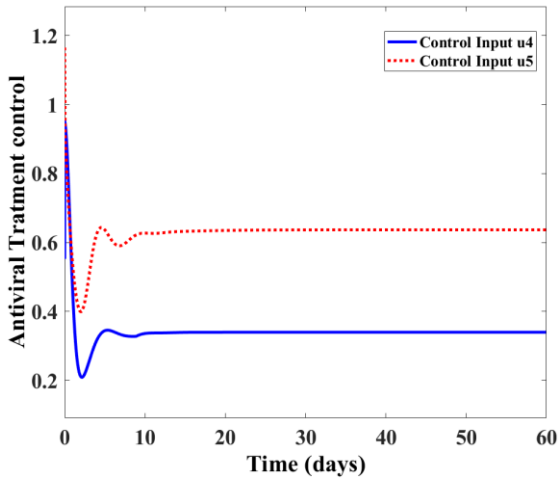

Fig. 13. The required rate of antiviral treatment applied to the two-group epidemic model

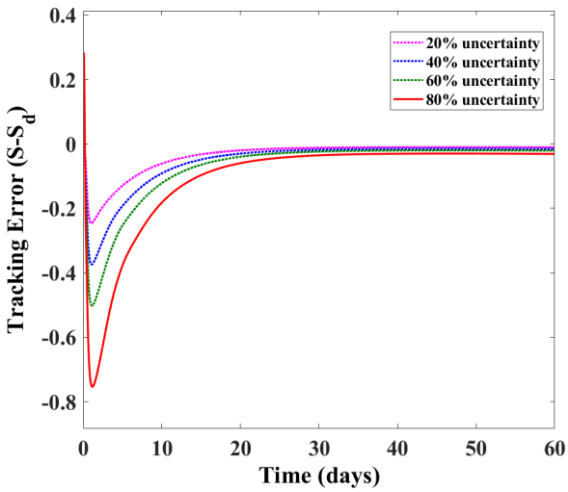

Fig. 14. The effect of 20%, 40%, 60% and 80% uncertainty in the estimated model parameters on tracking errors of the susceptible populations ($S - S_d$).

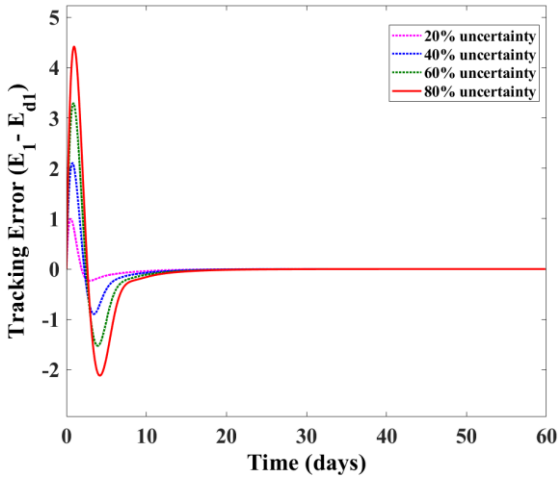

Fig.15. The effect of 20%, 40%, 60% and 80% uncertainty in the estimated model parameters on tracking errors of the exposed populations with comorbidities $(E_1 - E_{d_1})$.

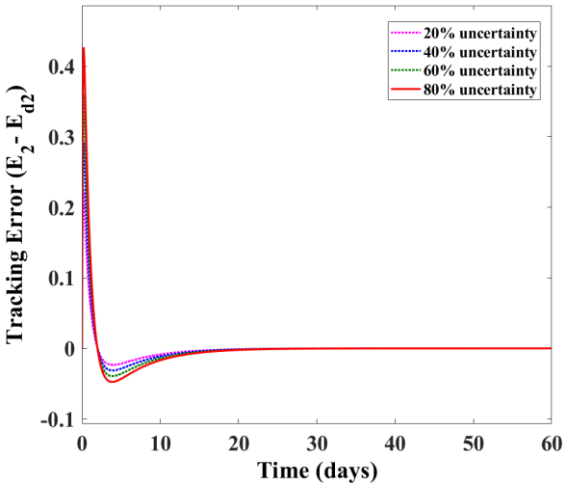

Fig.16. The effect of 20%, 40%, 60% and 80% uncertainty in the estimated model parameters on tracking errors of the exposed populations without comorbidities $(E_2 - E_{d_2})$.

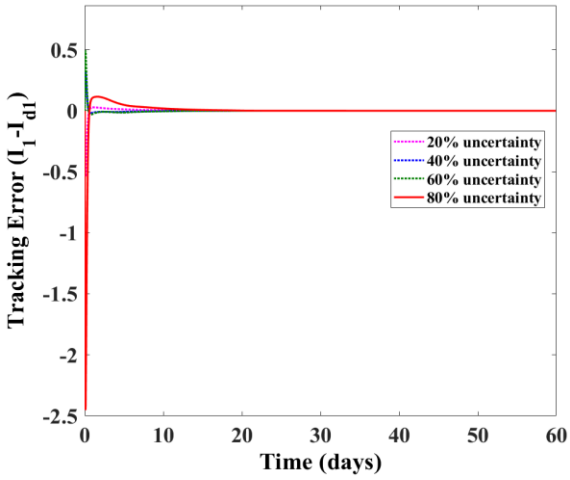

Fig. 17. The effect of 20%, 40%, 60% and 80% uncertainty in the estimated model parameters on tracking errors of the infected populations with comorbidities $(I_1 - I_{d_1})$.

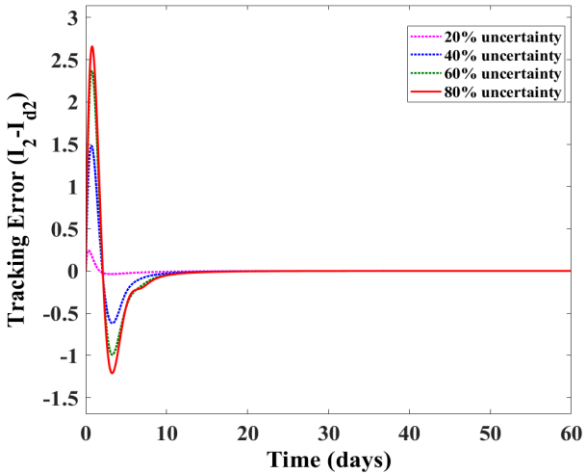

Fig. 18. The effect of 20%, 40%, 60% and 80% uncertainty in the estimated model parameters on tracking errors of the infected populations without comorbidities $(I_2 - I_{d_2})$.

These results underscore the robustness and adaptability of the proposed approach in handling uncertain system parameters while maintaining reliable performance.

To further evaluate the robustness of the proposed control approach, we investigate the required variation of vaccination, social distancing, and antiviral treatment in the control process of epidemic with different levels of uncertainty in model parameters. We consider three scenarios: 30%, 60%, and 90% uncertainty in model parameter compared to the nominal plant. As shown in Figs. 19, 20, and 21, the proposed control method effectively handles parameter uncertainty. Despite significant variations in the model parameters, the required control inputs remain within acceptable ranges, ensuring effective management of the epidemic. Therefore, the nonlinear control strategy demonstrates strong robustness against parametric uncertainties in the model.

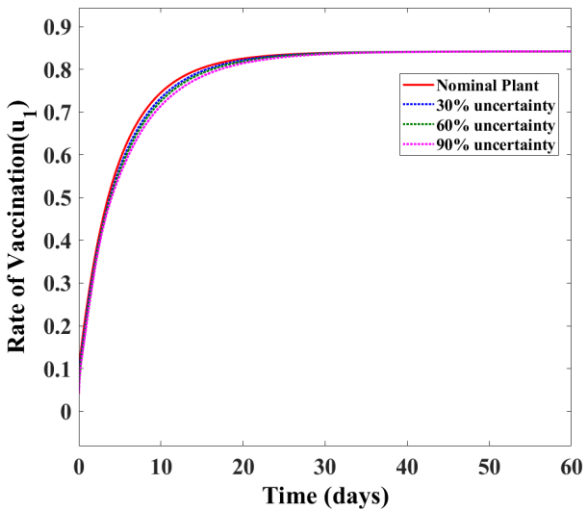

Fig. 19. Required variation of vaccination in control process of epidemic with 30%, 60% and 90% uncertainty in model parameters in comparison with the nominal plant.

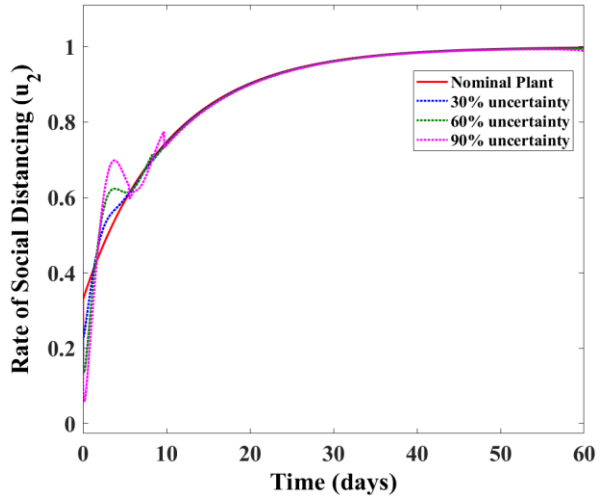

(a)

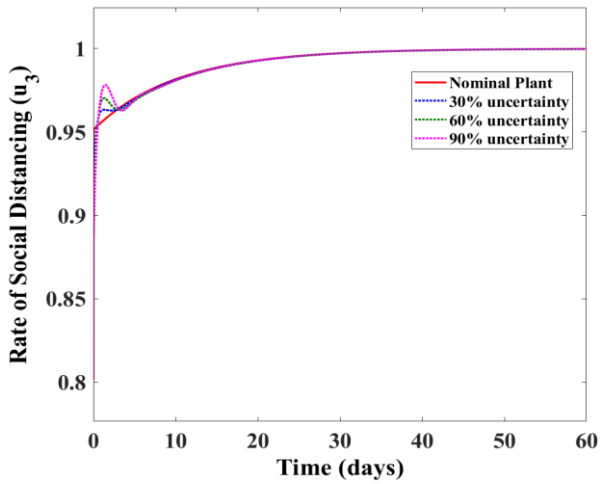

(b)

Fig. 20. Required variation of social distancing in control process of epidemic with 30%, 60% and 90% uncertainty in model parameters in comparison with the nominal plant.

In epidemic disease simulations, error bars serve a fundamental role in capturing the inherent uncertainty present in the model's predictions. They provide a visual representation of the variability in key epidemiological parameters, such as transmission rates, recovery rates, and other disease dynamics, under the influence of both model uncertainties and external disturbances. By including error bars that reflect both the mean and standard deviation, these simulations offer a more nuanced understanding of the reliability of the predictions, enabling the assessment of the potential range of outcomes rather than a single deterministic result.

This approach is particularly valuable when evaluating the effectiveness of intervention strategies, as it accounts for variations in real-world conditions, such as changes in public behavior, environmental factors, or external interventions. Moreover, error bars highlight the sensitivity of the model to fluctuations in parameter values, thus allowing researchers to identify critical parameters that most influence the disease progression. This information is essential for refining control strategies, ensuring that interventions remain robust even in the presence of substantial uncertainties.

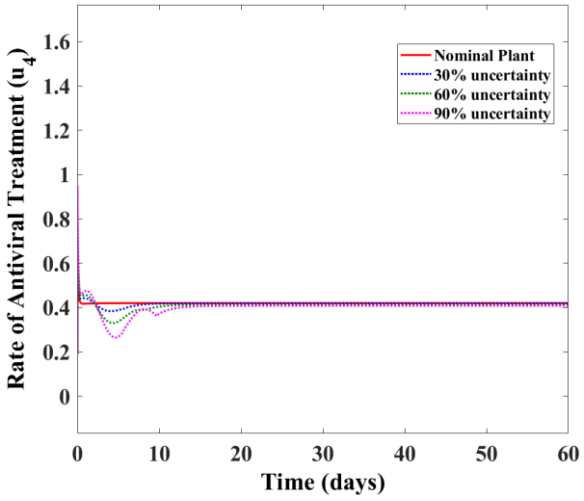

(a)

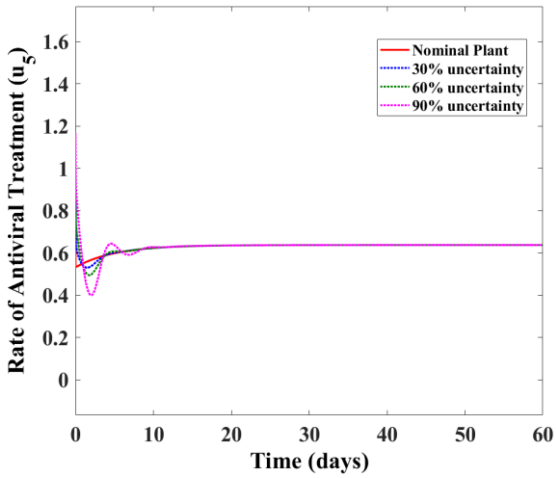

(b)

Fig. 21. Required variation of vaccination, social distancing, and antiviral treatment in control process of epidemic with 30%, 60% and 90% uncertainty in model parameters in comparison with the nominal plant.

Furthermore, the incorporation of error bars enhances the predictive power of the model by emphasizing the range of possible epidemic trajectories, thereby offering more realistic insights into the potential public health outcomes under varying levels of uncertainty. This aids policymakers in making informed decisions, particularly when there is a need to balance the trade-offs between control measures and their associated uncertainties. The error bars representing the mean and standard deviation of the simulation results are shown in Fig. 22, which visually underscores the uncertainty inherent in the model's predictions and highlights the variability in outcomes across different parameter scenarios.

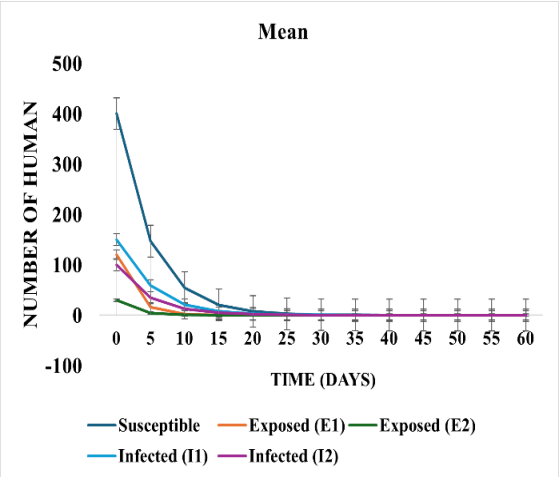

(a)

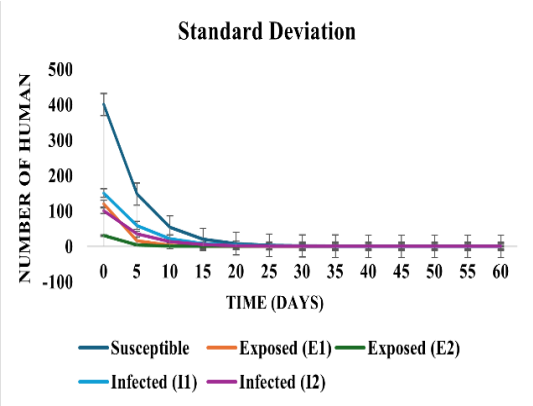

(b)

Fig. 22. Error bars representing (a) the mean value and (b) the standard deviation for the population dynamics over time

V. Conclusions

This study investigates the effectiveness of an anti-windup compensation method in a MIMO epidemic system modeled as a positive system, with a particular focus on input saturation, modeling uncertainties, and external disturbances. It is the first study to explore these specific aspects within the context of epidemic modeling and control, this research addresses practical constraints by incorporating input saturation and employing an anti-windup compensation method, thereby enhancing the robustness and performance of the epidemic control system. The proposed nonlinear robust adaptive backstepping sliding mode control (ABSMC) strategy combines the advantages of adaptive sliding mode control and backstepping control to tackle the spread of epidemic diseases within a host population.

One of the key challenges addressed in this study is input saturation, which necessitates a careful balance between stability and precision. To achieve this balance, the research introduces a novel approach using auxiliary systems and Nussbaum gain functions. The Nussbaum function serves as a mathematical tool to address the nonlinearities caused by input saturation, ensuring the stability and positivity of system states while enhancing the controller's robustness. When integrated with the auxiliary design system, this approach creates a resilient and adaptive control scheme capable of performing effectively under various challenging conditions.

To model the spread of the disease, a two-group SEIAR epidemic model with uncertain parameters is utilized, incorporating dynamic population changes. By accounting for uncertainties in the model's nonlinear dynamics, the proposed controller is better equipped to manage variations and unexpected changes in the disease transmission process. This results in improved control performance and resilience in real-world scenarios. The control strategy focuses on reducing the numbers of susceptible, exposed, infected, and asymptomatic individuals to zero while maximizing the recovered population through effective tracking of the total population. Simulation results demonstrate that the proposed ABSMC control scheme effectively addresses the challenges posed by input saturation and external disturbances, ensuring the stability of the nonlinear uncertain MIMO epidemic system while achieving the desired trajectory tracking performance.

Furthermore, this control method can have significant social and economic impacts. By reducing the number of infected individuals and accelerating population recovery, treatment costs are reduced, and societal productivity is increased. Compared to traditional control methods, this new approach offers greater flexibility and resilience to uncertainties and disturbances, making it a suitable option for controlling epidemics in real-world conditions.

However, practical implementation faces certain challenges. In real-world situations, the number of individuals in each group may not be readily accessible, necessitating the development of control methods that rely on observer output for the epidemic model. Future studies will explore observer-based design methods and effective control strategies for nonlinear epidemic and biological systems. Additionally, to address the limitations identified in this study, future work will investigate alternative strategies for improving the controller's robustness and computational efficiency in resource-constrained environments. This includes examining the impact of larger-scale uncertainties and unmodeled dynamics on system performance. For example, integrating machine learning techniques could enhance parameter estimation and adaptability in real-time applications, further advancing the method's effectiveness.

References

[1] I. Sekkak, B. R. Nasri, B. N. Rémillard, J. Dzevela Kong and M. El Fatini , "A stochastic analysis of a SIQR epidemic model with short and long-term prophylaxis," Communications in Nonlinear Science and Numerical Simulation, vol. 127, p. 107523, 2023, doi: 10.1016/j.cnsns.2023.107523.

[2] T. Li, Y. Li , Y. Zhang, Y. Wang and X.-F. Luo, "A possible method of selecting spatial epidemic models based on Turing's diffusive threshold," Physica A: Statistical Mechanics and its Applications, vol. 624, p. 128986, 2023, doi: 10.1016/j.physa.2023.128986.

[3] Z. Abbasi, I. Zamani, A. H. Amiri Mehra, M. Shafieirad and A. Ibeas, "Optimal Control Design of Impulsive SQEIAR Epidemic Models with Application to COVID-19," Chaos, Solitons & Fractals, vol. 139, p. 110054, 2020, doi: 10.1016/j.chaos.2020.110054.

[4] A. H. Amiri Mehra, I. Zamani, Z. Abbasi and A. Ibeas, "Observer-based adaptive PI sliding mode control of developed uncertain SEIAR influenza epidemic model considering dynamic population," Journal of Theoretical Biology, vol. 482, p. 109984, 2019, doi: 10.1016/j.jtbi.2019.08.015.

[5] S. Muthukumar, A. Balakumar, S. Ravikumar and V. Chinnadurai, "An optimal control of bi-modal COVID-19 SEIQR epidemic spreading model in India," Results in Control and Optimization, vol. 12, p. 100256, 2023, doi: 10.1016/j.rico.2023.100256.

[6] J. Wang and . B. Dai, "Dynamical analysis of a multi-group SIR epidemic model with nonlocal diffusion and nonlinear incidence rate," Nonlinear Analysis: Real World Applications, vol. 68, p. 103661, 2022, doi: 10.1016/j.nonrwa.2022.103661.

[7] Y. Luo , L. Zhang, Z. Teng and T. Zheng, "Analysis of a general multi-group reaction–diffusion epidemic model with nonlinear incidence and temporary acquired immunity," Mathematics and Computers in Simulation, vol. 182, pp. 428-455, 2021, doi :10.1016/j.matcom.2020.11.002.

[8] A. I. Abioye, J. P. Olumuyiwa, A. O. Hammed, A. O. Festus, O. Kayode, A. I. Abdullahi and K. Ilyas, "Mathematical model of COVID-19 in Nigeria with optimal control," Results in Physics, vol. 28, p. 104598, 2021, doi: 10.1016/j.rinp.2021.104598.

[9] A. A. Khan, S. Ullah and R. Amin, "Optimal control analysis of COVID-19 vaccine epidemic model: a case study," The European Physical Journal Plus, vol. 137, pp. 1-25, 2022, doi: 10.1140/epjp/s13360-022-02365-8.

[10] N. R. Sasmita, M. Ikhwan, S. Suyanto and V. Chongsuvivatwong, "Optimal control on a mathematical model to pattern the progression of coronavirus disease 2019 (COVID-19) in Indonesia," Global Health Research and Policy, vol. 5, pp. 1-12, 2020, doi: 10.1186/s41256-020-00163-2.

[11] A. Srivastava and Nilam , "Optimal control of a fractional order SEIQR epidemic model with non-monotonic incidence and quarantine class," Computers in Biology and Medicine, vol. 178, p. 108682, 2024, doi: 10.1016/j.compbiomed.2024.108682.

[12] A. Veisi and H. Delavari, "Fractional-order backstepping strategy for fractional-order model of COVID-19 outbreak," Mathematical Methods in the Applied Sciences, vol. 45, no. 7, pp. 3479-3496, 2021, doi: 10.1002/mma.7994.

[13] A. Rajaei, M. Raeiszadeh, V. Azimi and M. Sharifi, "State estimation-based control of COVID-19 epidemic before and after vaccine development," Journal of Process Control, vol. 102, pp. 1-14, 2021, doi: 10.1016/j.jprocont.2021.03.008.

[14] A. Rajaei, A. Vahidi-Moghaddam, A. Chizfahm and M. Sharifi, "Control of malaria outbreak using a non-linear robust strategy with adaptive gains," IET Control Theory & Applications, vol. 13, no. 14, pp. 2308-2317, 2019, doi: 10.1049/iet-cta.2018.5292.

[15] M. Sharifi and H. Moradi, "Nonlinear robust adaptive sliding mode control of influenza epidemic in the presence of uncertainty," Journal of Process Control, vol. 56, pp. 48-57, 2017, doi: 10.1016/j.jprocont.2017.05.010.

[16] M. Wan, M. Chen and M. Lungu, "Integral Backstepping Sliding Mode Control for Unmanned Autonomous Helicopters Based on Neural Networks," Drones , vol. 7, p. 154, 2023, doi: 10.3390/drones7030154.

[17] M. A. M. Basri, "Design and application of an adaptive backstepping sliding mode controller for a six-DOF quadrotor aerial robot," Robotica, vol. 36, no. 11, pp. 1701-1727, 2018, doi: 10.1017/S0263574718000668.

[18] H. Shen, J. Iorio and N. Li, "Sliding Mode Control in Backstepping Framework for a Class of Nonlinear Systems," journal of Marine Science and Engineering, vol. 7, no. 12, p. 452, 2019, doi: 10.3390/jmse7120452.

[19] N. Adhikary and C. Mahanta, "Integral backstepping sliding mode control for underactuated systems: Swing-up and stabilization of the Cart–Pendulum System," ISA Transactions, vol. 52, pp. 870-880, 2013, doi: 10.1016/j.isatra.2013.07.012.

[20] S.S. Yoon, J.K. Park and T.W. Yoon, "Dynamic anti-windup scheme for feedback linearizable nonlinear control systems with saturating inputs," Automatica, vol. 44, no. 12, pp. 3176-3180, 2008, doi: 10.1016/j.automatica.2008.10.003.

[21] H. Eliasi, "Design an anti-windup controller for a PWR power-level control in the," Annals of Nuclear Energy, vol. 132, pp. 415-426, 2019, doi: 10.1016/j.anucene.2019.04.040.

[22] W. Guo and D. Liu, "Adaptive second-order backstepping control for a class of 2DoF underactuated systems with input saturation and uncertain disturbances," Scientific Reports, vol. 14, p. 15840, 2024, doi: 10.1038/s41598-024-66552-6.

[23] Y. Zhao, X. Sun, G. Wang and Y. Fan, "Adaptive Backstepping Sliding Mode Tracking Control for Underactuated Unmanned Surface Vehicle With Disturbances and Input Saturation," IEEE Access, vol. 9, pp. 1304-1312, 2020, doi: 10.1109/ACCESS.2020.3046130.

[24] S. Neisarian, M. M. Arefi, A. Abooee and S. Yin, "Fast finite-time observer-based sliding mode controller design for a class of uncertain nonlinear systems with input saturation," Information Sciences, vol. 630, pp. 599-622, 2023, doi: 10.1016/j.ins.2023.02.051.

[25] M. De la Sen, A. Ibeas and S. Alonso-Quesada, "On vaccination controls for the SEIR epidemic model," Commun Nonlinear Sci Numer Simulat, vol. 17, pp. 2637-2658, 2012, doi: 10.1016/j.cnsns.2011.10.012.

[26] A. K. Jain and S. Bhasin, "Robust backstepping control of uncertain nonlinear systems with unknown time-varying input delay," IFAC-PapersOnLine, vol. 53, no. 2, pp. 4862-4867, 2020, doi: 10.1016/j.ifacol.2020.12.1043.

[27] Z. Chen, "Nussbaum functions in adaptive control with time-varying unknown," Automatica, vol. 102, pp. 72-79, 2019, doi: 10.1016/j.automatica.2018.12.035.

[28] Y. J. Liu and S. Tong, "Barrier Lyapunov functions for Nussbaum gain adaptive control of full state constrained nonlinear systems," Automatica, vol. 76, pp. 143-152, 2017, doi: 10.1016/j.automatica.2016.10.011.

[29] C. Wen, J. Zhou, .Z. Liu and H. Su, "Robust Adaptive Control of Uncertain Nonlinear Systems in the Presence

of Input Saturation and External Disturbance," IEEE Transactions on Automatic Control, vol. 56, pp. 1672-1678, 2011, doi: 10.1109/TAC.2011.2122730.

[30] A. Ibeas, M. de la Sen and S. Alonso-Quesada, "Robust Sliding Control of SEIR Epidemic Models," Mathematical Problems in Engineering, vol. 2014, p. 104764, 2014, doi: 10.1155/2014/104764.

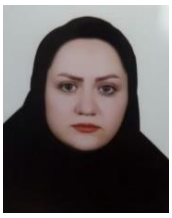

Fariba Nobakht was born in Mashhad, Iran, in 1982. She received the B.Sc. degree in electronic engineering from Semnan University, Semnan, Iran, in 2006 and the M.Sc. degree in control engineering from Islamic Azad University, Gonabad branch, Gonabad, Iran, in 2010. Now, she is an Instructor of Asrar Institute of Higher Education, Mashhad, Iran. Her research interests include Positive Nonlinear System, Constrained Systems, Stability Analysis and Robust Control.

Hussein Eliasi received the B.S. degree in electrical engineering from the Ferdowsi University of Mashhad (FUM), Iran, in 2001. He received the M.S. and the Ph.D. degrees from Amirkabir University of technology (Tehran), Iran, in 2005 and 2011, respectively. He is currently an assistance professor in faculty of electrical engineering at University of Birjand, Iran. His research interests include Constrained Nonlinear Dynamics Systems, Robust Control, Parameter Optimization of Model Predictive Control, Transient Stability in Power Systems and Load Following by Nuclear Power Plants.

IECO

This page intentionally left blank.

International Journal Of
Industrial Electronics Control and Optimization
Print ISSN: 3517-2645
Online ISSN: 3568-2645
Homepage: https://ieco.usb.ac.ir/

Sensorless Control of Direct-Current-Feed Doubly Fed Induction Generators Using T-Type Inverter

Hadi Afsharirad[1*] | Fahimeh Sadighi-Amandi[2] | Mohamad Reza Banaei[3] | Sara Misaghi[4]
Department of Electrical Engineering, Azarbaijan Shahid Madani University, Tabriz, Iran. [1,2,3,4]
Corresponding author's email: h.afsharirad@azaruniv.ac.ir

Article Info

Article type:
Research Article

Article history:
Received: 19-December-2024
Received in revised form: 09-March-2025
Accepted: 18-March-2025
Published online: 22-Dec-2025

Keywords:
DFIG-DC,
FOC,
Sensorless control,
T-type inverter.

ABSTRACT

The use of DFIG-DC systems without stator voltage and current sensors has gained attention due to reduced costs and simplified control. However, diode rectifiers in these systems introduce current harmonics, degrading power quality and limiting performance at higher power levels. This study proposes a new structure for DFIG-DC systems, replacing the conventional two-level inverter with a T-type converter to address these issues.The proposed system uses a T-type converter to enhance voltage levels, reducing current harmonics and improving power quality. It also eliminates stator voltage and current sensors, simplifying the control system and reducing costs. Performance analysis through MATLAB/Simulink simulations demonstrated the effectiveness of the proposed system compared to conventional methods.The proposed DFIG-DC system with a T-type converter offers a cost-effective and efficient solution for reducing current harmonics and improving power quality. Its simplified control system and enhanced performance make it a promising approach for high-power applications in wind energy systems and other industrial uses. These findings highlight the system's potential for improving reliability and operational efficiency in renewable energy and industrial applications.

NOMENCLATURE

DFIG	Doubly-Fed Induction Generators	*MMF*	magnetomotive force
MRF	Multiple Reference Frame	*THD*	Total Harmonic Distortion
NMCEC	Normalized Maximum Corr-Entropy Criterion	*SOGI*	Second Order Generalized Integrator
RSC	Rotor Side Converter	*FLL*	Frequency Locked Loop

I. Introduction

The use of DC transmission systems has gained significant attention in recent years. These systems are widely utilized as transmission lines interconnecting power networks [1]. Furthermore, DC networks eliminate certain power electronic converters, simplifying the network structure and facilitating the integration of renewable energy sources and storage systems while offering high efficiency and flexibility in power distribution [2].

One of the key features of doubly-fed induction generator (DFIG) is their ability to independently control active and reactive power, enabling variable-speed AC power generation using only rotor-side converter control. This characteristic has made DFIGs widely adopted in wind turbines [3].The output power of a DFIG can be regulated by controlling the rotor currents. Consequently, the rotor side of the generator is connected to the DC network through a controlled converter, while the AC output from the stator is transferred to the same DC network via a diode bridge this structure, known as DFIG-DC. This approach reduces costs and simplifies the system [4, 5] The main goals in this structures are to control the output power and the stator frequency, while DC link voltage regulation is managed through auxiliary control mechanisms [6]. Despite the numerous advantages of DFIG-DC systems, the presence of a diode rectifier introduces current harmonics in the stator windings. This results in distortions in the stator voltage and

flux waveforms, leading to increased torque ripple and reduced equipment lifespan [7].

Various studies have been conducted to mitigate these current harmonics and their adverse effects on DFIG systems. In reference [8] a new method for power angle control of DFIG-DC has been proposed. This method directly controls the output power without relying on current and voltage models. Additionally, an improved direct resonant controller is utilized in this study to reduce torque ripple and current harmonics. Reference [9] highlights that reducing current harmonics directly lowers torque ripple. It employs a resonant controller to minimize current harmonics, thereby reducing system losses. Resonant controllers have demonstrated excellent tracking capability for harmonic reference signals at a pre-designed resonant frequency. However, they are designed to target a specific harmonic frequency and do not account for frequency variations [10]. Moreover, resonant controllers have certain drawbacks, such as dependence on machine parameters, design complexity, and the requirement for positive and negative sequence control in unbalanced systems. Therefore, utilizing methods that not only reduce harmonics but also minimize computational burden in current and torque ripple calculations can significantly enhance the control system's performance [11,12].

Reference [10] proposes a method based on the multiple reference frame (MRF) approach to reduce torque ripple in DFIG-DC systems. It compensates for stator flux distortion caused by the diode rectifier by ensuring the rotor current tracks a pulsating reference signal. This method employs an estimator and regulator based on the MRF framework to accurately compute and track fundamental harmonics. The MRF-based controller provides a satisfactory dynamic response under unbalanced load conditions; however, its ability to eliminate harmonics is weak. Additionally, tuning this type of controller is challenging, involving complex mathematical computations and requiring a large amount of memory [13].

In Reference [14], a normalized maximum Corr-entropy criterion (NMCC) is utilized to reduce torque ripple and network power fluctuations in hybrid wind-solar systems. This approach eliminates the need for harmonic separation and compensates for distortions and voltage imbalances, resulting in distortion-free rotor currents and balanced, sinusoidal network currents. According to previous studies, this control method only reduces torque ripple; however, further research is needed to simultaneously improve stator current quality during unbalanced grid voltages [15].

One effective method for reducing harmonics is the use of multilevel converters. These converters help minimize the size of the output filter and reduce stress on switches, making them highly valuable in renewable energy systems [16].

Common types of multilevel inverters include T-type, diode-clamped, H-bridge, and flying capacitor inverters. Among these, the T-type inverter stands out due to its reduced circuit components, the requirement for only a single DC link for all phases, and other advantages. These features make it a practical choice for medium- and high-power applications. The unique design of T-type inverters makes them particularly useful in electric vehicles [17, 18]

Additionally, T-type inverters are widely used in applications such as uninterruptible power supplies (UPS) for critical infrastructure like data centers and hospitals. Despite their benefits, these power sources face challenges such as high total harmonic distortion (THD) and noise, which can impact local power quality. Multilevel inverters can effectively address these issues [19]. T-type inverters also significantly enhance motor performance by reducing the harmonic content of the voltage applied to motor terminals. Furthermore, the high dv/dt generated in power electronics-based inverters is a known cause of motor failure. Multilevel inverters mitigate this issue by reducing dv/dt, thereby preventing motor damage [20].

Therefore, multilevel inverters, particularly the T-type, offer significant advantages in various industries, renewable energy systems, electric vehicles, and electric propulsion for aircraft. They are also widely used in energy storage systems, energy conversion management in microgrids, and smart grid applications.

In this study, the focus is on employing a three-level T-type converter within a DFIG-DC system to address key challenges in power quality and control. The proposed approach highlights the advantages of integrating a T-type inverter, which effectively reduces stator current and voltage harmonics. This reduction leads to lower torque ripple, output power ripple, and harmonic losses, thereby enhancing overall system performance. Unlike conventional methods, this work emphasizes the novel application of the T-type converter in a DFIG-DC context, demonstrating its potential to improve the control system's efficiency and reliability.

The control strategy, based on rotor current vectors, eliminates the need for stator current and voltage sensors, simplifying the system structure and reducing costs. Although sensorless control methods have been explored in previous studies, the innovative aspect of this research lies in the synergistic integration of the T-type converter with advanced control techniques. This integration results in a more precise, cost-effective, and robust system.

In comparison to existing approaches, reference [21] highlights the use of a sensorless control method that involves modeling the system using a transformer between the stator and rectifier, considering 5th and 7th order voltage harmonics. The proposed scheme utilizes field-oriented control to enhance system performance. While the addition of a transformer improves stator voltage quality, it also increases costs and can lead to higher impedance in the circuit, potentially affecting overall system efficiency. This

increase in impedance needs careful analysis during the design and implementation phases.

Further, in reference [22] the stator winding voltages are calculated using the Second Order Generalized Integrator (SOGI) method, which is then used in a Frequency Locked Loop (FLL). Although this approach reduces costs, the high precision required for setting parameters like natural frequency can lead to issues in voltage estimation, disrupting the performance of the FLL block. Reference [23] explores a method based on rotor current vectors, eliminating the need for stator voltage and current models. This approach reduces system costs by removing sensors but does not fully address the effects of harmonics, which can impact the accuracy and stability of the control system.

To evaluate the effectiveness of the novel T-type inverter configuration, MATLAB/Simulink simulations were conducted, and the results were compared with conventional methods. The findings show significant improvements in power quality and control dynamics, emphasizing the suitability of the T-type inverter for advanced DFIG-DC systems.

II. Methodology

A. System Structure of DFIG-DC

The overall schematic of the DFIG-DC system is illustrated in Fig. 1. In this configuration, the rotor side is connected to the DC network via a rotor side converter (RSC), while the stator side is connected to the same DC network through a diode-based rectifier.

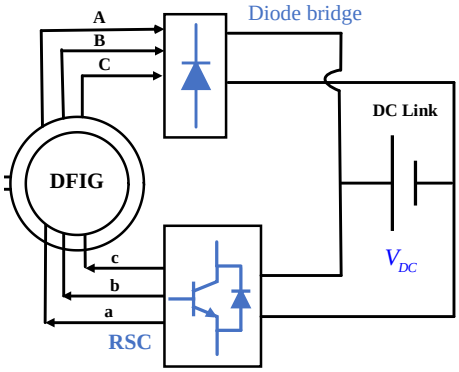

Fig. 1. Topology of a Conversion for a DFIG-DC System

The operational principle of a DFIG connected to a DC network involves two key processes: first, the excitation current is injected into the rotor windings via the RSC. Then, the power generated in the stator windings is transferred to the DC network through the stator-side rectifier.

In the DFIG system, the stator frequency is higher than the rotor frequency, and Fig.1 must be controlled in such a way that the MMF of the rotor windings is greater than that of the stator, as the control is performed from the rotor side. By adjusting the MMF, the generated torque can be effectively controlled.

Fig. 2 illustrates the equivalent circuit of the DFIG in the stator flux-oriented frame. In this figure; I_r and I_s represent the rotor and stator currents, respectively. V_r and V_s denote the rotor and stator voltages. $L_{\sigma r}$, $L_{\sigma s}$ and L_m refer to the leakage inductance of rotor and stator and mutual inductance. R_r and R_s indicate the rotor and stator resistances. ψ_s and ψ_r correspond to the stator and rotor flux, respectively. ω_r represents the angular frequency of the rotor winding voltages and currents, while ω_s represents the angular frequency of the stator winding voltages and currents.

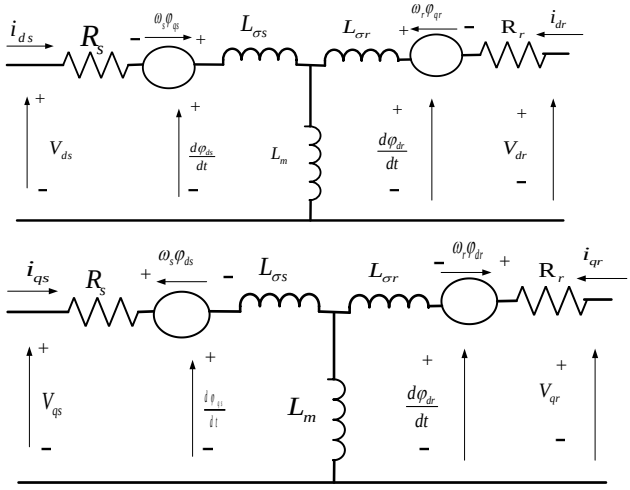

Fig. 2. Mathematical model of DFIG-DC

The stator and rotor voltage vector equations in the dq-axis, represented by Eq. 1 and Eq. 2, are derived from the equivalent circuit shown in Fig. 2. These equations can be expressed as follows:

$$\vec{V_s} = R_s \vec{i_s} + \frac{d\vec{\varphi_s}}{dt} + j\omega_s \vec{\varphi_s} \tag{1}$$

$$\vec{V_r} = R_r \vec{i_r} + \frac{d\vec{\varphi_r}}{dt} + j\omega_r \vec{\varphi_r} \tag{2}$$

The relationship between the flux and current vectors of the rotor and stator is expressed in Eq. 3 as follow.

$$\begin{cases} \vec{\varphi_s} = L_s \vec{i_s} + L_m \vec{i_r} \\ \vec{\varphi_r} = L_r \vec{i_r} + L_m \vec{i_s} \end{cases} \tag{3}$$

The torque equation can be defined using the stator flux and rotor current variables, as shown in Eq. 4.

$$Tem = \frac{3}{2} p \frac{L_m}{L_s} \mathrm{Im}\left\{\vec{\varphi_s}\vec{i}^{*}_{r}\right\} = \frac{3}{2} p \frac{L_m}{L_s}\left(\varphi_{sq} i_{rd} - \varphi_{sd} i_{rq}\right) \tag{4}$$

In this equation p represent as pole pair.

B. T-Type inverter

In the DFIG-DC system, one of the major challenges is the presence of voltage and current harmonics, which can disrupt the system's performance. These harmonics are primarily caused by the use of the diode rectifier, which introduces significant harmonic distortion.

One solution to reduce voltage and current harmonics is to use T-type inverters.In this approach, the focus is on rotor-side inverters. the T-type inverter have ability to produce multiple voltage levels, which improves harmonic performance and facilitates the generation of high-quality output waveforms with a lower total harmonic distortion (THD).

In the T-type inverter, pulse width modulation effectively prevents direct switching between the positive (P) and negative (N) terminals.

The T-type converter structure is shown in Fig. 3. In this converter, nine switches are used, with three of them being bidirectional switches. The central point of the three-level inverter on the left is connected to the node "n" Additionally, the voltage across the bidirectional switches is half of the output voltage, which helps to reduce voltage stress and improve the overall performance of the inverter.

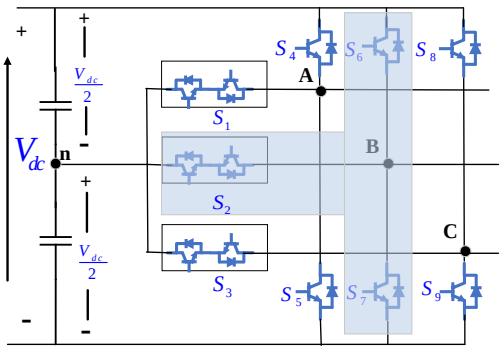

Fig. 3. Three phase three level T-Type inverter

Table 1 presents the switching states of the T-type converter for phase “A”. To prevent a short circuit in the converter's DC link, the switches within a single leg must not be switched on at the same time. In this configuration, if switch S1 is turned on the phase “A” output voltage is sested to zero. Activating switch S4 results in a phase “A” output voltage of $V_{dc}/2$, while turning on switch S5 sets the output voltage to $-V_{dc}/2$.

TABLE I SWITCHING MODES FOR PHASE A

Switching state	Phase voltage	S_1	S_4	S_5
Case 1	0	On	Off	Off
Case 2	$V_{dc}/2$	Off	On	Off
Case3	$-V_{dc}/2$	Off	Off	On

Table 2 provides an analysis of all voltage vectors and their corresponding switching states in the inverter. In the context of the three-phase system, there are 27 unique states, which are categorized into four main groups: zero states, small states, medium states, and large states.

TABLE 2 VOLTAGE VECTORS, SWITCHING STATES

State	On Switches	Voltage Vector
Zero vector	S_1,S_2,S_3	-
Zero vector	S_4,S_6,S_8	-
Zero vector	S_5,S_7,S_9	-
Small vector	S_1,S_7,S_9	$\overrightarrow{V_1}$
Small vector	S_4,S_2,S_3	$\overrightarrow{V_1}$
Small vector	S_4,S_6,S_3	$\overrightarrow{V_2}$
Small vector	S_1,S_2,S_9	$\overrightarrow{V_2}$
Small vector	S_1,S_6,S_3	$\overrightarrow{V_3}$
Small vector	S_5,S_2,S_9	$\overrightarrow{V_3}$
Small vector	S_1,S_6,S_8	$\overrightarrow{V_4}$
Small vector	S_5,S_2,S_3	$\overrightarrow{V_4}$
Small vector	S_1,S_2,S_8	$\overrightarrow{V_5}$
Small vector	S_5,S_7,S_3	$\overrightarrow{V_5}$
Small vector	S_4,S_2,S_8	$\overrightarrow{V_6}$
Small vector	S_1,S_7,S_3	$\overrightarrow{V_6}$
Medium vector	S_4,S_2,S_9	$\overrightarrow{V_7}$
Medium vector	S_1,S_6,S_9	$\overrightarrow{V_8}$
Medium vector	S_5,S_6,S_3	$\overrightarrow{V_9}$
Medium vector	S_5,S_2,S_8	$\overrightarrow{V_{10}}$
Medium vector	S_1,S_7,S_8	$\overrightarrow{V_{11}}$
Medium vector	S_4,S_7,S_3	$\overrightarrow{V_{12}}$
Large vector	S_4,S_7,S_9	$\overrightarrow{V_{13}}$
Large vector	S_4,S_6,S_9	$\overrightarrow{V_{14}}$
Large vector	S_5,S_6,S_9	$\overrightarrow{V_{15}}$
Large vector	S_5,S_6,S_8	$\overrightarrow{V_{16}}$
Large vector	S_5,S_7,S_8	$\overrightarrow{V_{17}}$
Large vector	S_4,S_7,S_8	$\overrightarrow{V_{18}}$

After excluding repetitive vectors, the T-type inverter features 21 unique independent vectors and it have 13 voltage vectors more than those in a conventional two-level inverter. This increase greatly reduces voltage harmonics, resulting in a corresponding decrease in current harmonics. The space vector diagram of the T-type inverter, shown in Fig. 4, is divided into 12 sectors. Each vector, excluding repetitive and zero vectors, corresponds to a specific switching state listed in Table 2.

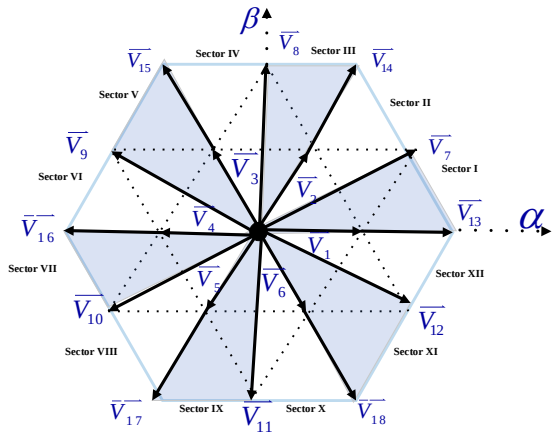

Fig. 4. T-Type inverter's voltage vectors' distribution in the αβ plane

During diode rectifier conduction, the steady-state equivalent circuit of the DFIG connected to the diode bridge is illustrated in Fig. 5. For simplified analysis, the rotor variables are referenced to the stator side, with the RSC and rotor modeled as an equivalent current source, I_r. In this representation, I_m is the magnetizing current, I_s is the stator current, v_g denotes the air-gap voltage, and v_s represents the stator voltage.

Using the equivalent circuit depicted in Fig. 5, the relationship between the stator and rotor currents can be mathematically expressed as shown in Eqs. 5. This equation establishes the connection between the two current components, offering insight into their interdependence within the system's operational framework.

$$I_r = I_s + I_m \tag{5}$$

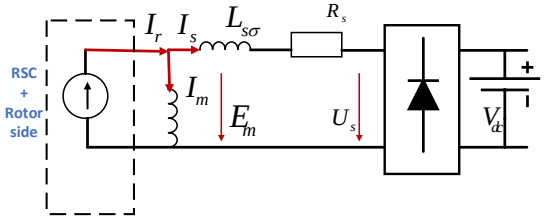

Fig. 5. Steady-State Equivalent Circuit of the DFIG-DC System

Given that the stator resistance is negligible compared to the stator leakage inductance, the air-gap voltage can be approximated and expressed as shown in Eq. 6.

$$E_m = j\omega_s L_m \mathrm{I}_m = U_s + j\omega_s L_{s\sigma} I_s \tag{6}$$

Because the diode bridge causes the stator voltage to be nearly in phase with the stator current, the rotor current can be derived using Eqs. 5 and 6. The resulting expression is presented in Eq. 7.

$$I_r = -j\frac{U_s}{L_m \omega_s} + \frac{L_s}{L_m} I_s \tag{7}$$

In Eq. 7, L_s represents the sum of the mutual inductance and the stator leakage inductance. Using this equation, the relationship between the stator current and the rotor current can be derived and expressed as shown in Eq. 8.

$$|I_r|\cos(\delta) = \frac{L_s}{L_m}|I_s| \;\rightarrow\; |I_s| = \frac{L_m}{L_s}|I_r|\cos(\delta) \tag{8}$$

The angle between the rotor current and the stator current is mathematically defined by Eq. 9. This equation captures the phase relationship between the two currents.

$$\delta = \arctan\left(\frac{|U_s|}{\omega_s L_s |I_s|}\right) \tag{9}$$

Using this angle, the stator power can be expressed as shown in Eq. 10. This equation incorporates the phase relationship between the rotor and stator currents to accurately represent the power dynamics in the system.

$$P_s = \frac{L_m}{L_s}|I_r||U_s|\cos(\delta) \tag{10}$$

From Eq. 10, it is clear that the stator active power can be effectively controlled using rotor current vector control. When the stator power is reduced to zero, the stator current also becomes zero, aligning the stator voltage with the air-gap voltage. In this condition, the stator voltage is 90 degrees out of phase with the rotor current. As the power output increases, the stator current rises, causing a reduction in the phase angle. This phase angle remains constrained within the range of 0 to 90 degrees, ensuring stable operation and predictable power dynamics.

In DFIG-DC systems, control of the system relies entirely on the RSC because the diode rectifier on the stator side is uncontrollable. The RSC plays a dual role: it manages the power transferred from the rotor and ensures that the generator operates at its nominal frequency, thereby maintaining optimal performance. This makes the RSC a critical component in the system's overall functionality.

Sensorless controllers offer a promising solution to simplify the system by eliminating the need for stator voltage and current sensors. By reducing computational complexity, these controllers enhance system performance and enable more precise control over the stator side. In sensorless control, the system is managed using the rotor current vector, which effectively governs the dynamics of the generator without direct stator-side measurements.

The control scheme for the T-type converter, designed to regulate stator power and frequency, is depicted in Fig. 6. In this configuration, the DC voltage V_{dc} and DC current I_{dc} on the stator side are sampled along with the rotor currents and rotor position to manage the rotor-side converter.

This control scheme has two primary components: stator active power control and stator frequency control, both implemented through rotor current vector control. The stator frequency control block generates a slip angle, which is utilized for Park and Clarke transformations to transition between reference frames. Meanwhile, the active power control block ensures proper regulation of stator active

power by adjusting the rotor current vector, facilitating precise and stable operation of the DFIG-DC system.

In steady state, the stator frequency matches the rotational speed of the rotor current vector in the dq reference frame, which is directly determined by the rotor speed. By using the rotor angle and the synchronous dq frame angle, the slip angle can be calculated as shown in Eq. 11.

$$\theta_{slip} = \frac{1}{s}\omega_s - \theta_r \tag{11}$$

The stator power can be represented in terms of the DC voltage V_{dc} and DC current I_{dc} measured on the stator side, as expressed in Eq. 12.

$$P_s = V_{dc} I_{dc} \tag{12}$$

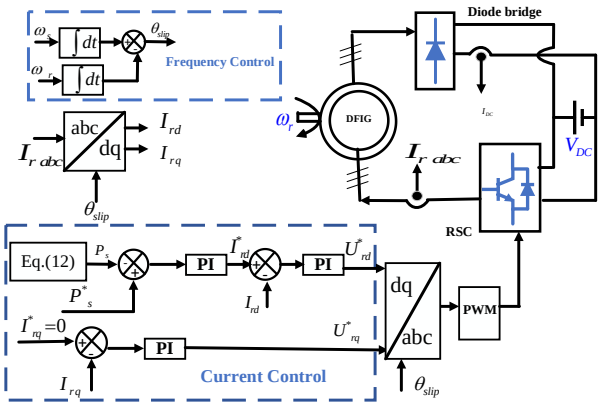

Fig. 6. Overall Control Scheme

The stator power is directly influenced by the rotor current, allowing it to be regulated through the magnitude of the rotor current. For maximum output power, the q-axis component of the rotor current should be controlled to zero, ensuring efficient power transfer. This relationship iss formalized in Eq. 13, which outlines the method for controlling the stator active power via the rotor current.

$$I^*_{rd} = \frac{k_{pp}s + k_{ip}}{s}(P^*_s - P_s) \tag{13}$$

When the q-axis current is set to zero, the rotor current simplifies to equal the d-axis current. In this control framework, K_p represents the proportional gain, and K_i denotes the integral gain of the feedback controller.

The proportional and integral gains of the inner current control loop are selected based on the system's bandwidth requirements. The bandwidth of the outer power control loop is designed to be one-tenth of the inner loop's bandwidth. These choices ensure proper dynamic response and stability in both control loops.

Variations in controller parameters, such as K_p and K_i, can significantly impact the system's response, particularly in terms of harmonic content and overall system stability. The tuning of these parameters directly affects system damping and the magnitude of its response to external disturbances. Therefore, precise adjustment of these parameters is crucial to achieving the desired power quality and control stability. For instance, in the rotor current control loop, the selection of K_p and K_i is made to achieve an appropriate open-loop bandwidth for rotor current, which is essential for maintaining system performance under varying operating conditions.

The controller design strategy aims to balance fast dynamic response and system stability. Specifically, the rotor current control loop is designed to respond faster than the power control loop, and its controller parameters are tuned to ensure that the open-loop transfer function achieves crossover at the desired frequency with an appropriate phase margin.

Using K_p =5.3 and K_i =500, the system's pole map has been plotted in fig.7. According to the transfer function of power loop shown in Eq.14 the results indicate that as the power varies from zero to one per-unit, the power control loop remains stable at all times [24].

$$\frac{\Delta P_s}{\Delta P^*_s} = \frac{\frac{(sk_p + k_i)}{s}\frac{L_m u_s}{L_s}\cos\varepsilon_0}{1-(\sin^2\varepsilon_0 - \frac{(sk_p+k_i)L_m u_s}{sL_s}\cos\varepsilon_0)} = \frac{\frac{(sk_p+k_i)}{s}\frac{L_m u_s}{L_s}/\cos\varepsilon_0}{s + \frac{(sk_p+k_i)L_m u_s}{L_s}/\cos\varepsilon_0} \tag{14}$$

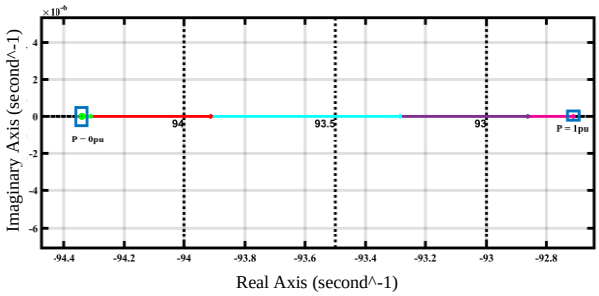

Fig. 7. Pole map of power control loop

III. TEST RESULTS

To assess the effectiveness of the proposed control strategy, simulations were conducted using the MATLAB/Simulink environment. The simulations were conducted on a system with an Intel Core i7 processor, 16 GB RAM, and MATLAB/Simulink R2021b. The average simulation time varied depending on the complexity of the model, with the proposed method requiring approximately 2% more computation time than conventional approaches due to the increased number of switching states and control calculations. However, the computational load remains manageable for real-time implementation with appropriate hardware.

The system's rotational speed is driven by a squirrel-cage induction motor mechanically coupled to the induction generator. The DC grid is modeled as a constant voltage source connected to a resistive load, simulating a realistic DC network. The specifications of the power supply and

squirrel cage induction motor match the specifications of the DFIG given in Table 3.

TABLE II Parameters of the DFIG

Parameters	Symbols	Value
Rated power	I_r	1000 W
Rated frequency	f_n	50 Hz
Rated voltage	V_n	110 V
Rotor resistance	R_r	0.88 Ω
Stator resistance	R_s	1.01 Ω
Mutual inductance	L_m	8.87 mH
DC voltage	V_{dc}	140 V
Stator leakage inductance	$L_{s\sigma}$	5.6 mH
Rotor leakage inductance	$L_{r\sigma}$	5.6 mH

This setup provides a robust framework for analyzing the performance improvements achieved by the proposed control strategy.

Fig. 8 illustrates the system's behavior in two stages. In the first stage, from t=0 s to t=1.5 s, a reference power of 200 is set, and the active power of the stator closely follows this reference value in both methods.

At t=1.5t s, the reference power is increased to 500. During this second stage, the active power of the stator reaches the desired value within 250 milliseconds without any steady-state error, as shown in Fig. 8(a). The proposed method achieves this with minimal fluctuations, and, compared to the conventional method shown in Fig. 8(b), the power ripple is significantly reduced.

Fig.9 shows the phase-to-phase rotor voltage. As can be seen, the output voltage of the T-type inverter has 5 levels, while the output voltage of the two-level inverter has 3 levels. The voltage range is the same for both methods. If the voltage levels are increased, the voltage harmonics are reduced because the waveform becomes closer to a sinusoidal shape due to the larger number of smaller voltage steps. Since the rotor voltage is positively correlated with the rotor current, the rotor current is also closer to an ideal sinusoid and the harmonics are reduced, and according to equation 8, the stator current is also improved, thereby reducing the harmonics of the entire system.

Reducing the harmonics of the rotor current directly affects the electromagnetic torque and reduces it, resulting in an overall improvement in the system. In addition, increasing the number of voltage levels increases the regulation of the MMF in the rotor, which is very important for maintaining optimal performance and controlling the power flow in the stator and rotor windings. Therefore, higher voltage levels contribute to a more stable system with less harmonic distortion.

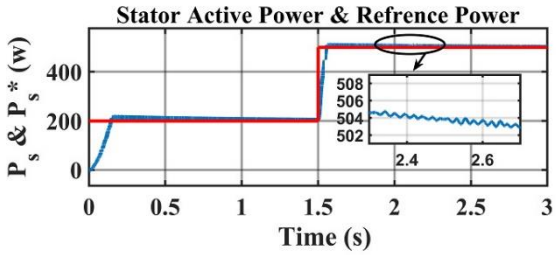

(a)

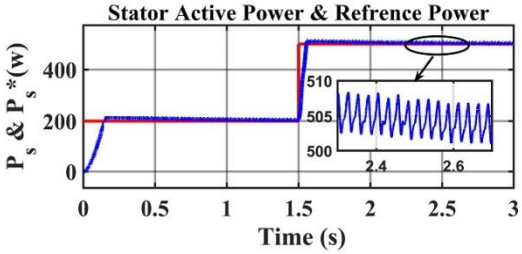

(b)

Fig. 8. The waveform of the stator active power and reference power. (a) Proposed Method (b) Conventional Method.

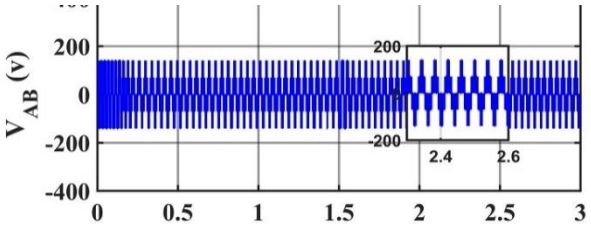

(a)

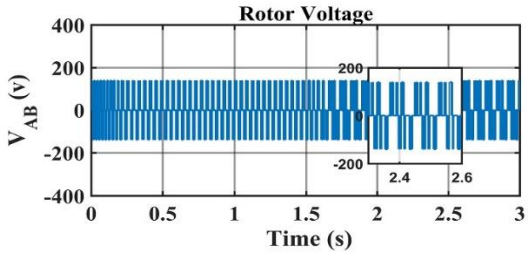

(b)

Fig. 9. Rotor Voltage Waveform (a) Proposed Method (b) Conventional Method

Fig. 10 shows the phase-to-phase stator voltage of the DFIG. As seen, the voltage amplitude is the same in both methods, but the voltage waveform in the proposed method is not only more desirable but also significantly has fewer harmonics compared to the conventional method. This reduction in harmonics contributes to improved power quality and optimized system performance.

Fig. 11 shows the torque behavior in both transient and steady-state conditions for both methods. A transient state occurs when the reference power changes from 200 to 500 at t=1.5 s. The figure clearly demonstrates that the proposed method leads to reduced torque ripple in the steady-state, with the torque value reaching 1 N.m. In contrast, the

conventional method results in a steady-state torque value of 10 N·m.

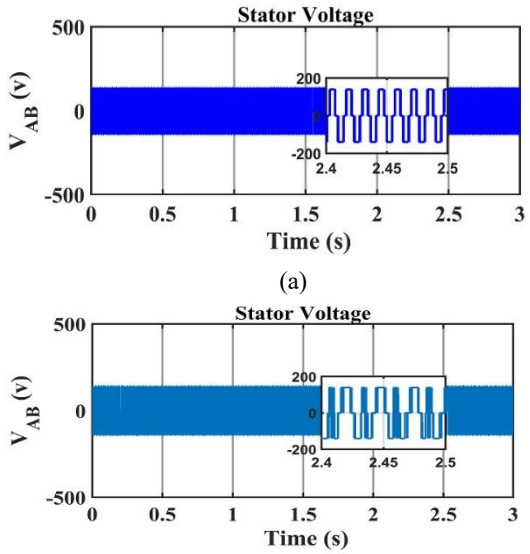

Fig. 10. Stator Voltage Waveform (a) Proposed Method (b) Conventional Method

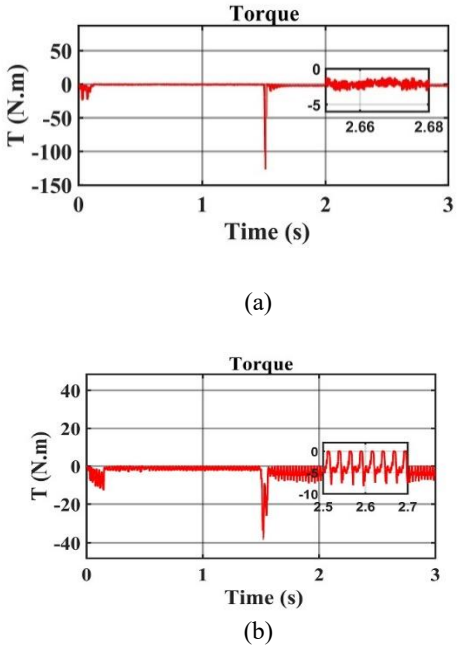

Fig. 11. Torque Waveform. (a) Proposed Method (b) Conventional Method

Fig. 12 and 13 illustrate the flux waveforms of the stator and rotor in the dq reference frame. The results from t = 2.4 s to t = 2.5 s indicate that the proposed method significantly reduces harmonics, leading to flux components in this reference frame exhibiting fewer variations and approaching nearly constant values. This demonstrates the optimal performance of the proposed control method in improving flux quality, highlighting its capability to reduce fluctuations and enhance system stability.

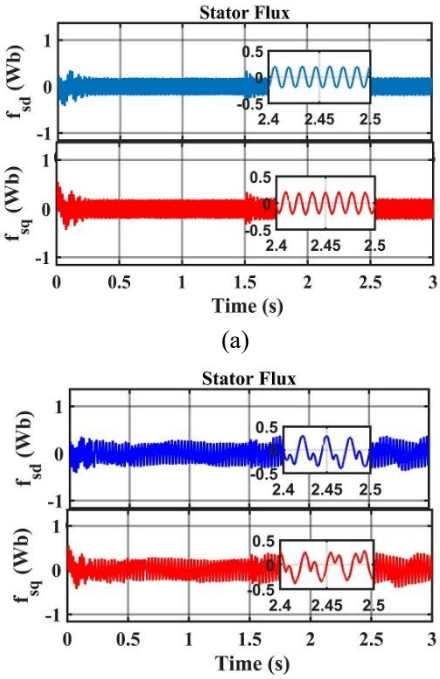

Fig. 12. Stator Flux Waveform (a) Proposed Method (b) Conventional Method

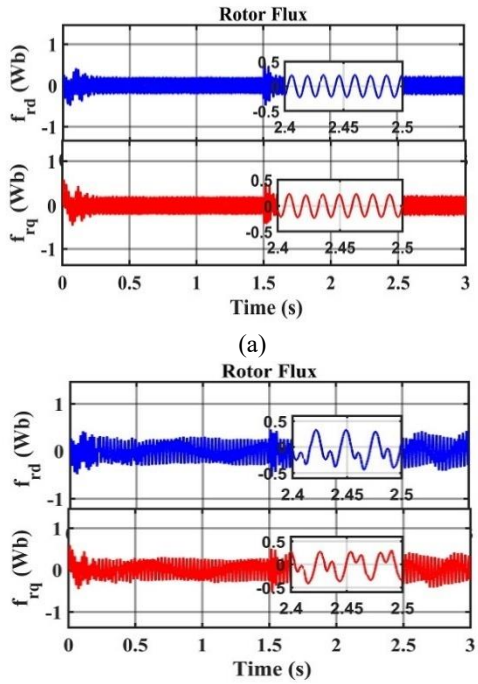

Fig. 13. Rotor Flux Waveform(a) Proposed Method (b) Conventional Method

The response to the step change in reference power for the stator and rotor currents for both control methods is shown in Fig. 14 and 15, respectively. By comparing the steady-state changes in Fig. 14 from t=2.45 s to t=2.49 s, it is observed that the proposed method significantly reduces the harmonics of the stator currents, and the waveform is much

closer to an ideal sine wave. Similarly, this comparison in the steady-state for the rotor current waveforms is clearly evident in Fig. 15. The results indicate that by using the T-type inverter, three-phase currents for both the rotor and stator can be achieved with better quality.

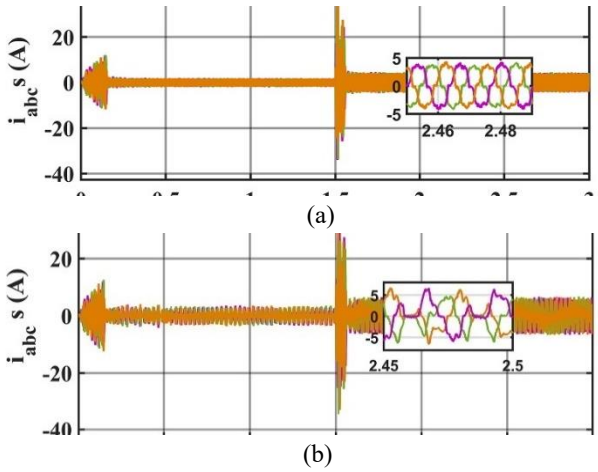

Fig. 14. Stator Current Waveform (a) Proposed Method (b) Conventional Method

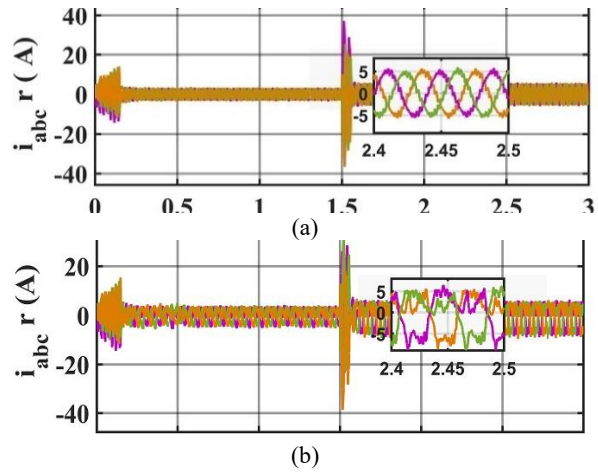

Fig. 15. Rotor Current Waveform (a) Proposed Method (b) Conventional Method

These results demonstrate the effectiveness of the proposed method in improving power quality and reducing harmonics. Fig. 16 shows the FFT analysis of rotor current harmonics in the steady-state, where the harmonic content for the conventional method is 52.26%, and for the proposed method, it is 13.09%. Additionally, Fig. 17 illustrates the FFT analysis of stator current harmonics in the steady-state, which is 51.76% for the conventional method and 14.43% for the proposed method.

Reducing harmonics can significantly enhance system performance, and the T-type inverter plays a crucial role in achieving this by offering advantages such as reduced distortion and improved sinusoidal voltage generation with fewer components. However, despite these benefits, the T-type inverter also introduces certain challenges. Compared to a conventional two-level inverter, it requires a more complex circuit topology due to the increased number of switches, making the switching process more challenging. Nonetheless, its ability to minimize harmonics and improve overall efficiency makes it a valuable choice in power electronics applications.

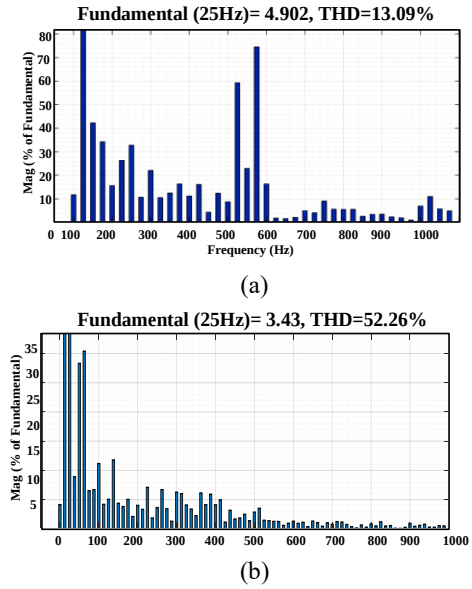

Fig. 16. FFT Analysis of Rotor Current (a) Proposed Method (b) Conventional Method

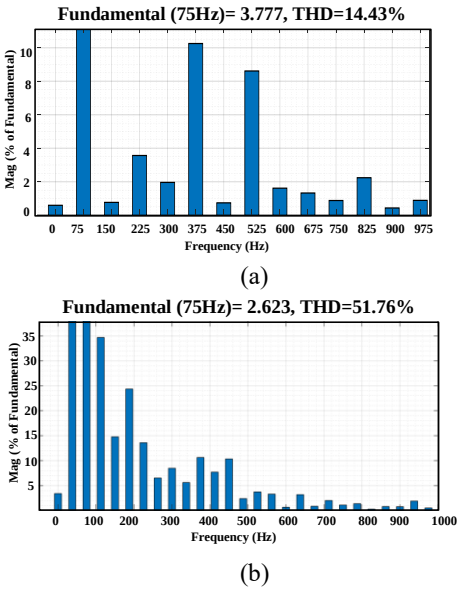

Fig. 17. FFT Analysis of Stator Current (a) Proposed Method (b) Conventional Method

IV. Conclusion

In this study, a novel approach for controlling a DFIG-DC system has been introduced through the integration of a three-level T-type inverter, leading to significant improvements in power quality and control performance.

Unlike conventional methods, which primarily focus on mitigating characteristic harmonics of the form 6n±1, the

proposed approach has been designed to effectively reduce lower-order harmonics such as the 5th and 7th without requiring additional complex control strategies. This improvement has been achieved while maintaining a relatively simple control structure, minimizing mathematical complexity, and ensuring practical feasibility.

A key advantage of the proposed method is the elimination of stator voltage and current sensors, which has simplified the control system, reduced costs, and enhanced system reliability. Instead, a current-oriented control strategy has been employed to regulate stator frequency and DFIG-DC power. Although a slight increase in complexity on the power system side has been observed, a substantial reduction in current harmonics, torque ripple, and power ripple has been demonstrated, resulting in superior output performance.

Compared to the closest existing methods, which often rely on resonant or advanced controllers for harmonic suppression, better harmonic reduction has been achieved by utilizing the advanced capabilities of the T-type inverter while maintaining a more straightforward control framework. The effectiveness of this method has been validated through MATLAB/Simulink simulations, where improved dynamic response and harmonic suppression have been observed in comparison to traditional two-level inverters.

These findings provide new insights into improving power quality in DFIG-DC systems, and it is expected that the proposed method will serve as a viable and implementable solution for wind energy applications. By setting a new benchmark in renewable energy systems, this work is anticipated to contribute to future research on optimizing multi-level inverter-based control strategies for grid-connected and stand-alone wind power systems.

References

[1] S. M. A. Cruz, G. D. Marques, P. F. C. Gonçalves and M. F. Iacchetti, "Predictive Torque and Rotor Flux Control of a DFIG-DC System for Torque Ripple Compensation and Loss Minimization," in IEEE Transactions on Industrial Electronics, vol. 65, no. 12, pp. 9301-9310, Dec. 2018, doi: 10.1109/TIE.2018.2818667.

[2] R. Zhang et al., "Protection and Power Smoothing of a DFIG/DC Microgrid Hybrid Power System With SMES-Based Unified Power Quality Conditioner," in IEEE Transactions on Applied Superconductivity, vol. 34, no. 8, pp. 1-5, Nov. 2024, Art no. 5401005, doi: 10.1109/TASC.2024.3425322.

[3] G. D. Marques and M. F. Iacchetti, "Minimization of Torque Ripple in the DFIG-DC System Via Predictive Delay Compensation," in IEEE Transactions on Industrial Electronics, vol. 65, no. 1, pp. 103-113, Jan. 2018, doi: 10.1109/TIE.2017.2716860.

[4] C. Wu, P. Cheng, H. Nian and F. Blaabjerg, "Rotor Current Oriented Control Method of DFIG-DC System Without Stator Side Sensors," in IEEE Transactions on Industrial Electronics, vol. 67, no. 11, pp. 9958-9962, Nov. 2020, doi: 10.1109/TIE.2019.2956415.

[5] A. Verma and A. K. Jain, "A Dual-VSI DFIG-Dc Voltage Generation System Based on Series Connected Dc-Link," in IEEE Transactions on Industrial Electronics, vol. 71, no. 11, pp. 13670-13681, Nov. 2024, doi: 10.1109/TIE.2024.3363760.

[6] C. Wu, D. Zhou and F. Blaabjerg, "Direct Power Magnitude Control of DFIG-DC System Without Orientation Control," in IEEE Transactions on Industrial Electronics, vol. 68, no. 2, pp. 1365-1373, Feb. 2021, doi: 10.1109/TIE.2020.2970666.

[7] C. Wu and H. Nian, "Sinusoidal Current Operation of a DFIG-DC System Without Stator Voltage Sensors," in IEEE Transactions on Industrial Electronics, vol. 65, no. 8, pp. 6250-6258, Aug. 2018, doi: 10.1109/TIE.2017.2786259.

[8] C. Wu, D. Zhou, P. Cheng and F. Blaabjerg, "A Novel Power-Angle Control Method of DFIG-DC System Based on Regulating Air Gap Flux Vector," in IEEE Transactions on Power Electronics, vol. 36, no. 1, pp. 513-521, Jan. 2021, doi: 10.1109/TPEL.2020.3001967.

[9] C. Wu and H. Nian, "Improved Direct Resonant Control for Suppressing Torque Ripple and Reducing Harmonic Current Losses of DFIG-DC System," in IEEE Transactions on Power Electronics, vol. 34, no. 9, pp. 8739-8748, Sept. 2019, doi: 10.1109/TPEL.2018.2888599.

[10] Y. Xiao, B. Fahimi, M. A. Rotea and Y. Li, "Multiple Reference Frame-Based Torque Ripple Reduction in DFIG-DC System," in IEEE Transactions on Power Electronics, vol. 35, no. 5, pp. 4971-4983, May 2020, doi: 10.1109/TPEL.2019.2941957.

[11] X. Wang, D. Sun and Z. Q. Zhu, "Resonant-Based Backstepping Direct Power Control Strategy for DFIG Under Both Balanced and Unbalanced Grid Conditions," in IEEE Transactions on Industry Applications, vol. 53, no. 5, pp. 4821-4830, Sept.-Oct. 2017, doi: 10.1109/TIA.2017.2700280.

[12] G. D. Marques and M. F. Iacchetti, "DFIG Topologies for DC Networks: A Review on Control and Design Features," in IEEE Transactions on Power Electronics, vol. 34, no. 2, pp. 1299-1316, Feb. 2019, doi: 10.1109/TPEL.2018.2829546.

[13] S. Bhattacharyya, S. Puchalapalli and B. Singh, "Operation of Grid-Connected PV-Battery-Wind Driven DFIG Based System," in IEEE Transactions on Industry Applications, vol. 58, no. 5, pp. 6448-6458, Sept.-Oct. 2022, doi: 10.1109/TIA.2022.3181124.

[14] S. Das and B. Singh, "Normalized Maximum Correntropy Criterion Based Ripple Mitigation Strategy for Wind–Solar Hybrid Generation System Under Nonideal Grid Conditions," in IEEE Transactions on Power Electronics, vol. 38, no. 1, pp. 956-967, Jan. 2023, doi: 10.1109/TPEL.2022.3199387

[15] S. Das and B. Singh, "Islanding Operation and Seamless Resynchronization in DFIG–SPV System Equipped With Functional Enhancements Through ATLLAD Control Framework," in IEEE Transactions on Power Electronics, vol. 38, no. 6, pp. 7634-7643, June 2023, doi: 10.1109/TPEL.2023.3259443.

[16] M. Lak, B. -R. Chuang and T. -L. Lee, "A Common-Mode Voltage Elimination Method With Active Neutral Point Voltage Balancing Control for Three-Level T-Type Inverter," in IEEE Transactions on Industry Applications, vol. 58, no. 6, pp. 7499-7514, Nov.-Dec. 2022, doi: 10.1109/TIA.2022.3201175.

[17] A. Sheir, M. Z. Youssef and M. Orabi, "A Novel Bidirectional T-Type Multilevel Inverter for Electric Vehicle Applications," in IEEE Transactions on Power

Electronics, vol. 34, no. 7, pp. 6648-6658, July 2019, doi: 10.1109/TPEL.2018.2871624.
[18] Kenneth E. Okedu, "Augmenting DFIG wind turbine transient performance using alternative voltage source T-type grid side converter, "Renewable Energy Focus, vol.18,2017,Pages 1-10,ISSN 1755-0084,https://doi.org/10.1016/j.ref.2017.02.004.
[19] Sánchez Vargas, Oscar, Luis Gerardo Vela Valdés, Monica Borunda, Ricardo Eliú Lozoya-Ponce, Jesus Aguayo Alquicira, and Susana Estefany De León Aldaco. 2024. "ANFIS-PSO-Based Optimization for THD Reduction in Cascaded Multilevel Inverter UPS Systems" Electronics 13, no. 22: 4456.
[20] Y. El. Khlifi, A. El. Magri, A. Mansouri, R. Lajouad, " Enhanced low voltage ride-through control of multilevel flying capacitor inverter based wind generation," Indonesian Journal of Electrical Engineering and Computer Science, vol.33,no.6, pp.: 854-861,Feb. 2024. DOI:10.11591/ijeecs.v33.i2.pp854-861.
[21] H. Misra and A. K. Jain, "Analysis of Stand-Alone DFIG-DC System and DC Voltage Regulation With Reduced Sensors," in IEEE Transactions on Industrial Electronics, vol. 64, no. 6, pp. 4402-4412, June 2017, doi: 10.1109/TIE.2017.
[22] C. Wu, H. Nian, B. Pang and P. Cheng, "Adaptive Repetitive Control of DFIG-DC System Considering Stator Frequency Variation," in IEEE Transactions on Power Electronics, vol. 34, no. 4, pp. 3302-3312, Apr. 2019, doi: 10.1109/TPEL.2018.2854261.
[23] C. Wu, Y. Jiao, H. Nian and F. Blaabjerg, "A Simplified Stator Frequency and Power Control Method of DFIG-DC System Without Stator Voltage and Current Sensors," in IEEE Transactions on Power Electronics, vol. 35, no. 6, pp. 5562-5566, June 2020, doi: 10.1109/TPEL.2019.2953677.
[24] D.Zhou, F. Blaabjerg,, "Bandwidth oriented proportional-integral controller design for back-to-back power converters in DFIG wind turbine system, " IET Renewable Generation, Vol.11, no.7, pp. 941-951, June. 2017, doi:org/10.1049/iet-rpg.2016.0760.

Hadi Afsharirad was born in Abhar, Iran, in 1985. He received the B.Sc. degree from the Zanjan University, Iran and M.Sc. and Ph.D. degrees, from the University of Tabriz, Tabriz, Iran, in 2008, 2010, and 2018, respectively, all in electrical engineering. He is an Assistant Professor with the Department of Electrical Engineering, Azarbaijan Shahid Madani University, Tabriz, which he joined in 2020. His main research interests include the electric and hybrid electric vehicles, renewable energy, linear electric machines and electrical drives.

Fahimeh Sadighi-Amandi was born in Tabriz, Iran, in 1997. she received the B.Sc degree from the Payame Noor University of Tabriz and M.Sc degree from the Azarbaijan Shahid Madani University, Tabriz, Iran in 2021, 2024 respectively. Her main research interests include electric machines, renewable energy and electrical drives.

Mohamad Reza Banaei was born in Tabriz, Iran. He received the M.Sc. degree in control engineering from the Polytechnic University of Tehran, Tehran, Iran, in 1999, and the Ph.D. degree in power engineering from the Faculty of Electrical Engineering, Tabriz University, Tabriz, in 2005. He is currently a Professor with the Department of Electrical Engineering, Azarbaijan Shahid Madani University, Tabriz, where he joined in 2005. His main research interests include the designing and controlling of power electronic converters, renewable energy systems, modeling and controlling of FACTS and custom power devices, and power systems dynamics.

Sara Misaghi was born in Iran, in 1997. she received the B.Sc. & M.Sc. degree from the Azarbaijan Shahid Madani University, Tabriz, Iran in 2018, 2024. she is a Phd. student of Azarbaijan Shahid Madani University. Her main research interests include electric machines and electrical drives.

IECO

This page intentionally left blank.

International Journal Of
Industrial Electronics Control and Optimization
Print ISSN: 3517-2645
Online ISSN: 3568-2645
Homepage: https://ieco.usb.ac.ir/

Design Optimization and Thermal Analysis of a Dual Three-Phase PM Motor for Electric Vehicles

Javad Rahmani-Fard

Department of Electrical and Computer Engineering, Qom University of Technology, Qom, Iran
Corresponding author's email: rahmanifard@qut.ac.ir

Article Info

Article type:
Research Article

Article history:
Received: 2025-03-14
Received in revised form: 2025-04-16
Accepted: 2025-04-22
Published online: 22-Dec-2025

Keywords:
Thermal Analysis,
Dual three-phase machine,
Optimal design,
PM machine.

ABSTRACT

This paper presents a comprehensive investigation into the design principles and operational characteristics of dual three-phase permanent magnet (PM) machines. The study focuses on optimizing the winding arrangement and slot-pole combinations for enhanced performance and reliability. Through detailed analysis, an optimal configuration is proposed, and a dual three-phase machine based on this design is developed. The operational behavior of the machine is thoroughly examined under healthy conditions, with particular attention given to its thermal performance to ensure it can sustain high power density and output power without compromising reliability. The effectiveness of the proposed design and thermal analysis is validated through advanced simulation results, which demonstrate the motor's robust performance, efficiency, and ability to maintain stable operation under demanding conditions. Under natural cooling, the dual three-phase motor operates safely within its thermal limits, with a maximum winding temperature of 139.99℃, below the 180℃ insulation limit, and a maximum magnet temperature of 105.62℃, below the 150℃ limit. This research highlights the potential of dual three-phase PM machines for applications requiring high reliability and performance.

I. Introduction

With the increasing emphasis on environmental sustainability, developing clean transportation has become a global priority. Electric vehicles (EVs) stand out due to their high efficiency, low noise, and zero emissions [1]. Advancements in EV technology are closely tied to improvements in power system performance, enhancing reliability and reducing costs [2].

A critical aspect of EV powertrains is the reliability of electric drive systems. Traditional three-phase motors are vulnerable to faults, which can reduce torque, cause vibrations, and compromise safety [3]. To address these challenges, modern motor designs prioritize fault tolerance, allowing continued operation under fault conditions to ensure passenger safety [4].

This paper analyzes a dual three-phase permanent magnet motor with integrated fault detection. This system identifies faults and applies control strategies to maintain torque output, ensuring safe EV operation [5,6]. Dual three-phase motors offer benefits such as low torque ripple, high torque density, and compatibility with standard inverters [7].

Key advantages of dual three-phase motors include [6]:

- High Fault Tolerance: Continued operation even with winding failures.
- Simplified Fault Control: Low harmonic content and minimal unbalanced magnetic pull.
- Enhanced Fault Performance: Ability to handle additional loads and maintain output under fault conditions.

Since the introduction of fractional-slot concentrated winding motors in 1996, fault-tolerant multi-phase motors have seen increasing use in critical applications [1,2]. Research has focused on optimizing pole and slot numbers, refining winding configurations, and reducing losses while improving fault tolerance [8-11].

Innovations in materials, such as Soft Magnetic Composites (SMC), have enabled modular motor construction, reducing costs and improving flexibility [12]. More recently, dual-rotor permanent magnet machines have been explored for their improved fault-tolerant control capabilities, optimized torque, and efficiency [13-15].

Recent advancements over the past years in dual three-phase permanent magnet (PM) machines have concentrated on fault tolerance, thermal management, and control strategies.

In the area of fault-tolerant control and winding optimization, Huang et al. [13] proposed a triple-redundancy control strategy for dual three-phase PM motors that maintained 85% of rated torque under single-phase open faults, ensuring continuous operation. While effective in maintaining performance during faults, this approach increases inverter complexity and computational load for real-time fault detection. Similarly, Zhou et al. [4] introduced an MMF reconstruction method to suppress vibrations and reduce torque ripple by 40% during open-phase faults through harmonic cancellation. However, their method relies heavily on accurate motor parameter identification, making it sensitive to parameter variations. Moreover, Yoshida and Akatsu [12] analyzed winding structures and showed that a 30° phase shift in winding reduces current total harmonic distortion (THD) by 15%, thus improving efficiency. This improvement is limited by a trade-off between harmonic suppression and torque density, restricting applications in high-power motors.

Regarding thermal and efficiency improvements, Wang et al. [8] designed an aviation-grade dual three-phase PM motor with integrated liquid cooling, which kept winding temperatures under 130°C at 20 kW, enabling high power density. However, integrating the liquid cooling system increased weight and system complexity. Tang and Sha [15] developed a biplane virtual voltage vector for model predictive control (MPC) in flux-weakening operations, improving efficiency by 3% at high speeds. Nonetheless, this approach is susceptible to permanent magnet demagnetization at elevated temperatures.

In sensorless and high-speed applications, Liu et al. [2] proposed a position-error correction method for sensorless dual three-phase PMSMs, achieving position errors below 1° at medium speeds without encoders. However, performance declines at speeds under 10% of rated speed due to low back-EMF signals. Azadrou [16] optimized a high-speed bearingless induction motor with a multi-cage rotor for compressors, achieving 15,000 rpm with minimal magnetic interference suitable for oil-free applications. The trade-offs include complex rotor fabrication and increased iron losses at ultra-high speeds.

For control strategies in mono-inverter dual-parallel (MIDP) systems, Fadaie et al. [17] introduced a simplified MPC approach that reduces computation time by 45% compared to traditional FCS-MPC and achieves minimal torque ripple. However, this method depends on accurate load torque estimation for optimal performance.

While previous studies have enhanced fault tolerance and efficiency, few have addressed combined electromagnetic-thermal optimization for high power-density electric vehicle motors. This paper fills that gap by proposing a 24-slot/22-pole design with optimized winding and pole arc geometry, validating thermal safety with winding temperatures of 139.99°C and PM temperatures of 105.62°C under natural cooling. The design achieves 94% efficiency and low torque ripple of 2.1% without requiring complex cooling systems.

This paper builds on these advancements, offering a detailed analysis of dual three-phase permanent magnet motors for EV applications. By enhancing fault tolerance, thermal performance, and efficiency, this research contributes to the development of more reliable and sustainable electric drive systems.

II. Analysis of MMF in Multi-Phase Motor Windings

Ideally, multi-phase motors with symmetrical windings and currents create a circular rotating magnetic field. However, real-world factors like slot effects and inverter nonlinearities (dead-time) introduce spatial and time harmonics. These harmonics interact, creating spatiotemporal harmonic MMFs that negatively impact motor performance (torque, noise, vibration). Therefore, analyzing these harmonic MMFs is crucial for understanding multi-phase motor behavior, considering both symmetrical and asymmetrical winding configurations.

A. MMF of Symmetrical Multi-Phase Windings

According to the theory of AC motor winding functions, the MMF can be expressed as the product of the winding function and the current. The MMF of the *m*-th phase of a symmetrical n -phase motor is:

$$F_m(\varphi,t) = n_m(\varphi) i_m(t) \tag{1}$$

For concentrated full-pitch windings, as shown in Figure 1(a), the Fourier series representation of the winding function is:

$$n_m(\varphi) = \sum_{v=1}^{\infty} N_v \cos\left[v\left(\varphi - \frac{m-1}{n}2\pi\right)\right] \tag{2}$$

where N_v is the amplitude of the v -th harmonic winding, and $N_v = 2Nk_w k_{pv}\sin(v\pi/2)/(v\pi)$ for $v = 1,3,5,\ldots$.

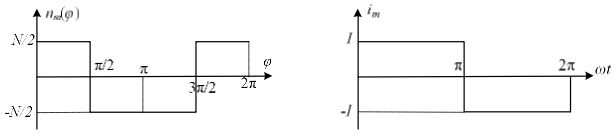

(a) (b)

Fig. 1. Winding function and phase current. (a) Winding function (b) phase current

The stator winding current is a 180° square wave, as shown in Figure 1(b). The *m*-th phase current can be expressed using the Fourier series as:

$$i_m(t) = \sum_{\mu=1}^{\infty} I_\mu \sin\left[\mu\left(\omega t - \frac{m-1}{n}2\pi\right)\right] \tag{3}$$

where ω is the angular frequency of the fundamental current, I_μ is the amplitude of the μ-th harmonic current, and $I_\mu = 4I/\mu\pi$.

Substituting equations (2) and (3) into equation (1), the MMF of the m -th phase of a symmetrical n-phase motor is:

$$F_m(\varphi,t)=\sum_{\nu=1}^{\infty}\sum_{\mu=1}^{\infty}N_\nu I_\mu\cos\left[\nu\left(\varphi-\frac{m-1}{n}2\pi\right)\right]\sin\left[\mu\left(\omega t-\frac{m-1}{n}2\pi\right)\right] \quad (4)$$

Therefore, the harmonic MMF generated by the μ-th harmonic current and the ν -th harmonic winding is:

$$F_{\nu\mu}(\varphi,t)=\sum_{m=1}^{n}N_\nu I_\mu\cos\left[\nu\left(\varphi-\frac{m-1}{n}2\pi\right)\right]\sin\left[\mu\left(\omega t-\frac{m-1}{n}2\pi\right)\right] \quad (5)$$

$$=\frac{nN_\nu I_\mu}{2}\left(F_{\mu\nu}\sin(\mu\omega t+\nu\varphi)+F_{\mu\nu}\sin(\mu\omega t-\nu\varphi)\right)$$

where:

$$F_{\mu\nu}=\frac{\sin[(\mu+\nu)\pi]}{n\sin[(\mu+\nu)\pi/n]}\quad F_{\mu\nu+}=\frac{\sin[(\mu-\nu)\pi]}{n\sin[(\mu-\nu)\pi/n]} \quad (6)$$

It can be seen that the harmonic MMF generated by the μ-th harmonic current and the ν -th harmonic winding consists of forward and backward traveling waves, and the condition for the existence of the resultant MMF is:

$$\mu\pm\nu=kn\quad k=0,\pm1,\pm2,\cdots \quad (7)$$

When the positive sign holds, the harmonic is a backward traveling wave; when the negative sign holds, it is a forward traveling wave. When both signs hold, it is a standing wave. The speed of the harmonic MMF is $\mu\omega/\nu$, meaning the speed of the harmonic MMF is proportional to the time harmonic and inversely proportional to the spatial harmonic.

B. MMF of Asymmetrical Multi-Phase Windings

The above analysis is for symmetrical multi-phase windings. Since asymmetrical multi-phase windings are composed of several sets of symmetrical windings shifted in space, the MMF of asymmetrical multi-phase windings can be analyzed using the superposition principle.

Assume an asymmetrical multi-phase winding consists of λ sets of n-phase symmetrical windings, each shifted by $\pi/(\lambda n)$ electrical degrees. The harmonic MMF generated by the μ-th harmonic current and the ν -th harmonic winding is:

$$F_{\mu\nu}(\varphi,t)=\sum_{i=1}^{n}N_i I_\mu\begin{pmatrix}\cos\left[\nu\left(\varphi-\frac{m-1}{n}\pi-\frac{i-1}{\lambda n}\pi\right)\right]\times\\ \sin\left[\mu\left(\omega t-\frac{m-1}{n}\pi-\frac{i-1}{\lambda n}\pi\right)\right]\end{pmatrix}$$

$$=\frac{\lambda nN_i I_\mu}{2}\left(F_{\mu\nu-}\sin(\mu\omega t+\nu\varphi)+F_{\mu\nu+}\sin(\mu\omega t-\nu\varphi)\right) \quad (8)$$

where:

$$F'_{\mu\nu-}=\frac{\sin[(\mu+\nu)\pi/(2n)]\sin[(\mu+\nu)\pi]}{\lambda n\sin[(\mu+\nu)\pi/(2n)]\sin[(\mu+\nu)\pi/n]} \quad (9)$$

$$F'_{\mu\nu+}=\frac{\sin[(\mu-\nu)\pi/(2n)]\sin[(\mu-\nu)\pi]}{\lambda n\sin[(\mu-\nu)\pi/(2n)]\sin[(\mu-\nu)\pi/n]} \quad (10)$$

It can be seen that for asymmetrical multi-phase motors, the condition for the existence of the harmonic MMF is:

$$\mu\pm\nu=k(2\lambda n)\quad k=0,\pm1,\pm2,\cdots \quad (11)$$

Similarly, when the positive sign holds, the harmonic is a backward traveling wave; when the negative sign holds, it is a forward traveling wave. For the 30° phase-shifted dual three-phase motor (asymmetrical six-phase motor) studied in this project, λ= 2 and n = 3. According to equation (9), $\mu\pm\nu=12k$. Comparing this with equation (5), it can be seen that the harmonic MMF distribution is the same as that of a symmetrical 12-phase motor, but the amplitude is halved.

Tables I and II show the harmonic MMF distributions for traditional 60° phase-band three-phase motors and dual three-phase motors, respectively. The MMF distribution of symmetrical six-phase motors is identical to that of three-phase motors, but the amplitude is doubled. The advantages of dual three-phase motors over three-phase and symmetrical six-phase motors are mainly reflected in the following two aspects:

1. Dual three-phase motors minimize torque ripple by eliminating 5th and 7th harmonic MMFs, resulting in the lowest harmonic MMFs being the 11th and 13th. This pushes the lowest torque ripple order to the 12th.
2. Dual three-phase motors lack standing waves. Injecting a 3rd harmonic current (with a single neutral point) can boost output torque, similar to symmetrical multi-phase motors.

TABLE I THE RESULTANT MMF FOR THREE-PHASE MOTOR

	Spatial harmonics generated by the winding (v)							
Current time harmonics (μ)		1	3	5	7	9	11	13
	1	1	×	-1/5	1/7	×	-1/11	1/13
	3	×	Standing Wave	×	×	Standing Wave	×	×
	5	-5	×	1	-5/7	×	5/11	-5/13
	7	7	Standing Wave	-7/5	1	Standing Wave	-7/11	7/13
	9	×	×	×	×	×	×	×
	11	-11	×	11/5	-11/7	×	1	-11/13
	13	13	×	-13/5	13/7	×	-13/11	1

TABLE II THE RESULTANT MMF FOR DUAL THREE-PHASE MOTOR

	Spatial harmonics generated by the winding (v)							
Current time harmonics (μ)		1	3	5	7	9	11	13
	1	1	×	×	×	×	-1/11	1/13
	3	×	1	×	×	×	×	×
	5	×	×	1	×	×	×	×
	7	×	×	-7/5	-5/7	1/3	×	×
	9	×	-3	×	1	×	×	×
	11	-11	×	×	×	1	×	-11/13
	13	13	×	×	×	-13/11	1	1

III. Determination of poles and slots

Dual three-phase motor design with concentrated windings requires specific stator slot numbers (multiples of 12 for symmetric distribution or Y dual-winding). Rotor pole pairs should match stator MMF harmonics (1, 5, 7, 11, 13 for symmetric; 1, 11, 13, 23, 25 for star). Rotor poles should be close to the number of teeth for a high winding factor, but excessive poles/slots are avoided for mechanical strength and motor size. The text then points to figures (2, 3, and 4) illustrating three example structures: 12-slot/10-pole (symmetric), 12-slot/10-pole (star), and 24-slot/22-pole (star).

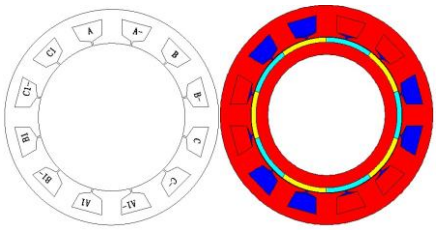

Fig. 2. Symmetric six-phase 12-slot/ 10-pole arrangement

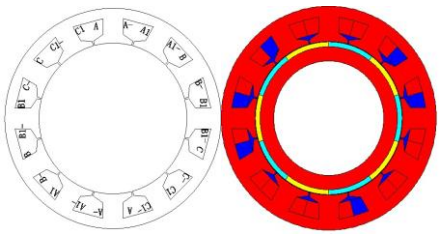

Fig. 3. Dual-star configuration with a 30-degree phase difference, 12-slot/ 10-pole arrangement

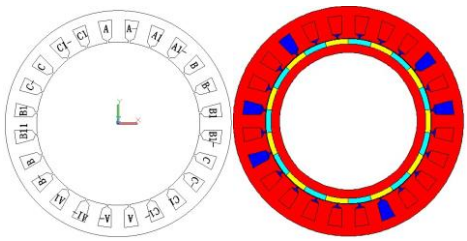

Fig. 4. Dual-star configuration with a 30-degree phase difference, 24-slot/ 22-pole arrangement

For the performance comparison of these three motors, their fundamental parameters are considered the same. These parameters include the volume of the iron core, the diameter of the stator, the air gap length, the axial length, the rated current, and the number of revolutions per phase. The other parameters extracted for these three motors are shown in Table III.

TABLE III COMPARISON OF PARAMETERS FOR THE THREE MOTORS

Parameters	12S/10P	12S/10P (Y30deg)	24S/22P
Winding factor	0.966	0.996	0.991
Average torque (N.m)	220.6	213.6	254.7
Torque ripple (%)	15.9	11.7	2.1
Peak short-circuit current (A)	48.5	76.7	25.4
Steel volume (m^3)	2.54×10^{-3}	2.54×10^{-3}	2.37×10^{-3}
Iron losses (W)	95.98	114.51	152.01
PM losses (W)	100.57	95.68	80.56

From the comparison of the above table, the following results can be extracted:

1) The dual three-phase motor with a 24-slot/ 22-pole single-layer winding has higher stator and rotor losses, but in other aspects such as average torque, torque ripple, and short-circuit current, it has superiority.

2) The 12-slot/10-pole design (compared to 24-slot/22-pole) requires a larger rotor and stator diameter, and a larger rotor yoke, due to the reduced number of poles. This lower pole number leads to greater interference between stator and rotor MMF harmonics, resulting in increased torque oscillations.

Therefore, the final structure is selected as the 24-slot/ 22-pole single-layer winding with a 30-degree phase difference.

IV. Optimization of no-load back-EMF

To optimize the no-load back-EMF, two methods are used: optimization of the pole arc coefficient and the inequality of the inner and outer iron core arcs.

A. Optimization of the pole arc coefficient

The pole arc coefficient is defined as the ratio of the pole shoe to the pole pitch. Since the number of slots and poles in the dual three-phase machine is close to each other, the pole pitch (slot to pole ratio) is almost one. By changing the pole arc coefficient, the main component and harmonic content of the back-EMF change, as shown in Figures 5 and 6.

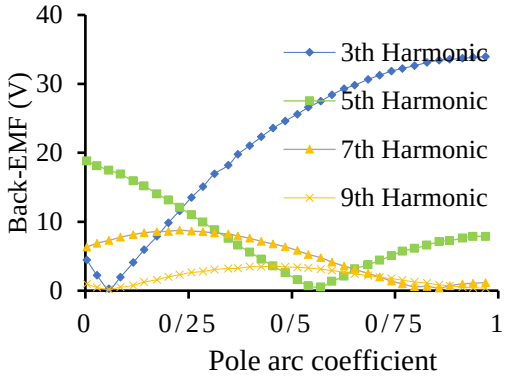

Fig. 5. Harmonic amplitude based on the pole arc coefficient

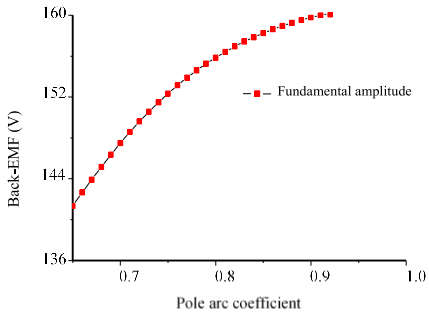

Fig. 6. Main component amplitude based on the pole arc coefficient

Figures 5 and 6 show that increasing the pole arc coefficient increases the main back-EMF component's amplitude, leveling off around 0.9. The 3rd harmonic is minimized at 0.67, and the 5th at 0.85. While the main component generates torque, the harmonics cause vibration and losses. Increasing the coefficient from 0.9 to 1 only improves the main component by 0.63% (small gain) but increases excitation current by 10%. Therefore, the optimal pole arc coefficient is 0.9. The back-EMF waveform shown in Figure 7.

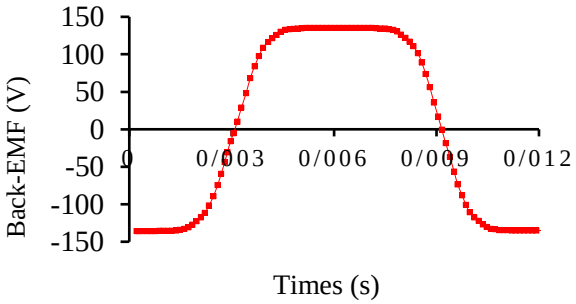

Fig. 7. Back-EMF waveform for a pole arc coefficient of 0.9

B. Permanent magnet eccentricity optimization

The inequality of the inner and outer PM arcs results in non-uniform air gap lengths. Therefore, the air gap flux is not a pure sine wave and becomes closer to a sinusoidal waveform. As a result, the back-EMF waveform becomes sinusoidal. However, due to the decrease in excitation current, the magnitude of the back-EMF also decreases. The difference in the inner and outer iron core arcs is shown in Figure 8.

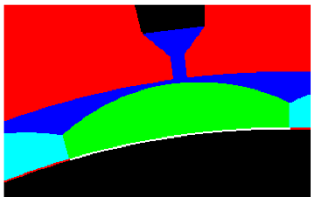

Fig. 8. Eccentric PM optimization

When the difference in the inner and outer iron core radii is 86 mm, the back-EMF waveform becomes the most sinusoidal, as shown in Figure 9.

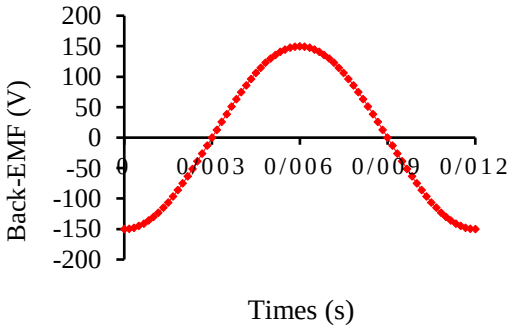

(a)

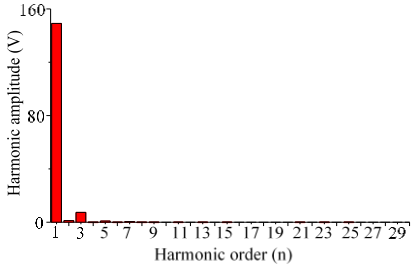

(b)

Fig. 9. (a) No-load back-EMF waveform with PM eccentricity optimization (b) Back-EMF harmonic spectrum

As observed, the waveform is sinusoidal with only a small amount of third harmonic. To evaluate the performance of this modified iron core configuration, it is compared with a conventional surface-mounted permanent magnet motor. For this comparison, the key parameters such as the outer diameter of the stator, axial length, rated current, and number of pole pairs are kept the same. Table IV shows the performance comparison of these two motors.

TABLE IV COMPARISON OF THE EFFECT OF PM SHAPE

Parameters	Conventional surface-mounted PM	Eccentric PM
Average torque (N.m)	254.7	211.1
Torque ripple (%)	2.1	0.24
No-load back-EMF (V)	159.75	150.1
Total Harmonic Distortion (THD)	12.8	2.4
Iron losses (W)	152.01	141.5
Volume of the PM (m^3)	2.64×10^{-4}	2.68×10^{-4}

Since using an iron core with unequal inner and outer arcs requires increasing the pole arc coefficient to enhance the permanent magnet flux, the leakage flux between the poles increases. This leads to a reduction in the no-load back-EMF and affects the motor's output torque.

Although the motor with this iron core shape has slightly lower torque ripple, its power generation capacity also decreases. Since torque ripple is not our main goal, the final structure of the motor is chosen to be a 24-slot/ 22-pole star-wound configuration with a 30-degree phase difference and a conventional iron core shape. The final dimensions of the main machine are specified in Table V.

TABLE V THE FINAL DIMENSIONS OF THE MAIN MACHINE

Parameters:	value
Outer diameter of the stator (mm)	350
Inner diameter of the stator (mm)	170
Axial length (mm)	109
Air gap length (mm)	0.6
Thickness of the PMs (mm)	5
Pole arc coefficient	0.9
Slots/pole	22/24
Number of turns per slot	80
Slot area (mm^2)	420

V. Analysis of Dual Three-Phase Motor Performance

When the motor operates under normal conditions, the motor torque, maximum torque, maximum speed, maximum power efficiency, and output characteristics are performance indicators of the motor. The nominal performance parameters of the motor are shown in Table VI. These values are investigated using finite element simulation in MAXWELL software. The nominal torque and maximum torque of the dual three-phase motor are shown in Figure 10.

TABLE VI PERFORMANCE PARAMETERS OF DUAL THREE-PHASE MOTOR

Number of Phases:	Dual Three-Phase
Nominal Voltage (V)	288
Nominal Power (kW)	12
Maximum Power (kW)	24
Nominal Speed (rpm)	450
Maximum Speed (rpm)	1200
Maximum Torque (N.m)	300
Maximum Efficiency	94%
Efficiency in the operational range above 80%	≥ 65%

When the effective current is 20 A, the nominal torque is obtained, and to reach the maximum torque, the effective current should be 23.6 Amperes.

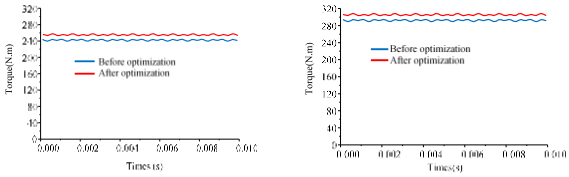

(a) (b)

Fig. 10. Output Torque (a) Nominal Torque (b) Maximum Torque

The cogging torque and iron losses of the motor are shown in Figures 11 and 12. Cogging torque is one of the problems of these motors that arises from the interaction between the rotor iron cores and the stator teeth. This torque causes vibration and noise during motor operation [17]. The peak cogging torque is 1.2 N.m, which is approximately 0.5% of the nominal torque. Additionally, the iron losses in the nominal torque are 152 W.

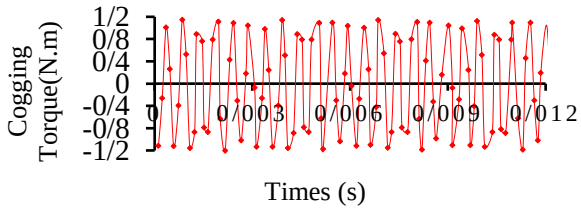

Fig. 11. Cogging Torque

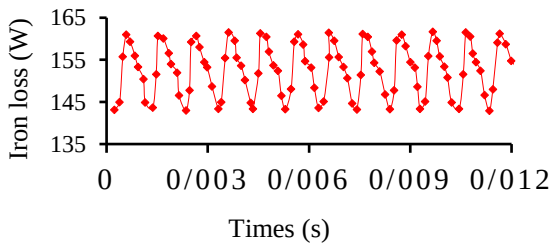

Fig. 12. Iron Losses

In an electric vehicle, achieving desired speed is important. In permanent magnet motors, rotor flux is constant and can't be reduced by field current. Above the nominal speed, induced EMF exceeds maximum input voltage, making current injection impractical. To solve this, air gap flux is weakened to limit induced EMF. Flux weakening is inversely proportional to stator frequency, keeping induced EMF constant as speed increases. For motor performance at speeds higher than the nominal speed, a specific flux weakening capacity is required. The flux weakening capacity depends ψ_s and $L_d i_s$ [18, 19]:

$$i_q = \frac{\sqrt{\left(u_{lim}/\omega\right)^2 - \left(L_d i_d + \psi_m\right)^2}}{L_q} \tag{12}$$

$$P = p i_q \omega \left(L_d i_d + \psi_m\right) \tag{13}$$

$$\omega = \frac{u_{lim}}{p\left(\psi_m - L_d i_d\right)} \tag{14}$$

where, ψ_m is rotor flux, L_d, L_q are inductances of q and d axes, i_d, i_q are currents of q and d axes, u_{lim} is voltage constraint, i_s is current constraint, p is number of pole pairs of the rotor and ω is angular speed.

when $\psi_m \approx L_d i_s$, the motor has the best flux weakening capability. In this motor, $\psi_m = 3.384\times10^{-2} Wb$, $L_d = 1.53 mH$, $i_s = 23.6A$, as result $L_d i_s = 3.384\times10^{-2} Wb$. Therefore, theoretically, this motor is in the best flux weakening condition. In the speed range below the rated speed, the reference value of ψ_m is equal to its nominal value, and in the flux weakening region (motor speed greater than rated speed), it changes inversely with speed, i.e. [20]:

$$\psi_m^{new} = \begin{cases} \psi_m, & n_r \le n_r^N \\ \dfrac{n_r^N}{n_r}\psi_m, & n_r^N \le n_r^N \le n_r^{max} \end{cases} \tag{15}$$

where ψ_m^{new} is the flux value in the flux weakening region, ω_{nom} is the rated speed (600 rpm), and ω_{max} is the maximum speed of the studied motor (1200 rpm). The speed-torque curve in the flux weakening region of the dual three-phase motor is extracted using MAXWELL simulation. Considering the design limitations, V_{max}=208V. Below the rated speed, i_d equals zero, and above the rated speed, the flux weakening strategy is employed. The efficiency constraint is such that the efficiency should be higher than 65% in more than 80% of the operating range. The motor efficiency map is shown in Figure 13.

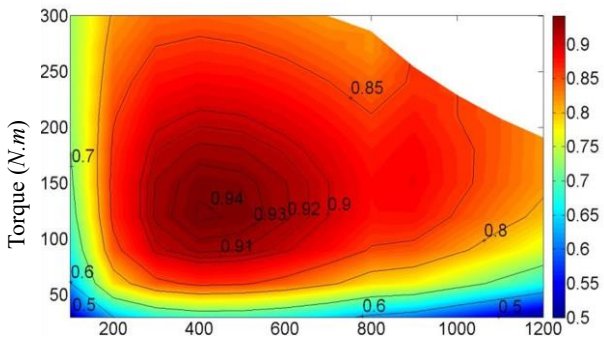

Fig. 13. Motor Efficiency Map

As seen from Figure 13, the maximum motor efficiency is 94.3%, which is higher than 94%, and in more than 80% of the operating range, the motor efficiency is around 71%,

which is higher than 65%. Therefore, the design considerations are taken into account. The motor efficiency at the rated operating point is approximately 90%.

VI. Thermal Rise Characteristics Analysis

Key to maximizing power density is ensuring thermal performance. The process involves: 1) calculating equivalent thermal conductivity coefficients, 2) creating a 3D model in Solidworks, and 3) analyzing the temperature field in Ansys.

A. Basic theory of heat exchange in dual three-phase motors

1) Heat Conduction

Heat conduction transfers energy between objects with a temperature difference, driven by microscopic particle movement. Heat flux density is proportional to the temperature gradient. The text implies an equation expressing this relationship is as

$$d\Phi = \lambda \frac{\partial T}{\partial n} dA \tag{16}$$

where, Φ is heat transferred, T is temperature of the part of the object being calculated, dA represents the micro-area at the specified point and λ is thermal conductivity coefficient of the material. Then, the relationship between heat flux density $\boldsymbol{q}$ and thermal conductivity is:

$$q = \frac{d\Phi}{dt} = -\lambda \frac{\partial T}{\partial n} \tag{17}$$

Eq (16) and (17) summarize the famous Fourier's Law. In equation (17), $\partial T/\partial n$ is the temperature gradient $grad\mathbf{T}$, thus, the thermal conductivity coefficient $\lambda = -q/gradT$.

2) Convection

Convection refers to the relative flow within a fluid due to temperature differences between its parts, where heat is transferred from one part of the object to another through fluid motion. Generally, heat dissipation within an object is based on Newton's Law of Cooling, equating the process to convection, i.e.,

$$q = a(T_1 - T_2) = a\Delta T \tag{18}$$

The heat flux density (q) is related to the heat transfer coefficient (a) and object temperature (T). In this motor, air in the air gap is the only cooling medium. For air, flow velocity dictates the heat transfer coefficient. Empirical Eq. (19) (valid for wind speeds 1-40 m/s) summarizes the relationship

$$\alpha = \alpha_0(1 + k\sqrt{v}) \tag{19}$$

where, α_0 is the heat transfer coefficient at zero gas velocity; and k is the correction coefficient obtained from experiments.

3) Radiation

Heat transfer inside the motor also involves radiation, though it can sometimes be negligible. Radiative energy transfer occurs via electromagnetic waves. According to the radiation law, the radiative energy $(s^{-1}m^{-1})$ is given by:

$$q = \sigma\upsilon(T^4 - T_0^4) \tag{20}$$

where, σ is the Boltzmann constant for a perfect black body, $\sigma = 5.7\times10^{-8} W/m^2 \cdot K$, υ is the physical parameter related to the surface condition of the heat-dissipating body.

B. Temperature Field Simulation of Dual Three-Phase Motor

1) Analysis of Heat Sources in Dual Three-Phase Motor

The dual three-phase motor in this study has a high electrical load, leading to significant copper losses in the windings, which is the main heat source. Fractional-slot concentrated windings create harmonic components in the stator magnetic field, causing eddy current losses in the rotor magnets and iron losses in the stator/rotor. Winding heat source is calculated using $P_{cu} = mI^2R$, while other losses are found via finite element simulation. Loss distribution is shown in Table VII.

TABLE VII LOSSES OF COMPONENTS INSIDE DUAL THREE-PHASE MOTORS

Heat Source	Loss (W)	Heat Generation Rate (W/m³)
Armature Winding	720	7,559,362
Stator Teeth	104.25	90,159
Stator Core	47.83	36,897
PMs	80.56	205,698

2) Selection of Thermal Conductivity and Heat Transfer Coefficients for Dual Three-Phase Motor

The motor is composed of various materials, including silicon steel sheets, permanent magnets, insulating materials, copper wires, and air, each with different thermal conductivity coefficients. The thermal conductivity coefficient λ represents a material's ability to conduct heat and depends on factors such as temperature and material type. The definition of thermal conductivity is given by:

$$\lambda = \frac{q}{gradT} \tag{21}$$

In practical engineering, temperature is considered a primary factor affecting the thermal conductivity of materials. For most materials encountered in engineering, the thermal conductivity is approximately linearly related to temperature, as

$$\lambda = \lambda_0(1 + bt) \tag{22}$$

where, λ_0 is the Thermal conductivity at 0°, b is the Correction coefficient obtained from experiments, related to the material. The thermal conductivity coefficients of different materials in the motor are listed in Table VIII.

TABLE VIII Gas thermal conductivity depends on molecular collision rate and intensity. Higher temperature increases

THERMAL CONDUCTIVITY COEFFICIENTS OF MATERIALS IN DUAL THREE-PHASE MOTOR

Material	Stator Core	Windings	PMs
Thermal Conductivity W/(m.K)	40.05	396	8.9

molecular speed and collision frequency, thus increasing thermal conductivity. Air's thermal conductivity increases with temperature. The relationship is given by:

$$\lambda = \lambda_0 \left(\frac{T}{273} \right)^n \tag{23}$$

where n is a constant, and for air, n=0.82. The thermal conductivity coefficients of air at different temperatures are shown in Table IX.

TABLE IX THERMAL CONDUCTIVITY OF AIR AT DIFFERENT TEMPERATURES

Temperature	0℃	20℃	40℃	60℃
Thermal Conductivity W/(m·K)	0.0234	0.0260	0.0281	0.0289
Temperature	**70℃**	**80℃**	**100℃**	**120℃**
Thermal Conductivity W/(m·K)	0.02916	0.0301	0.0321	0.0329

3) Temperature Field Analysis of Dual Three-Phase Motor

Based on the above analysis, a temperature field model for the 24-slot 22-pole dual three-phase motor was established. The three-dimensional model of the dual three-phase motor was created using Solidworks, and the temperature field analysis was performed using the finite element software Ansys. The three-dimensional model and the meshed grid are shown in Figure 14.

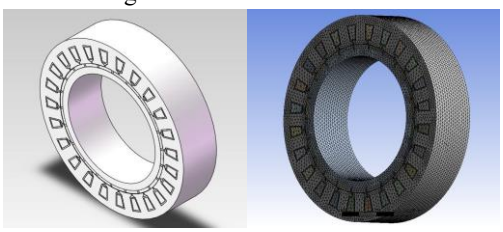

Fig. 14. 3D model and mesh generation of dual three-phase motors, (a) 3D model. (b) mesh generation results

From the temperature analysis results in Figure 15, the designed dual three-phase motor operates with temperatures ranging between 24.053℃ and 139.88℃ under natural cooling. The highest temperature, 139.99℃, occurs in the middle of the windings due to copper losses under rated conditions. The motor's class H insulation can withstand up to 180℃, ensuring no risk to winding insulation. The permanent magnets reach a maximum temperature of 105.62℃, well below their SH-grade heat resistance limit of 150℃, preventing damage or demagnetization. Thus, the motor operates safely within thermal limits.

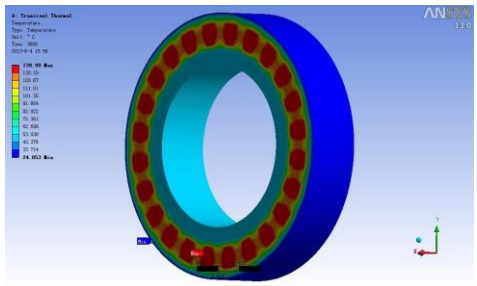

Fig. 15. Temperature field analysis results of dual three-phase motors

As summarized in Table X, our 24-slot/22-pole design demonstrates distinct advantages over contemporary solutions. While Huang et al.'s approach achieves fault tolerance at the cost of inverter complexity, and Wang et al.'s liquid-cooled system enables high power density with added weight, our optimized configuration delivers superior efficiency (94%) using natural cooling. This balanced performance profile - combining competitive torque output (254.7 N·m), minimal ripple (2.1%), and thermal stability (139.99°C windings) - positions our design as particularly suitable for mid-power EV applications where system simplicity and energy efficiency are paramount.

TABLE X COMPARATIVE SUMMARY OF THIS WORK VERSUS RECENT ADVANCES IN DUAL THREE-PHASE PM MACHINES

Study (Year)	Contribution	Advantage	Limitation
Huang et al. (2023)	3-redundancy fault-tolerant control	85% torque during faults	Complex inverter design
Wang et al. (2024)	Liquid-cooled aviation motor	20 kW at 130°C windings	Added weight/cost
This work	24-slot/22-pole + thermal optimization	94% efficiency, natural cooling	Limited to mid-power EV applications

VII. Conclusion

Compared to conventional electric machines, dual three-phase permanent magnet electric machines have more advantages such as high fault tolerance, simple control method under fault conditions, and good performance characteristics during faults. In this article, two winding configurations (star with 30-degree phase difference and symmetrical six-phase) were investigated for the dual three-phase motor. Based on harmonic analysis, the rules for selecting pole-slot combinations were extracted, and a comparison was made between the best possible configurations. It was shown that the 24-slot/ 22-pole structure with a star winding configuration and a 30-degree phase difference had superiority over other combinations. Then, the unloaded back-EMF was optimized. The results indicate that using an unequal iron core with inner and outer notches, although it makes the back-EMF waveform sinusoidal, it reduces the torque and motor power.

Furthermore, the internal temperature rise characteristics of the dual three-phase motor are analyzed, and the temperature field under steady-state conditions is studied.

REFERENCES

[1] H. T. Canseven, I. Petrov, and J. Pyrhönen, "Impact of Stator Core Magnetic Asymmetry on the Properties of a High Specific Power PMSM," IEEE Transactions on Industry Applications, vol. 60, no. 3, pp. 3830–3839, May 2024, doi: https://doi.org/10.1109/tia.2024.3357048.

[2] T. Liu, Z. Q. Zhu, X. Wu, Z. Wu, D. A. Stone, and M. P. Foster, "A Position Error Correction Method for Sensorless Control of Dual Three-Phase Permanent Magnet Synchronous Machines," IEEE Transactions on Industry Applications, vol. 58, no. 3, pp. 3589–3601, May 2022, doi: https://doi.org/10.1109/tia.2022.3152682.

[3] Y. Li, Z.-Q. Zhu, X. Wu, A. S. Thomas, and Z. Wu, "Comparative Study of Modular Dual 3-Phase Permanent Magnet Machines With Overlapping/Non-overlapping Windings," IEEE Transactions on Industry Applications, vol. 55, no. 4, pp. 3566–3576, Jul. 2019, doi: https://doi.org/10.1109/tia.2019.2908138.

[4] Y. Zhou, W. Zhao, X. Zhao, J. Ji, and Y. Sun, "Multi-Objective MMF Reconstruction Design for Vibration Suppression in Modular Dual 3-Phase PMSM With Open-Phase Fault," IEEE Transactions on Energy Conversion, pp. 1–10, 2024, doi: https://doi.org/10.1109/tec.2024.3479749.

[5] W. Huang, W. Hua, and Q. Fan, "Performance analysis and comparison of two fault-tolerant model predictive control methods for five-phase PMSM drives," CES Transactions on Electrical Machines and Systems, vol. 5, no. 4, pp. 311–320, Dec. 2021, doi: https://doi.org/10.30941/cestems.2021.00036.

[6] C. Zhang, Y. Wang, Z. Wu, W. Hua, and M. Zhang, "Implementation of Dual Three-Phase Linear Hall Sensor-Based Embedded Magnetic Encoder in Permanent Magnet Synchronous Motors," IEEE Transactions on Power Electronics, vol. 39, no. 9, pp. 10688–10692, Sep. 2024, doi: https://doi.org/10.1109/tpel.2024.3404848.

[7] M. Barcaro, N. Bianchi, and F. Magnussen, "Analysis and Tests of a Dual Three-Phase 12-Slot 10-Pole Permanent-Magnet Motor," IEEE Transactions on Industry Applications, vol. 46, no. 6, pp. 2355–2362, Nov. 2010, doi: https://doi.org/10.1109/tia.2010.2070784.

[8] J. Wang, L. Yan, X. Gao, and H. Su, "Electromagnetic thermal design and analysis of aviation dual three-phase permanent magnet machine," IET Conference Proceedings, vol. 2024, no. 13, pp. 2352–2357, Jan. 2025, doi: https://doi.org/10.1049/icp.2024.3382.

[9] D. Ishak, Z. Q. Zhu, and D. Howe, "Comparison of PM Brushless Motors, Having Either All Teeth or Alternate Teeth Wound," IEEE Transactions on Energy Conversion, vol. 21, no. 1, pp. 95–103, Mar. 2006, doi: https://doi.org/10.1109/tec.2005.853765.

[10] Y. Zhang et al., "Analysis of the Influence of Winding Phase Shift of Dual Winding Permanent-Magnet Synchronous Machines on Inter-turn Short Circuit Fault," Journal of Electrical Engineering & Technology, vol. 19, no. 8, pp. 5165–5176, Jun. 2024, doi: https://doi.org/10.1007/s42835-024-01934-4.

[11] J. Yu, W. Mi, Z. Cai, Z. Song, S. Liu, and C. Liu, "Design Principle Considering Structural Mutual Effects of Double-Stator V-Shape-PM Vernier Machines for Electric Ship Propulsion," IEEE Transactions on Transportation Electrification, vol. 10, no. 1, pp. 496–508, Mar. 2024, doi: https://doi.org/10.1109/tte.2023.3279202.

[12] A. Yoshida and K. Akatsu, "Study of Winding Structure to Reduce Harmonic Currents in Dual Three-Phase Motor," World Electric Vehicle Journal, vol. 14, no. 4, p. 100, Apr. 2023, doi: https://doi.org/10.3390/wevj14040100.

[13] L. Huang, W. Zhao, J. Ji, T. Tao, Y. Du, and Q. Zhang, "Enhanced Fault Tolerance of Dual Three-Phase Permanent Magnet Motor With Three-Redundancy Control," IEEE Transactions on Energy Conversion, vol. 38, no. 3, pp. 2211–2222, Sep. 2023, doi: https://doi.org/10.1109/tec.2023.3267786.

[14] K. Jankowska and M. Dybkowski, "Design and Analysis of Current Sensor Fault Detection Mechanisms for PMSM Drives Based on Neural Networks," Designs, vol. 6, no. 1, p. 18, Feb. 2022, doi: https://doi.org/10.3390/designs6010018.

[15] H.-Y. Tang, Q. Sha, and D.-Z. Xu, "Study on model predictive control of dual three-phase permanent magnet synchronous motor based on biplane virtual voltage vector," Archives of Electrical Engineering, pp. 869–890, Sep. 2024, doi: https://doi.org/10.24425/aee.2024.152100.

[16] Azadrou, H. . "Design and Optimization of a Very High Speed Three Phase Bearingless Induction Motor", International Journal of Industrial Electronics Control and Optimization, 6, 4, 2023, 283-289. doi: 10.22111/ieco.2023.45551.14.

[17] M. Fadaie , K. Abbaszadeh and A. Siadatan, "Simplified and Accurate Predictive Control Method in Mono-Inverter Dual-Parallel Permanent Magnet Synchronous Motors," International Journal of Industrial Electronics Control and Optimization, 5, 3, 2022, 251-260, doi: 10.22111/ieco.2022.41196.1405.

[18] Y. Wei, J. Si, Z. Cheng, S. Xu, L. Dong, and J. Liang, "Design and characteristic analysis of a six-phase direct-drive permanent magnet synchronous motor with 60° phase-belt toroidal winding configuration for electric vehicle," IET electric power applications, vol. 14, no. 13, pp. 2659–2666, Dec. 2020, doi: https://doi.org/10.1049/iet-epa.2020.0083.

[19] Sadiq Ur Rahman and C. Xia, "Rotor Speed and Position Estimation Analysis of Interior PMSM Machines in Low and Medium-High Speed Regions Adopting an Improved Flux Observer for Electric Vehicle Applications," Machines, vol. 11, no. 5, pp. 574–574, May 2023, doi: https://doi.org/10.3390/machines11050574.

[20] Y. Li and P. Gong, "Fault-Tolerant Control of Induction Motor with Current Sensors Based on Dual-Torque Model," Energies, vol. 16, no. 8, p. 3442, Apr. 2023, doi: https://doi.org/10.3390/en16083442.

Javad Rahmani-Fard received the B.S. degree from Shahed University, Tehran, Iran, in 2009, and the M.S. and Ph.D. degrees in electrical engineering from the K.N. Toosi University of Technology, Tehran, in 2012 and 2018, respectively. Currently, he is an assistant professor of the electrical engineering at Qom University of Technology, Qom, Iran. His research interests include the analysis and design of electrical machines, and sensor-less variable-speed drives, multiphase variable-speed drives.

IECO

This page intentionally left blank.

International Journal Of
Industrial Electronics Control and Optimization
Print ISSN: 3517-2645
Online ISSN: 3568-2645
Homepage: https://ieco.usb.ac.ir/

An Optimal Nonlinear Fractional Order Virtual Inertia Control Strategy for Islanded Microgrids with Renewables

Abbas-Ali Zamani[1,2]

Department of Electrical Engineering, National University of Skills (NUS), Tehran, Iran.[1]
Department of Electrical Engineering, Technical and Vocational University (TVU), Tehran, Iran.[2]
Corresponding author's email: a.zamani.edu@gmail.com

Article Info

Article type:
Research Article

Article history:
Received: 20-March-2025
Received in revised form: 02-May-2025
Accepted: 10-May-2025
Published online: 22-Dec-2025

Keywords:
Virtual Inertia,
Sustainable Energy Resources,
Nonlinear Fractional Order Controller,
Islanded Microgrid.

ABSTRACT

The large-scale integration of renewable generation into microgrids can lead to decreased inertia, resulting in high rates of change of frequency and frequency instability. This issue is even more complex in islanded MGs that incorporate a high proportion of RGs and need to deliver power to loads in islanded mode. To address this problem, a virtual inertia control scheme can be employed to enhance system inertia and maintain frequency stability. In this article, we propose a novel control strategy named the optimal nonlinear fractional-order PI-based virtual inertia controller, which integrates a nonlinear fractional-order PI controller into the conventional VIC loop. The designed ONFOPI+VI controller, which considers both inertia and damping properties, is optimized using the Coot optimization algorithm. Furthermore, an alternative control methodology, denoted as OFOPI+VI, has been developed to analyze and evaluate the outcomes obtained from the proposed ONFOPI+VI control structure. This paper compares the performance of the proposed ONFOPI+VI strategy to that of the OFOPI+VI and other VIC techniques for different RG and load variations under various scenarios. Simulation results and detailed analyses confirmed that the ONFOPI+VI controller significantly outperformed conventional methods, yielding at least a 30% improvement in IAE and a 20% improvement in ITAE compared to other control techniques.

I. Introduction

A. Virtual Inertia Control Background

In recent years, there has been a growing trend towards the integration of renewable generation (RG) into utility power systems. This shift is expedited in reaction to the adverse effects stemming from fossil fuel usage like environmental deterioration, global warming, and the consequences of greenhouse gas emissions [1-2]. The appeal of RGs lies in their clean, infinite, and cost-effective nature [3-4]. However, the inclusion of RGs into modern interconnected electricity networks can pose certain challenges and issues for utility grids. One such challenge is the diminished system inertia of interconnected electricity networks, which can be attributed to the use of power converters to interface RGs with the utility grid. Studies have shown that these converters can cause a drop in the inertia of the power system, leading to alterations in the frequency and voltage stability of the system [5]. The concept of virtual inertia (VI) control has been widely adopted in low inertia systems to enhance their inertia, as evidenced by previous studies [6-8].

B. Literature Review

One effective method for emulating the benefits of virtual inertia control (VIC) and improving system inertia is through the use of the derivative technique, as demonstrated in previous research [9]. For example, the application of this control methodology within interconnected power systems has demonstrated enhancements in frequency stability [3]. In a separate investigation [10], researchers introduced a VIC mechanism. This approach involves estimating the rates of change of frequency to effectively supply tailored inertia management for contingencies, thereby augmenting frequency stability in networks with limited inherent rotational inertia. Furthermore, a proportional-derivative control system was employed to improve the microgrid (MG) frequency stability in the presence of PV arrays [11].

Besides this approach, a range of VIC mechanisms have been deployed with the objective of fortifying frequency

stability. Based on several review papers, such as [12-14], various VIC techniques have been proposed for low inertia systems, including droop control, hidden inertia emulation, and energy storage integration. For example, the utilization of a blend of fuzzy interval-type-2 and proportional integral controllers in islanded microgrids has been investigated [15]. Equilibrium optimization is employed in this study to fine-tune controller parameters. In [16], VIC methods were classified into energy storage-based and non-energy storage-based techniques. Some researchers have proposed specific VIC schemes for certain systems, such as a VI and frequency control scheme for wind power-based systems [17] and VI control techniques for improving dynamic stability in microgrids [18]. Other studies have explored derivative-type VIC using different controllers, such as PSO-optimized Proportional-Integral (PI) controllers [19], Genetic Algorithm (GA)-based PI controllers [20], fuzzy logic controllers [21], and H-infinity controllers [21, 22]. Some of the previous studies [17-19, 21] have not incorporated the damping constant component in their design of the VI control system. As a consequence, the frequency response exhibits sub-optimal dynamic characteristics characterized by elevated peak values and prolonged settling times.

The appeal of the Fractional Order Controller (FOC) family has attracted many researchers, particularly in the realm of power system control [23-27]. The application of FOCs extends to the domain of VI control. For instance, in a study denoted as [28], researchers explored the efficacy of fractional-order controllers within a modern power grid incorporating solar photovoltaic plants (SPP), wind power plants (WPP), and a thermal unit. The study utilized the flower pollination algorithm as an efficient method to finely tune the controller. In another investigation, a Fractional Order (FO) integral-based control strategy, incorporating VIC, was deployed in a multi-area electricity network [29]. Despite achieving commendable results, it is noteworthy that the damping effect of virtual inertia was not included in this particular reference. Subsequently, in a separate study, a genetic algorithm-optimized FO controller was introduced to enhance the stability of modern power systems featuring RGs [30]. However, none of these studies [28-30] have utilized nonlinear fractional order controllers as the designed controllers in the VIC loops.

C. Motivation and Research Gap

One of the primary challenges in microgrids with renewable energy sources (RESs) is maintaining frequency stability. Despite the advancements in virtual inertia control, several aspects of this issue still require further investigation. In particular, it has become clear that the control gains of virtual inertia significantly influence the power flow in and out of Energy Storage Systems (ESSs), which in turn has a profound impact on the stability of the MG and its ability to respond to disturbances. Therefore, optimizing these control parameters is critical to ensure system stability and performance.

Additionally, many existing studies overlook the importance of integrating into VIC systems. The absence of Virtual Damping (VD) can lead to suboptimal power flow in ESSs and diminish the effectiveness of VI control, especially in MGs where the inherent inertia and damping are constrained. Conventional PI controllers, although widely applied, face limitations in inverter-based ESSs. These controllers struggle to replicate the behavior of synchronous generators or emulate synthetic inertia in MGs. The intermittent nature of renewable generation and the variability in load conditions further exacerbate the performance issues of PI controllers. Moreover, these controllers often encounter difficulties in maintaining system stability under uncertain conditions.

In response to these challenges, non-linear control theories, including non-linear fractional-order control methods, have emerged as viable solutions. Traditional linear control methods, though often employed due to their mathematical simplicity, are limited to specific operational points where linearization is feasible. However, many real-world systems, particularly power systems, exhibit inherent non-linearities that demand more advanced control strategies. Non-linear techniques, such as reset control, sliding mode control, and non-linear PID control, are increasingly being considered. Among these, fractional calculus stands out as an effective approach for dealing with the complexities of control engineering.

Given the inherent non-linearity of modern power systems and the growing complexity introduced by high penetration of renewable generation, there is a clear need for innovative control solutions. Non-linear fractional-order control represents an interdisciplinary field that combines the mathematical intricacies of non-linearity and fractional calculus, offering a departure from traditional control paradigms [31, 32]. This approach has the potential to address the persistent challenges in VIC, particularly in low-inertia, islanded MGs.

Upon reviewing the existing literature on VIC, it is evident that various controllers have been employed to improve the stability of MGs. However, significant gaps remain, particularly regarding the integration of VD and the use of nonlinear fractional-order controllers in VIC systems. Given the uncertainties and non-linearities of today's electrical networks, exacerbated by the intermittent nature of renewable generation, this study introduces the Optimal Nonlinear Fractional-Order PI-based Virtual Inertia (ONFOPI+VI) methodology as a promising solution. This approach aims to enhance control performance and stability in low-inertia, islanded MGs, thereby addressing critical control challenges in modern microgrid systems.

D. Contribution

In the pursuit of heightened MG stability, this research introduces a novel VIC configuration, employing an Optimal Nonlinear Fractional Order Proportional-Integral (NFOPI) controller. This technique enhances control performance, stability, and robustness even in the presence of nonlinearities and uncertainties. While the configuration takes into account both virtual inertia and virtual damping for VI emulation, the proposed ONFOPI+VI framework incorporates the Coot Optimization Algorithm (COA) to determine optimal VI parameters, integral order, as well as gains for the ONFOPI. The method's flexibility ensures that VI, damping, and ONFOPI parameters are precisely set to the specific system conditions, thereby enhancing stability and performance amidst power oscillations. As opposed to customary control methodologies, this technique allows for optimal adjustments to controller and damping sizes. The ability of the proposed framework to control nonlinear systems and the optimal gain utilization enables the controller to effectively respond to system changes in the presence of nonlinearities and uncertainties.

The contributions of this article can be summarized as follows:

•Introduction of a new control mechanism, ONFOPI+VI, tailored for VIC emulation in islanded microgrids with a significant RG share.

•Consideration of both inertia and damping components in the VIC system within the control system model.

•Determination of optimal values for VIC system parameters, including inertial and derivative gains, as well as NFOPI controller gains and its non-integer orders, using the COA.

•Design and comparison of an alternative control strategy, Optimal Fractional-Order PI-based Virtual Inertia (OFOPI+VI), integrating Fractional Order Proportional-Integral (FOPI) into the VIC loop.

•Proposition of various scenarios to assess the functionality of the proposed control framework, evaluating their efficacy over a broad spectrum of load and generation variations.

•The superior performance of the proposed ONFOPI+VI over the traditional VI (T-VI), COA-optimized VI (COA-VI), GA-optimized PI-based VI (GAPI+VI), and OFOPI+VI are demonstrated.

The T-VI and GAPI+VI controllers from [15, 20] were employed for comparative analysis.

The upcoming sections of this research manuscript are structured as follows: Section 2 provides an extensive introduction to the model of the microgrid being studied. In Section 3, we present a summary of the virtual inertia control mechanism, whereas Section 4 delves into the innovative virtual inertia control system introduced in this investigation. Section 5 comprehensively presents the numerical findings, and lastly, Section 6 furnishes a conclusive summary of the outcomes.

II. Modeling of the Islanded Microgrid

To assess the efficacy of the proposed ONFOPI+VI controller, a thorough examination is carried out on a disconnected MG. The MG configuration consists of varied elements, incorporating a thermal power plant and RGs such as WPPs and SPPs, as indicated in Fig. 1. The studied MG is comprised of a 20 MW thermal power generation (TPG), an 8 MW WPP, a 4 MW SPP, a residential demand of 5 MW, and a 10 MW industrial power consumption. The baseline power of the grid is established at 20 MW, as outlined in previous works [15, 19, 20].

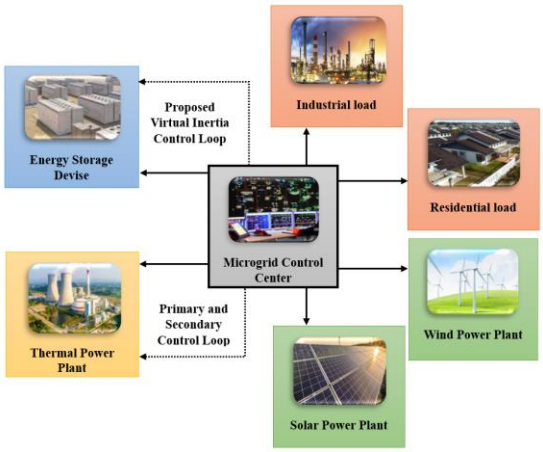

Fig. 1. Diagram of depicting the analyzed islanded microgrid

Fig. 2 illustrates the dynamic model of the microgrid that is currently being investigated [15, 20, 26, 28, 33]. The model comprises block diagrams of a typical frequency control study, which includes the Generator Rate Constraint (GRC) for the governor unit and the rate limitation of the turbine-valve/gate closing or opening speed (V_U, V_L) for the turbine unit. The GRC value was estimated to be 20% P.U. MW/min in this study. Appendix 1 lists the parameters of the microgrid system that was studied [15, 20].

Taking into account the inertia, primary and secondary control, as well as the dynamic effects of the generations and loads shown in Fig. 2, The variation in frequency and fluctuations in the power of the RGs is obtained as follows [33]:

$$\Delta f(s) = \frac{1}{2Hs + D}\left(\Delta P_m(s) + \Delta P_W(s) + \Delta P_{PV}(s) + \Delta P_{VI}(s) - \Delta P_L(s)\right) \quad (1)$$

in this equation:

$$\Delta P_m(s) = \frac{1}{1 + sT_t}\Delta P_g(s) \quad (2)$$

$$\Delta P_g(s) = \frac{1}{1 + sT_g}\left(\Delta P_C(s) - \frac{1}{R}\Delta f(s)\right) \quad (3)$$

$$\Delta P_C(s) = \frac{K_S}{s}(\beta \cdot \Delta f(s)) \quad (4)$$

$$\Delta P_W(s) = \frac{1}{1+sT_{WT}}\Delta P_{\text{wind}}(s) \quad (5)$$

$$\Delta P_{PV}(s) = \frac{1}{1+sT_{PV}}\Delta P_{\text{solar}}(s) \quad (6)$$

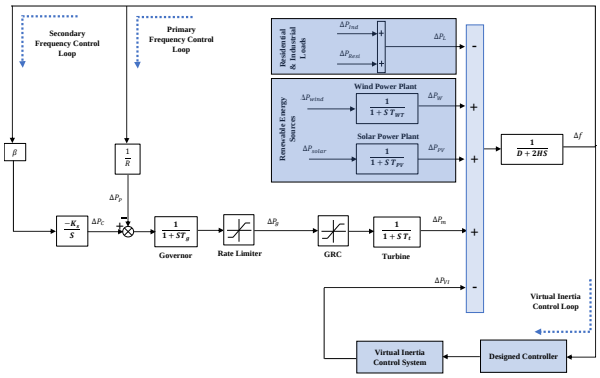

Fig. 2. The dynamic model of the MG under study

In the presented equations, the variables are defined as follows: P_C represents changes in the area control error action resulting from secondary control, ΔP_m denotes fluctuations in the output power of the TPG, ΔP_P signifies variations in the primary control's control action, ΔP_W accounts for fluctuations in the generated power from the WPP, ΔP_{wind} characterizes changes in the initial wind power, ΔP_g indicates the generated power from turbines, ΔP_{solar} represents alterations in the initial solar energy level, ΔP_{PV} captures fluctuations in the generated power from the SPP, ΔP_{Ind} signifies alterations in the demand from industries, ΔP_{Resi} denotes shifts in residential load power usage, ΔP_L denotes the overall shift in the system's load profile, and ΔP_{VI} accounts for shifts in the output power of the VI module.

III. Virtual Inertia Mechanism

In traditional electricity networks, the stability of the electricity grid is maintained by the kinetic energy stored in the rotational mass of traditional generators, which provides the network's inertia. However, in islanded MGs, RGs are tasked with delivering electricity power to the demand side. With the increasing adoption of inverter-connected RGs into MGs characterized by limited inertia, the system inertia is reduced, which can lead to instability and cascading failures in frequency events. To address this issue, VIC can be employed in low-inertia MGs to emulate the inertia of conventional generation units. In this paper, virtual damping and virtual inertia control as depicted in Fig. 3, which have been utilized in many investigations [15, 20, 30, 33], are considered for the energy storage system to calculate the ESS active power and add it to the target value for the microgrid in the event of disturbances. By employing VIC in the ESS, the requisite VIC power can be provided to strengthen the stability of grid frequency. The equation for VIC is expressed as:

$$\Delta P_{VI}(s) = \frac{sK_{VI}+D_{VI}}{1+sT_{INV}}(\Delta f(s)) \quad (7)$$

In this equation, K_{VI} is the Virtual inertia gain and D_{VI} indicates the Virtual damping gain.

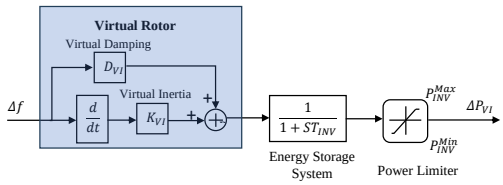

Fig. 3. Virtual inertia control mechanism.

IV. The designed procedures of the proposed control strategies

In this part, we will present three distinct control approaches for simulating inertia in the MG. These approaches consist of the innovative ONFOPI+VI controller, which is the main contribution of this article, along with the optimal COA-VI and the OFOPI+VI control strategies. We will use the COA-VI and OFOPI+VI control strategies for analyzing and comparing the findings.

A. Optimal Design of VIC Using the COA

We first designed the COA-VI controller for the MG system. The block diagram of the proposed COA-VI controller is shown in Fig. 4. In this approach, the parameters of the VIC are optimally tuned using the COA.

With regard to the cost function as per Equation (8) and the θ_v^{VI} VI's designing array, the parameters of optimal VI will be devised.

$$C_f(\theta_v^{VI}) = \int_{t=0}^{T_f} t|\Delta f|\,dt \quad (8)$$

$$\theta_v^{VI} = [\mathrm{K_{VI}\ D_{VI}}]^{\mathrm{T}} \quad (9)$$

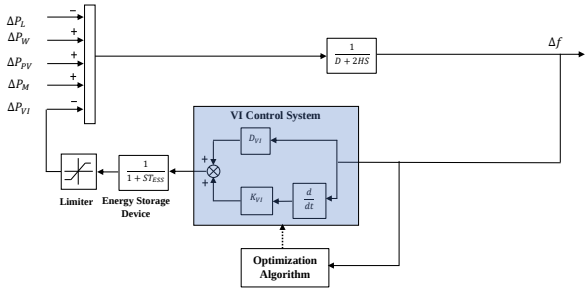

Fig. 4. The block diagram of COA-VI control structure.

The design vector is constrained within the bounds of $0 \leq K_{VI} \leq 5$ and $0 \leq D_{VI} \leq 5$. To minimize the objective function presented in Equation (8) and determine the optimal VI gains, the COA is employed. The COA, originally proposed by Naruei and Keynia [34], draws inspiration from the collective behavior of coots, a type of waterfowl. This algorithm aims to replicate both the regular and irregular movements observed in coots on the water's surface. The stages of the COA can be succinctly outlined as follows [34]:

Step1: The population is first randomly generated using the equation:

$$Cootpos\ (i) = rand\ (1, d) * (ub - lb) + lb \quad (10)$$

in which $Cootpos\ (i)$, d, ub, and lb refer to the position of i^{th} coot, the number of decision variables, and the upper and lower bands of search space, respectively.

Step 2: For each coot location, the cost function is calculated. Additionally, the parameters N_L and N_{coot}, denoting the number of leaders and coots, are randomly selected to identify the best coot or leader as the global optimum.

Step 3: In this stage, the coots' locations are then updated through four movements:

A. Random movement of the swarm to both sides:

Firstly, a stochastic location Q is produced using the equation:

$$Q = rand\ (1, d) * (ub - lb) + lb \quad (11)$$

To prevent being trapped in local optima, this location is updated as outlined below:

$$\text{Cootpos}\ (i) = \text{Cootpos}\ (i) + \Lambda_{cootpos} * R_2 * (Q - \text{Cootpos}\ (i)) \quad (12)$$

$$\Lambda_{cootpos} = 1 - iter * \left(\frac{1}{maxiter}\right) \quad (13)$$

In the above equation, R_2 refers to a random number in the interval [0,1] and $iter$ and $maxiter$ are the current interaction and the maximum iteration, respectively.

B) Chain Movement

To simulate this movement, the average position of two coots is obtained using Eq. (14).

$$Cootpos\ (i) = 0.5 * (Cootpos\ (i-1) + Cootpos\ (i)) \quad (14)$$

C) Location Adjustment Based on the Leaders of the Group.

As the coots navigate, they align their positions with the group leaders. This entails adapting their positions according to the leaders of the group. Denoting K as the leader's index number, i as the index number of the current coot, and N_L as the total number of leaders, the coot's selection of a leader can be expressed as outlined below:

$$K = 1 + (i\ MOD\ N_L) \quad (15)$$

In the above-mentioned movement, the position of coots is updated as follows:

$$Cootpos\ (i) = Leaderpos\ (k) + 2 * R_1 * cos\ (2\pi R) * (Leaderpos\ (k) - Cootpos\ (i)) \quad (16)$$

in which R_1 is a random number in the interval [0,1]. Also, $Leaderpos\ (k)$ and R are chosen leader locations and a stochastic number in the interval [-1,1], respectively.

D) Leader movement

To converge towards the optimal region, the group leader's location is updated according to Equation (17)

$$Leaderpos(i) = \begin{cases} B_{cootpos} * R_3 * \cos(2\pi R) * \big((gbest - Leaderpos(i)\big) + gbest,\ R_4 < 05 \\ B_{cootpos} * R_3 * \cos(2\pi R) * \big((gbest - Leaderpos(i)\big) - gbest,\ R_4 \geq 05 \end{cases} \quad (17)$$

$$B_{cootpos} = 2 - iter * \left(\frac{1}{maxiter}\right) \quad (18)$$

here, R_3 and R_4 are the stochastic numbers in the interval [0,1] and $gbest$ is the position ever found.

Step 4: Achieving Algorithm Convergence by Increasing Iterations.

Increasing the number of iterations leads to the discovery of the best cost function and ensures the convergence of the algorithm.

B. The Design Procedure of the Proposed FOPI-Based VI Controller

In this section, at first, the preliminaries of the fractional order PI controller are presented, and then the design procedure of the designed FOPI-based VI controller is described.

Initially, the OFOPI+VI controller is implemented to replace the inertia necessary for the electricity network. This framework is meticulously crafted in accordance with frequency and power control criteria. It's essential to highlight the significance of VI parameters and FOPI coefficients in ensuring the stability of microgrids and their ability to handle disturbances effectively. Consequently, fine-tuning these gains becomes paramount for achieving optimal functionality. The OFOPI+VI control strategy leverages the COA algorithm to find the optimum values of VI and FOPI gains, K_{VI}, D_{VI}, K_P, K_I, and λ.

B.1. Preliminaries of Fractional Order Controller

Combining differentiation with the fundamental non-integer order operator, defined as follows, results in fractional calculus.

$${}_aD_t^{\beta} = \begin{cases} \frac{d^{\beta}}{dt^{\beta}} & \beta > 0 \\ 1 & \beta = 0 \\ \int_a^t (d\tau)^{\beta} & \beta < 0 \end{cases} \quad (19)$$

In Equation (19), the operation's bounds are a and t, while its order is determined by β ($\beta \epsilon R$). Several methods, such as

Grunwald-Letnikov, Riemann-Liouville, and Caputo, can be used to represent fractional integro-differential equations. However, Caputo's formula is the most widely used approximation for this purpose, and it is given by the following equation.

$$D^{\alpha}f(t) = \frac{1}{\Gamma(m-\alpha)}\int_0^t \frac{D^m f(t)}{(t-\tau)^{\alpha+1-m}}d\tau, \alpha \in R^+, m \in Z^+, m-1 \le \alpha \le m \quad (20)$$

where α represents the order of the derivative of f(t) with zero initial conditions, and Γ(·) denotes the Gamma function.

Oustaloup [35] was a pioneer in applying FOC for dynamic system control, leading to the development of the CRONE controller (a French acronym for Commande Robuste d'Ordre Non-Entier). His studies demonstrated that this controller outperforms the classical PID controller in various applications. On the other hand, Podlubny [36] introduced the FOPID controller as an extension of the PID controller. This controller exhibits strong performance in both the time and frequency domains. The FOPID controller provides greater flexibility by incorporating non-integer orders for integration and differentiation, allowing for more accurate adjustments. In contrast to traditional PID controllers, FOPID can more effectively model systems with complex dynamics. This results in better transient performance, enhanced stability under parameter changes, and improved frequency regulation in microgrids. The following equations present the output expressions for PID and FOPID controllers in the time domain.

$$u_{PID}(t) = K_P e(t) + K_I \int_0^t e(\tau)\,d\tau + K_D \frac{de(t)}{dt} \quad (21)$$

$$u_{FOPID}(t) = K_P e(t) + K_I D^{-\lambda} e(t) + K_D D^{\mu} e(t) \quad (22)$$

In these equations, K_P, K_I, and K_D represent the gains associated with the proportional, integral, and derivative terms, respectively. The parameters λ and μ define the orders of the integral and derivative operators. The function e(t) denotes the error, which is the difference between the desired reference value and the actual system output. Unlike conventional PID controllers, the FOPID controller introduces two additional tuning parameters, making the adjustment process more complex.

B.2. The Design Procedure of the Designed OFOPI+VI Control Methodology

In this paper, the fractional order PI controller as described in the following equation is used to improve the performance of the VIC.

$$u_{FOPI}(t) = K_P e(t) + K_I D^{-\lambda} e(t) \quad (23)$$

The block diagram of the proposed OFOPI+VI controller is depicted in Fig. 5.

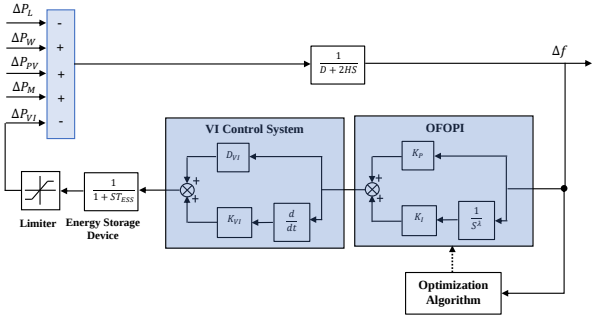

Fig. 5. The schematic diagram of OFOPI+VI controller.

Taking into account the cost function outlined in the previous section, the design procedure utilizes the following design vector:

$$\theta_v^{VI} = [\mathrm{K}_P\ K_\mathrm{I}\ \lambda]^\mathrm{T} \quad (24)$$

The upper and lower bounds of the design vector are defined as $0 \le K_P \le 200, 0 \le K_I \le 200$, and $0 \le \lambda \le 2$, respectively.

C. The Design Procedure of the Proposed Nonlinear Fractional-Order PI-Based VI Controller

In this section, at first, the preliminaries of the nonlinear fractional order PI controller are presented, and then the design procedure of the proposed ONFOPI+VI controller is described.

C.1. Preliminaries of Nonlinear Fractional Order Controller

The Nonlinear Fractional-Order Controller (NFOC) was introduced by Petras [32, 37-38]. Through various examples, he demonstrated the effective performance of NFOC in nonlinear control systems. The output expression for the nonlinear FOPID controller is given as follows:

$$u_{NFOPID}(t) = g\big(e(t)\big)\Big(K_P e(t) + K_I D^{-\lambda} e(t) + K_D D^{\mu} e(t)\Big) \quad (25)$$

$$g\big(e(t)\big) = K_0 + (1-K_0)|e(t)|\ , \qquad K_0 \epsilon (0,1) \quad (26)$$

When $K_0 = 1.0$, the classical form of the FOPID controller in Eq. (22) is obtained. However, when $K_0 \neq 1.0$, the system defines a nonlinear FOPID controller with six degrees of freedom.

C.2. The Design Procedure of the Proposed ONFOPI+VI Controller

In this section, the nonlinear fractional order PI controller as described in the following equation is used to improve the performance of the optimal COA-VI designed in section A.

$$u_{NFOPI}(t) = g(\Delta f)\big(K_P \Delta f + K_I D^{-\lambda} \Delta f\big) \quad (27)$$

$$g(\Delta f) = K_0 + (1-K_0)|\Delta f|\ , \qquad K_0 \epsilon (0,1) \quad (28)$$

The block diagram of the proposed ONFOPI+VI controller is depicted in Fig. 6.

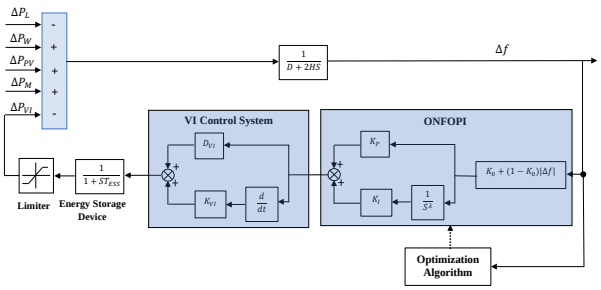

Fig. 6. The schematic diagram of the ONFOPI+VI controller.

Using the cost function of relationship (8), the following design vector is used for the design procedure.

$$\theta_v^{VI} = [\mathrm{K}_P\ K_\mathrm{I}\ \ K_0\ \ \lambda]^\mathrm{T} \tag{29}$$

The upper and lower bounds of the design vector are $0 \leq K_P \leq 200$, $0 \leq K_I \leq 200$, $0 \leq K_0 \leq 1$ and $0 \leq \lambda \leq 2$, respectively.

V. Results, Analysis, and Discussion.

This section examines the significance and efficiency of implementing the suggested ONFOPI+VI to enhance the grid's frequency response. The industrial and residential loads were simulated using the signal builder block, as shown in Fig. 2. The TPG has been modeled using first-order transfer functions, GRC, and limiter blocks. Additionally, the WT and PV systems have been simulated using first-order transfer function blocks. The ESS modeling has been presented using first-order transfer function blocks. To demonstrate the effectiveness of the proposed inertia control design, nonlinear simulations have been conducted using MATLAB/Simulink software. These simulations involve contrasting critical cases with different penetration rates of RGs and load patterns to examine the microgrid frequency response. In this research article, we evaluate the performance of different VI controller strategies in three different cases. We use *Δf*, as an indicator to assess the grid's functionality.

In power system stability assessment, four principal performance indicators are typically utilized: the Integral Square Error (ISE), Integral Absolute Error (IAE), Integral Time Weighted Absolute Error (ITAE), Maximum Overshoot (MO), and Maximum Undershoot (MU). These metrics have become standard evaluation tools in dynamic system studies, defined mathematically as follows:

$$IAE = \int_{t=0}^{t=T_{sim}} |\Delta f|\, dt \tag{30}$$

$$ISE = \int_{t=0}^{t=T_{sim}} (\Delta f)^2\, dt \tag{31}$$

$$ITAE = \int_{t=0}^{t=T_{sim}} t|\Delta f|\, dt \tag{32}$$

$$MO = max(f(t)) - f_{nominal} \tag{33}$$

$$MU = f_{nominal} - min(f(t)) \tag{34}$$

The comparative analysis shows that the ONFOPI+VI control methodology outperforms other control approaches. Specifically, the ONFOPI+VI controller yielded better outcomes than the T-VI, COA-VI, GAPI+VI, and OFOPI+VI control methods, resulting in an enhanced frequency response. The results yielded from utilizing the COA algorithm to the OFOPI+VI controllers in comparison with those of the T-VI and GAPI+VI are shown in Table 1. Furthermore, Table 2 displays the characteristics of the ONFOPI-based VI controller tailored for the assessed MG. The swarm size and the maximum iterations of the COA algorithm for COA-VI, OFOPI+VI, and ONFOPI+VI are selected as 500 and 100, respectively.

TABLE I PARAMETERS OF T-VI, COA-VI, GAPI+VI, AND OFOPI+VI CONTROLLERS PERTAINING TO THE EVALUATED MG

Control Method	K_P	K_I	K_{VI}	D_{VI}	λ
W-VI	-	-	-	-	-
T-VI	-	-	0.5	-	-
COA-VI	-	-	2.962	3.862	-
GAPI+VI	113.663	122.14	3.710	4.794	-
OFOPI+VI	136.412	142.677	2.962	3.862	0.865

TABLE II PARAMETERS OF THE DEVELOPED ONFOPI+VI CONTROLLER FOR THE MG UNDER EXAMINATION

	K_P	K_I	K_{VI}	D_{VI}	λ	K_0
ONFOPI+VI Controller	197.101	189.962	2.962	3.862	0.585	0.895

A. Case I: Dynamic Response of the MG to Sever Load Changes

This subsection presents the results of Case I, which investigates the impact of connecting and disconnecting various loads in the presence of RGs. In this case, the residential load ΔP_{Resi} was disconnected after 40 seconds at a level of 0.05. The industrial load ΔP_{Ind} became grid-connected after 20 seconds at a level of 0.1. The generation from the W_{PP} had an initial change ΔP_W of 0.12 from the beginning, while the generation from the SPP also had an initial change ΔP_{PV} of 0.08 from the start. It is worth mentioning that all changes are in P.U. Table 3 summarizes the different operational conditions studied in Case I.

The changes in frequency deviation for this scenario are shown in Fig.7 and Table 4. These results indicate that the ONFOPI+VI control method is better than the T-VI, COA-VI, GAPI+VI, and OFOPI+VI methods.

B. Case II: Dynamic Response of the MG to Sever Changes of Different RGs

At the outset, the residential load undergoes a 0.05 change, whereas the industrial load sees a 0.1 increase. The

TABLE III OPERATIONAL CONDITIONS UNDER CASE I.

	Connecting	Disconnecting	(P.U.)
ΔP_{Resi}	$0s$	$40s$	0.05
ΔP_{Ind}	$20s$	-	0.1
ΔP_W	$0s$	-	0.12
ΔP_{PV}	$0s$	-	0.08

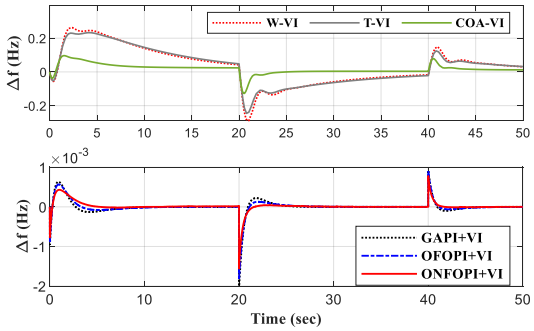

Fig. 7. Performance comparison of T-VI, COA-VI, GAPI+VI, OFOPI+VI, and proposed ONFOPI+VI control frameworks for the microgrid under examination pertaining to Case I

TABLE IV EVALUATING THE PERFORMANCE OF VARIOUS CONTROL METHODOLOGIES FOR THE MICROGRID IN CASE I.

Control Method	IAE	ISE	ITAE	MU	MO
W-VI	4.8268	0.7068	87.378	-0.2903	0.2625
T-VI	4.7372	0.6425	86.142	-0.2457	0.2326
COA-VI	1.1904	0.0573	20.180	-0.1279	0.0963
GAPI+VI	0.0032	2.00e-06	0.0522	-0.0021	0.0010
OFOPI+VI	0.0031	2.00e-06	0.0475	-0.0021	0.0010
ONFOPI+VI	0.0022	1.00e-06	0.0319	-0.0015	0.0008

generation from the WPP changes by 0.12 but is disconnected after 40 seconds. Meanwhile, the input from the SPP experienced a 0.08 change after 20 seconds, when it became grid-connected. Table 5 summarizes the different operational conditions studied in Case II.

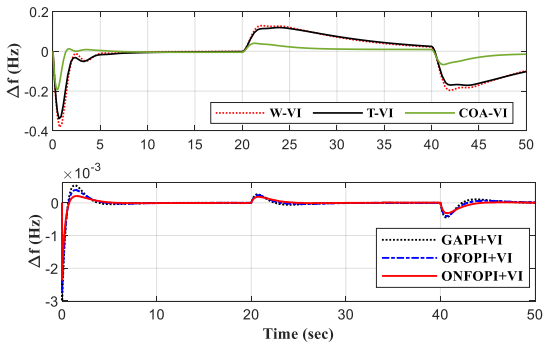

i) Performance comparison of T-VI, COA-VI, GAPI+VI, OFOPI+VI, and proposed ONFOPI+VI control frameworks for the microgrid under examination pertaining to Case II

TABLE V OPERATIONAL CONDITIONS UNDER CASE II.

	Connecting	Disconnecting	(P.U.)
ΔP_{Resi}	$0s$	-	0.05
ΔP_{Ind}	$0s$	-	0.1
ΔP_W	$0s$	$40s$	0.12
ΔP_{PV}	$20s$	-	0.08

TABLE VI EVALUATING THE PERFORMANCE OF VARIOUS CONTROL METHODOLOGIES FOR THE MICROGRID IN CASE II

Control Method	IAE	ISE	ITAE	MU	MO
W-VI	3.4333	0.4896	104.234	-0.3814	0.1293
T-VI	3.3563	0.4274	101.886	-0.3382	0.1195
COA-VI	0.8721	0.0427	23.864	-0.1930	0.0405
GAPI+VI	0.0033	2.0e-06	0.0566	-0.0031	0.00054
OFOPI+VI	0.0032	2.0e-06	0.0529	-0.0027	0.00039
ONFOPI+VI	0.0023	1.0e-06	0.0419	-0.0024	0.00021

The changes in frequency deviation for this scenario are shown in Fig.8 and Table 6. These results indicate that the ONFOPI+VI control method is better than the T-VI, COA-VI, GAPI+VI, and OFOPI+VI methods.

C. Case III. Dynamic Response of the MG to Sever and Simultaneous Changes of Different Types of Loads and RGs

In Case III, various components undergo changes in power supply and demand. The residential load disconnects by 0.05 at 65 seconds, while the industrial load connects by 0.1 after 25 seconds. The WPP connects by 0.12 after 45 seconds. Concurrently, the SPP disconnects by 0.08 at 85 seconds. Table 7 summarizes the different operational conditions studied in Case III. The changes in frequency deviation for this scenario are shown in Fig.9 and Table 8.

TABLE VII OPERATIONAL CONDITIONS UNDER CASE III.

	Connecting	Disconnecting	(P.U.)
ΔP_{Resi}	$0s$	$65s$	0.05
ΔP_{Ind}	25 s	-	0.1
ΔP_W	$45s$	-	0.12
ΔP_{PV}	$0s$	$85s$	0.08

In Case III, the ONFOPI+VI stands out among four other controllers (W-VI, T-VI, GAPI+VI, and OFOPI+VI) regarding MO, MU, ISE, ITAE, and IAE. In particular, the ONFOPI+VI makes significant strides, with roughly 99.60% better performance contrasted with the T-VI control methodology, 99.17% contrasted with the COA-VI controller, 30.00% contrasted with the GAPI+VI controller, and 30.00% contrasted with the OFOPI+VI control methodology in terms of MO. Regarding MU, the ONFOPI+VI demonstrates significant enhancements of around 99.43% contrasted with the T-VI, 98.92% contrasted

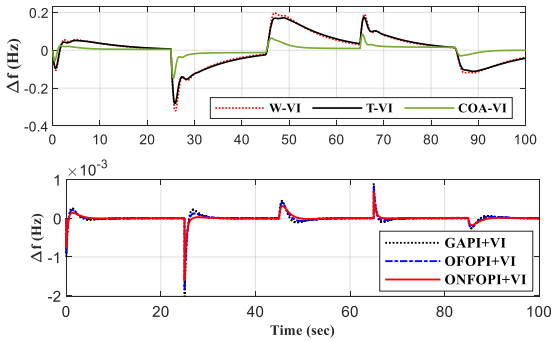

Fig. 8. Performance comparison of T-VI, COA-VI, GAPI+VI, OFOPI+VI, and proposed ONFOPI+VI control frameworks for the microgrid under examination pertaining to Case III

TABLE VIII EVALUATING THE PERFORMANCE OF VARIOUS CONTROL METHODOLOGIES FOR THE MICROGRID IN CASE III

Control Method	IAE	ISE	ITAE	MU	MO
W-VI	6.8463	0.7513	355.853	-0.3205	0.1972
T-VI	6.8150	0.6943	357.646	-0.2823	0.1738
COA-VI	1.6389	0.0530	79.271	-0.1479	0.0842
GAPI+VI	0.0041	2.00e-06	0.1670	-0.0021	0.001
OFOPI+VI	0.0038	1.98e-06	0.1531	-0.0019	0.001
ONFOPI+VI	0.0028	1.00e-06	0.1226	-0.0016	0.0007

with the COA-VI, 23.80% contrasted with the GAPI+VI control methodology, and 15.78% contrasted with the OFOPI+VI control methodology. Furthermore, regarding IAE, the ONFOPI+VI demonstrates remarkable enhancements of nearly 99.95% contrasted with the T-VI, 99.82% contrasted with the COA-VI, 31.70% contrasted with the GAPI+VI, and 26.31% contrasted with the OFOPI+VI controllers. These findings confirm the excellence of the ONFOPI+VI over the other four control methodologies studied, showcasing its ability to significantly reduce MO, MU, and IAE, thereby enhancing control precision and overall performance.

The proposed ONFOPI+VI control methodology also demonstrated a noteworthy reduction of 50.00% in ISE, 28.65% in IAE, 11.11% in the MU, and 46.15% in MO in Case II when compared with the OFOPI+VI control methodology, highlighting its superior performance and efficacy across diverse scenarios and metrics.

In the first case, the ONFOPI+VI control methodology showed notable advancements of roughly 99.95% contrasted with the T-VI, 99.84% contrasted with the COA-VI, 38.87% contrasted with the GAPI+VI, and 32.84% contrasted with the OFOPI+VI controller in terms of ITAE.

VI. Conclusion

This study introduced an innovative ONFOPI+VI control methodology to enhance frequency stability in low-inertia islanded microgrids. By integrating nonlinear fractional-order PI control with virtual inertia and damping mechanisms, the approach effectively manages energy storage systems and addresses uncertainties in renewable generation. The proposed controller was optimized using the COA algorithm, demonstrating significant improvements in system performance. Simulation results demonstrated that the ONFOPI+VI controller outperformed conventional methods, achieving at least a 30% improvement in IAE, a 22% reduction in MU, and a 20% improvement in ITAE. The proposed approach is adaptable to varying renewable generation levels and offers a robust solution for dynamic stability. Future research could explore hybrid controllers combining intelligent and fractional-order strategies, integrate electric vehicle batteries as mobile energy storage, and assess the real-time implementation of the ONFOPI+VI methodology, with a focus on communication delays and practical applicability.

References

[1] E. S. Parizy, S. Choi, and H. R. Bahrami, "Grid-Specific Co-Optimization of Incentive for Generation Planning in Power Systems With Renewable Energy Sources," *IEEE Transactions on Sustainable Energy,* Vol. 11, no. 2, pp. 947-957, 2020.

[2] Y. Li, M. Han, M. Shahidehpour, J. Li, and C. Long, "Data-driven distributionally robust scheduling of community integrated energy systems with uncertain renewable generations considering integrated demand response," *Applied Energy*, Vol. *335*, p. 120749, 2023.

[3] S. Jain, R. K.Ahuja, , A. Gupta, Y. Arya, "Hybrid intelligent h-AFSA-ANN controller for the SPV-BESS-DG-based DC microgrid integrated system," *Electrical Engineering*, pp. 1-26, 2024.

[4] M. El-Hendawi, H. A. Gabbar, G. El-Saady, and E.-N. A. Ibrahim, "Control and EMS of a Grid-Connected Microgrid with Economical Analysis,"*Energies,*Vol. 11, no. 1, p.129, 2018.

[5] M. Deepak, R. J. Abraham, F. M. Gonzalez-Longatt, D. M. Greenwood, and H.-S. Rajamani, "A novel approach to frequency support in a wind integrated power system," *Renewable Energy,* Vol. 108, pp. 194-206, 2017.

[6] A. Khazali, N. Rezaei, H. Saboori, and J. M. Guerrero, "Using PV systems and parking lots to provide virtual inertia and frequency regulation provision in low inertia grids," *Electric Power Systems Research,* Vol. 207, p. 107859, 2022.

[7] S. M. Said, M. Aly, B. Hartmann, and E. A. Mohamed, "Coordinated fuzzy logic-based virtual inertia controller and frequency relay scheme for reliable operation of low-inertia power system," *IET Renewable Power Generation,* Vol. 15, no. 6, pp. 1286-1300, 2021.

[8] B. Khokhar and K. P. S. Parmar, "A novel adaptive intelligent MPC scheme for frequency stabilization of a microgrid considering SoC control of EVs," *Applied Energy,* Vol. 309, p. 118423, 2022.

[9] T. Mahto, R. Kumar, H. Malik, S. M. S. Hussain, and T. S. Ustun, "Fractional Order Fuzzy Based Virtual Inertia Controller Design for Frequency Stability in Isolated Hybrid Power Systems," *Energies,* Vol. 14, no. 6, p. 1634, 2021.

[10] [G. Magdy, H. Ali, and D. Xu, "A new synthetic inertia system based on electric vehicles to support the frequency stability of low-inertia modern power grids," *Journal of Cleaner Production,* Vol. 297, p. 126595, 2021.

[11] P. Saxena, N. Singh, and A. K. Pandey, "Enhancing the dynamic performance of microgrid using derivative controlled solar and energy storage based virtual inertia system," *Jour. of Energy Storage,* Vol. 31, p. 101613, 2020.
[12] A. Fernández-Guillamón, E. Gómez-Lázaro, E. Muljadi, and Á. Molina-García, "Power systems with high renewable energy sources: A review of inertia and frequency control strategies over time," *Renewable and Sustainable Energy Reviews,* Vol. 115, p. 109369, 2019.
[13] M. Dreidy, H. Mokhlis, and S. Mekhilef, "Inertia response and frequency control techniques for renewable energy sources: A review," *Renewable and Sustainable Energy Reviews,* Vol. 69, pp. 144-155, 2017.
[14] K. S. Ratnam, K. Palanisamy, and G. Yang, "Future low-inertia power systems: Requirements, issues, and solutions - A review," *Renewable and Sustainable Energy Reviews,* Vol. 124, p. 109773, 2020.
[15] M. Sajadinia, "An adaptive virtual inertia control design for energy storage devices using interval type-2 fuzzy logic and fractional order PI controller," *Journal of Energy Storage,* Vol. 84, p. 110791, 2024.
[16] K. Komala, K. P. Kumar, and S. H. C. Cherukuri, "Storage and non-Storage Methods of Power balancing to counter Uncertainty in Hybrid Microgrids - A review," *Journal of Energy Storage,* Vol. 36, p. 102348, 2021.
[17] J. Liu, Z. Yang, J. Yu, J. Huang, and W. Li, "Coordinated control parameter setting of DFIG wind farms with virtual inertia control," *International Journal of Electrical Power & Energy Systems,* Vol. 122, p. 106167, 2020.
[18] E. Unamuno, J. Paniagua, and J. A. Barrena, "Unified Virtual Inertia for ac and dc Microgrids: And the Role of Interlinking Converters," *IEEE Electrification Magazine,* Vol. 7, no. 4, pp. 56-68, 2019.
[19] G. Magdy, G. Shabib, A. A. Elbaset, and Y. Mitani, "A novel coordination scheme of virtual inertia control and digital protection for microgrid dynamic security considering high renewable energy penetration," *IET Renew. Power Gener.,* Vol. 13, no. 3, pp. 462-474, 2019.
[20] R. Mandal and K. Chatterjee, "Virtual inertia emulation and RoCoF control of a microgrid with high renewable power penetration," *Electric Power Systems Research,* Vol. 194, p. 107093, 2021.
[21] T. Kerdphol, F. S. Rahman, Y. Mitani, M. Watanabe, and S. K. Küfeoğlu, "Robust Virtual Inertia Control of an Islanded Microgrid Considering High Penetration of Renewable Energy," *IEEE Access,* Vol. 6, pp. 625-636, 2018.
[22] A. Fathi, Q. Shafiee, and H. Bevrani, "Robust Frequency Control of Microgrids Using an Extended Virtual Synchronous Generator," *IEEE Transactions on Power Systems,* Vol. 33, no. 6, pp. 6289-6297, 2018.
[23] S. Asgari, A. A. Suratgar, and M. Kazemi, "Feedforward Fractional Order PID Load Frequency Control of Microgrid Using Harmony Search Algorithm," *Iranian Journal of Science and Technology, Transactions of Electrical Engineering,* Vol. 45, no. 4, pp. 1369-1381, 2021.
[24] A.X.R. Irudayaraj, N.I.A. Wahab, M.G. Umamaheswari, M.A.M. Radzi, N.B. Sulaiman, V. Veerasamy, S.C. Prasanna, and R. Ramachandran, "A Matignon's Theorem Based Stability Analysis of Hybrid Power System for Automatic Load Frequency Control Using Atom Search Optimized FOPID Controller," *IEEE Access,* Vol. 8, pp. 168751-168772, 2020.
[25] A. Fathy, D. Yousri, H. Rezk, S. B. Thanikanti, and H. M. Hasanien, "A Robust Fractional-Order PID Controller Based Load Frequency Control Using Modified Hunger Games Search Optimizer," *Energies,* Vol. 15, no. 1, p. 361, 2022.
[26] A.-A. Zamani, M. Shafiee, and M. Sajadinia, "Optimal self-tuning fractional order fuzzy load frequency control considering sustainable energy sources and electric vehicle," *International Journal of Ambient Energy,* pp. 1-15, 2023.
[27] Y. Arya, R. Ahmad, I. Nasiruddin, and M. F. Ahmer, "LFC performance advancement of two-area RES penetrated multi-source power system utilizing CES and a new CFOTID controller," *Journal of Energy Storage*, Vol.*87*, p.111366., 2024.
[28] K. Hongesombut and R. Keteruksa, "Fractional order based on a flower pollination algorithm PID controller and virtual inertia control for microgrid frequency stabilization," *Electric Power Systems Research,* Vol. 220, p. 109381, 2023.
[29] S.A. Zaid, A. Bakeer, G. Magdy, H. Albalawi, A.M. Kassem, M.E. El-Shimy, H. AbdelMeguid, and B. Manqarah, "A new intelligent fractional-order load frequency control for interconnected modern power systems with virtual inertia control," *Fractal and Fractional,* Vol. 7, no. 1, p. 62, 2023.
[30] R. Mandal and K. Chatterjee, "Design of a maiden synthetic inertia controller using super-capacitor energy storages and electric vehicles and real-time validation of the performance of the controller," *Journal of Energy Storage,* Vol. 55, p. 105559, 2022.
[31] C. A. Monje, Y. Chen, B. M. Vinagre, D. Xue, and V. Feliu-Batlle, *Fractional-order systems and controls: fundamentals and applications*. Springer Science & Business Media, 2010.
[32] I. Petráš, *Fractional-order nonlinear systems: modeling, analysis and simulation*. Springer Science & Business Media, 2011.
[33] T. Kerdphol, FS. Rahman, M. Watanabe, and Y. Mitani, Virtual inertia synthesis and control. Cham, Switzerland, Springer, 2021.
[34] I. Naruei and F. Keynia, "A new optimization method based on COOT bird natural life model", *Expert Systems with Applications*, Vol. *183*, p. 115352, 2021.
[35] A. Oustaloup, La commande CRONE: commande robuste d'ordre non entier. Hermes. 1991.
[36] P. Shah, and S. Agashe, "Review of fractional PID controller", *Mechatronics*, Vol. *38*, pp. 29-41, 2016.
[37] I. Petráš, "A note on fractional-order non-linear controller: possible neural network approach to design". In *2016 International Joint Conference on Neural Networks (IJCNN)*, 2016, IEEE, pp. 603-608.
[38] I. Petráš, "Tuning of the non-linear fractional-order controller". In *2019 20th International Carpathian Control Conference (ICCC),* 2019, IEEE, pp. 1-4.

Appendix A

Microgrid Control System: $H = 0.083 P.U.MWs$, $D=0.015\ P.U.\ MW/Hz$; Inertia Control: $T_{INV} = 10s$, $P_{ESS}^{U} = 0.3\ P.U.MW$, $P_{ESS}^{L} = -0.3\ P.U.MW$; Primary Control: $R = 2.4\ Hz/P.U.MW$, $T_g = 0.1s$, $T_t = 0.4\ s$, $GRC= 20\%$, $V_U = 0.3\ P.U.MW$, $V_L = -0.3\ P.U.MW$; Secondary Control: $\beta = 1.0\ P.U.MW/Hz$, $K_s = 0.05$; Renewable Energy Sources: $T_{WT} = 1.5s$, $T_{PV} = 1.8s$

Abbas-Ali Zamani was born in 1986 in Isfahan, Iran. He earned a B.Sc. degree in electronic engineering from Hakim Sabzevari University in Iran in 2009, and an M.Sc. degree in control engineering from Isfahan University of Technology in 2011. In 2018, he received his Ph.D. in control engineering from the University of Sistan and Baluchestan in Iran. Dr. Zamani is currently an assistant professor in the Department of Electrical Engineering, National University of Skills (NUS), Tehran, Iran and Technical and Vocational University (TVU) , Tehran, Iran. Seismic control, power system control, smart grids, renewable energies, and artificial intelligence are among his research interests.

IECO

This page intentionally left blank.

International Journal Of
Industrial Electronics Control and Optimization
Print ISSN: 3517-2645
Online ISSN: 3568-2645
Homepage: https://ieco.usb.ac.ir/

Torque Ripple Reduction in Modular Drive of a Non-Sinusoidal, Asymmetric Six-Phase, Permanent Magnet Synchronous Motor with Double Stator Windings using Harmonic Current Injection Strategy

Davood Maleki | Abolfazl Halvaei Niasar

Department of Electrical & Computer Engineering, University of Kashan, Kashan, Iran
Corresponding author's email: halvaei@kashanu.ac.ir

Article Info

Article type:
Research Article

Article history:
Received: 02-April-2025
Received in revised form: 15-May-2025
Accepted: 26-May-2025
Published online: 22-Dec-2025

Keywords:
H-bridge inverter,
Quasi-proportional resonant controller,
Reliability,
Six-phase PMSM.

ABSTRACT

Multiphase permanent magnet synchronous motors (PMSMs) are widely adopted in high-power-density and high-efficiency applications, particularly where reliability is a critical design requirement. This paper presents a control strategy for an asymmetric six-phase PMSM with a dual-winding per-phase stator configuration, where each phase consists of two physically aligned and symmetrically distributed windings relative to the stator center to ensure enhanced drive reliability. The system employs a fully modular control and power architecture, with each winding pair in a phase supplied by an independent single-phase H-bridge inverter. To mitigate torque ripple caused by non-sinusoidal back-EMF waveforms, an optimized harmonic current injection technique is implemented alongside quasi-proportional resonant (QPR) current controllers for precise harmonic compensation. Additionally, under fault conditions (e.g., winding failure), a fault-tolerant control (FTC) algorithm is applied, focusing on the suppression of second-order harmonic torque oscillations to maintain stable operation. The proposed control methodologies are validated through detailed Simulink simulations and further supported by experimental results, confirming their effectiveness in improving performance and reliability.

NOMENCLATURE

e_{x_i}	Back-EMF voltage of winding x_i	v_{x_i}	Voltage of winding x_i
i_{x_i}	Current of winding x_i	i_{y_j}	Current of winding y_j
ψ_{x_i}	Linkage flux of winding x_i	P_{x_i}	Air gap power of the winding x_i
L_{x_i}	Self-inductance of winding x_i	$M_{x_i y_j}$	Mutual inductance between windings x_i and y_j
h	Order of harmonic in currents or back-EMFs	θ_r	Rotor position in electrical rad.
K_P	Proportional gain of PI controller	K_I	Integral gain of PI controller
K_P	Proportional gain of h^{th} harmonic in QPR	K_{Rh}	Resonant gain of h^{th} harmonic in QPR
ω_{ch}	Cut-off frequency of h^{th} harmonic in QPR	ω_o	Resonant frequency in QPR
ω_r	Rotor speed in electrical rad/sec	ω_m	Rotor speed in mechanical rad/sec
T_e	Electromagnetic or airgap torque	P_e	Airgap power
T_e^*	Reference torque	J	Inertia moment
T_l	Electromagnetic load	I_1, I_3, I_5	Injected harmonic current contents
E_1, E_3, E_5	Back-EMF harmonic contents	I_1^*, I_3^*, I_5^*	Reference injected harmonic current contents
T_0, P_0	Constant value of torque/airgap power	T_6, P_6	6^{th} harmonic of torque/airgap power

I. Introduction

Multiphase electric motors, defined as motors with more than three phases, have gained significant attention from researchers and industry professionals in recent years [1,2]. These motors are commonly used in medium- to high-power applications—such as large ships, submarine, and industrial mills—where enhanced reliability and reduced phase current stress are critical [3,4]. However, realizing these advantages depends on several factors, including motor structure and design. The most common multiphase configurations include 5, 6, 9, and 12-phase systems, with six-phase motors being the most prevalent. Compared to other multiphase motors, six-phase motors offer distinct benefits, such as control simplicity (similar to three-phase systems), ease of design and construction, and straightforward control implementation. As a result, they are widely used in sensitive applications requiring high redundancy, reliability, and fault tolerance, particularly in underwater propulsion systems [5,6].

In critical applications like electric drives for submarines and underwater vehicles, drive reliability is paramount. To ensure robust operation, redundancy is incorporated at both hardware and software levels. Hardware redundancy may involve increasing the number of phases, adding extra power switches, employing independent inverters for each phase, and incorporating redundant sensors and microcontrollers. Additionally, fault-tolerant control (FTC) methods are essential to maintaining uninterrupted operation in the event of a fault [7].

Fig. 1 illustrates the common topology of stator windings in six-phase PMSMs [8], which are classified into two categories: symmetric and asymmetric. In the asymmetric type (Fig. 1(a)), the distance between the axes of two adjacent windings is 30°, whereas in the symmetric type (Fig. 1(b)), it is 60°. Additionally, as seen in Fig. 1(a,b), a six-phase motor can be constructed using two three-phase windings with star connections, leading to its designation as a double-star three-phase PMSM (DTP-PMSM). The star points of these windings may either remain separate or coincide, and in such configurations, two three-phase inverters are typically employed to power the motor.

To enhance reliability, an open-ended connection can replace the double-stranded connection for each winding, as depicted in Fig. 1(c,d). In this setup, each phase is powered by a single-phase H-bridge inverter. For greater reliability, independent local control systems (microcontrollers) can be assigned to each single-phase inverter in the structures shown in Fig. 1(c,d), with an upstream central microcontroller coordinating the operation of all six local microcontrollers. This modular drive topology, featuring separate control and power circuits for each phase, offers a high degree of fault tolerance.

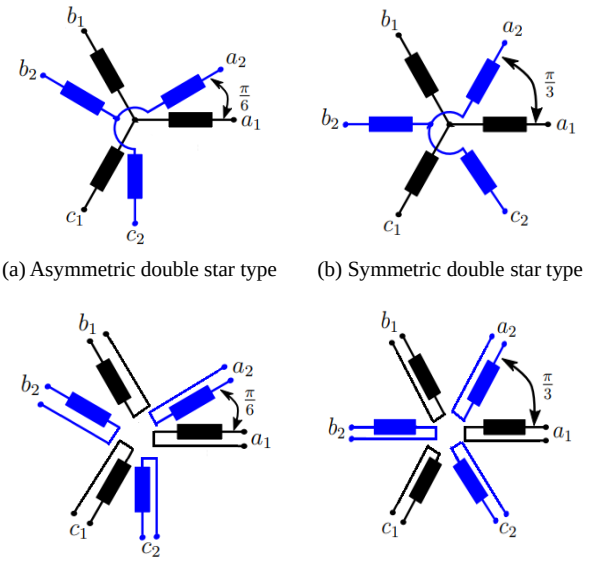

(a) Asymmetric double star type (b) Symmetric double star type

(c) Asymmetric open-end type (d) Symmetric open-end type

Fig. 1. Common types of six-phase PMSMs

In this study, a specialized asymmetric six-phase PMSM is investigated to reduce current stress on the windings and enable higher power output. This motor features a unique stator configuration where each phase consists of two separate windings positioned in two distinct physical halves of the stator, symmetrically arranged around the stator's center. This design can also be termed a six-phase asymmetric motor with dual stator windings. Fig. 2 presents the schematic of the stator winding for this asymmetric six-phase motor with double windings. The windings are connected in an open-end configuration, with each winding in a phase independently controlled by a single-phase H-bridge inverter, all managed by a single microcontroller. Fig. 3 depicts the drive schematic for this modular asymmetric six-phase PMSM with dual stator windings. Notably, the reference currents for both windings of a given phase, sent by the central microcontroller to the corresponding local microcontroller, are identical, ensuring that the resulting MMFs from the two windings remain aligned.

One of the limitations of this structure is that the modular design of the control system prevents data exchange between the local microcontrollers of different phases. As a result, the controllers in each module operate independently without awareness of the voltage and current information from other modules. This restriction poses challenges for modeling and control strategies based on dq reference frame theory, which are commonly applied to three-phase or six-phase motors but rely on certain assumptions about system coupling and information sharing. In the modular drive system under investigation in this research—whose structure is illustrated in Fig. 3—

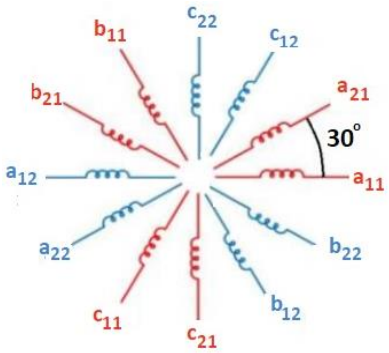

Fig. 2. The schematic of an asymmetric six-phase PMSM with double stator winding

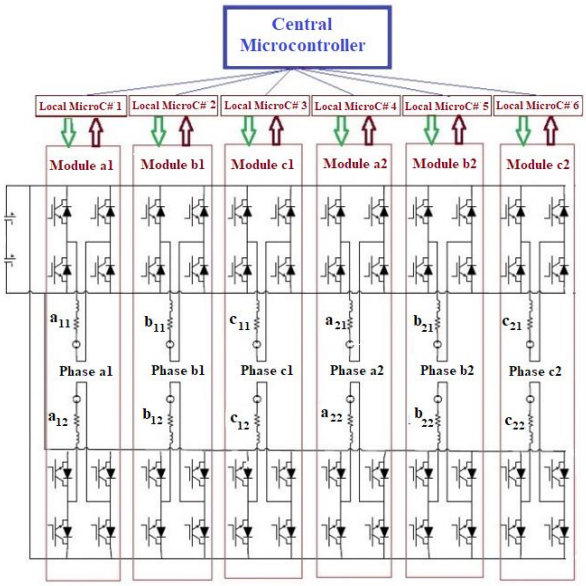

Fig. 3. Schematic of the drive for six-phase, double winding PMSM used in this research

transformations such as 3-to-2 or their inverses cannot be implemented. Consequently, for modeling the modular six-phase PMSM in this study, a six-axis stationary reference frame approach is adopted.

The control methods for three-phase PMSMs are highly diverse. While these methods can also be applied to six-phase PMSMs, their practical use is less common due to the increased number of phases, higher computational burden, processing limitations in microcontrollers, and the poor performance of some methods in high-power motors [9]. Vector control is the most widely used primary method for both three-phase and six-phase PMSMs, offering relatively fast dynamics and smoother torque compared to other approaches. For six-phase PMSMs, vector control is implemented in independent dq frames, decoupled dq frames, and the Vector Space Decomposition (VSD) method. A comparison of various vector control strategies for asymmetric six-phase PMSMs with double-star winding configurations (DTP-PMSM) has been presented in [10]. However, vector control for six-phase PMSMs has several drawbacks, including the computational complexity of Park transformations, challenges in tuning multiple PI controller coefficients, and sensitivity to changes in motor parameters. To address some limitations of vector control, such as the need for multiple PI controllers and their tuning, Direct Torque Control (DTC) has been proposed [11,12]. Nevertheless, DTC also suffers from inherent disadvantages, such as persistent current and torque ripple, along with significant high-frequency noise. Model Predictive Control (MPC) has emerged as an effective and optimal strategy for controlling switching and nonlinear systems, gaining widespread adoption in electric drive applications, including PMSM drives. Several studies have explored MPC for six-phase PMSMs using two-level and three-level inverters [13,14]. However, MPC is also sensitive to parameter variations, and while model-free and robust predictive methods have been proposed for three-phase PMSMs, they have not yet been extended to six-phase PMSMs.

Most conventional control methods rely on motor models in two-axis reference frames, necessitating transformations such as abc-to-dq or αβ. However, in the modular drive structure investigated in this research—where each phase is controlled independently—these conventional methods cannot be applied. In summary, due to the modular architecture of the control system studied here, none of the existing modeling and control methods based on two-axis theory (for either three-phase or six-phase PMSMs) are suitable. Instead, phase-independent modeling and control approaches must be developed.

The primary reason for using multiphase PMSM motors, particularly six-phase motors, is to enhance the fault-tolerant capability and reliability of the drive system under faulty conditions [15]. Fault-tolerant control strategies for six-phase motor drives are crucial to ensure reliable operation under various fault conditions such as open-phase or short-circuit faults. One effective approach is phase redundancy, where healthy phases compensate for faulty ones by redistributing currents, though this may lead to increased torque ripple in severe faults [16]. Model predictive control (MPC) offers dynamic fault handling by optimizing future system behavior, providing excellent performance at the cost of higher computational complexity [17]. Sliding mode control (SMC) is another robust method that maintains stability despite faults by forcing the system into a predefined sliding surface, but its inherent chattering can affect smooth operation [18]. Field-oriented control (FOC) with adaptive current regulation adjusts d-q axis currents to minimize torque disturbances, offering a good balance between performance and simplicity, though it relies heavily on accurate fault detection. Compared to these, MPC and SMC demonstrate superior fault tolerance and adaptability, with MPC being more computationally demanding while SMC suffers from chattering issues [19]. In contrast, FOC and phase redundancy methods are simpler to implement but may lack the same level of precision under extreme fault conditions. The choice of

method ultimately depends on the specific application requirements, including computational resources, desired response time, and acceptable torque ripple levels, with advanced methods like MPC being preferred for high-performance applications where reliability is critical [20]. Due to the independent control structure of each phase relative to the others, most aforementioned fault-tolerant control methods relying on dq transformations are not applicable. Therefore, this paper proposes a compensation-based fault-tolerant control strategy for open-circuit faults in one or more windings, which operates independently without requiring dq transformations.

The rest of this paper is organized as follows: Section 2 presents the modeling of the modular non-sinusoidal six-phase PMSM. Section 3 discusses the motor's control using an optimal harmonic current injection strategy with quasi-proportional resonant (QPR) current controllers, followed by a fault-tolerant control method. Simulation results are provided in Section 4, while experimental validation is presented in Section 5. Finally, Section 6 concludes the paper with key findings and insights.

II. Modeling of the Non-Sinusoidal, Asymmetric Six-Phase PMSM with Double Winding

For dynamic modeling of sinusoidal three-phase PMSMs, Park (dq) or Clarke (αβ) transformations are typically employed to represent the system in either rotating or stationary reference frames. Similarly, for six-phase PMSMs, various modeling approaches exist, analogous to those used for three-phase motors. These methods include:

(1) Modeling in independent $\boldsymbol{dq}$ reference frames [21]
(2) Modeling in independent, decoupled $\boldsymbol{dq}$ frames [22]
(3) Modeling using vector space decomposition (VSD) [23]
(4) Modeling in six-axis stationary reference frame [24]

For a six-phase PMSM with sinusoidal back EMF, the first three modeling methods are commonly employed, with no significant difference in computational complexity among them. However, modeling non-sinusoidal PMSMs requires additional considerations when applying these methods. Proposed approaches for modeling non-sinusoidal PMSMs include:

(a) Non-sinusoidal vectorial or extended Park method [25]
(b) Modeling in one dq reference frame considering harmonic components [26]
(c) Modeling in multiple harmonic dq reference frames (MRF) [27]
(d) Vector space decomposition (VSD) method [28]

In the extended Park transformation-based modeling method, the argument and amplitude used in the Park transformation vary according to the rotor angle. When modeling in a single dq reference frame while accounting for harmonic components, the conventional Park transformation is applied, incorporating the effects of harmonic back-EMF voltages in the voltage-current equations and the electromagnetic torque relationship. Alternatively, the multiple harmonic dq reference frames method involves creating rotating dq frames corresponding to the harmonic orders present in the back-EMF voltage, each synchronized to the respective harmonic frequency. The VSD method is one of the most powerful modeling methods that, although originally proposed for modeling sinusoidal multiphase motors, also performs well for modeling non-sinusoidal three-phase motors. In this method, using appropriate 3-to-2 transformations, the main component of the motor signals along with the harmonics of orders $k = 12m \pm 1\ (m = 1,2,3,\dots)$ are transferred to the main subspace $\alpha\beta$, while the harmonics of orders $k = 6m \pm 1$ are transferred to the secondary subspace $z1z2$, and the zero-order harmonics $k = 3m$ are mapped to the zero-sequence subspace $o1o2$. The VSD modeling method offers several advantages, including the ability to work with simplified models across three two-dimensional subspaces, facilitating easier controller design and more straightforward harmonic control. Additionally, this method enables the modeling of non-sinusoidal motors—such as those with non-sinusoidal back-EMF voltages—as sinusoidal motors, simplifying analysis and control.

However, both the VSD method and other dq-based modeling techniques are only applicable when the motor employs a centralized control system. Due to the modular structure of the drive system studied in this research, conventional two-axis-based modeling methods cannot be applied. Furthermore, the non-sinusoidal nature of the back-EMF voltages adds to the complexity. Therefore, for the six-phase PMSM with double winding, as illustrated in Fig. 2, modeling in the six-axis stationary reference frame is required. In this approach, the six stationary reference axes are aligned with the winding axes depicted in Fig. 1(c). Assuming the phase naming and arrangement of the PMSM shown in Fig. 2, the voltage-current relationship for each phase is given by:

$$v_{x_i} = R_s i_{x_i} + \frac{d}{dt}\psi_{x_i} + e_{x_i} \tag{1}$$

where R_s is resistance of each stator phase, and v_{x_i} is voltage in the winding x_i, $(x = a, b, c \ \& \ i = 11,12,21,22)$ and other nomenclature are defined at the beginning of the paper. The value of the flux linkage for each winding depends on the current of that winding and the currents of the other 11 windings, and can be calculated from the following relationship:

$$\psi_{x_i} = L_{x_i} i_{x_i} + \sum_{\substack{y=a,b,c \\ i,j=11,12,21,22 \\ (x_i \neq y_j)}} M_{x_i y_j} i_{y_j} \tag{2}$$

The stator inductance matrix, in the case of the two windings of each phase being separate (for instance, a_{11} and a_{12}) is a 12×12 matrix. Two windings of a phase for improvement the motor performance at low speeds is connected in series and so, the inductance matrix is converted to a 6×6 matrix. The electromagnetic torque T_e and motor speed ω_m for the asymmetric six-phase PMSM with double stator windings can be calculated using as follows:

$$T_e = \sum_{\substack{x=a,b,c \\ i=11,12,21,22}} \frac{e_{x_i} i_{x_i}}{\omega_r} \tag{3}$$

$$\omega_m = \frac{1}{J} \int (T_e - T_l) dt \tag{4}$$

To implement of the model in Simulink, a 12-phase winding can be used, that to each phase, a dependent voltage source with desired harmonic waveform function of rotor position θ_r and amplitude as function of rotor speed, can be added in series.

In the presented motor model in the stationary reference frame with constant inductance values, it is assumed that the rotor is of the surface-mounted permanent magnet type. Additionally, saturation effects and armature reaction are neglected. The presence of these uncertainties and the nonlinear effects manifest themselves in the distortion of the back-EMF voltage waveforms and changes in their harmonic content within the model, which must be taken into account when applying the control method.

III. Control of the Non-Sinusoidal, Asymmetric Six-Phase PMSM with Double Winding using Optimal Harmonic Current Injection Method

In the introduction section it has been explained that due to the modular structure of the drive system under study in this research, the use of control methods based on the two-axis theory is not possible. Moreover, the many numbers of windings and the non-sinusoidal back-EMF voltages also add to the challenge. In this section, to reduce the torque ripple caused by the non-sinusoidal back-EMFs of the windings, an optimal current shaping (or harmonic current injection) strategy is employed in the six-axis stationary reference frame, which will be briefly discussed as follows.

A. Torque Ripple Reduction Using Optimal Harmonic Current Injection Strategy

In harmonic current injection strategy, corresponding to the harmonics present in the phase back-EMF voltages, the fundamental phase current is injected as well as harmonic currents so that the harmonics of torque become zero, leaving only the constant part of the torque [29]. For the six-phase motor in this research, it is assumed that harmonics with orders 1, 3, and 5 are present in the back-EMF voltage. Therefore, the back-EMF voltage of the winding x_i (here $x_i = a_{11}$) can be written as follows:

$$e_{x_i}(t) = E_1 \sin \omega_r t + E_3 \sin 3\,\omega_r + E_5 \sin 5\,\omega_r t \tag{5}$$

where E_1, E_3, and E_5 are respectively 1, 0.07, and -0.03 per unit in this research. The injected current into winding x_i (here $x_i = a_{11}$) is considered as follows:

$$i_{x_i}(t) = I_1 \sin \omega_r t + I_3 \sin 3\,\omega_r t + I_5 \sin 5\,\omega_r t \tag{6}$$

For other windings, the argument of the sinusoidal functions changes according to Fig. 1(c). The air gap power of the winding $\boldsymbol{x_i = a_{11}}$ will only include even order harmonics up to the 10th order as follows:

$$P_{x_i}(t) = P_0 + P_2 \sin 2\,\omega_r t + \cdots + P_{10} \sin 10\,\omega_r t \tag{7}$$

The total air gap power of all windings in a PMSM with phase number multiple of 3, contains only harmonic with orders 6, 12, and 18. Assuming current and voltage harmonics are limited to the 5th order for the motor in this study, the total instantaneous air gap power P_e is obtained as follows:

$$P_e(t) = P_0 + P_6 \sin 6\,\omega_r t \tag{8}$$

The instantaneous electromagnetic torque can also be calculated as:

$$T_e(t) = \frac{P_e(t)}{\omega_r} = T_0 + T_6 \sin 6\,\omega_r t \tag{9}$$

where:

$$T_0 = \frac{3}{2\omega_r}[E_1 I_1 + E_3 I_3 + E_5 I_5] \tag{10}$$

$$T_6 = \frac{3}{2\omega_r}[-I_1 E_5 + I_3 E_3 - I_5 E_1] \tag{11}$$

To determine the amplitudes of the current harmonics for each phase, by setting $\boldsymbol{T_0}$ equal to the reference torque $\boldsymbol{T_e^*}$ (the output of the speed controller) and setting $\boldsymbol{T_6}$ to zero, the following matrix equation must be solved:

$$\begin{bmatrix} E_1 & E_3 & E_5 \\ -E_5 & E_3 & -E_1 \end{bmatrix} \times \begin{bmatrix} I_1 \\ I_3 \\ I_5 \end{bmatrix} = \frac{2\omega_r}{3} \begin{bmatrix} T_e^* \\ 0 \end{bmatrix} \tag{12}$$

It should be noted that in non-sinusoidal PMSM with the star connection, the third harmonic current cannot flow, and despite the presence of the third harmonic back-EMF voltage, the third harmonic current is not included in the reference current. However, in a motor with an open-end

winding, the third harmonic current can flow. One solution—based on the fact that the third harmonic current does not involve in torque generation—is to set the third harmonic current component in the reference current to zero. In this case, in (12), the number of equations and currents becomes equal, allowing the amplitudes of the current harmonics to be determined. However, if the third harmonic is considered, it can be adjusted in such a way that the total RMS current (and thus copper losses) is minimized. In this case and in (12), the number of unknown currents is 3 that is more than the number of equations. This refer that it has not a unique solution. Hence, an optimization must be performed to extract the best solution. An optimal method to solve this equation is such that, in addition to satisfying the above equations, the rms value of the current vector $\boldsymbol{I} * \boldsymbol{I^t}$ should be also minimized, thereby obtaining the optimal harmonic values of the current. Thus, consider the following optimization problem [30]:

$$\begin{aligned} &Minimize\ C = xx^T \\ &x = [I_1 \quad I_3 \quad I_5] \\ &if; Ax = B \\ &B = \frac{2\omega_r}{3}\begin{bmatrix} T_e^* \\ 0 \end{bmatrix},\ A = \begin{bmatrix} E_1 & E_3 & E_5 \\ -E_5 & E_3 & -E_1 \end{bmatrix} \end{aligned} \tag{13}$$

The optimal solution of above problem is obtained as follows [37]:

$$x_{opt} = A^T \times (A \times A^T)^{-1} \times B \tag{14}$$

Using the above solution, the optimal values of the current harmonic amplitudes are obtained as follows:

$$\begin{bmatrix} I_1^* \\ I_3^* \\ I_5^* \end{bmatrix} = \begin{bmatrix} 0.9956 \\ 0.0736 \\ 0.0247 \end{bmatrix} \frac{2\omega_r T_e^*}{3} \tag{15}$$

B. Harmonic Current Regulation for Windings using Proportional-Resonant Controllers

Using (6) and (15), the time relation of the reference current for both windings of the phase $\boldsymbol{a_1}$, based on the reference torque, can be determined as follows:

$$i_{a_1}^*(t) = I_1^* \sin \omega_r t + I_3^* \sin 3\,\omega_r t + I_5^* \sin 5\,\omega_r t \tag{16}$$

The current of phase $\boldsymbol{a_1}$ windings, in all transient and steady states, must accurately track the aforementioned reference value. For this purpose, appropriate current controllers should be used. The simplest type of controller is the hysteresis controller, which, due to its steady-state error in current and high, and variable switching frequency, is not suitable for high-power applications sensitive to acoustic noise. On the other hand, the traditional PI controller is also not suitable for this application because the PI controller, due to its small bandwidth, is not capable of tracking AC signals containing high-order harmonics [31]. An effective and suitable solution for tracking harmonic reference signals is the using of proportional-resonant (PR) controllers or quasi-proportional-resonant (QPR) controllers. The transfer function of the QPR controller can be expressed as:

$$G_{QPR}(s) = K_P + K_R \frac{2\omega_c s}{s^2 + 2\omega_c s + \omega_o^2} \tag{17}$$

The QPR controller has four parameters: $\omega_o, \omega_c, K_P,$ and $K_R,$ which must be correctly chosen. The resonance frequency ω_o is exactly equal to the fundamental system's sinusoidal signal frequency. However, the other three parameters should be selected to maximize the gain around the resonance frequency while appropriately attenuating neighboring frequencies. There are various methods for designing and determining the parameters of QPR controllers, the most important of which are: (i) trial-and-error method, (ii) the forced oscillation method (time domain), (iii) the frequency response method (frequency domain).

The trial-and-error method involves manually adjusting the gains and controller parameters and observing the motor's response to various input signals that is briefly presented [31]. (1) Selecting initial values; Choose initial values for the parameters K_R, K_P, and ω_c based on prior experience or knowledge of the PMSM drive system. These initial values serve as the starting point for the tuning process. (2) Tuning the proportional gain K_P; First, adjust the proportional gain K_P to achieve the desired steady-state performance. This can be done using methods such as trial and error or systematic tuning approaches like the Ziegler-Nichols method. (3) Tuning the resonance gain K_R; After tuning the K_P, adjust the K_R to achieve the desired tracking performance. This can also be done using trial and error or systematic tuning methods such as the Internal Model Control (IMC) method. (4) Tuning the cut-off frequency ω_c; adjust the ω_c to achieve the desired compromise between dynamic response and stability. This can be done by observing the system's step response to a reference current and adjusting ω_c to achieve the desired settling time and overshoot, (5) Validating the tuned parameters; evaluate the controller's performance under various operational conditions and disturbances to ensure it meets the desired performance criteria.

If, in addition to fundamental signal with frequency ω_o, the higher-order harmonics of the signal are available, the QPR controller should be modified. For reference harmonic

current given by (16), the transfer function of the QPR controller can be expressed as follows:

$$G_{QPR,H}(s) = K_P + K_{R_1}\frac{2\omega_{c_1}s}{s^2 + 2\omega_{c_1}s + {\omega_o}^2} + K_{R_3}\frac{2\omega_{c_3}s}{s^2 + 2\omega_{c_3}s + (3\omega_o)^2} + K_{R_5}\frac{2\omega_{c_5}s}{s^2 + 2\omega_{c_5}s + (5\omega_o)^2} \quad (17)$$

The optimal values for the parameters K_P, K_{R_h}, and ω_{c_h} for the six-phase motor drive in this research are determined using the trial-and-error method.

Fig. 4 illustrates the block diagram of the six-phase PMSM control system in this paper using harmonic current injection strategy as well as QPR controllers for winding current regulation. A PI controller generates the reference torque based on tracking error of speed. Using harmonic current injection strategy and based on eq. (15) the current reference for all phases is determined and finally by 12 QPR controllers, the current regulation is implemented.

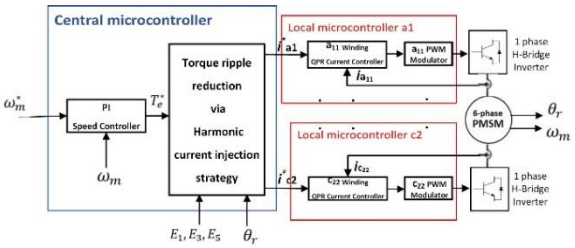

Fig. 4. Schematic of control system for the six-phase PMSM with double windings using harmonic current injection strategy

C. Motor Control Under Single-Phase Fault

The modular six-phase PMSM with open-end winding configuration provides the best control capabilities under fault conditions compared to other 6-phase or even 12-phase motors with star- connections. It has the ability to eliminate torque ripple using the allowable current capacity of the remaining healthy phases for each fault condition. In healthy condition, ignoring the effect of high frequency switching and cogging, the developed electromagnetic torque is constant and free of any oscillations. However, when a fault occurs in one or more windings, the generated torque becomes oscillatory, adding a second harmonic oscillatory torque component to the constant torque. The fault-tolerant control (FTC) strategy used in this study is based on reconstructing the amplitude and angle of the main harmonic current of one or some healthy windings to re-establish the balance between the second harmonic torques of the healthy winding [32]. To demonstrate the proposed FTC, assume that the back-EMF voltage and current of the windings of the six-phase shown in Fig. 1 are sinusoidal. The air-gap powers resulting from six-windings $a_{11}b_{11}c_{11}a_{21}b_{21}c_{21}$ (group 1) can be obtained as follows:

$$\begin{aligned}
P_{a_{11}}(t) &= \frac{E_1 I_1}{2} + \frac{E_1 I_1}{2}cos(2\omega_r t)\\
P_{a_{21}}(t) &= \frac{E_1 I_1}{2} + \frac{E_1 I_1}{2}cos(2\omega_r t + 60^O)\\
P_{b_{11}}(t) &= \frac{E_1 I_1}{2} + \frac{E_1 I_1}{2}cos(2\omega_r t + 120^O)\\
P_{b_{21}}(t) &= \frac{E_1 I_1}{2} + \frac{E_1 I_1}{2}cos(2\omega_r t + 180^O)\\
P_{c_{11}}(t) &= \frac{E_1 I_1}{2} + \frac{E_1 I_1}{2}cos(2\omega_r t + 240^O)\\
P_{c_{21}}(t) &= \frac{E_1 I_1}{2} + \frac{E_1 I_1}{2}cos(2\omega_r t + 300^O)
\end{aligned} \quad (18)$$

From the above relationships, it is observed that the air-gap power and consequently the electromagnetic torque of each windings includes a second harmonic oscillatory component, and the sum of these oscillations in the six windings is zero. Fig. 5(a) shows the direction of the six-phase motor current vector, and Fig. 5(b) shows the corresponding second harmonic torque vectors generated by each phase in the healthy condition. It is observed that the sum of all the second harmonic torque vectors in Fig. 5(b) is zero. This balance is there for the second windings of phases $a_{12}b_{12}c_{12}a_{22}b_{22}c_{22}$ (group 2). When one or more windings fails, the balance between the second harmonic torques is disturbed, and torque ripple occurs.

With an open-circuit fault in the a_{11} winding of phase a_1 or corresponding H-bridge inverter, this winding is not capable of producing torque. Hence, the second harmonic oscillatory component in the total torque is created. In other words, as shown in Fig. 6(a), with the lack of the second harmonic torque vector of the a_{11} winding, the balance of the remaining 5 vectors is disrupted. To re-establish balance between these 5 remaining vectors, the directions of the two remaining windings in this three-phase group (b_{11} and c_{11}), must be aligned. For this purpose, their angles can be changed by -30° and $+30^\circ$ respectively, or only the direction of one of them (for example c_{11}) can be changed by $+60^o$. Here, the second solution is chosen, that the new current vector c'_{11} is obtained as shown in Fig. 6(b). It is clear that three vectors $a_{21}b_{21}c_{21}$ are balanced with each other, and two vectors $b_{11}c'_{11}$ are balanced as well. Also, the amplitudes of all windings are adjusted to appropriate and permissible values to meet the load torque requirements.

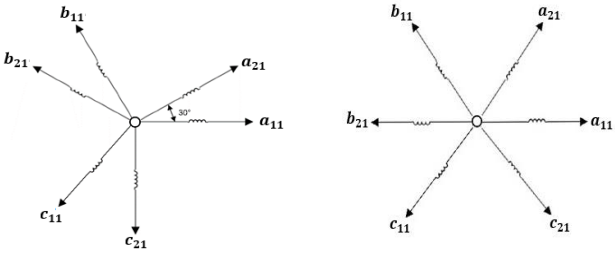

(a) Main harmonic of current (b) Second harmonic of torque

Fig. 5. Current and torque vectors of each phase in the open-ended winding, asymmetrical six-phase PMSM

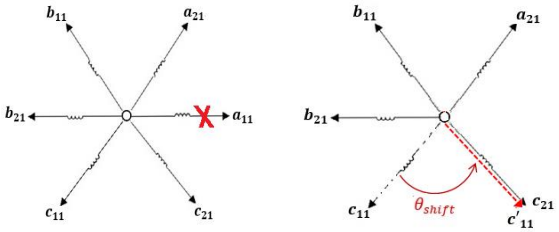

(a) Fault condition (b) Fault compensation

Fig. 6. Single-phase fault compensation in a modular six-phase PMSM (in group 1) by shifting angle current of c_{11} by +60°

There are six possible single-phase faults for each six-phase group, which are described in Table I along with their compensation methods. The proposed FTC method does not consider the source of the fault, which could be a short circuit in the single-phase H-bridge inverter of any winding, an open-circuit fault in the winding, a short-circuit fault in the winding, or even a fault in the microcontroller of any phase. It is based on measuring the effective current of each winding, which becomes zero.

TABLE I. VARIOUS SCENARIOS OF SINGLE-PHASE FAULT IN GROUP 1 AND COMPENSATOR (CORRECTED) WINDING

Faulty winding	Corrected winding	Angle shift
a_{11}	c_{11}	$+60^o$
b_{11}	a_{11}	$+60^o$
c_{11}	b_{11}	$+60^o$
a_{21}	b_{21}	$+60^o$
b_{21}	c_{21}	$+60^o$
c_{21}	a_{21}	$+60^o$

D. Motor Control Under Multiple-Phases Fault

In the case of faults in multiple windings, such as faults in two or more windings, a similar FTC method can be applied without any specific limitations. Generally, for n-phase fault scenario, the number of fault conditions in each group of 6 windings equals the combination $\binom{6}{n}$. Therefore, the number of possible fault conditions for 2, 3, 4, and 5 windings is 6, 15, 20, 15, and 6, respectively. The total number of possible fault conditions employed motor in this research in each group is 62, and for both groups, it is 124. For each condition, the compensating phases can be easily determined. Table II lists the 15 different fault scenarios occurring in two windings, including the compensating winding. The same FTC method, based on balancing the second torque harmonics in healthy phases, remains applicable. Please note that in some fault conditions, such as faults in two windings a_{11}, c_{21}, the balance of the second-harmonic torque vectors in the remaining healthy windings is inherently maintained and does not require compensation.

IV. Simulation Results

In this section, for the double-winding six-phase PMSM with rated specifications 200 kW, 245 V, $R_s = 50\,m\Omega$, $L_s = 232\,0\mu H$, back-EMF voltage constant $1.37\,rad/s$, and inertia $0.1\,kg \cdot m^2$, the motor behavior is compared using the harmonic current injection control method and two types of current controllers, quasi-proportional-resonant (QPR) and PI, through simulation.

TABLE II. VARIOUS SCENARIOS OF TWO-PHASE FAULT IN GROUP 1 AND COMPENSATOR (CORRECTED) WINDINGS

Faulty winding	Corrected winding	Angle shift
a_{11}, b_{11}	b_{21}	$+60^o$
$a_{11}\ c_{11}$	c_{21}	$+60^o$
$b_{11}\ , c_{11}$	a_{21}	$+60^o$
$a_{21}\ , c_{21}$	a_{11}	$+60^o$
$a_{21}\ \ , b_{21}$	c_{11}	$+60^o$
$b_{21}\ , c_{21}$	b_{11}	$+60^o$
a_{11}, a_{21}	c_{11}	$+120^o$
$a_{11}\ , b_{21}$	c_{21}	$+120^o$
a_{11}, c_{21}	**No compensation needed**	
$b_{11}\ , a_{21}$	b_{21}	$+120^o$
$b_{11}\ , b_{21}$	**No compensation needed**	
$b_{11}\ , c_{21}$	a_{11}	$+120^o$
c_{11}, a_{21}	**No compensation needed**	
c_{11}, b_{21}	b_{11}	$+120^o$
c_{11}, c_{21}	a_{21}	$+120^o$

The gains of the QPR controllers for all phases are set to K_P = 35, K_{R1} = 10, K_{R3} = 0.1, K_{R5} = 0.1, and ω_{ci} = 10. Fig. 7 shows the behavior of the drive in tracking the reference speed and under an increasing load torque proportional to the square of the speed $T_l = 6.43\omega_m^2$. The reference speed is 120 rpm, and the load torque at this speed is approximately $1000\,N \cdot m$. The reference speed tracking error is very small and below 0.5%. The fourth chart in Fig. 7 shows the waveform of the non-sinusoidal back-EMF voltages of the motor. The current winding a_{11} accurately

follows the non-sinusoidal reference current using QPR current controllers, with minimal torque ripple of about 3%, as shown in the third chart in Fig. 7.

Fig. 8 shows the drive behavior using PI current controllers, where the gain values of the controllers for all phases are set to $K_I = 100$ and $K_P = 20$. It is observed that this type of controller, due to bandwidth limitations, cannot accurately track the harmonic reference current. Hence, the PI controller is not suitable. Also, the hysteresis current controller, due to the excessively high and variable unacceptable switching frequency, exhibits similar behavior to the PI controller. Therefore, the QPR controller, is a suitable type of controller for phase current regulation in the modular six-phase motor drive system that using harmonic current injection.

To investigate the performance of the proposed fault-tolerant control (FTC), the drive behavior under single-phase fault windings a_{11}, is examined through simulation.

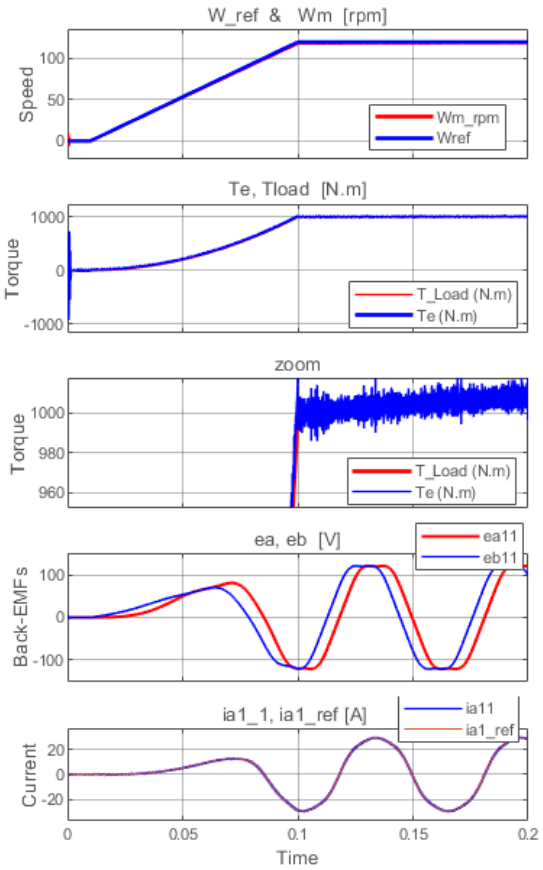

Fig. 7. Drive behavior using QPR current controllers at nominal speed and under nominal load torque.

According to Fig. 9, it is assumed that winding a_{11} experiences a fault at 0.2 seconds. According to the fourth chart in Fig. 9, the developed torque experiences oscillations with the second harmonic order of the stator current. These oscillations, as shown in the second chart, results in oscillations in the motor speed. According to the current charts in Fig. 9, the amplitude of the healthy winding currents (e.g. a_{11}) increases slightly after the fault occurrence to develop the load demanded torque. At 0.3 seconds, fault compensation is carried out by adjusting the current angle of the healthy winding c_{11} by 60° as shown in Fig. 6(b). It is observed that the amplitude of the windings' current increases after compensation at 0.3 sec due to phase difference between the current and back-EMF voltage of winding c_{11}. Moreover, the torque and speed oscillations decrease after this compensation. After compensation, the phase difference between currents of c_{11} and c_{12} windings increase to 60° as shown in sixth chart in Fig. 9. Also, as shown in last chart in Fig. 9, phase difference between currents of c_{11} and b_{11} windings decrease from 120° to 60°.

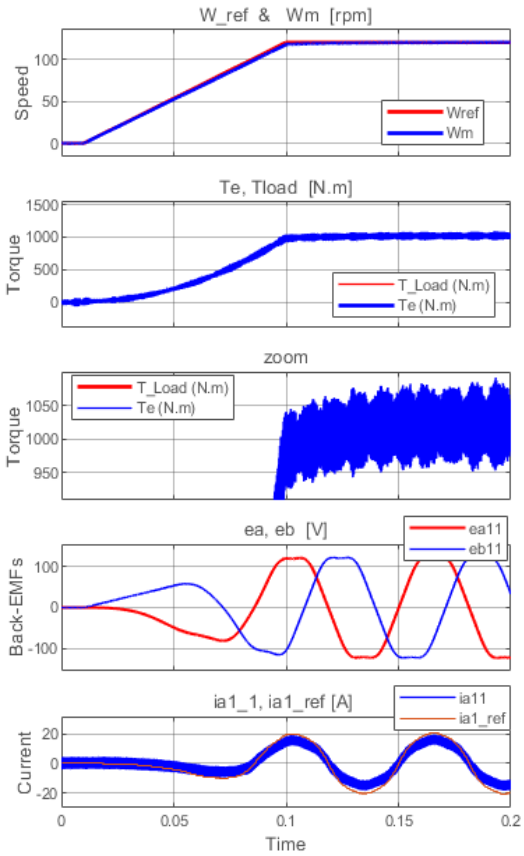

Fig. 8. Drive behavior using PI current controllers at nominal speed and under nominal load torque.

V. Experimental Results

To confirm the proposed control methods in healthy and fault conditions for the double-winding six-phase PMSM drive, some practical tests were conducted on the laboratory setup using the 200 kW double-winding six-phase PMSM. The schematic of the setup is shown in Fig. 10, where seven microcontrollers type STM32F407VGT6 have been used as central and local controllers. The drive of each

phase consists of a microcontroller board as well as double H-bridge single-phase inverters and a separate excited DC generator is employed as load. The parameters for all winding QPR controllers are the same and, according to (17), are K_P = 1, K_{R1} = 15, K_{R3} = 0.1, K_{R5} = 0.1, and ω_{ci} = 10.

Fig. 11 shows the speed response of the motor using the harmonic current injection strategy as well as QPR controllers for current regulation and a PI controller for speed regulation. The reference speed is 120 rpm and the tracking is satisfactorily performed.

Fig. 12 shows the harmonic current of winding c_{11} as well as expanded speed, that the speed ripple ($\Delta\omega_m$) in this condition is equal to 1 rpm. Fig. 13 illustrates the current waveforms of three windings $a_{11}b_{11}c_{11}$.

Fig. 14 shows the results of the practical test where open circuit fault has occurred in winding a_{11} and the fault tolerant control method has not yet been applied. The speed reference is 40 rpm. It can be seen that due to the torque ripple created, the speed fluctuation becomes very large and reaches a value of 9 rpm, which is about 22.5% of the rated speed.

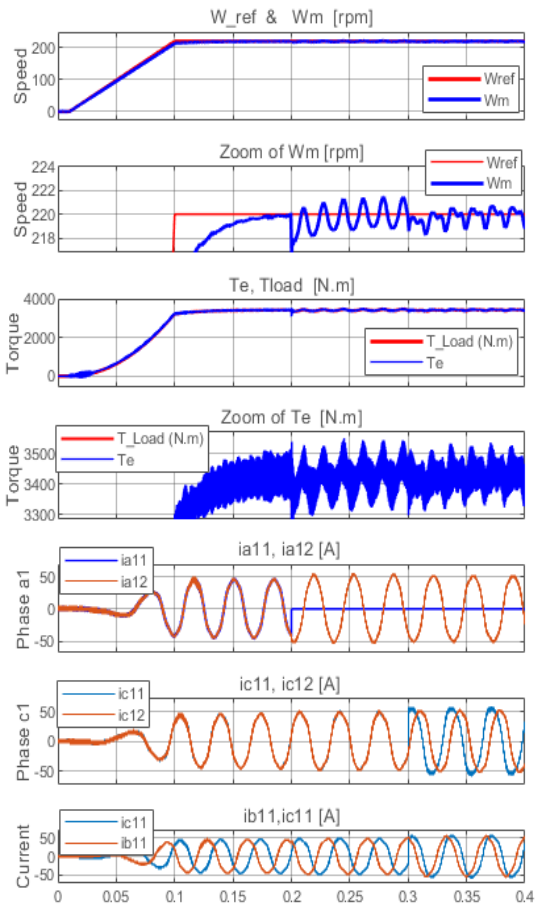

Fig. 9. Drive behavior under single-phase fault of winding a_{11} at 0.2 sec and compensation by adjusting the current angle of winding c_{11} at 0.3 sec by 60°

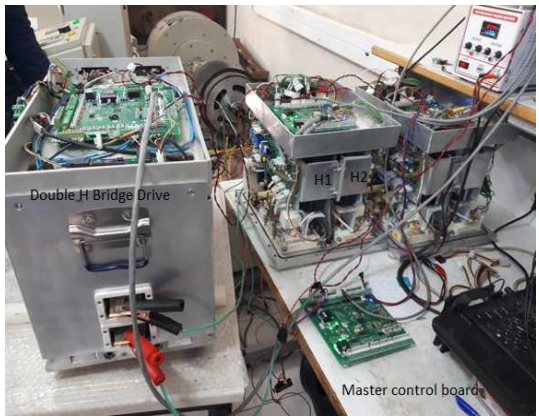

Fig. 10. Experimental setup of modular six-phase PMSM drive

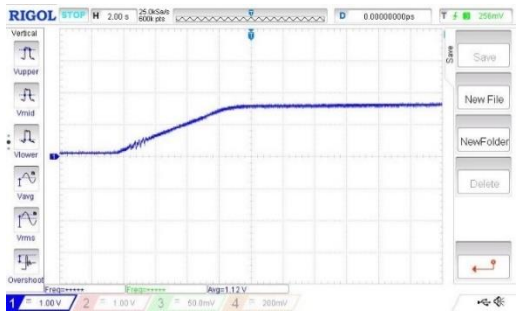

Fig. 11. Motor speed response with using harmonic current injection in healthy condition

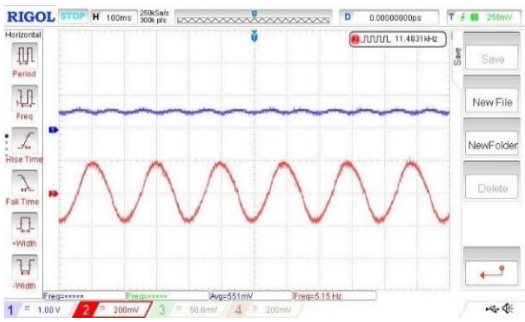

Fig. 12. Current of winding $\boldsymbol{c_{11}}$ (red) as well as enlarged speed waveform (blue) with using harmonic current injection in healthy condition of the motor

Fig. 15 shows the practical results for applying the proposed FTC method under open circuit single-phase fault in winding a_{11}. As mentioned in section 3.C and according to Fig. 6, to re-establish balance between five remaining vectors, the direction of c_{11} must be shifted by +60°, resulting in the new current vector c'_{11}. Fig 15(a) shows the motor speed and current of winding c'_{11}. The speed fluctuation decreases to 5 rpm, which means 10% improvement in speed fluctuations. Fig. 15(b) shows the

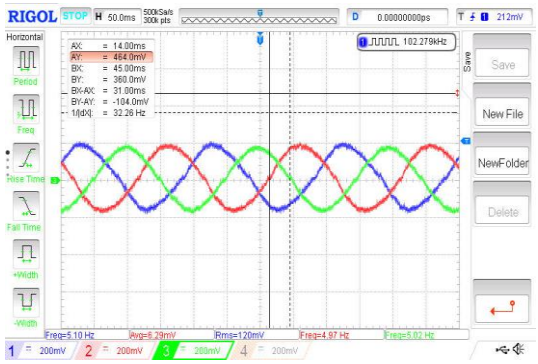

Fig. 13. Currents of three windings $\boldsymbol{a_{11}b_{11}}$ and $\boldsymbol{c_{11}}$ by using harmonic current injection strategy in healthy condition of the motor

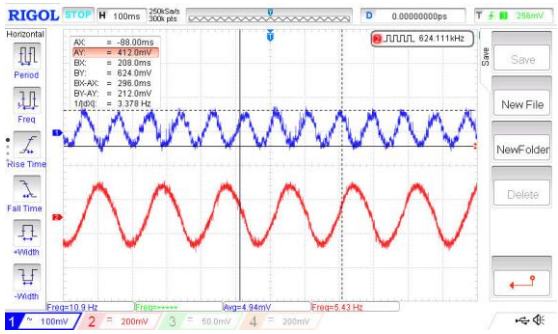

Fig. 14. Motor speed (blue) and current (red) of winding c_{11} during single-phase fault in winding a_{11} **without** compensation

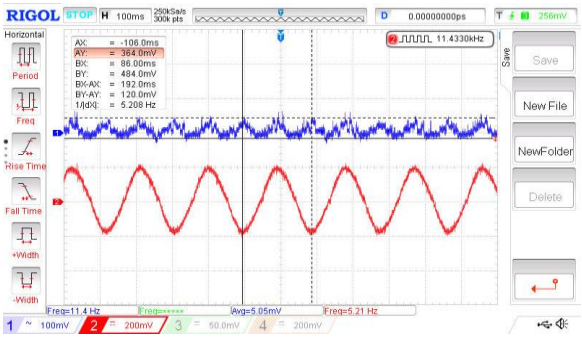

(a) Motor speed (blue) and current (red) of winding c_{11}

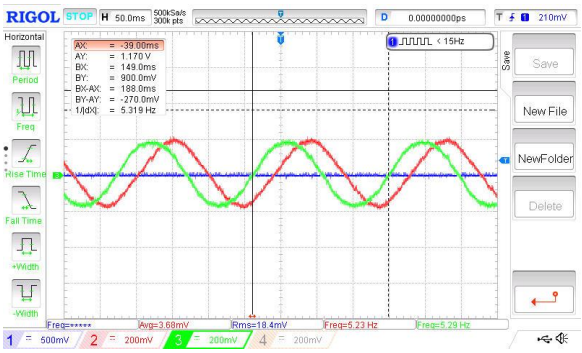

(b) The currents of winding c'_{11} (shifted of c_{11}) and b_{11}

Fig. 15. Behavior of the drive during single-phase fault in winding a_{11} **with** compensation by adjusting the angle of current in c_{11}

currents of two windings c'_{11} and b_{11}, which are observed to have a phase difference of 60° with respect to each other, while in the healthy condition, their difference is 120°.

VI. Conclusions

In this study, torque ripple reduction in a six-phase PMSM with a fully modular drive system was investigated. Due to the modular architecture of the drive's control system, modeling was conducted in a six-axis stationary reference frame, with each phase controlled independently in its stationary reference frame. To address non-sinusoidal back-EMF voltage, an optimized harmonic current injection strategy was proposed, minimizing the effective current amplitude and associated losses while eliminating torque harmonics. Harmonic quasi-proportional-resonant (QPR) current controllers were employed to track the harmonic reference currents, demonstrating highly effective performance. Furthermore, to mitigate torque ripple under single-phase fault conditions, a fault-tolerant control (FTC) strategy was introduced. This method balances the second harmonic of torque generated by the interaction of the fundamental harmonic of current and back-EMF voltage. However, it should be noted that the proposed FTC cannot fully eliminate the second harmonic torque component arising from higher-order current and back-EMF harmonics. It is also worth mentioning that this method has no specific limitation for being extended to higher-power motors. Its only dependency is on the harmonic content of the motor's back-EMF voltages, which may not remain constant at higher power levels. In such cases, the harmonic content must be estimated online. The presented FTC method can also be extended to multi-phase fault scenarios.

References

[1] M. Furmanik, L. Gorel, D. Konvi, P. Rafajdus, “Comparative Study and Overview of Field-Oriented Control Techniques for Six-Phase PMSMs”, *Applied. Science*, vol. 11, no. 7841, pp. 1-16, 2021, [**DOI:**10.20944/preprints202108.0022.v1]

[2] K.S. Khan, W.M. Arshad, S. Kanerva, “On performance figures of multiphase machines”, *IEEE 18th International Conference on Electrical Machines*, 2008. [**DOI:** 10.1109/ICELMACH.2008.4799836]

[3] J.R. Fu, T.A. Lipo, “Disturbance-free operation of a multiphase current-regulated motor drive with an opened phase”, *IEEE Trans. on Ind. Appl*., vol. 30, pp. 1267–1274, 1994. [**DOI:** 10.1109/28.315238]

[4] S. Kuznetsov, “Machine design and configuration of a 7000 hp hybrid electric drive for naval ship propulsion”, *IEEE International Electric Machines & Drives Conference*, 2011. [**DOI:** 10.1109/IEMDC.2011.5994605]

[5] J.F. Hansen, F. Wendt, “History and state of the art in commercial electric ship propulsion, integrated power

systems, and future trends", *Proceedings of IEEE*, vol. 103, pp. 2229–2242, 2015.
[**DOI:** 10.1109/JPROC.2015.2458990]

[6] J. Rahmanifard, "Design Optimization and Thermal Analysis of a Dual Three-Phase PM Motor for Electric Vehicles, International Journal of Industrial Electronics, Control and Optimization", Articles in Press, Available Online from 03 May 2025,
[**DOI:** 10.22111/ieco.2025.51426.1674]

[7] J.S. Thongam, M. Tarbouchi, A.F. Okou, D. Bouchard, R. Beguenane, "Trends in naval ship propulsion drive motor technology", *IEEE Electrical Power & Energy Conference*, 2013.
[**DOI:** 10.1109/EPEC.2013.6802942]

[8] D. Benatti, C. Alosa, E. Carfagna, F. Immovilli, E. Lorenzani, "Assessment of Master-Slave and Droop Control Strategies in Multi-Three-Phase Drives", *IEEE Workshop on Electrical Machines Design, Control and Diagnosis (WEMDCD)*, pp. 163-168, 2021.
[**DOI:** 10.1109/WEMDCD51469.2021.9425685]

[9] Z. Zhu, S. Wang, B. Shao, L. Yan, P. Xu, Y. Ren, "Advances in Dual-Three-Phase Permanent Magnet Synchronous Machines and Control Techniques," *Energies*, vol. 14, no. 7508, pp. 1-46, 2021.
[**DOI:**10.3390/en14227508]

[10] M. Furmanik, L. Gorel, D. Konvi, P. Rafajdus, "Comparative Study and Overview of Field-Oriented Control Techniques for Six-Phase PMSMs", *Applied. Science*, vol. 11, no. 7841, pp. 1-16, 2021.
[**DOI:**10.20944/preprints202108.0022.v1]

[11] Y. Ren, Z.Q. Zhu, "Enhancement of steady-state performance in direct torque controlled dual-three phase permanent magnet synchronous machine drives with modified switching table", *IEEE Trans. Ind. Electron*. vol. 62, pp. 3338–3350, 2015
[**DOI:** 10.1109/TIE.2014.2376881]

[12] Y. Ren, Z.Q. Zhu, J.E. Green, Y. Li, S. Zhu, Z. Li, "Improved duty-ratio-based direct torque control for dual three-'phase permanent magnet synchronous machine drives", *IEEE Trans. Ind. Appl*. vol. 55, pp. 5843–5853. 2019.
[**DOI:** 10.1109/TIA.2019.2938468]

[13] T. Luan, Z. Wang, Y. Long, Z. Zhang, Q. Li, "Multi-Virtual-Vector Model Predictive Current Control for Dual Three-Phase PMSM", *Journals of Energies*, vol. 14, no. 21, 2021.
[**DOI:** 10.3390/en14217292]

[14] S.W. Hwang, D.K. Son, S.H. Park, G.H. Lee, Y.D. Yoon, M.S. Lim, "Design and Analysis of Dual Stator PMSM With Separately Controlled Dual Three-Phase Winding for eVTOL Propulsion", *IEEE Trans. on Transportation Electrification*, vol. 8, no.4, pp. 4255-4264, 2022.
[**DOI:** 10.1109/TTE.2022.3192353]

[15] E. Levi, "Multiphase Electric Machines for Variable-Speed Applications, IEEE Press, 2018,
[**DOI:**10.1109/TIE.2008.918488]

[16] W. Lee, S.G. Min, B. Sarlioglu, "Fault-Tolerant Operation of Six-Phase Permanent Magnet Motor Drive with Open-Circuit Failures", IEEE Trans. on Transportation Electrification, vol. 10, no. 3, pp. 5910-5920, 2024,
[**DOI:** 10.1109/TTE.2023.3326089]

[17] F.C. Gonçalves Pedro, M.A. Cruz Sérgio, M.S. Mendes André, "Fault-Tolerant Predictive Current Control of Six-Phase PMSMs With Minimal Reconfiguration Requirements", IEEE Journal of Emerging and Selected Topics in Power Electronics, vol. 11, no. 2, pp. 2084-2093, 2023,
[**DOI:** 10.1109/JESTPE.2022.3223515]

[18] F.J. Lin, Y.C. Hung, M.T. Tsai, "Fault-Tolerant Control for Six-Phase PMSM Drive System via Intelligent Complementary Sliding-Mode Control Using TSKFNN-AMF", IEEE Trans. on Industrial Electronics, vol. 60, no. 12, pp. 5747-5762, 2013,
[**DOI:** 10.1109/TIE.2013.2238877]

[19] F. Baneira, J. Doval-Gandoy, A.G. Yepes, O. López, D. Pérez-Estévez, "Comparison of Postfault Strategies for Current Reference Generation for Dual Three-Phase Machines in Terms of Converter Losses", IEEE Trans. on Power Electronics, vol. 32, no. 11, pp. 8342-8346, 2017,
[**DOI:** 10.1109/TPEL.2017.2691401]

[20] A. Mohammadpour, L. Parsa, "Global Fault-Tolerant Control Technique for Multiphase Permanent-Magnet Machines", IEEE Trans. on Industry Applications vol. 51, no. 1, pp. 178-186, 2014,
[**DOI:** 10.1109/TIA.2014.2326084]

[21] 8F. Barrero, M.J. Duran, "Recent Advances in the Design, Modeling, and Control of Multiphase Machines—Part I", *IEEE Trans. on Industrial Electronics*, vol. 63, no. 1, pp. 449-458, 2016.
[**DOI:** 10.1109/TIE.2015.2447733]

[22] S. Kallio, M. Andriollo, A. Tortella, J. Karttunen, "Decoupled d-q Model of Double-Star Interior-Permanent-Magnet Synchronous Machines", *IEEE Trans. on Industrial Electronics*, vol. 60, no. 6, pp. 2486-2494, 2013.
[**DOI:** 10.1109/TIE.2012.2216241]

[23] Y. Hu, Z.Q. Zhu, M. Odavic, "Comparison of Two-Individual Current Control and Vector Space Decomposition Control for Dual Three-Phase PMSM", *IEEE Trans. on Industry Application*, vol. 53, no. 5, pp. 4483-4492, 2017.
[**DOI:** 10.1109/TIA.2017.2703682]

[24] A.H. Almarhoon, "Sensorless Control of Dual Three-phase Permanent Magnet Synchronous Machine Drives", *Ph.D. Thesis, The University of Sheffield*, 2016.
[**DOI :10.3390/en16031326**]

[25] L.R. Rocha, E.C. Silva, P.H.A. Silva, G.X. Prestes, B.C.R. Cordeiro, L.F. Pessoa, R.P. Vieira, "Evaluation Methodology of Current Control Techniques for Torque Ripple Reduction in Non-Sinusoidal PMSM", *IEEE 8th Southern Power Electronics Conference (SPEC)*, 2023.
[**DOI:**10.1109/SPEC56436.2023.10407773]

[26] M.J. Nam, J.H. Kim, K.Y. Cho, H.W. Kim, Y. Cho, "Torque Ripple Reduction of an Interior PM Synchronous Motor by Compensating Harmonic Currents Based on Flux Linkage Harmonics*", Journal of Power Electronics*, vol. 17, no. 5, pp. 1223-1230, 2017.
[**DOI:**10.6113/JPE.2017.17.5.1223]

[27] S. Mu, J. Kang, Z. Zhong, Z. Ma, "Improved detecting method for multiple rotating reference frames based harmonic control of PMSMs", *Chinese Automation Congress (CAC)*, pp. 5458-5463, pp. 2020.
[**DOI:** 10.1109/CAC51589.2020.9327812]

[28] J. Taylor, D.F. Valencia Garcia, W. Taha, M. Mohamadian, "Dynamic Modelling of Multiphase Machines Based on the VSD Transformation," *SAE Technical Paper 2021-01-0774*, doi:10.4271/2021-01-0774, 2021.
[**DOI:**10.4271/2021-01-0774]

[29] A. Halvaei Niasar, M. Ahmadi, S.H. Edjtahed, "Sensorless Control of Non-Sinusoidal Permanent Magnet Brushless Motor Using Selective Torque Harmonic Elimination Control Method Based on Full-Order Sliding Mode Observer", *Advances in Power Electronics Journal*, vol. 2016, no. 9358604, pp. 1-13, 2016.
[**DOI**:10.1155/2016/9358604]

[30] D.G. Luenberger, Y. Ye, "Linear and Nonlinear Programming," *Springer*, 2008.
[**DOI:** 10.2307/1240727]

[31] 24H. Ghanayem, M. Alathamneh, R.M. Nelms, "A Comparative Study of PMSM Torque Control using Proportional-Integral and Proportional-Resonant Controllers", *IEEE SoutheastCon*, pp. 453-458, 2022.
[**DOI:** 10.1109/SoutheastCon48659.2022.9764111]

[32] 25H. Park, T. Kim, Y. Suh, "Fault-Tolerant Control Methods for Reduced Torque Ripple of Multiphase BLDC Motor Drive System Under Open-Circuit Faults", *IEEE Trans. on Industry Applications*, vol. 58, no. 6, pp. 7275-7285, Nov./Dec. 2022.
[**DOI:** 10.1109/TIA.2022.3191633]

Davood Maleki, was born in 1980 in Malayer, Iran. He received a Bachelor's degree in Electronics and a Master's degree in Electrical Machines from Malek Ashtar Industrial University in Shahin Shahr, Isfahan. His Bachelor's thesis was on the design of a buck-boost regulator for a 400 to 24 converter, and His Master's thesis focused on the construction of an LSPMSM drive. He is currently a PhD student at University of Kashan. His interests are control and implementation of multi-phase PMSM drives.

Abolfazl Halvaei Niasar, (S'04–M'06–SM'14) was born in Kashan, Iran in 1974. He received his B.Sc., M.Sc., and Ph.D. in 1996, 1999, and 2008 from Isfahan University of Technology (IUT), University of Tehran (UT) and Iran University of Science and Technology (IUST) respectively, all in electrical engineering. He has joined the Department of Electrical and Computer Engineering at University of Kashan, Kashan, Iran since 2008 as assistant professor. He has authored more than 150 technical papers published in journals and conference proceedings. He is the holder of two Iranian patents and has directed some industrial research projects in field of electrical drives. His current major research interests include PM and brushless DC motor (BLDC) drives, sensorless drives, design, analysis and control of electrical machines. Dr. Halvaei is senior member of the Institute of Electrical and Electronics Engineers, IEEE.

IECO

This page intentionally left blank.

International Journal Of
Industrial Electronics Control and Optimization
Print ISSN: 3517-2645
Online ISSN: 3568-2645
Homepage: https://ieco.usb.ac.ir/

Secure PDM: A novel Byzantine Fault Tolerant federated learning framework using a robust PCA-based anomaly detection approach

Khalil Jahani[1] | Behzad Moshiri[2] | Babak Hossein Khalaj[3]

[1]Department of Computer Science, kish International Campus, University of Tehran, Tehran, Iran
[2]School of ECE, College of Engineering, University of Tehran, Tehran, Iran
[3]Department of Electrical Engineering, Sharif University of Technology, Tehran, Iran
Corresponding author: e-mail: moshiri@ut.ac.ir

Article Info

Article type:
Original Article

Article history:
Received: 23-February-2025
Received in revised form: 17-May-2025
Accepted:30-May-2025
Published online: 22-Dec-2025

Keywords:
Federated Learning,
Byzantine fault tolerant,
Predictive Maintenance,
Anomaly detection.

ABSTRACT

With the proliferation of federated learning programs as a suitable framework for protecting user privacy and reducing the computational overhead of AI algorithms, various industries have also turned to the widespread use of this framework in industrial applications such as improving predictive maintenance (PDM). However, despite its increasing applications, several security challenges, such as Byzantine attacks, make the application of federated learning in industries questionable. Byzantine attacks in FL can degrade model performance by injecting malicious updates, causing model divergence or biased learning. This reduces accuracy, and can introduce security vulnerabilities such as backdoors. To address this problem, we propose a Byzantine Fault Tolerant (BFT) federated learning algorithm designed to improve PDM in industrial applications. Our proposed approach uses a PCA-based anomaly detection algorithm to detect and mitigate local Byzantine updates. Also, a game theory-based reward mechanism is designed to promote honest participation and discourage malicious behavior among federated users. The proposed framework is evaluated using the predictive maintenance datasets "AI4I 2020" and "NASA Acoustics and Vibration". The results show that our proposed framework effectively detects and mitigates Byzantine attacks, enhancing the overall reliability of PDM in industrial applications.

I. Introduction

Today, federated learning has been a promising computational field that enables decentralized training of models across multiple devices while preserving data privacy [1, 2]. One of the main capabilities of federated learning is the distributed learning capability. It allows the use of distributed data sources without centralized data processing or storage. The main advantage of this capability is that this practical feature of federated learning reduces concerns about the data privacy of network users. It also reduces the computational overhead. Despite its advantages, one of the significant challenges this FL capability brings is ensuring the integrity and reliability of the learning process [3]. One of the most critical challenges is the presence of Byzantine faults—malicious or faulty updates from compromised participants that can degrade the performance of the global model or even lead to catastrophic failures [4, 5].

In federated learning, one of the main assumptions that can be made about local Byzantine nodes is that they are malicious or faulty participants that intentionally change the weights or gradients of their local updates before sending them to the central server for aggregation [6, 7]. These nodes can significantly disrupt the training process by injecting corrupted or misleading data, compromising the global model's integrity and accuracy. Because the central federated learning server relies on collecting local updates from multiple distributed nodes to refine the global model repeatedly, the presence of Byzantine nodes distorts the aggregated results, leading to a corrupted or biased global model that may perform poorly in the overall data distribution [7, 8].

To handle this problem, we propose a BFT federated learning framework using a PCA-based anomaly detection algorithm. Our proposed algorithm prevents local Byzantine updates after detection and ensures the reliability of the federated learning process. The proposed algorithm

identifies anomalous patterns in local model updates that exhibit potential Byzantine behavior. Then, it filters them before they affect the global model.

Enhancing PDM with our proposed PCA-based anomaly detection algorithm improves the accuracy and reliability of predictive maintenance models. It also leads to more effective maintenance plans, reduced downtime, and extended equipment lifetime.

This paper describes our proposed BFT-FL framework and how to integrate it with PDM applications. Then, we evaluate our framework and demonstrate its effectiveness in detecting and mitigating Byzantine attacks. We also discuss the impact of our proposed framework on improving PDM parameters (precisely, the Remaining Useful Life criterion).

A. Our contributions

This paper proposes a Byzantine fault-tolerant federated learning framework that can be integrated with PDM systems to enhance predictive maintenance. Our approach proposes a novel PCA-based anomaly detection algorithm, which detects anomalous local updates sent by byzantine local nodes. The anomaly detection algorithm also specifies the anomaly severity of each local update, indicating the potential impact of that malicious update if it has not been prevented. After the byzantine updates are detected and prevented, the benign updates will be given to an aggregation module, obtaining the new global model, which will be sent to local nodes as the updated global model.

To encourage the local nodes to behave honestly, a game theory-based reward/penalty module has been designed that uses historical trust scores of nodes and assigns them rewards/penalties based on their scores. This module also uses the weights given by the anomaly detection algorithm to update the historical scores of local nodes. Briefly, our main contributions are:

- A novel byzantine fault tolerant federated learning framework with appropriate performance for use in PDM system to improve the PDM technology.
- Designing a PCA-based anomaly detection system that detects and prevents anomalous local updates.
- Using a Game Theory-based incentivization and reward/penalty mechanism encourages local nodes to behave honestly and minimizes the impact of byzantine local nodes on the global model.
- Designing an interactive weighted aggregation mechanism that takes the weight vector of local updates from the Game Theory-based incentivization module and then implements a weighted aggregation of local updates.
- Ability to detect and prevent dynamic byzantine nodes on each round.

B. Paper organization

The remainder of this paper is organized as follows. In section 2, we explain some related works. Section 3 explains our proposed federated learning architecture by describing the designed anomaly detection and incentivization/reward-penalty modules. In Section 4, we present and discuss the achieved results. Finally, Section 5 concludes the paper and proposes possible future works.

II. Related work

In this section, we review several of the most critical secure aggregation techniques to mitigate the impact of Byzantine attacks. The goal of these methods is to detect and prevent malicious updates and ensure that the aggregation process is robust to adversarial attacks. For example, Byzantine- resistant Cosine Similarity Aggregation [9], Krum [10], and Trimmed Mean [11] are designed to filter out or mitigate the impact of outlier updates that deviate significantly from the majority. In addition, anomaly detection mechanisms can identify and remove updates that exhibit suspicious patterns indicative of Byzantine behavior. By combining these strategies, FL systems can increase their robustness and reliability and maintain global model integrity even in the presence of adversarial participants. This section briefly describes previous work on secure aggregation mechanisms and BFT ML algorithms.

The work in [12] introduces “BytoChain”, a framework that integrates blockchain technology with federated learning to enhance security and integrity, especially at the network’s edge. BytoChain uses a Byzantine-resistant consensus mechanism, Proof of Accuracy (PoA). This approach also decentralizes the aggregation process to reduce the influence of malicious nodes.

In [13], a blockchain-based FL framework is proposed to address Byzantine challenges. It uses fully homomorphic encryption to ensure all data is encrypted during aggregation, preventing data manipulation. Blockchain technology records and verifies transactions to increase the transparency of the learning process.

In [14], an approach called “BDFL” focuses on the specific needs of autonomous vehicles by developing a centralized, decentralized, fault-tolerant, Byzantine learning method. It combines Peer-to-Peer (P2P) learning with strong Byzantine fault-tolerant protocols, including publicly verifiable secret sharing, to enhance the safety of data exchange and model aggregation.

The FLTH algorithm introduced in [15] uses reliable data and historical performance metrics to assess the reliability of participating nodes. The method dynamically adjusts the influence of each node based on its reputation and filters out malicious or untrustworthy contributions.

The research in [16] presents the BREA framework, which incorporates stochastic quantization, verifiable outlier detection, and secure aggregation to defend against Byzantine users in federated learning environments. BREA

is designed to detect and exclude anomalous updates, ensuring the integrity of the model aggregation process.

The study in [17] explores a decentralized approach to federated learning that enhances resistance to Byzantine faults by distributing the aggregation function across multiple nodes. Using consensus mechanisms similar to those in blockchain technology, the method ensures that multiple parties validate all updates before integration.

The research in [18] proposes a federated learning framework that ensures Byzantine fault tolerance even under semi-honest and Byzantine behaviors among participants. The approach leverages the Expectation-Maximization algorithm to distinguish between benign and Byzantine participants. The framework can reliably identify malicious participants by evaluating the performance of randomly generated candidate models using all participants' datasets.

The study in [19] addresses the challenge of Byzantine resilience in edge-based clustering. The authors introduce a distributed gradient descent algorithm with Byzantine resilience optimized for convex and non-convex stochastic problems. In this study, gradient compression is also used to increase communication efficiency and maintain an optimal statistical error rate in the presence of Byzantine adversaries.

The study in [20] introduces a local gradient descent algorithm with a comparative elimination filter to effectively counter Byzantine attacks. It is assumed that agents may provide incorrect data intentionally or due to errors caused by system failures in the considered system. The study distinguishes between deterministic settings (exact error tolerance) and stochastic settings (approximate error tolerance) and examines the algorithm's robustness under different adversarial conditions.

Despite the numerous advantages of previously proposed schemes, they suffer from certain challenges and limitations that drive us toward designing a new secure aggregation mechanism. One of the main limitations associated with the implementation of most of these schemes is the low speed of the aggregation process due to the use of blockchain-based, peer-to-peer, secret sharing, and distributed architectures. Moreover, it should be noted that the use of blockchain-based and peer-to-peer architectures potentially leads to the violation of the confidentiality of clients' local models.

Our proposed scheme addresses the challenges and limitations mentioned in previous works by introducing a lightweight and computationally efficient secure aggregation mechanism that ensures minimal information disclosure among clients while maintaining high accuracy in detecting and mitigating Byzantine nodes in FL environments.

III. The proposed approach

In this section, we explain our proposed approach. The system architecture of our method comprises a PCA-based anomaly detection module, a Game Theory-based incentivization/reward-penalty mechanism, and an aggregation integrator module, which takes the outputs of those modules as inputs and sends the final benign updates and their weights to the central server for aggregation. Figure 1 shows the proposed architecture.

The PCA-based anomaly detection module sits between the end nodes and the federated learning server, taking local updates sent by end devices to the central server. It detects anomalous updates and prevents them from reaching the server. Finally, it sends a severity vector of local updates to the aggregation integrator module. The severity of each local update indicates the value of its outlierness and anomaly. Severity values near 1 show a high probability of the client being anomalous, while values near 0 show a potentially normal client.

The Game Theory-based incentivization/reward-penalty mechanism upgrades the historical status of local devices, using their historical records and the current severity vector of their updates calculated by the anomaly detection module. It then sends the upgraded historical status of local devices to the aggregation integrator module.

Finally, the aggregation integrator module sends the upgraded historical status of local devices and their updates to the server. This process repeats at each global training round.

Here, we explain the architecture of our PCA-based anomaly detection, Game Theory-based incentivization/reward- penalty mechanism, and global model, which is updated using this architecture.

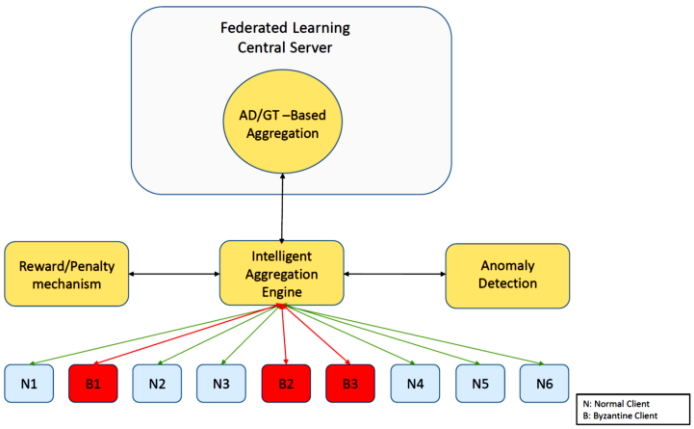

Fig. 1. The architecture of proposed Byzantine Fault Tolerant federated learning framework

A. PCA-Based anomaly detection

In this section, we describe the proposed anomaly detection algorithm. This algorithm works as follows:

1. Preprocessing: converting local models' weights to vectors with fixed length
2. Feeding the PCA algorithm with an initial set of benign local models' weights
3. Transforming the local updates using the PCA algorithm
4. Calculating the upper and lower bounds of the principal components with eigenvalues less than a

fixed threshold (in this case, below 1% of total variance)

5. Finding the outliers and calculating the severity of each one, according to their outliers' values on each of the principal components
6. Sending the index of anomalous updates and their severity values as the output

Figure 2 shows an example of principal components (PC) 1 and 15 without Byzantine nodes. The transformed data are divided into time intervals for a specific end device. Since the smoothed updated weight vector of the model resulting from each local device has more than 3500 elements, we divided it into vectors with lengths equal to 50 to facilitate the analysis. Therefore, each end device has about 70 rows of data.

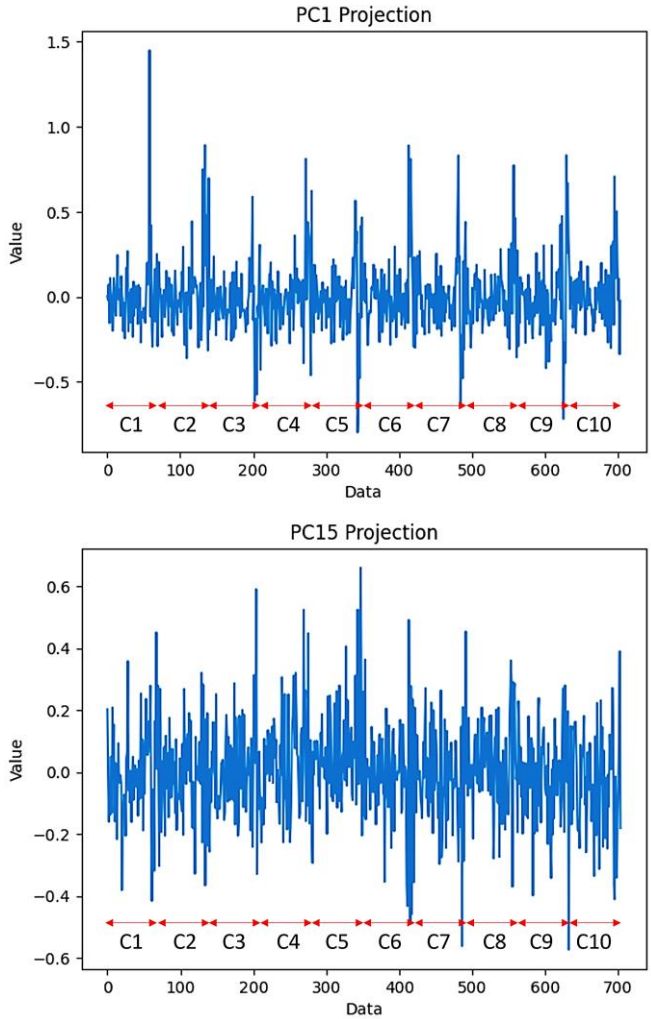

Fig. 2. The principal components PC1 and PC15 of benign local updates. In this example, we have ten end devices.

B. Incentive mechanism

In this section, we describe the exponential weighting incentive mechanism. This mechanism is a practical approach used in the proposed BFT federated learning framework to assign weights to local updates from different local devices. It uses the historical score of each local device to determine the impact of its new update in the network.

At the beginning, each device is assigned an initial score (denoted S_0). We assume this initial score to be uniform across all devices.

$$s_{t+1} = s_t + \gamma \Delta s_t \tag{1}$$

For each device, this score is continuously updated over time, based on the validity of its submitted updates. In the next step, valid updates increase the score, while malicious updates decrease it. We formulate the score update rule as follows:

where s_t is the score at time t, γ is a constant coefficient, which we set to 1 for simplicity. Δs_t is the change in the score at time t, determined by whether the update is valid or malicious and is formulated as follows:

$$\Delta s_t = \begin{cases} +\beta_1 & \text{If update is valid} \\ -\beta_2 & \text{If update is malicious} \end{cases} \tag{2}$$

where β_1 is the positive reward increment for valid updates, and β_2 is the penalty for malicious updates. Since we want our mechanism to be as strict as possible with Byzantine nodes and ensure that the impact of any malicious update from a client remains negligible on the global model updates for a long time, we choose the values of β_1 and β_2 such that $\beta_1 \ll \beta_2$. In this case, we assume β_1=1 and β_2=10.

These calculated historical scores show the reliability of each local client at each timestamp. Our mechanism then uses these scores to calculate new weights for each user through an exponential function. This weighting mechanism ensures that local users with higher scores receive higher exponential weights. The proposed method makes a significant distinction between trusted users and Byzantine users of trust, which increases the overall robustness of the federated learning model against Byzantine attacks.

We calculate a normalized exponential function for each historical score to calculate its weight in the final exponential weighting. We normalize these values so that their sum stands equal to one. Mathematically, this is expressed as:

$$\alpha_i(t) = \frac{\exp(s_i(t))}{\sum_{j=1}^{N} \exp(s_j(t))} \tag{3}$$

This approach also amplifies the differences in scores and makes the influence of trusted local devices more prominent. The progressive weighting gives local devices a high incentive to maintain or improve their performance over time because, given the scoring mechanism, even a slight improvement in their scores can significantly increase their weights. This approach causes a better performance of the BFT federated learning framework.

C. Global model update

The global model update module in a Byzantine Fault Tolerant (BFT) federated learning framework is essential for integrating local updates into a single, cohesive global model. This module uses weights obtained from the Exponential Weighting incentivization mechanism, ensuring that participants with a history of reliable contributions significantly influence the global model. The weighted aggregation of the local updates is mathematically expressed as:

$$w_{\text{global (t)}} = \sum_{i=1}^{N} \alpha_{i(t)} w_{i(t)} \tag{4}$$

where $w_{\text{global (t)}}$ is the global model, $w_{\text{i(t)}}$ represents the local update from local client i, and $a_{\text{i(t)}}$ denotes the weight assigned to local client i at time t. As said before, this weight is derived from the mentioned incentivization mechanism.

In addition to the weighting mechanism, the global model update module also utilizes the scores of each client in another way. This algorithm, in each round, removes the updates of clients with negative scores from the global aggregation process before it is performed. This pipeline design helps the final global model by allowing it to correct local updates before weighting and aggregation, ensuring greater integrity of the global model.

IV. Results and discussion

This section evaluates our model by implementing several byzantine scenarios and comparing federated learning performance with and without our proposed architecture.

Byzantine scenarios

In a federated learning scenario, imagine a network of local devices in a distributed system participating in collaborative training of a machine learning model. These local devices are responsible for updating their weights based on their local data and sending them to a central server for aggregation and model updating. However, in this scenario, some local devices are compromised or malfunctioning, exhibiting Byzantine behavior.

Byzantine local devices intentionally modify their updated weights before sending them to the central server. This can include injecting spurious gradients by manipulating the weight updates and producing incorrect weight values. As a result, the central server needs to receive consistent and correct information from these Byzantine local devices during the aggregation process.

Unaware of Byzantine behavior, the central server incorporates these falsified weights into its model aggregation process, leading to erroneous global model updates. This can have significant repercussions, mainly if the central server heavily relies on the accuracy of the weights provided by the local devices for global model training.

Datasets

In the following sections, we evaluate our proposed model on two useful predictive maintenance datasets:

- AI4I 2020 Predictive Maintenance: This is a labeled sensory dataset that contains values for air temperature, process temperature, rotational speed, torque, and tool wear sensors for various industrial equipment. Each row of this dataset is labeled with a binary value indicating machine failure.
- NASA Acoustics and Vibration: This is an unlabeled sensory dataset that records the simulated vibrational behavior of four bearings over two weeks, capturing their normal and abnormal behavior until the end of their lifespan.

The reason for choosing the AI4I 2020 dataset is its suitable structure for partitioning it among different clients. In this dataset, the sensor data associated with each machine is listed in different situations along with its failure or non-failure status. This makes it an ideal candidate for federated learning environments where each client can process its respective machine's data. The reason for choosing the NASA Acoustics and Vibration dataset is that it has a time series structure to analyze the failure status of 4 bearings throughout the entire life of the equipment, from the initial anomaly observation to their failure. Therefore, using this dataset in the analyses provides a good visual and numerical view of the impact of our proposed system on system performance in estimating the remaining life of each equipment.

A. Evaluation on AI4I 2020 Dataset:

This section evaluates our Federated Learning model on the "AI4I 2020" dataset. To evaluate this labeled dataset, we assess the system under three scenarios:

- A normal scenario without Byzantine behavior.
- Scenarios with Byzantine ratios of 0.2, 0.4, and 0.6, but without the anomaly detection module.
- Scenarios with Byzantine ratios of 0.2, 0.4, and 0.6, including the anomaly detection module.

We compare the accuracy and loss of the federated learning framework across these three scenarios to demonstrate the importance and effectiveness of our proposed BFT architecture. Under the first scenario, where there are no Byzantine nodes, the federated learning algorithm achieves an accuracy of 90% and a loss of 0.22. In the second situation, where there are Byzantine nodes in 3 different scenarios (Byzantine portions equal to 0.2, 0.4, and 0.6) but no anomaly detection module, Table I indicates the accuracy and loss values of the federated learning algorithm. The results indicate the adverse impact of Byzantine nodes on

system performance, causing, for instance, a 17% reduction in accuracy in one scenario. Finally, the third scenario repeats the Byzantine cases, but our anomaly detection module is applied to the architecture this time. The results show that our approach significantly improves the performance of the FL algorithm by detecting and reducing all Byzantine updates. For example, in this scenario, our approach improves the accuracy by approximately 16% and reduces the loss by approximately 0.53, which emphasizes the effectiveness of our proposed architecture.

We have also compared the results of our proposed method with those of two well-known approaches, Krum aggregation and Trimmed-Mean. As shown in Table I, our proposed method achieves better results in all three Byzantine scenarios.

TABLE I COMPARISON OF THE RESULTS OF THE FL ALGORITHM EVALUATION USING AI4I 2020 DATASET WITH DIFFERENT PORTIONS OF BYZANTINE NODES WITH AND WITHOUT ANOMALY DETECTION MODULE

Scenarios	Metrics	Byzantine = 0.2	Byzantine = 0.4	Byzantine = 0.6
Without anomaly detection	Accuracy	86.5%	84.1%	73.56%
	Loss	0.28	0.33	0.78
Krum aggregation [10]	Accuracy	88.92%	88.70%	88.61%
	Loss	0.258	0.269	0.277
Trimmed-Mean [11]	Accuracy	89.48%	89.4%	84.3%
	Loss	0.238	0.261	0.497
One-Shot Federated Learning with PCA-based detection	Accuracy	82.57%	82.35%	78.29%
	Loss	0.326	0.367	0.511
Our Proposed Framework	**Accuracy**	**89.90%**	**89.83%**	**89%**
	Loss	**0.237**	**0.245**	**0.256**

Figures 3 and 4 show the performance of the anomaly detection module in two different scenarios. In the first scenario, nodes 2 and 8 are Byzantine, while nodes 4 and 6 are Byzantine in the second scenario. As the figures show, our proposed anomaly detection can successfully detect all Byzantine nodes due to their outlierness.

B. Evaluation on NASA Acoustics Dataset:

In this section, we evaluate our Federated Learning model using the "NASA Acoustics and Vibration" dataset under similar conditions discussed in the previous section. We extend our evaluation by calculating each scenario's RUL and

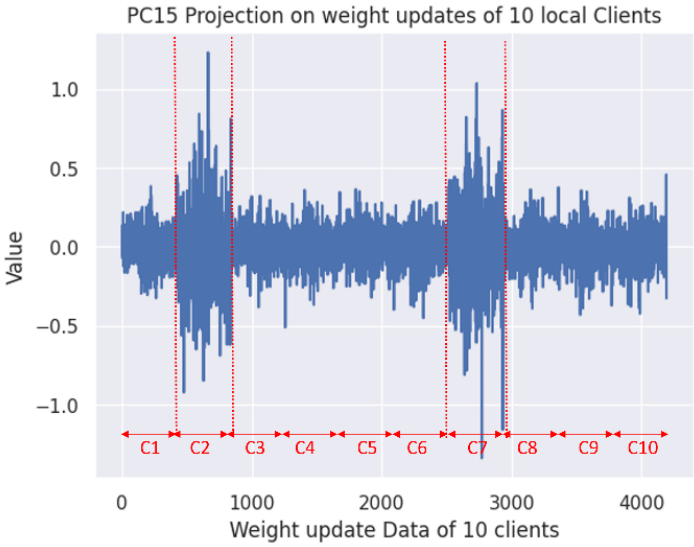

Fig. 3. The principal components PC15 of local updates. In this example, we have ten end devices. In this example, nodes 2 and 7 are byzantine.

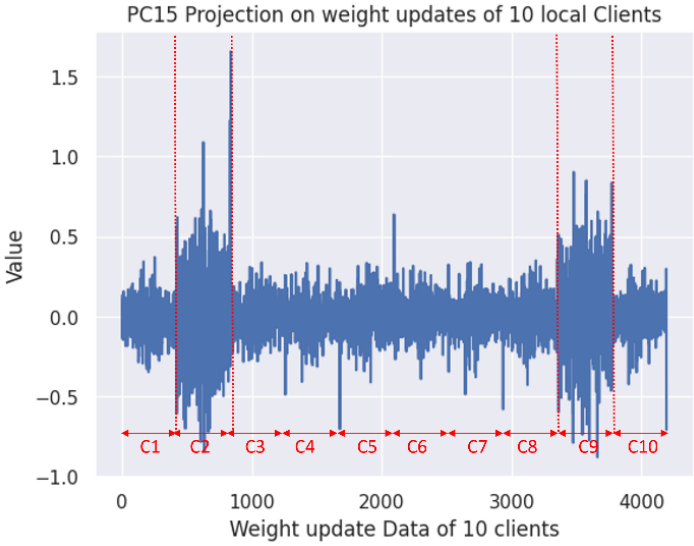

Fig. 4. The principal components PC15 of benign local updates. In this example, we have ten end devices. In this example, nodes 2 and 9 are byzantine.

RMSE parameters. We demonstrate the negative impact of Byzantine attacks on calculating the RUL criterion, one of the most critical parameters in PDM. The byzantine attack may deceive industry experts by suggesting incorrect RUL values. We investigate this in two main cases: producing overestimated or underestimated RUL values.

Overestimated RUL values lead to incorrect planning for equipment replacement and repair. This planning error occurs when maintenance experts mistakenly believe the equipment has more remaining life than it actually does. As a result, they schedule repairs or replacements too late after the equipment has already failed, which leads to equipment failure before repairs are scheduled. It causes significant damage and financial losses for the organization. Such failures may result

in irreparable damage to the equipment, damage to related machinery, and costly production line shutdowns during the time needed for repairs.

Conversely, underestimated RUL values cause maintenance specialists to schedule repairs or replacements much earlier than necessary. This leads to premature repairs or replacements, significantly increasing maintenance costs. In this case, in a fixed period, specialists are called more often to repair and replace the equipment, and secondly, more equipment is purchased because the entire life of the equipment is not used.

To evaluate the effectiveness of our proposed framework under the aforementioned Byzantine scenarios, we implemented and trained an LSTM-Autoencoder (LSTM-AE) as the core anomaly detection model. This model is utilized to construct a robust Health Index (HI) based on its reconstruction error, which reflects the deviation of input data from learned normal behavior.

The selection of the LSTM-AE architecture is motivated by its synergistic integration of two powerful components:

- Long Short-Term Memory (LSTM) networks, which are well-established for their ability to capture and model complex temporal dependencies inherent in time-series data.
- Autoencoders, which are proficient at learning compressed latent representations of the input data and identifying anomalous patterns by detecting deviations from the training distribution.

Together, these characteristics make the LSTM-AE model particularly well-suited for anomaly detection in sequential industrial data, enabling effective identification of Byzantine behaviors within the federated learning environment.

Table II summarizes the architecture of the LSTM-Autoencoder model. The Health Index (HI), derived from the reconstruction error, is passed through a Kernel Density Estimation (KDE) function to analyze the distribution of training loss values. Based on this distribution, an anomaly detection threshold is determined, set to exceed 95% of the training error values. This threshold is used to identify anomalous behavior. Following anomaly detection, the resulting reconstruction error sequence is used to train an LSTM regression model, which estimates the Remaining Useful Life (RUL) at each time step.

The results of our implementation are shown in Table III. Figure 5 shows the RUL curve in a normal scenario with no byzantine behavior. The RMSE value calculated in this scenario is equal to 63.47. Figure 6 shows the RUL curve in the first byzantine scenario in which there 20% of nodes have byzantine behavior. The RMSE values calculated in this scenario where there is no byzantine detection module and where our proposed method is used are equal to 149.85 and 78.21, respectively. Finally, Figure 7 shows the RUL curve in the second byzantine scenario in which 40% of nodes have byzantine behavior. The RMSE values calculated in this scenario where there is no byzantine detection module and where our proposed method is used are equal to 409.06 and 97.01, respectively. The results indicate the effectiveness of our proposed Byzantine detection model, which reduces the RMSE in Byzantine scenarios by up to 76%.

TABLE II COMPARISON OF THE RESULTS OF THE FL ALGORITHM EVALUATION USING NASA ACOUSTICS AND VIBRATION DATASET WITH DIFFERENT PORTIONS OF BYZANTINE NODES WITH AND WITHOUT ANOMALY DETECTION MODULE

Layer (type)	Output Shape	Params
input1(Input Layer)	(None, 1, 4)	0
lstm (LSTM)	(None, 1, 32)	4736
Leaky relu (Leaky ReLU)	(None, 1, 32)	0
Batch normalization (Batch Normalization)	(None, 1, 32)	128
dropout (Dropout)	(None, 1, 32)	0
lstm1(*LST M)*	(None, 16)	3136
leakyrelu1(Leaky ReLU)	(None, 16)	0
Batch normalization1(Batch Normalization)	(None, 16)	64
Repeat vector (Repeat V ector	(None, 1, 16)	0
lstm2(*LST M)*	(None, 1, 16)	2112
leakyrelu2(Leaky ReLU)	(None, 1, 16)	0
batchnormalization2(Batch Normalization)	(None, 1, 16)	64
dropout1(*Dropout*)	(None, 1, 16)	0
lstm3(*LST M)*	(None, 1, 32)	6272
leakyrelu3(Leaky ReLU)	(None, 1, 32)	0
batchnormalization3(Batch Normalization)	(None, 1, 32)	128
time distributed (Time Distributed)	(None, 1, 4)	132

Similar to the previous part, we have also compared the results of our proposed method with those of two aggregation methods, Krum and Trimmed-Mean. As shown in Table III, our proposed method achieves better results in all three scenarios: without Byzantine nodes, with Byzantine nodes at a ratio of 0.2, and with Byzantine nodes at a ratio of 0.4.

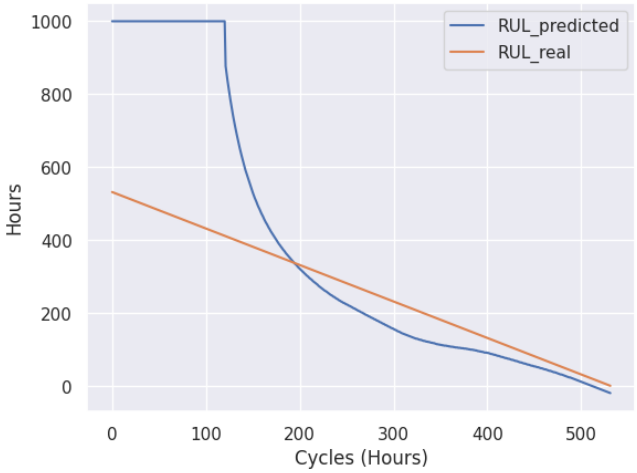

Fig. 5. The RUL curve is estimated in case no byzantine behavior exists.

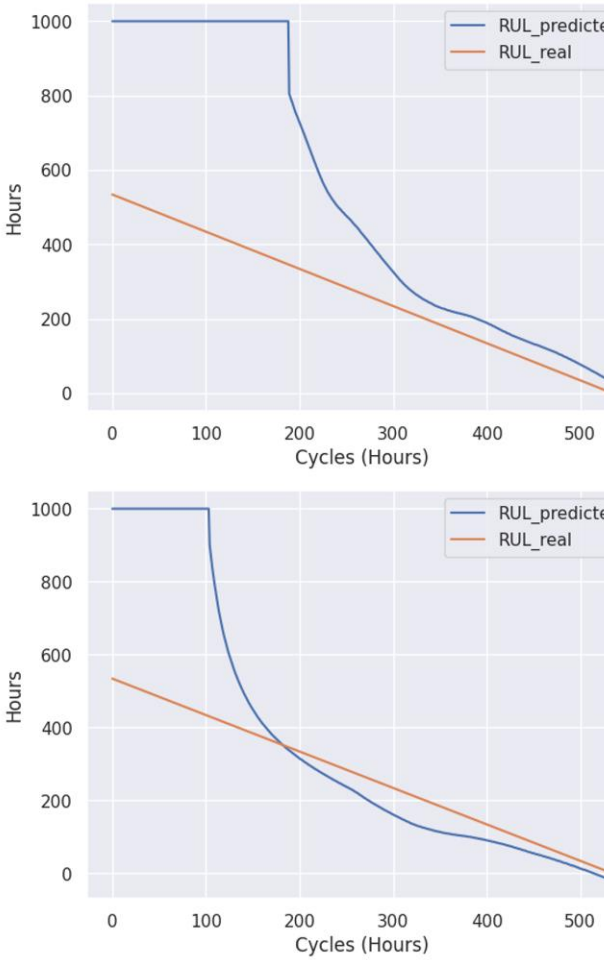

Fig. 6. Comparison of RUL estimations in two scenarios. When 20% of nodes are byzantine without any detection module(above), and when our detection module is used (below).

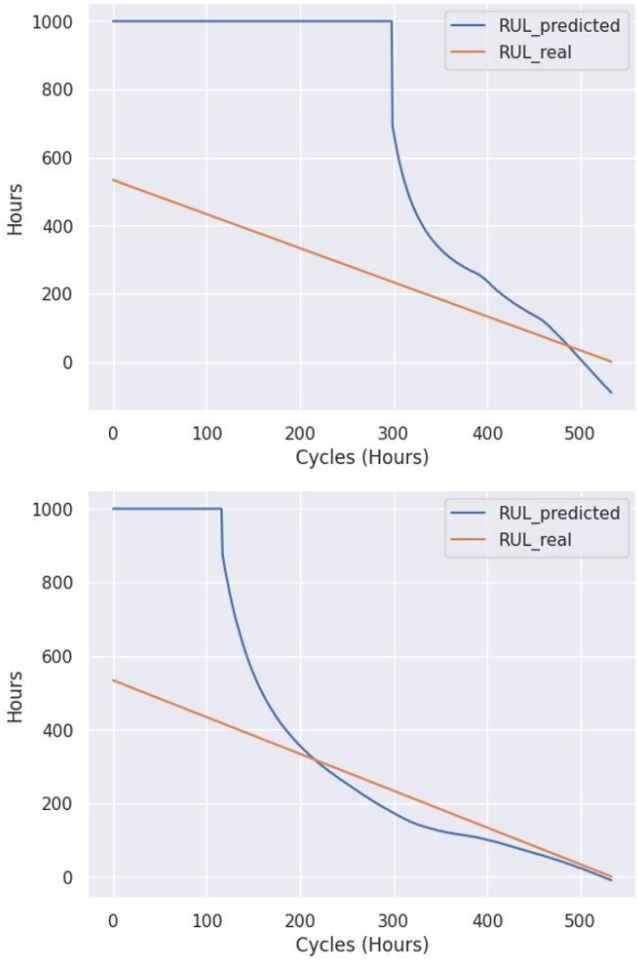

Fig. 7. Comparison of RUL estimations in two scenarios. When 40% of nodes are byzantine without any detection module(above), and when our detection module is used (below).

TABLE III COMPARISON OF THE RMSE RESULTS OF THE FL ALGORITHM EVALUATION WITH THE NASA ACOUSTICS AND VIBRATION DATASET FOR DIFFERENT PORTIONS OF BYZANTINE NODES, WITH AND WITHOUT THE ANOMALY DETECTION MODULE.

Scenarios	Byzantine = No Byzantine	Byzantine = 0.2	Byzantine = 0.4
Without anomaly detection	67.43	149.85	409.06
Krum aggregation [10]	67.43	116.19	166.98
Trimmed-Mean [11]	67.43	163.41	175.31
One-Shot Federated Learning with PCA-based detection	67.43	158.1	173.9
Our Proposed Framework	**67.43**	**78.21**	**97.01**

C. Comparison with One-Shot PCA-FL

To provide a comprehensive performance comparison, we also implemented a one-shot federated learning approach that uses PCA-based anomaly detection only in a single round—without historical scoring or incentivization. This method performs anomaly detection at the first round, filters out suspected updates, and aggregates the remaining updates once to form the global model.

The results showed that while the one-shot approach is faster due to its non-iterative structure, its performance in terms of accuracy and Byzantine resilience was significantly lower than our proposed multi-round BFT-FL framework. For example, in the AI4I 2020 dataset with 40% Byzantine nodes, the one-shot method achieved an accuracy of ~82.3%, compared to 89.83% for our proposed approach. Similarly, on the NASA Vibration dataset, the RMSE in RUL estimation was ~173.9 for the one-shot method, whereas our framework achieved 97.01.

These results confirm that while one-shot PCA-based FL may offer slight computational advantages, it lacks the robustness and adaptability of our iterative design, especially in dynamic or adversarial environments.

D. Convergence Analysis

We also examined the impact of our proposed BFT-FL framework on the convergence time of the federated learning process. Convergence was defined as the point at which the global model's validation accuracy stabilized with minimal fluctuation. Figure 8 shows the convergence time analysis of our proposed method. In the scenario with no Byzantine nodes on the AI4I 2020 dataset, the baseline FL without any anomaly detection converged in 8 rounds with an average accuracy of ~90%. Our proposed method reached convergence in 9 rounds but achieved a significantly the accuracy of ~89.8% in the scenario with 40% Byzantine nodes. Although the convergence required one additional round, the trade-off is justified by the improved model robustness and reliability. This indicates that the proposed enhancements introduce only a negligible delay in convergence while providing substantial gains in resilience.

E. Computational Cost Analysis

To support our claim that the proposed framework is computationally lightweight, we measured the average runtime of the federated training process across five global rounds with ten clients. The total runtime with the PCA-based anomaly detection module enabled was 985.0410 seconds, while the runtime without the detection module was 980.7393 seconds. This demonstrates that the additional computational cost introduced by our detection mechanism is minimal—approximately 4.3 seconds over five rounds, or less than 1% overhead. Such a negligible increase confirms the efficiency of our design and shows that the anomaly detection process can be integrated into industrial PDM systems without introducing significant latency or resource burden.

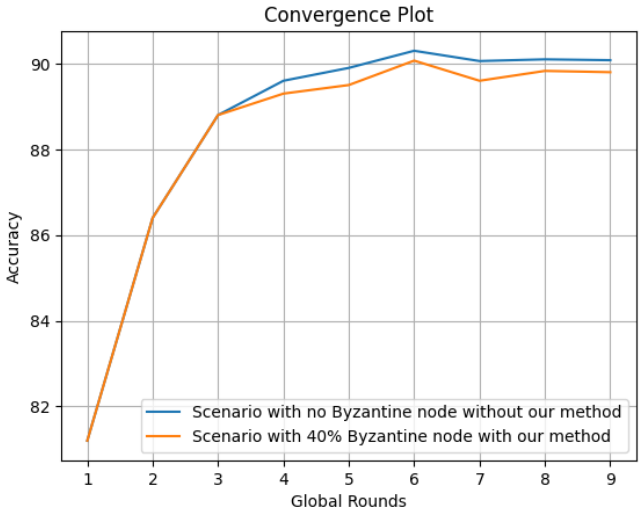

Fig. 8. The convergence time analysis of our proposed method in comparison with the scenario which our method is not used.

V. CONCLUSION AND FUTURE WORK

In this paper, we proposed a novel Byzantine Fault-Tolerant Federated Learning framework, designed improve the reliability of PDM application in industry. The proposed frame- work employed a PCA-based anomaly detection algorithm to detect and mitigate Byzantine local updates, ensuring the integrity and accuracy of the global model. Additionally, we incorporated a game theory-based incentive mechanism to motivate normal behavior and deter malicious behavior among local clients.

The results of evaluating our framework using the "AI4I 2020" and "NASA Acoustics and Vibration Predictive Maintenance" Datasets showed significant improvements in fault tolerance and so model performance.

Our approach provides a secure and scalable solution for maintaining federated learning models' performance, security, and integrity in critical industrial applications. By ad- dressing the challenges associated with Byzantine faults and promoting honest participation through incentivization, our framework ensures that the benefits of federated learning can be realized even in adversarial environments.

While our proposed framework has shown promising results, several avenues for future research and improvements exist, including extending to more complex datasets, enhancing anomaly detection, scalability, and efficiency, real-world implementation, exploring other incentive mechanisms, and security enhancements.

The current study assumes an ideal communication channel between clients and the central server. In practice, communication noise (e.g., due to fading or interference) can corrupt transmitted model updates. We plan to investigate how such non-idealities affect the integrity of weight transmission and evaluate whether our PCA-based anomaly

detection mechanism can also mitigate channel-induced distortions. Exploring the use of error-correcting codes or robust compression techniques will be an important step in enhancing the framework's resilience.

By addressing these future directions, we can continue to advance secure federated learning and its applications in industrial predictive maintenance, ensuring that these systems are resilient, reliable, and capable of delivering accurate and timely insights.

Strengthening the PCA-based anomaly detection module to detect more complex Byzantine scenarios and exploring more advanced reward/penalty mechanisms can be considered as our future work.

It is worth noting that this approach has been able to lead to significant performance improvements in a real industrial PDM scenario. Specifically, the proposed model has shown a 16% improvement in prediction accuracy and a 76% reduction in RMSE compared to the baseline methods. These results indicate the high potential of the proposed method for application in industries to more accurately and quickly detect potential equipment failures.

REFERENCES

[1] H. Brendan McMahan, E. Moore, D. Ramage, S. Hampson, B. Agüera y Arcas, "Communication-Efficient Learning of Deep Networks from Decentralized Data," Proceedings of the 20 th International Conference on Artificial Intelligence and Statistics (AISTATS) 2017. JMLR: W&CP volume 54, last revised 26 Jan 2023 (v4), doi: https://doi.org/10.48550/arXiv.1602.05629.

[2] L. Li, Y. Fan, M. Tse, and K.-Y. Lin, "A review of applications in federated learning," Computers & Industrial Engineering, vol. 149, p. 106854, 2020, doi: https://doi.org/10.1016/j.cie.2020.106854.

[3] J. Zhang, H. Zhu, F. Wang, J. Zhao, Q. Xu, and H. Li, "Security and Privacy Threats to Federated Learning: Issues, Methods, and Challenges," Security and Communication Networks, vol. 2022, no. 1, p. 2886795, 2022, doi: https://doi.org/10.1155/2022/2886795.

[4] K. Jahani, B. Moshiri and B. Hossein Khalaj, "PPFL: Privacy-Preserving Techniques in Federated Learning", JAIAI, vol. 1, no. 3, pp. 49–67, Jul. 2024, doi: 10.61838/jaiai.1.3.6.

[5] Q. Xia, W. Ye, Z. Tao, J. Wu, and Q. Li, "A survey of federated learning for edge computing: Research problems and solutions," High-Confidence Computing, vol. 1, no. 1, p. 100008, 2021, doi: 10.1016/j.hcc.2021.100008.

[6] J. Shi, W. Wan, S. Hu, J. Lu, L. Y. Zhang, "Challenges and Approaches for Mitigating Byzantine Attacks in Federated Learning," vol. cs. CR,2022, doi: https://arxiv.org/abs/2112.14468.

[7] A. Gouissem, K. Abualsaud, E. Yaacoub, T. Khattab and M. Guizani, "Federated Learning Stability Under Byzantine Attacks," 2022 IEEE Wireless Communications and Networking Conference (WCNC), Austin, TX, USA, 2022, pp. 572-577, doi: 10.1109/WCNC51071.2022.9771594.

[8] M. Fang, X. Cao, J. Jia, and N. Z. Gong, "Local model poisoning attacks to byzantine-robust federated learning," in 29th USENIX Security Symposium, ed: USENIX Association, 2020, pp. 1623–1640.

[9] T. Zhu Z. Guo, C. Yao, J. Tan, S. Dou, W. Wang, Z. Han, "Byzantine-robust Federated Learning via Cosine Similarity Aggregation," Computer Networks, vol. 254, p. 110730, 2024, doi: https://doi.org/10.1016/j.comnet.2024.110730.

[10] P. Blanchard, E. M. El Mhamdi, R. Guerraoui, and J. Stainer, "Machine Learning with Adversaries: Byzantine Tolerant Gradient Descent," NIPS'17: Proceedings of the 31st International Conference on Neural Information Processing Systems Pages 118 - 128, 2017.

[11] D. Yin, Y. Chen, R. Kannan, and P. Bartlett, "Byzantine-Robust Distributed Learning: Towards Optimal Statistical Rates," presented at the Proceedings of the 35th International Conference on Machine Learning, Proceedings of Machine Learning Research, 2018. [Online]. Available: https://proceedings.mlr.press/v80/yin18a.html.

[12] Z. Li, H. Yu, T. Zhou, L. Luo, M. Fan, Z. Xu, G. Sun "Byzantine Resistant Secure Blockchained Federated Learning at the Edge," IEEE Network, vol. 35, no. 4, pp. 295–301, 2021, doi: 10.1109/MNET.011.2000604.

[13] Y. Miao, Z. Liu, H. Li, K. K. R. Choo, and R. H. Deng, "Privacy-Preserving Byzantine-Robust Federated Learning via Blockchain Systems," IEEE Transactions on Information Forensics and Security, vol. 17, pp. 2848–2861, 2022, doi: 10.1109/TIFS.2022.3196274.

[14] J. H. Chen, M. R. Chen, G. Q. Zeng, and J. S. Weng, "BDFL: A Byzantine-Fault-Tolerance Decentralized Federated Learning Method for Autonomous Vehicle," IEEE Transactions on Vehicular Technology, vol. 70, no. 9, pp. 8639–8652, 2021, doi: 10.1109/TVT.2021.3102121.

[15] X. Luo and B. Tang, "Byzantine Fault-Tolerant Federated Learning Based on Trustworthy Data and Historical Information," Electronics, vol. 13, no. 8, 2024, doi: 10.3390/electronics13081540.

[16] J. So, B. Güler, and A. S. Avestimehr, "Byzantine-Resilient Secure Federated Learning," IEEE Journal on Selected Areas in Communications, vol. 39, no. 7, pp. 2168–2181, 2021, doi: 10.1109/JSAC.2020.3041404.

[17] X. Lin, Y. Li, X. Xie, Y. Ding, X. Wu, and C. Ge, "SF-CABD: Secure Byzantine fault tolerance federated learning on Non-IID data," Knowledge-Based Systems, vol. 296, p. 111851, 2024, doi: https://doi.org/10.1016/j.knosys.2024.111851.

[18] X. Tang, H. Gu, L. Fan, and Q. Yang, "Achieving Provable Byzantine Fault-tolerance in a Semi-honest Federated Learning Setting," in Advances in Knowledge Discovery and Data Mining, Cham, H. Kashima, T. Ide, and W.-C. Peng, Eds., 2023: Springer, https://doi.org/10.1007/978-3-031-33377-4_32.

[19] Y. Tao, S. Cui, W. Xu, H. Yin, D. Yu, W. Liang, X. Cheng, "Byzantine-Resilient Federated Learning at Edge," IEEE Transactions on Computers, vol. 72, no. 9, pp. 2600–2614, 2023, doi: 10.1109/TC.2023.3257510.

[20] N. Gupta, T. T. Doan, and N. Vaidya, "Byzantine Fault-Tolerance in Federated Local SGD Under 2f-Redundancy," IEEE Transactions on Control of Network Systems, vol. 10, no. 4, pp. 1669–1681, 2023, doi: 10.1109/TCNS.2023.3237489.

Khalil Jahani holds a B.Sc. (2012) and M.Sc. (2014) in Information Technology Engineering – Computer Networks from IUST, Tehran. He is currently a Ph.D. candidate in Computer Science – Artificial Intelligence at the University of Tehran, having commenced in 2020. An experienced researcher and developer, he possesses extensive expertise in algorithm design for machine learning, AI, signal processing, and computer vision. As a Senior Algorithm Developer in aviation, he specializes in deep learning applications for anomaly detection, condition monitoring, PHM, and predictive maintenance. He earned AML CAT.B1 (A&P) and CAT.B2 (Avionics) licenses from Iran's Civil Aviation Organization in 2019.

Behzad Moshiri (IEEE Senior Member) received his B.Sc. degree in mechanical engineering from Iran University of Science and Technology (IUST) in 1984 and M.Sc. and Ph.D. in control systems engineering from the University of Manchester, Institute of Science and Technology (UMIST), U.K. in 1987 and 1991, respectively. He has been senior member of IEEE since 2006. He is the author/co-author of more than 360+ articles. He has been an adjunct professor of the Department of ECE at the University of Waterloo since May 2014. He has been a member of "Waterloo AI Institute" since 2018. His research fields include advanced industrial control, advanced instrumentation systems, data fusion theory, and feasibility studies on applications and implementations of sensor/data fusion.

Babak Hossein Khalaj (IEEE Senior Member) received the B.Sc. degree in electrical Engineering from the Sharif University of Technology, Tehran, Iran, in 1989, and the M.Sc. and Ph.D. degrees in electrical engineering from Stanford University, Stanford, CA, USA, in 1993 and 1996, respectively. He has been with the pioneering team at Stanford University, where he was involved in adopting multi-antenna arrays in mobile networks. Since 1999, he has been a Senior Consultant in data communications and a Visiting Professor with CEIT, San Sebastian, Spain, from 2006 to 2007. He has coauthored many papers in signal processing and digital communications and holds four U.S. patents. He received the Alexander von Humboldt Fellowship from 2007 to 2008 and the Nokia Visiting Professor Scholarship in 2018.